Titre: Title:	Development of Fe3Al-Based HVOF Coatings for Wear-Resistant Applications
Auteur: Author:	Fabrice Pougoum
Date:	2018
Type:	Mémoire ou thèse / Dissertation or Thesis
Référence: Citation:	Pougoum, F. (2018). Development of Fe3Al-Based HVOF Coatings for Wear-Resistant Applications [Thèse de doctorat, École Polytechnique de Montréal]. PolyPublie. https://publications.polymtl.ca/3019/

Document en libre accès dans PolyPublie
Open Access document in PolyPublie

URL de PolyPublie: PolyPublie URL:	https://publications.polymtl.ca/3019/
Directeurs de recherche: Advisors:	Ludvik Martinu, Robert Schulz, & Jolanta-Ewa Sapieha
Programme: Program:	Génie physique

UNIVERSITÉ DE MONTRÉAL

DEVELOPMENT OF Fe$_3$Al-BASED HVOF COATINGS FOR WEAR-RESISTANT APPLICATIONS

FABRICE POUGOUM

DÉPARTEMENT DE GÉNIE PHYSIQUE

ÉCOLE POLYTECHNIQUE DE MONTRÉAL

THÈSE PRÉSENTÉE EN VUE DE L'OBTENTION

DU DIPLÔME DE PHILOSOPHIÆ DOCTOR

(GÉNIE PHYSIQUE)

FÉVRIER 2018

UNIVERSITÉ DE MONTRÉAL

ÉCOLE POLYTECHNIQUE DE MONTRÉAL

Cette thèse intitulée :

DEVELOPMENT OF Fe$_3$Al-BASED HVOF COATINGS FOR WEAR-RESISTANT APPLICATIONS

présentée par : POUGOUM Fabrice

en vue de l'obtention du diplôme de : Philosophiæ Doctor

a été dûment acceptée par le jury d'examen constitué de :

Mme SANTATO Clara, Doctorat, présidente

Mme KLEMBERG-SAPIEHA Jolanta-Ewa, Doctorat, membre et directrice de recherche

M. MARTINU Ludvik, Ph. D., membre et codirecteur de recherche

M. SCHULZ Robert, Ph. D., membre et codirecteur de recherche

M. TURENNE Sylvain, Ph. D., membre

M. MEUNIER Jean-Luc, Doctorate, membre externe

DEDICATION

To Fabrice Jr., Hazelle and Hillary...

ACKNOWLEDGEMENTS

I would like to thank my thesis directors, Prof. Jolanta Sapieha and Prof. Ludvik Martinu for offering me the opportunity to work in the Functional Coatings and Surface Engineering Laboratory (FCSEL), and Dr. Robert Schulz for allowing me to carry out my research activities and to collaborate with researchers and technicians of the Institut de Recherche d'Hydro-Québec (IREQ). You trusted me, you supported me, and you guided me throughout this Ph. D. project, I thank you all for that.

I wish to acknowledge the National Sciences and Engineering Research Council of Canada and Hydro-Québec for their financial support without which this project could not be completed.

At the FCSEL, I had the pleasure to work and collaborate with many people. I would like to express my gratitude to all my former and present colleagues from the FCSEL for their constructive discussions and social interactions. In particular, I thank Dr. Simon Gaudet for introducing me to many aspects of this project; Dr. Etienne Bousser and Dr. Thomas Schmitt for teaching me the rigorousness in the experimental research.

The completion of this Ph. D. project could not be possible without the help and assistance of technicians, Francis Turcot, Sébastien Chenard and Yves Drolet from Polytechnique Montreal, and Sylvio Savoie from IREQ. Thank you all for making things work.

I would like to show appreciation to all co-authors of my papers, and to those who in one way or another contributed to this Ph. D. project.

Finally, I would like to express my sincere gratitude to my lovely wife Amelie and my beautiful daughters Hazelle and Hillary. Amelie has unconditionally accepted to endure all these years of doctorate while offering me her love, support, encouragement and inspiration. Without you and the girls, I could not have made it today. Thank you!

RÉSUMÉ

Le vieillissement des infrastructures, caractérisé par la détérioration des propriétés de surface, est causé par l'action de l'usure, la corrosion ou la synergie des deux. C'est un problème commun à plusieurs secteurs industriels tels que l'hydroélectricité, l'aérospatiale, l'automobile, etc. Les conséquences de ce phénomène peuvent varier de la perte de l'efficacité du système, de l'augmentation du coût de la réparation, de la maintenance ou du remplacement des pièces. La dégradation des composants commence souvent par la surface. Pour cette raison, l'ingénierie de surface peut être utilisée pour fournir à la surface des propriétés adéquates ou des revêtements protecteurs pour prévenir ou retarder l'enlèvement de la matière.

L'usure se produit dans des situations où au moins deux surfaces solides en mouvement relatif interagissent. De telles interactions sont à prévoir lorsqu'une surface est exposée à des contacts tribologiques résultant de l'altération des propriétés de surface. Dans ce contexte, l'enlèvement de la matière est généré par divers modes de dégradation qui comprennent l'abrasion, la fatigue, l'adhésion et l'oxydation. En effet, plusieurs modes de dégradation peuvent avoir lieu simultanément dans un processus d'usure. Lorsque la perte de la matière d'une surface est provoquée par des réactions chimiques ou électrochimiques avec l'environnement (liquide ou gazeux), le processus est appelé corrosion.

Afin de répondre à ces préoccupations, l'objectif principal de cette thèse de doctorat vise à développer des matériaux résistants à l'usure à base d'aluminure de fer (Fe_3Al) en utilisant le concept de modification structurelle par l'ajout de particules dures et en contrôlant la microstructure. Les principaux résultats de cette recherche sont présentés sous forme d'articles dans des revues à comité de lecture.

Dans le premier article, l'influence de l'ajout du BN, du traitement thermique et du temps de broyage sur les propriétés mécaniques et tribologiques des revêtements composites à base de Fe_3Al ont été étudiées. Dans ce contexte, le broyage à boulets a été appliqué sur le mélange de poudres de Fe_3Al et de BN à différentes énergies. Ensuite, les revêtements ont été déposés à partir de poudres broyées en utilisant la technique HVOF (High Velocity Oxy-Fuel), et leurs propriétés mécaniques et tribologiques ont été évaluées. Il a été montré que les revêtements avec les grandes inclusions céramiques réparties aléatoirement dans la matrice Fe_3Al présentent une performance d'usure plutôt médiocre. Cependant, l'ajout du BN dans la matrice Fe_3Al a

considérablement amélioré la dureté et la résistance à l'usure du revêtement Fe_3Al. Pour améliorer davantage les propriétés tribomécaniques des revêtements composites, un traitement thermique a été appliqué aux poudres broyées afin de précipiter *in situ* les phases Fe_2B et AlN dans la matrice Fe_3Al. Ainsi, le rebroyage permet de réduire la taille des précipités durs et de les répartir uniformément dans la matrice Fe_3Al, ce qui améliore considérablement la résistance mécanique et à l'usure. L'étude du mécanisme de dégradation montre que la fatigue était dominante pour le revêtement Fe_3Al, tandis que l'abrasion était le mode principal de l'enlèvement de la matière pour les revêtements composites.

Dans le deuxième article, nous étudions les propriétés d'usure des revêtements HVOF à base de Fe_3Al renforcés avec des inclusions céramiques beaucoup plus dures. Ces matériaux composites ont été obtenus par broyage à boulets du mélange de poudres Fe_3Al, BN et Ti, suivi d'un traitement thermique pour précipiter *in situ* les particules de TiB_2 et de TiN dans la matrice. Cette approche de fabrication est appelée dans cette thèse la voie de fabrication *in situ*. L'influence de la teneur en céramique sur les propriétés tribomécaniques des revêtements a été étudiée. Les résultats montrent que la résistance à l'usure du revêtement de Fe_3Al pur augmente significativement lorsqu'une quantité optimale de particules de TiB_2 et de TiN a été ajoutée. Nous avons également montré que le taux d'usure est lié aux propriétés mécaniques tels que la dureté, le module de Young et le coefficient de plasticité (c'est-à-dire le rapport entre la dureté et le module de Young). Dans le contexte de cet article, l'enlèvement de matière était régi par l'usure adhésive, abrasive et par la fatigue.

Une étude comparative a été réalisée dans le troisième article entre deux types de voies de fabrication de la poudre à savoir le procédé *in situ* et le procédé *ex situ*. Dans la voie de fabrication *in situ*, la matrice Fe_3Al est renforcée par des phases céramiques formées dans la matrice, alors que la méthode *ex situ* fait référence au processus dans lequel la matrice Fe_3Al est renforcée avec des particules de céramique pure préformées. Les poudres *in situ* ont été obtenues comme décrit dans le deuxième article. Pour les poudres composites *ex situ*, les phases de TiB_2 et de TiN formées dans la matrice Fe_3Al par la voie *in situ* ont été quantifiées puis une quantité équivalente des poudres TiB_2 et TiN pures a été ajoutée au Fe_3Al et broyée dans un broyeur à boulets. L'influence de la voie de fabrication des poudres a été étudiée sur les propriétés mécaniques et d'usure des revêtements HVOF dans différentes conditions de glissement. Les résultats montrent que les revêtements *in situ* présentent des inclusions de taille nanométrique par

comparaison à la taille du micron dans le cas de revêtements *ex situ*. En outre, les revêtements in situ présentent la dureté la plus élevée et le taux d'usure le plus faible par rapport à *ex situ*. La distribution de la dureté et du module de Young à l'échelle micro et nanométrique indique que la meilleure performance tribomécanique du revêtement *in situ* peut être associée à l'homogénéité de sa microstructure et la finesse de ses renforts.

Dans le quatrième article, deux types différents de systèmes de revêtement mince-sur-épais (duplex) consistant en une couche supérieure de CrN ou de DLC déposée par pulvérisation cathodique sur un revêtement HVOF ou sur un substrat en acier inoxydable 304 (SS304) ont été fabriqués. Deux types de revêtements HVOF ayant des propriétés mécaniques différentes ont été utilisés, à savoir les revêtements Fe_3Al (dureté 4,3 GPa) et Fe_3Al-TiN-TiB_2 (dureté 14,2 GPa). Les propriétés tribomécaniques des revêtements mince-sur-épais ont été évaluées, ainsi que la capacité de charge des revêtements HVOF. Les résultats ont montré que l'ajout d'une couche mince de CrN et de DLC améliore la résistance à l'usure du substrat SS304 et des revêtements HVOF. Les revêtements duplex PVD/HVOF présentent de bonnes propriétés tribomécaniques par rapport au revêtement PVD/SS304. Il a également été montré que les couches épaisses de HVOF sont soumises à moins de déformation plastique et présentent une capacité de charge plus élevée par rapport au substrat SS304. La résistance à l'usure du système de revêtement mince-sur-épais augmente avec la dureté de la couche inférieure dans l'ordre suivant: SS304 (1,7 GPa) <Fe_3Al (4,3 GPa) <Fe_3Al-TiN-TiB_2 (14,2 GPa). Les revêtements mince-sur-épais à base de DLC présentent une meilleure performance tribomécanique par rapport au CrN en raison de la très faible friction du film DLC et de sa capacité à maintenir son intégrité pendant l'essai d'usure. Dans ces systèmes, la perte de matière s'est produite par déformation plastique, fracture et l'usure abrasive.

Dans le cinquième article, l'influence des couches minces de CrN et DLC déposées par pulvérisation cathodique sur la résistance à la corrosion des revêtements HVOF à base de Fe_3Al dans une solution contenant du chlore a été étudiée. Le comportement à la corrosion et les mécanismes de dégradation des revêtements mince-sur-épais ont été étudiés en utilisant la spectroscopie d'impédance électrochimique (EIS) et l'étude de l'action simultanée de l'usure et de la corrosion. Les résultats ont montré que les couches minces de CrN et DLC aident à augmenter le potentiel de corrosion du revêtement Fe_3Al de -0,71 V à -0,34 V et -0,09 V, et à diminuer le taux de corrosion d'un et trois ordres de grandeur, respectivement. La faible résistance à la

corrosion à température ambiante du revêtement de Fe_3Al est liée à la présence de défauts et de porosités favorisant l'infiltration de la solution de NaCl dans le revêtement. La spectroscopie d'impédance électrochimique révèle que les couches supérieures déposées par pulvérisation ont tendance à agir comme une barrière entre l'électrolyte et le revêtement de Fe_3Al. Les résultats de la tribocorrosion ont montré que l'ajout des couches de CrN et DLC aide lorsque le revêtement est soumis à de l'usure pendant une polarisation cathodique. Par contre, l'action simultanée de l'usure et de la corrosion dans une solution aqueuse de NaCl à 3,5% dans des conditions de polarisation anodique entraîne des dommages importants lorsque les couches minces de CrN et DLC ont été fracturées par le contre-corps de Al_2O_3 conduisant à la formation de couplages galvaniques tels que CrN-Fe_3Al et DLC-Fe_3Al après l'infiltration de la solution de NaCl dans le revêtement Fe_3Al. La contribution majeure à la perte totale de matériaux est celle due aux effets synergiques entre l'usure et la corrosion.

ABSTRACT

Aging infrastructure characterized by the deterioration of surface properties of components is caused by the action of wear, corrosion or a synergy of both. It is a problem common to many industrial sectors such as hydroelectric power, aerospace, automotive, etc. Consequences of this process can vary from the loss of the system efficiency, the increase of the cost of repairs, maintenance or replacement of components. The degradation of components often starts from the surface. For that reason, surface engineering can be used to provide surfaces with adequate properties or protective coatings to prevent and/or to delay material removal and deterioration.

Wear occurs in situations where at least two solid bodies in relative motion interact. Such interactions are expected when a surface is exposed to tribological contacts resulting in the alteration of surface properties. In this context, material removal is generated via various degradation modes that include abrasion, fatigue, adhesion and oxidation or corrosion. Indeed, several degradation modes can take place simultaneously in a wear process. When material loss from a surface is prompted by chemical or electrochemical reactions with the environment, the process is referred to as corrosion. Here, the environment can be liquid or gaseous containing corrosive species.

In order to address these concerns, the principal objective of this Ph.D. thesis is to develop wear resistant materials based on iron aluminide (Fe_3Al) using the concept of structural modification by adding hard particles and controlling the microstructure. The main results of this research are presented in the form of articles in refereed journals.

In the first article, the effect of BN addition, heat-treatment, and ball-milling on the mechanical and tribological properties of Fe_3Al-based composite coatings were investigated. In this context, the ball-milling was applied on a mixture of Fe_3Al and BN powders at different energies. Then, coatings were deposited from milled powders using the high velocity oxy-fuel (HVOF) technique, and their mechanical and tribological properties were evaluated. It was shown that the microstructure of the composite powders was preserved in the HVOF coatings. Moreover, the addition of BN significantly enhances the hardness and wear resistance of the Fe_3Al matrix. To further improve the tribo-mechanical properties of the composite coating, heat-treatment was applied on milled powders in order to precipitate Fe_2B and AlN phases into the Fe_3Al matrix. It was shown that coatings with large ceramic inclusions randomly distributed in

the Fe$_3$Al matrix exhibit relatively poor wear performance. Re-milling helps to decrease the size of hard precipitates and uniformly distribute them within the Fe$_3$Al matrix leading to a substantial enhancement of the mechanical and wear resistance. The investigation of the degradation mechanisms shows that fatigue, delamination and abrasive wear were predominant modes of material loss for the pure Fe$_3$Al and hard particles containing coatings.

In the second article, we study the wear properties of Fe$_3$Al-based HVOF coatings reinforced with much harder phases. The composite materials were obtained by ball-milling the mixture of Fe$_3$Al, BN and Ti powders then follows by heat-treatment in order to precipitate *in situ* TiB$_2$ and TiN particles in the matrix. This fabrication approach is referred in this thesis as the *in situ* fabrication route. The influence of the ceramic contents was investigated on the tribo-mechanical properties of Fe$_3$Al-based coatings. The results show that the wear resistance of the pure Fe$_3$Al coating significantly increases when an optimum amount of TiB$_2$ and TiN particles were added. We have also shown that the wear rate is strongly related to the mechanical properties such as hardness, Young's modulus and plasticity coefficient (i.e. the ratio of the hardness and the Young's modulus). In the context of this article, the material removal was governed by the adhesive, abrasive and fatigue wear.

A comparative study was carried out in the third article between two types of powder fabrication routes namely the *in situ* and the *ex situ* process. In the *in situ* fabrication route, the ceramic phases are formed within the Fe$_3$Al matrix whereas the *ex situ* refers to the process in which the Fe$_3$Al matrix is reinforced with pre-formed pure ceramic particles. The *in situ* powders were obtained as described in the second article. For the *ex situ* composite powders, the *in situ* TiB$_2$ and TiN phases formed in the Fe$_3$Al matrix were quantified then an equivalent amount of the pure TiB$_2$ and TiN powders was added to the Fe$_3$Al, and ball-milled. The influence of the powder fabrication route was investigated on the mechanical and wear properties of the HVOF coatings under different sliding conditions. The results show that the *in situ* coatings exhibit nano size inclusions compared to micron size in the case of *ex situ* coatings. In addition, the *in situ* coatings exhibit the highest hardness and the lowest wear rate compared to *ex situ*. The distribution of the hardness and Young's modulus at the micro and nano scale indicated that the better tribo-mechanical performance of the *in situ* coating can be associated with the homogeneity of its microstructure and the small size of the reinforcing components.

In the fourth article, two different types of thin-on-thick (duplex) coating systems consisting of a sputter-deposited CrN or DLC top layer on a HVOF coating or a stainless-steel type 304 substrate (SS304) were fabricated. Two types of HVOF coatings with different mechanical properties were used namely the Fe_3Al (hardness 4.3 GPa) and the Fe_3Al-TiN-TiB$_2$ (hardness 14.2 GPa) coatings. The tribo-mechanical properties of the thin-on-thick coatings were evaluated, and the load-carrying capacity of HVOF coatings as well. The results have shown that the addition of a thin film of CrN and DLC enhances the wear resistance of the SS304 substrate and the HVOF coatings. The PVD/HVOF duplex coatings show good tribo-mechanical properties compared to the PVD/SS304 coating. It was also shown that the thick HVOF layers are subjected to less plastic deformation and exhibit higher load-carrying capacity compared to the SS304 substrate. The wear resistance of the thin-on-thick coating system increased with the hardness of the underneath layer in the following order: SS304 (1.7 GPa) < Fe_3Al (4.3 GPa) < Fe_3Al-TiN-TiB$_2$ (14.2 GPa). The DLC-based thin-on-thick coatings exhibit better tribo-mechanical performance compared to CrN-based due to the ultra-low friction of the DLC film and its ability to maintain its integrity during the wear test. In these systems, material loss occurred via plastic deformation, fracture and abrasive wear.

In the fifth article, the influence of the sputter-deposited CrN and DLC top coats on the corrosion resistance of the Fe_3Al-based HVOF coatings in chlorine containing solution was studied. The corrosion behavior and the degradation mechanisms of the thin-on-thick coatings was studied using the electrochemical impedance spectroscopy (EIS) and the investigation of the simultaneous action of wear and corrosion as well. The results have shown that the CrN and DLC top coats have help to increase the corrosion potential of the Fe_3Al coating (-0.71 V) to -0.34 V and -0.09 V, and decrease the corrosion rate by one and three orders of magnitude, respectively. The poor room temperature corrosion resistance of the Fe_3Al coating is related to the presence of defects that favors the infiltration of the NaCl solution in the coating facilitating the corrosion of the Fe_3Al alloy. The EIS reveals that the sputter-deposited top coats tend to act as a barrier between the electrolyte and the Fe_3Al coating. The tribocorrosion results shown that the addition of the CrN and DLC top coats helps when the thin-on-thick coating is subjected to wear during a cathodic polarization. On the other hand, the simultaneous action of wear and corrosion in a 3.5% NaCl aqueous solution under anodic polarization conditions leads to severe damages when the sputter-deposited DLC and CrN top coats have been fractured by the hard Al_2O_3 counterpart

leading to the formation of strong CrN-Fe$_3$Al and DLC-Fe$_3$Al galvanic couples after the infiltration of the NaCl solution in the Fe$_3$Al coating. The major contribution to the total materials loss is the contribution due to synergistic effects between wear and corrosion.

TABLE OF CONTENTS

LIST OF TABLES

LIST OF FIGURES

LIST OF SYMBOLS AND ABBREVIATIONS

Abbreviations

AlN	Aluminum nitride
APB	Anti-phase boundary
APS	Atmospheric plasma spray
ASTM	American Society for Testing and Materials
bcc	Body-centered cubic
BN	Boron nitride
CE	Counter electrode
CPE	Constant phase element
CrN	Chromium nitride
dc	Direct current
DLC	Diamond-like carbon
DTA	Differential thermal analysis
EDS	Energy dispersive spectroscopy
EELS	Electron energy loss spectroscopy
EIS	Electrochemical impedance spectroscopy
Fe_2B	Iron boride
FEG	Field emission gun
h-BN	Hexagonal boron nitride
HEBM	High-energy ball milling
HQ	Hydro-Québec
HV	Vickers hardness
HVOF	High velocity oxy-fuel

ICDD	International Centre for Diffraction Data
IREQ	Institut de Recherche d'Hydro-Québec
MM	Mechanical milling
MMC	Metal matrix composite
NaCl	Sodium chloride
NSERC	Natural Science and Engineering Research Council
OCP	Open circuit potential
RE	Reference electrode
rpm	Rotation per minute
SCE	Standard calomel electrode
SEM	Scanning electron microscopy
SHE	Standard hydrogen electrode
STEM	Scanning transmission electron microscopy
TiB_2	Titanium diboride
TiC	Titanium carbide
TiN	Titanium nitride
VPS	Vacuum plasma spray
WE	Working electrode
XRD	X-ray diffraction

Symbols

a	Lattice parameter of the unit cell of the D03 structure
a_0	Lattice parameter of the unit cell of the B2 structure
A	Projected area

A_p	Projected area of a particle on the plane perpendicular to the flow direction
at%	Atomic percent
B2	Imperfectly ordered structure
C_d	Drag coefficient
C_{dl}	Double layer capacitor
C_p	Specific heat pf the particle
d	Length of the diagonal of an indentation imprint
d_B	Distance between two atomic planes
d_p	Particle diameter
$D0_3$	Ordered structure of Fe_3Al
e^-	Electrons
E	Indentation modulus
E_0	Amplitude of the voltage signal
E_{corr}	Corrosion potential
E_i	Young's modulus of the diamond tip
E_p	Applied potential
E_r	Reduced modulus
E_s	Voltage signal

E_v	Energy transferred to powder particles
f	frequency
F	Faraday constant
F	Applied normal load
F_T	Tangential force
H	Hardness
h	Indentation depth
I	Current signal
i	Kinetics of the electrochemical corrosion
I_0	Amplitude of the current
i_a	Anodic current density
i_c	Cathodic current density
i_{corr}	Corrosion current density
I_{corr}	Corrosion current
K	Wear rate
K_a	Constant that depends on the elasticity of the collision
K_b, K_v	Constant that depends on the geometry of the milling device
k_g	Thermal conductivity of the gas
L	Total sliding distance
M	Molar mass

M	Metal
M^{n+}	Metal ions
m_b	Mass of the milling ball
mol.%	Mole percent
m_p	Mass of a single particle
N_b	Number of milling balls
N_u	Nusselt number
P	Applied normal force in indentation
pr	Represents product
Q, Q_1, Q_2	Constant phase element
R_1, R_2	Resistance to ion migration of the first R/C group
R_{ct}	Resistance due to charge transfer
Re	Reynolds number
R_p	Resistance due to polarization
R_p	Radius of the motor
R_s	Resistance of the electrolyte
st	Represents stoichiometric
S	Stiffness
t	Time in seconds
T_g	Gas temperature

T_p	Particle temperature
V	Volume of material loss or displaced
V_b	Relative impact velocity
vol%	Volume percent
v_s	Sliding velocity
W_{syn-c}	Material loss due to the effect of wear on corrosion
W_{syn-w}	Material loss due to the effect of corrosion on wear
W_{corr}	Material loss due to corrosion
W_{mech}	Material loss due to mechanical wear
W_{syn}	Material loss due to the synergistic effect between wear and corrosion
wt%	Weight percent
W_{total}	Total material loss
Y_o	Parameter of the constant phase element
z	Number of electrons transferred
Z	Complex impedance
Z_0	Amplitude of the complex impedance
Z_{im}	Imaginary part of the complex impedance
Z_Q	Impedance of the constant phase element
Z_{real}	Real part of the complex impedance

Greek symbols

α	Disordered solid solution
γ	Constant between -1 and 1
β	Angle of rotation of a purely capacitive line on a complex plane plot
β_a	Tafel anodic slope
β_c	Tafel cathodic slope
ϕ	Phase shift
η	Overpotential
η_a	Overpotential in the anodic polarization
η_c	Overpotential in the cathodic polarization
φ	Equivalent ratio
λ	Wavelength of the monochromatic light
μ	Coefficient of friction
ν	Collision frequency of a single ball
ν_t	Total collision frequency
θ	Angle of diffraction
ρ_g	Density of the gas
τ	Time constant
υ	Poisson coefficient

υ_d Drag velocity

ν_i Poisson coefficient of the diamond tip

υ_p Particle axial velocity

ϖ Line broadening at half maximum

ω Radial frequency

ω_p Angular velocity of motor

ξ_i Molar fraction of component i

CHAPTER 1   INTRODUCTION

Aging infrastructure is a major concern for many industrial sectors that includes hydroelectric power generation, aerospace, automotive, and construction. This problem is a result of a progressive deterioration of materials exposed to tribological contacts (material loss due to interactions between at least two surfaces), corrosive environments (material loss due to chemical or electrochemical reactions (Figure. 1.1)) or to a synergy of both actions. This problem can lead to a decrease of system efficiency, loss of performance or to a high cost of maintenance, repair or replacement of components or devices.

Figure 1.1: Part of a crank component of a Pelton
turbine after service in a corrosive environment.

Hydro-Québec (HQ) commits approximately 900 million Canadian dollars annually for aging infrastructure, and an increase of this budget is to be considered if no action is taken [1]. The principal source of electricity in Canada is hydroelectricity and more than half of this source of energy is produced in the province of Quebec [2]. With a generating capacity of approximately 37,000 megawatts annually (over 99% comes from renewable sources), HQ exports ~33 TWh of its electricity outside the province, and employs about 20,000 skilled workers. To keep this performance and standard, knowing that HQ's facilities were built more than 80 years ago, it is important to act accordingly with respect to aging infrastructure. An innovative approach to take is to develop appropriate and cost-effective solutions to protect and to extend the life time of systems' components.

In tribology, interactions between a solid body and the environment (tribological contacts or corrosive agents) take place at the surface level, and can lead to its alteration or deterioration. When at least two solids in contact are in relative motion in dry conditions, material removal is caused by the individual action or a combination of various degradation modes (abrasive, plastic deformation, adhesion etc.) (Figure 1.2a). For corrosion, the material loss initiated by the chemical or electrochemical reactions between the surface and corrosive agents in a liquid or gaseous environment can occur in various forms (pitting, crevice corrosion, fatigue corrosion etc.) (Figure 1.2b). In some situations, wear and corrosion can coexist and their simultaneous actions can be catastrophic. A surface deterioration that results from wear and corrosion is often referred to as tribocorrosion. In this context, surface engineering can be used to provide surfaces with new properties, functionality or protection to prevent and/or delay material loss. However, to select a coating for a specific application condition, it is necessary to better understand the mechanisms of the material loss.
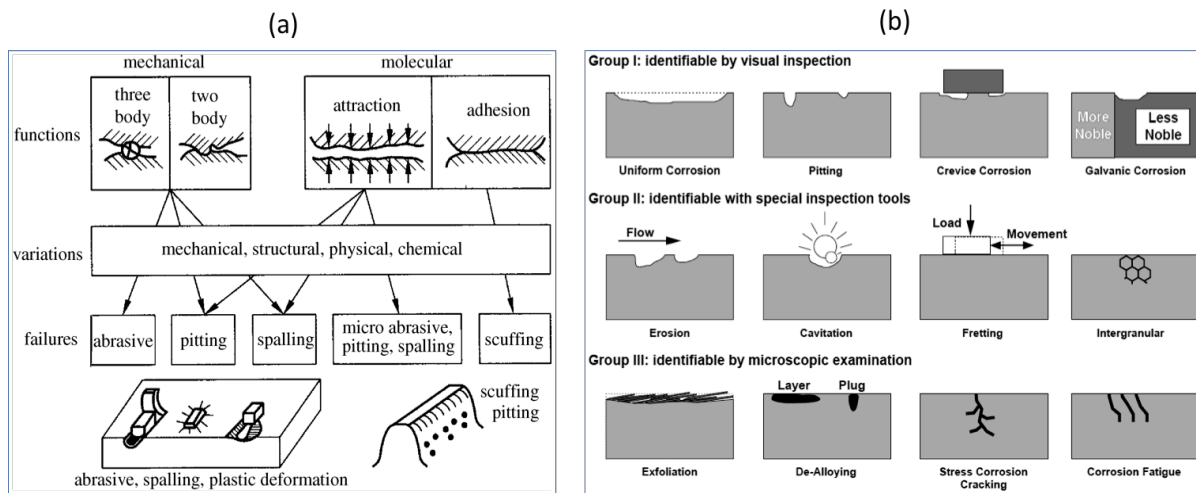
Figure 1.2: Surface degradation modes under the effect (a) of various tribological contacts [3], and (b) of corrosion [4].

Hydroelectric dams built by HQ in Quebec consist of different types of hydropower turbines (e.g. Francis, Kaplan and Pelton turbines) depending on the use [5]. The role of a hydropower turbine is to transform the energy of water into the mechanical energy which in turn is transformed to an electrical energy using an alternator. In service, hydropower turbines are susceptible to wear, to corrosion or to a simultaneous action of both degradation mechanisms.

In HQ's power system, the Francis turbine is the most commonly used turbine (Figure 1.3). It helps to provide a high level of efficiency compared to other hydroelectric turbines. In principle, water strikes the edge of the runner, pushes the blades and then flows towards the axis of the turbine. The Francis turbine operates best for medium to high range heads (from 10 m to 300 m), and high-flow conditions [5]. The principal degradation mechanisms of the Francis turbines are cavitation and solid particle erosion. However, the shaft and the radial bearing system of the Francis turbine can be subjected to tribological contacts (e.g. sliding wear, abrasion, etc.) during the operation [6].

Figure 1.3: Image of a Francis turbine, adapted from [6].

The Kaplan turbine is used for dams with fall height below 30 meters, and behaves like a propeller turbine. It can be used to provide high rotation speeds using its adjustable blades (Figure 1.4). However, a Kaplan turbine operates at low head conditions, and may be exposed to wear from entrained debris in the water (cavitation and solid particle erosion). During the orientation of the blades, the radial bearings of the Kaplan blades are subjected to sliding wear. In addition, the crank and the crank pin can also be damaged by sliding wear since all these components are affected by a relative motion during the orientation of the blades [7].

Figure 1.4: Image of a Kaplan turbine [8].

Pelton turbines usually operate in high head conditions and several components may be exposed to severe wear degradation mechanisms (e.g. sliding wear, abrasion, erosion, cavitation etc.) [7]. On the one hand, the spear needle, the deflector plate as we[ll] that are susceptible to movements when the turbine is in operation (Fi[g] parts can be exposed to sliding wear. On the other hand, the Pelton b[ucket] components of the turbine can be subjected to abrasive and erosion wea[r].

Schem

Impeller (runner)

Nozzle

Spear

Spear rod

Deflector plate

Discharge

Inlet

Penstock

Figure 1.5: Image of a Pelton turbine, adapted from [9]. Pelton turbine with si[ze]

Stainless steels are extensively used as base (or bulk) materials in various applications operating under harsh environmental conditions due to their good corrosion properties [10].

However, their poor mechanical and tribological properties have motivated the use of advanced materials for protective coatings.

Iron aluminides have gained interest and became an attractive class of materials for high temperature applications since the 1930s when its good resistance to corrosion and oxidation at high temperature was noticed. The use of iron aluminides for heating elements, furnace components, compressor blades in a jet engine, piping and tubing for automotive was considered as an important advancement in the field of intermetallics [11]. Furthermore, the application area of iron aluminides was extended to fossil fuel energy applications due to additional benefits such as good sulfidation resistance at high temperature [12, 13].

Beside all advantages at high temperature, iron aluminide alloys are known to be low-density (5.4 - 6.5 g/cm^3) materials and inexpensive to manufacture compared to many steels, bulk materials and other intermetallics. Such attributes have motivated the consideration of this class of intermetallics for structural applications under ambient conditions [14]. However, the low ductility (<5 %) and the low tensile strength at ambient temperatures limits the use of iron aluminides in the field where wear resistance is required [15-18].

The work carried out at the Oak Ridge National Laboratory by McKamey and his colleagues have significantly contributed to the recognition of iron aluminide alloys as potential materials for structure applications. They have demonstrated that satisfactory ductility of about 10 to 15 % could be achieved by controlling the composition and the microstructure of iron aluminide alloys [11]. Therefore, renewed interest in iron aluminides for applications where excellent mechanical properties are required grows significantly over the years.

Research on iron aluminides has been intensified since an increase of the room temperature ductility was reported [17, 19]. Thereafter, various microstructure modification approaches (solid-solution, precipitates and particles strengthening) have led to a significant enhancement of the mechanical, tribological and corrosion properties of iron aluminide alloys. Surface engineering approaches have also been used to provide the material with new functionality at the surface level.

Although each of these fabrication approaches helps to enhance the tribo-mechanical properties, their influence on the microstructure, the mechanical and the tribological properties of the iron aluminides could not be clarified from independent studies in the literature. In addition,

the wear behavior or the corrosion behavior of almost all existing materials have been studied and reported in the literature. However, the knowledge of wear in the absence of corrosion, and that of corrosion in the absence of wear is insufficient to predict the tribocorrosion behavior of materials [20].

In this chapter, I will present the context of this work and the objectives of my Ph.D. thesis. Then, I will continue with the list of publications resulting from this work and conclude with the general outline of this thesis.

1.1 Context and previous studies

The search for new challenges is something that has fascinated me since my young age. After my bachelor's degree in Physics at the University of Buea, Cameroon, I was offered the possibility to continue my graduate studies in Sweden; a country where the name reminded me, at the time, of tricky math problems in high school called "le concours suédois" from Monge, and the Swedish winter.

I was slowly introduced to the world of scientific research from multiple group projects within the Master program in Physics, and I was fortunate to have carried out my final-year project at the Angstrom Laboratory, Uppsala University in collaboration with ChromoGenics AB. It was an exciting project about studying the effect of insertion and extraction of different types and sizes of cation into electrochromic films on the coloration and de-coloration of the transparent flat panel devices. I participated in the conception, the fabrication and the testing of the devices. In this project, I could assess a correlation between the fundamental research and the applications. I was fascinated to have to identify the conditions in which devices will degrade and ultimately lose their efficiency. At the end of the project, the perspective pointed toward understanding the degradation mechanism of devices. Few months later, after completing my Master's thesis, I was facing another challenge which was to travel to Canada via the skilled worker program.

In my determination of pursuing my career, I met Prof. Ludvik Martinu, Prof. Jolanta Sapieha and their collaborators at Polytechnique Montréal few months later after my arrival in Montréal. I had told them my research orientations and my interest to work in a project similar to that carried out at the Angstrom Laboratory. I expected to study and to understand the

degradation mechanism of electrochromic devices using the characterization tools they have in their laboratories. Unfortunately, no such project was available at that time. For the mean time, I registered to a Master's program with a project in Engineering Physics, and few months later I met again with Ludvik. This time his research group, the Functional Coating and Surface Engineering Laboratory (FCSEL) was involved in an R&D project with Hydro-Québec who later became partner of the Industrial Research Chair. The project was related to the design, fabrication, and testing of coatings, prepared using thermal spray of powder particles in which ceramic phases are dispersed, for their tribo-mechanical properties. It wasn't about electrochromic materials; however, characterization was a large part of the project. I accepted the project even though powder fabrication, thermal spray, and tribology were very new for me.

I joined the FCSEL as a Master's student and my project was focused on the tribo-mechanical evaluation of composite coatings prepared using the HVOF technique. I worked with Dr. Simon Gaudet, a postdoc at the FCSEL at the time, and I was able to develop my sample preparation protocol, and to define my mechanical, tribological and corrosion characterization methods.

After my transfer to the Ph.D. program, I continued with the same project with more responsibilities. Beside the tribo-mechanical characterization of composite coatings, I was involved in the powder and coating fabrication. Therefore, I was participating in every aspect of the development from the fabrication to the characterization of coatings. It was easy for me to make a link between the resulting tribo-mechanical properties and the coating fabrication conditions.

1.2 Objectives

In the context of this collaborative project and the needs of the industrial partner, the principal objective of this project was to apply the concept of structural modification and surface engineering to the iron aluminide to enhance the mechanical, tribological and the corrosion properties. To accomplish this Ph.D. project, the main goal can be divided into specific objectives namely:

a) To develop wear-resistant coatings based on iron aluminides reinforced with boride and nitride phases. Basically, the main goal was to obtain significantly enhanced tribo-

mechanical properties by the addition of an optimum amount of different types of secondary phases formed within the matrix via solid state reactions during the powder fabrication process.

b) To characterize the properties of the materials and to establish a relationship between the microstructure and the resulting tribo-mehanical properties.

c) To evaluate the influence of the microstructural design on the corrosion and tribocorrosion properties of coating systems.

d) To identify and to understand the mechanisms of the material loss.

From the previously mentioned objectives, this Ph.D. work has led to five publications, three already published and two manuscripts submitted to peer reviewed journals (Table 1.1). Note that this thesis is presented by articles, and Chapters 4 to 8 represent the five published or submitted articles. Indeed, my collaboration on various projects during the past four years has also resulted in the publication of two other articles in international journals (Table 1.1) and conference proceedings (Table 1.3).

1.3 Thesis outline

This thesis is divided into nine chapters including the introductory section (Chapter 1). The list of peer-reviewed articles that resulted from this research and other collaborations will be presented as well as a list of contributions from international conferences and highlights. In Chapter 2, I present the essential knowledge for understanding the context of this research; it includes the general characteristics of iron aluminide, the description of metal matrix composites, the fabrication of enhanced Fe_3Al-based materials, the different types of mechanical surface response, the tribo-mechanical and corrosion properties of Fe_3Al-based coatings. In Chapter 3 the experimental methods used in this thesis are described in detail.

In Chapter 4, which is the integral copy of the first published article, the effect of high-energy ball milling on the mechanical and tribological properties of Fe_3Al-based coatings fabricated using the high velocity oxy-fuel (HVOF) technique is described. Composite powders are prepared from elementary powders with the purpose of forming ceramic precipitates in the Fe_3Al matrix during the fabrication process. It will be shown that by combining the mechanical ball-milling, the heat treatment and the HVOF techniques, stable boride and nitride phases are

formed in the Fe₃Al matrix leading to a significant enhancement of the tribo-mechanical properties. It will also be shown that the microstructure and the mechanical properties of composite powders are preserved in the HVOF coatings.

The second published article is presented in Chapter 5, where the wear behavior of the Fe₃Al-based HVOF coatings strengthened with different contents of secondary phases will be described. It will be shown that the wear resistance is related to the plasticity coefficient (i.e. the ratio of the hardness and the elastic modulus) of the coating and not necessarily with the content of the secondary phases. The weakness in the microstructure of thermal spray coatings (i.e. porosity, inter-splat boundaries) will be highlighted with respect to the mechanical and tribological properties of the HVOF coatings.

In Chapter 6, I present my third published article where the mechanical and the wear behavior of the HVOF Fe₃Al-TiN-TiB₂ coatings prepared from two different ways namely the *in situ* and the *ex situ* powder fabrication routes will be compared with respect to different sliding velocities. In fact, the *in situ* fabrication approach is the one in which secondary phases are formed within the matrix during the fabrication process while the *ex situ* approach is the situation where pre-formed phases are added into the matrix. It will be shown that *in situ* coatings exhibit nano scale inclusions uniformly dispersed in the Fe₃Al matrix compared to randomly distributed micron sized inclusions in the *ex situ* case. The tribo-mechanical performance and the degradation mechanisms will be discussed with respect to the characteristics (microstructure, plasticity coefficient etc.) of the coatings.

The tribo-mechanical behavior of two thin-on-thick (duplex) coating systems consisting of a sputter-deposited CrN and DLC top layers on the SS304 substrate, the Fe₃Al and the Fe₃Al-TiN-TiB₂ coatings will be investigated under different loading conditions in Chapter 7. It will be shown that the addition of the CrN and DLC top coats can help to increase the wear resistance of the SS304 substrate and HVOF coatings. The load carrying capacity of the thick HVOF coatings will be compared to the SS304 substrate.

In Chapter 8, the influence of the sputter-deposited CrN and DLC top coats on the corrosion behavior of the Fe₃Al coatings, prepared using the HVOF technique, will be studied in a chlorine-containing NaCl aqueous solution. The corrosion behavior and the degradation

mechanisms of the thin-on-thick systems will be investigated using electrochemical impedance spectroscopy and the assessment of the simultaneous action of wear and corrosion.

In the last chapter, I present a summary of the main results presented in this thesis as well as the general discussion. This is followed by the open questions and research orientations that can be considered in the future in order to further improve the tribo-mechanical characterization of thermal spray coatings.

Table 1.1: Peer reviewed publications resulting from this thesis.

F. Pougoum, J. Qian, Z. Zhou, K. Y. Li, L. Martinu, J. Klemberg-Sapieha, S. Savoie, R. Lacasse, E. Potvin, R. Schulz, "*Study of corrosion and tribocorrosion of Fe$_3$Al-based duplex PVD/HVOF coatings against alumina in NaCl solution* "submitted to Journal of Materials Science and Technology.

 F. Pougoum, J. Qian, Z. Zhou, K. Y. Li, L. Martinu, J. Klemberg-Sapieha, S. Savoie, R. Schulz, "*Tribo-mechanical properties of Fe$_3$Al-based PVD/HVOF duplex coatings* " submitted to Wear.

F. Pougoum, T. Schmitt, L. Martinu, J. Klemberg-Sapieha, S. Savoie, R. Schulz, "*Wear behavior of Fe$_3$Al-TiN-TiB$_2$ HVOF coatings: A comparative study between in situ and ex situ powder processing routes*" (2017) Ceramics International, 43, 8040 - 8050.

 F. Pougoum, L. Martinu, J. Klemberg-Sapieha, S. Savoie, R. Schulz, "*Wear properties of Fe$_3$Al-based HVOF coatings strengthened with in situ precipitated nitride and boride particles*" (2016) Surface and Coatings Technology, 307, 109-117.

F. Pougoum, L. Martinu, P. Desjardins, J. Klemberg-Sapieha, S. Gaudet, S. Savoie, R. Schulz, "*Effect of high energy ball-milling on the characteristics of Fe$_3$Al-based HVOF coatings containing boride and nitride phases*" (2016) Wear, 358, 97-108.

Table 1.2: Peer reviewed publications resulting from collaborations.

S. Lavigne, **F. Pougoum**, R. Schulz, S. Savoie, L. Martinu, J. Klemberg-Sapieha. "*Cavitation erosion behavior of HVOF CaviTec coatings*" (2017) Wear, 386, 90-98.

G. Taillon, **F. Pougoum**, S. Lavigne, L. Ton -That, R. Schulz, E. Bousser, S. Savoie, L. Martinu, J. Klemberg-Sapieha. "*Cavitation erosion mechanisms in stainless steels and in composite metal-ceramic HVOF coatings*" (2016), Wear, 364, 201-210.

Table 1.3: Conferences and other contributions.

F. Pougoum, T. Schmitt, L. Martinu, J. Klemberg-Sapieha, S. Savoie, R. Schulz, "*Wear behavior of Fe₃Al-TiN-TiB₂ HVOF coatings: A comparative study between in situ and ex situ powder processing routes*". Presentation, CMSC, 2017, Ottawa, Qc, Canada.

S. Lavigne, **F. Pougoum**, R. Schulz, S. Savoie, L. Martinu, J. Klemberg-Sapieha. "*Cavitation erosion behavior of HVOF CaviTec coatings*". Presentation, CMSC, 2017, Ottawa, Qc, Canada.

F. Pougoum, T. Schmitt, L. Martinu, J. Klemberg-Sapieha, S. Savoie, R. Schulz, "*Wear behavior of Fe₃Al-TiN-TiB₂ HVOF coatings: A comparative study between in situ and ex situ powder processing routes*". Poster, FCSE, 2017, Montréal, Qc, Canada.

S. Lavigne, **F. Pougoum**, R. Schulz, S. Savoie, L. Martinu, J. Klemberg-Sapieha. "*Cavitation erosion behavior of HVOF CaviTec coatings*". Presentation, ICMTCF, (2017), San Diego, CA, USA.

F. Pougoum, L. Martinu, J. Klemberg-Sapieha, S. Savoie, R. Schulz, "*Wear properties of Fe₃Al-based HVOF coatings strengthened with in situ precipitated nitride and boride particles*". Presentation, Nano2016, (2016), Québec City, Qc, Canada.

F. Pougoum, L. Martinu, P. Desjardins, J. Klemberg-Sapieha, S. Gaudet, S. Savoie, R. Schulz, "*Effect of high energy ball-milling on the characteristics of Fe₃Al-based HVOF coatings containing boride and nitride phases*". Presentation, ICMTCF, (2016), San Diego, CA, USA.

F. Pougoum, L. Martinu, P. Desjardins, J. Klemberg-Sapieha, S. Gaudet, S. Savoie, R. Schulz, "*Effect of high-energy ball milling and heat-treatment on the microstructure and tribo-*

mechanical properties of Fe₃Al-AlN-Fe₂B composite-based HVOF coatings". Poster FCSE, 2014, Montréal, Qc, Canada.

F. Pougoum, L. Martinu, J. Klemberg-Sapieha, S. Gaudet, S. Savoie, R. Schulz, "*Mechanical and tribological properties of HVOF sprayed iron aluminide-based nanocomposite coatings reinforced with hard ceramics*". Poster ASM Student night (2013), Montréal, Qc, Canada.

CHAPTER 2   LITERATURE REVIEW

In this chapter, I will give an overview of the general characteristics of iron aluminides and an introduction to composite materials. The various microstructural changes that can lead to the enhancement of mechanical, tribological and corrosion properties of the Fe_3Al will be presented.

2.1   General characteristics of Fe_3Al

2.1.1   Phase diagram

Iron aluminides is a class of intermetallics that exhibit a variety of structural forms. In the context of this thesis, the base material consists of the iron aluminide with the Fe_3Al phase. The phase diagram of the binary Fe-Al system is shown in Figure 2.1. In the iron-rich region there exists a disordered solid solution (α), an imperfectly ordered B2 structure, an ordered Fe_3Al with a $D0_3$ structure, and regions of the phase diagram of α + B2 and α + $D0_3$. The range of composition of iron aluminides suitable for structural applications is in the iron-rich region where the Fe_3Al phase is found [11, 19].
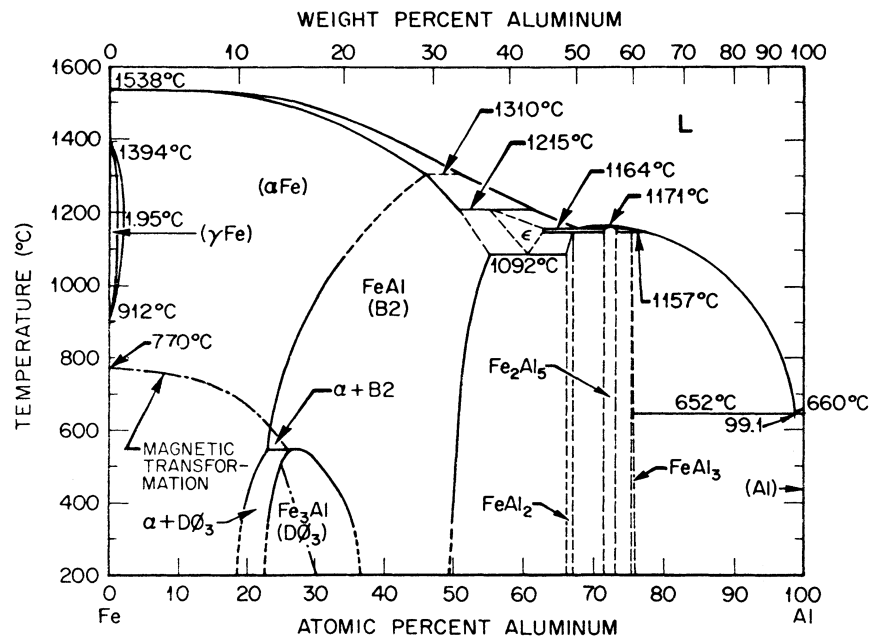
Figure 2.1: Phase relationships in the Fe-Al system, adapted from [11].

The schematic representation of the crystal structure of the Fe_3Al phase (ordered $D0_3$ structure) and the FeAl phase are shown in Figure 2.2. The $D0_3$ structure is a body-centered cubic

(b.c.c) structure which consists of eight B2 superlattices arranged such that aluminum and iron body-centered atoms alternate so as to maximize the spacing between aluminum atoms [14]. The B2 structure can be viewed as two interpenetrating simple-cubic lattices with iron atoms occupying one sublattice and aluminum atoms the other one, resulting in an AB-type stoichiometry, namely the FeAl.

During the ordering transformation, small ordered regions nucleate and grow on different sublattice sites until they occupy the entire volume of the crystal. This process results in the creation of a planar ordering fault at the interface of the small regions which is known as the anti-phase boundary (APB). Different APB faults exist depending on the structure of the iron aluminide phase. In the B2 structure, only one type of APB can be found; this formed during the transformation from disordered α-phase to the B2 phase; it consists of a fault vector of 1/2 a_0 <111> (a_0 is the lattice parameter of the unit cell of the B2 superlattice). In the ordered $D0_3$ structure, two types of APB occured. The first APB appears in a similar transformation as in the B2 phase with a fault vector of 1/4 a<111>; the second APB ($D0_3$-type) forms during the B2-$D0_3$ transformation with a fault vector of 1/2 a<100> (a is the lattice parameter of the unit cell of the $D0_3$ superlattice).
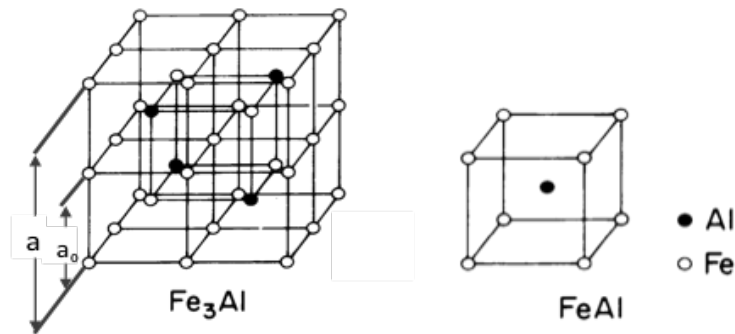
Figure 2.2: Schematic representation of a unit cell of the Fe_3Al
($D0_3$) and FeAl (B2) superlattices, adapted from [11].

2.1.2 Mechanical properties

In general, the mechanical properties of iron aluminides are influenced by many factors that include the composition, the type and amount of ordered structure, the environment, alloying additions and defects. In such a binary system, the hardness and the tensile yield strength of iron

aluminides increase with respect to the aluminum contents. Thus, the stoichiometric composition near the Fe_3Al phase (e.g. between 20 and 40 at% of Al) has been shown to be the optimum composition range. Such compositions can lead to good mechanical properties in the iron-rich region of the Fe-Al phase diagram compared to austenite steel (e.g. stainless steel 300 series) [11]. Moreover, a higher amount of ordered $D0_3$ phases is expected near this range inducing a high number of APB which can help to stop the movement of dislocations. Nevertheless, a decrease of the mechanical properties can be observed when the aluminum content increases above the $D0_3$ limit (Figure 2.3). This limit is related to the decrease of the APB's energy. Strengthening in iron aluminides has also been related to grain refinement and to some extent the presence of defects [14].
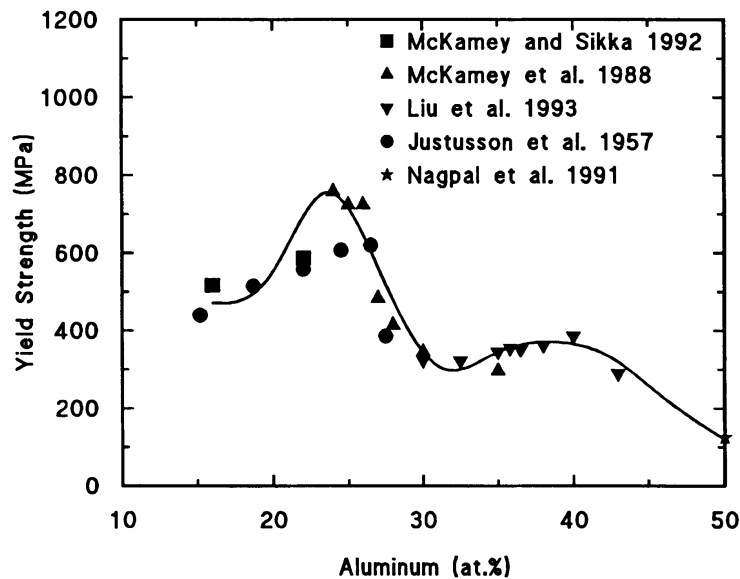
Figure 2.3: Room temperature tensile yield strength as a function of
aluminum content in binary Fe-Al alloys, adapted from [11].

Iron aluminides with the Fe_3Al phase is known to be intrinsically ductile. However, its room-temperature ductility is low (below 2 %) regardless of the type of the ordered structure ($D0_3$ or B2) present. The poor ductility of iron aluminides at ambient temperatures with the presence of moisture or water vapor is attributed to the effect of hydrogen embrittlement. In this situation, the reaction between the water vapor and aluminum in the alloy produces alumina, and generates hydrogen atoms which are chemisorbed at the surface of the material, migrate into crack tips causing brittle cleavage crack propagation [21]. Nevertheless, the alloy addition such as chromium [19] or the grain refinement (down to micron scale) [15] can be used to enhance the

ductility of iron aluminides at ambient temperatures. The addition of chromium will favor the formation of an oxide layer to protect the surface of iron aluminide while grain refinement will generate a large number of interfaces that can stop crack propagation.

2.2   Development of Fe$_3$Al-based metal matrix composites

Metal matrix composites (MMC) are considered as a combination of at least two chemically and physically distinct phases such that the resulting properties are unachievable by only one component. A MMC consists of a matrix material and a specific volume or number of secondary phases (e.g. hard particles) randomly dispersed. MMC materials have been used in various engineering applications due to their excellent mechanical and tribological properties. For a specific application, the design of a MMC material is chosen accordingly [22], and it can be classified with respect to the type of inclusions (particles, whiskers or fibers).

2.2.1   Matrix materials

Matrix materials commonly used for MMC are metals and intermetallics due to their ability to be deformed and processed at low temperature, and also to their low density and low melting temperature. Iron aluminide is a promising candidate for the matrix component in a MMC, it is inexpensive to produce, and it exhibits good corrosion and oxidation properties at high temperature (advantage for high temperature applications) [15, 23]. In addition, a wide range of ceramic materials can be used as secondary phases, and it has been shown that these inclusions are thermodynamically stable an iron aluminide matrix [24].

2.2.2   Secondary phase materials

The choice of secondary phases for a MMC is based on their compatibility with the matrix, their mechanical properties, their morphology (shape and size), as well as their cost. Among the inclusions that are used as secondary phases, particulates have been shown to be suitable for MMC. Particulates are used in a MMC to provide isotropic properties, and a substantial enhancement in strength and stiffness can be achieved [25]. In general, ceramic materials such as boride, carbide, nitride and oxide phases have been commonly used as secondary phases in MMC. They exhibit excellent mechanical characteristics compared to various alloys (Figure 2.4).
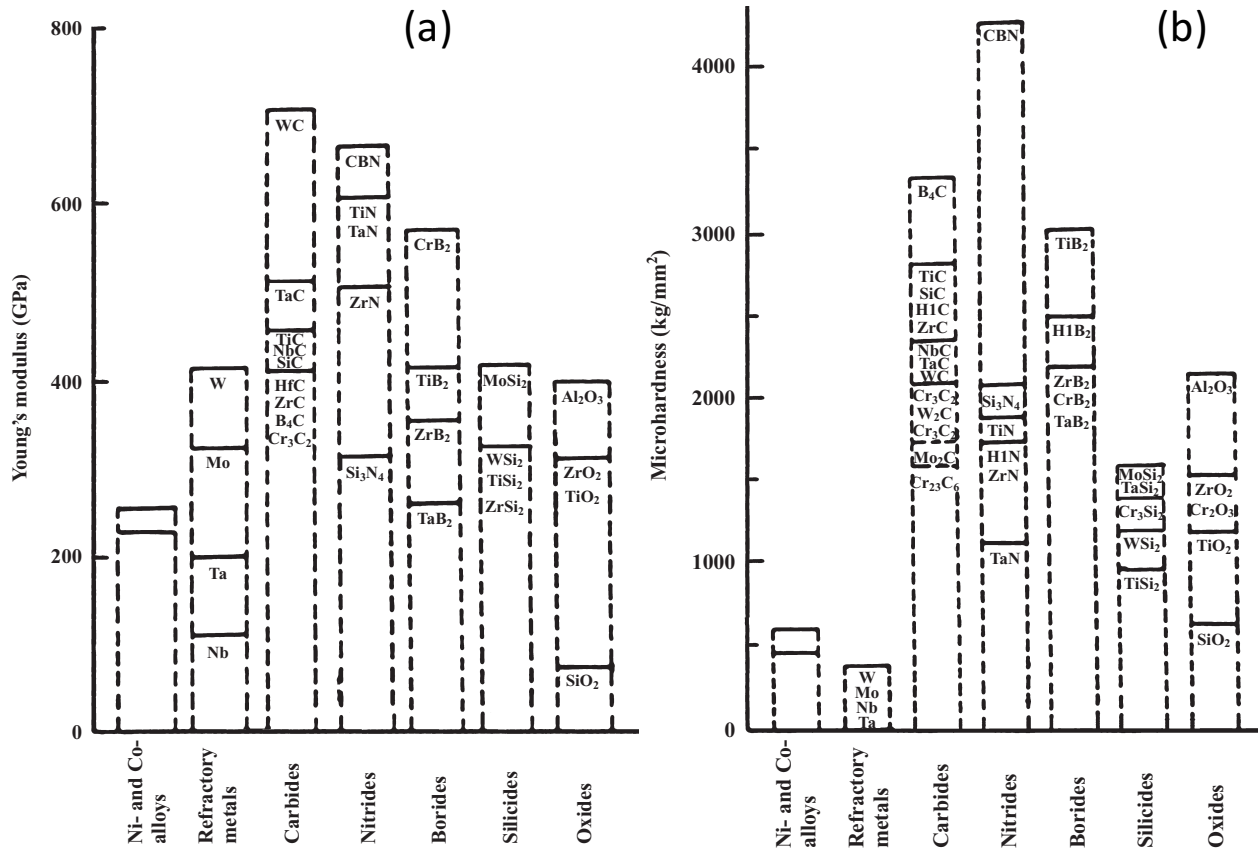
Figure 2.4: Comparison of various materials in terms of basic mechanical properties: (a) elastic modulus and (b) microhardness, adapted from [26].

The type and volume fraction of secondary phases dispersed in an iron aluminide matrix have been shown to influence the mechanical properties. Schneibel *et al.* have shown that irrespective of the chemical composition of ceramic materials, a maximum hardness is achieved with a specific number of secondary phases (Figure 2.5) [27]. The size of secondary phases and their spatial distribution in the matrix are important aspects that can also affect the mechanical properties of materials. The reduction of particle (or grain) size can lead to enhanced mechanical properties due to the increase of the amount of grain boundaries that block or stop crack propagation and dislocations in the material. However, the critical limit of grain refinement (grain size) is defined by the Hall-Petch relationship [28] which states that the yield strength is inversely proportional to the square root of the grain size. This relation was independently demonstrated by Hall [29] and Petch [30].
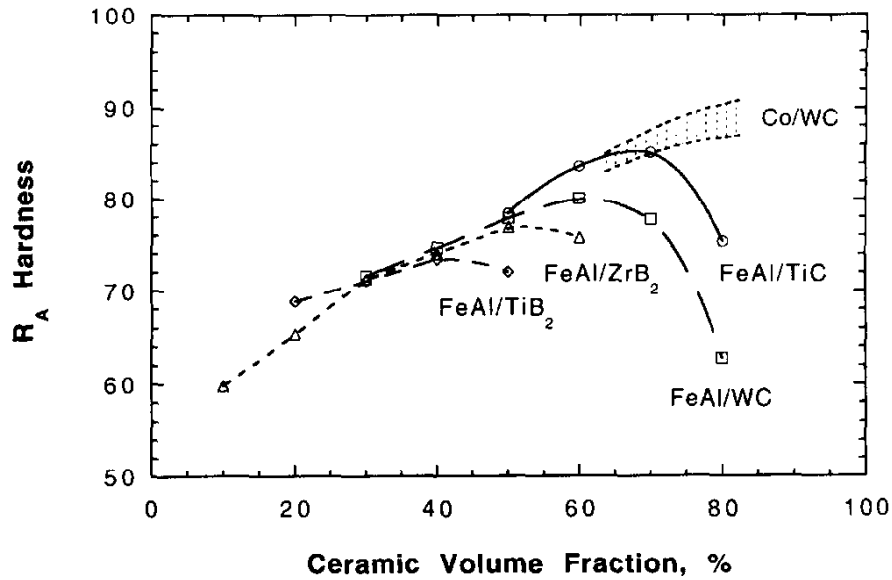
Figure 2.5: Comparison between Rockwell-A hardness FeAl composite prepared by the liquid phase sintering and melt infiltration, and WC/Co [31].

2.3 Fabrication of enhanced Fe₃Al-based materials

2.3.1 Mechanical milling

Mechanical milling (MM) is a typical powder processing method widely used to produce materials in powder form with a fine and homogeneous microstructure that cannot be achieved from other conventional techniques. In the MM process, some number of elementary powders and milling balls are mixed in a jar or vial, and agitated at constant frequency for a specific period of time. During milling, the mechanical energy provided to powder particles depends on the milling system used. The horizontal arrangement (Figure 2.6) of a MM system is commonly used because it eliminates the effect of gravity on the grinding media and powder particles during processing, and provide a homogeneous particle size reduction [32].
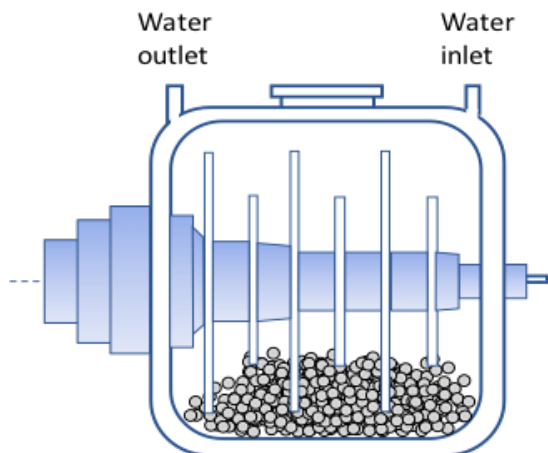
Figure 2.6: Schematic representation of the
side-view of a horizontal MM apparatus.

In a horizontal MM system, the energy transferred to the powder materials (pre-crushed or atomized) comes from the grinding media (rotors, vial and milling balls). During contact with milling balls, powder particles are highly stressed by high-energy collisions leading to severe deformation, particle reduction and/or particle growth by cold-welded [32]. Knowing that the primary source of energy transferred to powder materials is collision, different models have been developed to understand the effect of milling parameters (ball size, rotation frequency) on the milling time and reaction paths. For a single collision, the energy transferred to powder particles, E_v can be expressed as [33]

$$E_v = \frac{1}{2} K_a m_b V_b^2 \tag{2.1}$$

where, m_b is the mass of the milling ball and V_b the relative impact velocity. K_a is a constant that depends on the elasticity of the collision: if the collision is perfectly elastic, $K_a = 0$, no energy is transferred. For perfectly inelastic collision, $K_a = 1$, i.e. the total energy generated is transferred. The relative impact velocity can be expressed as follows

$$V_b = K_b \omega_p R_p \tag{2.2}$$

where, ω_p and R_p are the angular velocity and the radius of the motor. K_b is a constant that depends on the geometry of the milling device. The collision frequency of a single milling ball can be expressed as

$$\nu = K_\nu \omega_p \tag{2.3}$$

where, K_ν is a constant that depends on the geometry of the milling device. For a suitable number of milling balls, N_b, the total collision frequency ν_t can be given by the following expression

$$\nu_t = \nu N_b = N_b K_\nu \omega_p \tag{2.4}$$

These energy transferred characteristics can be applied to various milling systems with the consideration that the number of milling balls is the same [34]. Note, control agents can be added to the powder mixture to reduce the excess cold-welding, and avoid sticking of powder materials on the walls of the grinding vessel and milling balls during the process. In general, the HEBM process is carried out in a controlled environment (argon, nitrogen etc.), and the grinding vessel is usually cooled to avoid overheating of the system.

During collisions, the mechanical energy transferred to powder materials can promote structural changes and/or phase transformations in the mixture. Such transformations usually happen through mechanosynthesis, and depend on the characteristics of powders (composition, mechanical properties, particle size etc.) as well as milling parameters (ball size, rotation speed). In principle, powder particles flattened and their surface area increases, as the milling process evolves. The exposure of new surfaces and the reduction of powder particle sizes can help to decrease the diffusion path, and increases the reaction activity between elementary powders [35]. In addition, a solid-state reaction can occur if the transferred energy is sufficiently higher than the activation energy of the new phase [34].

Iron aluminide alloys have been prepared using the MM processing [36-38]. It has been reported that several properties or characteristics of iron aluminides can be influenced by the mechanical milling. The ordered B2 or $D0_3$ phases can be transformed to a disordered structure upon MM since powder particles are subjected to intense plastic deformation [39]. An increase of

the lattice parameter of iron aluminide alloys of about 0.8 % has been reported as well as the reduction of the grain size [40]. Consequently, the latter effect can cause a slight enhancement of the mechanical properties of iron aluminides [36].

2.3.2 Thermal spray techniques

Thermal spray is a large group of techniques that can be used to deposit materials prepared in the form of wires, rods or powders. Materials to be sprayed range from metallic to nonmetallic. In principle, materials in a molten, semi-molten or solid particles are accelerated and propelled onto a substrate at high speed. The mechanism of the coating formation is similar to all thermal spray deposition systems. Deposits are formed from a buildup of splats (flattened droplets, melted or semi-melted particles) via mechanical bonding upon impinging the substrate (Figure 2.7). The substrate is often roughened to improve adhesion of particles or splats.
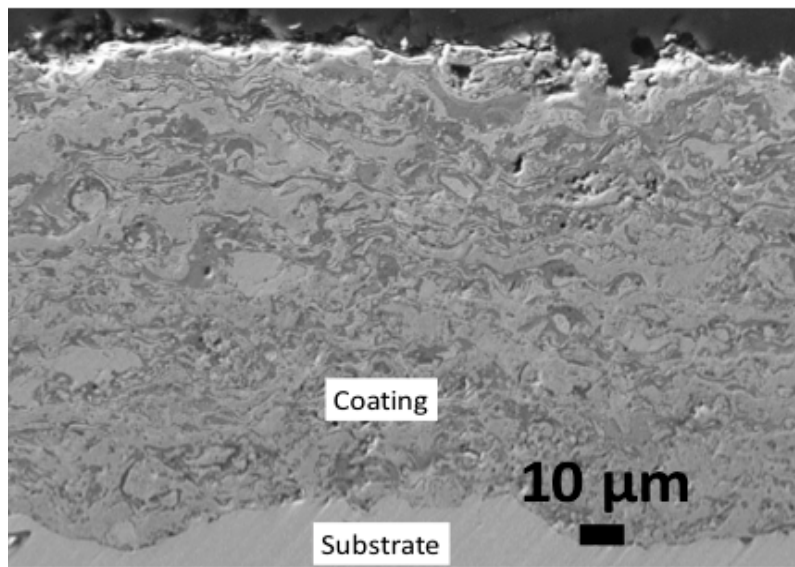
Figure 2.7: Scanning electron spectroscopy micrograph of a cross-section
showing the typical lamellar microstructure of thermal spray coatings.

In thermal spray techniques, heat is the source of energy used to process materials. This source of energy can be grouped in three main categories namely flame, electric arc and plasma. Thermal spray techniques can also be classified in terms of the initial form of materials to be sprayed (wire, rod or powder) the pressure inside the spray gun, the gas temperature, and the particle temperature and velocity (Figure 2.8).
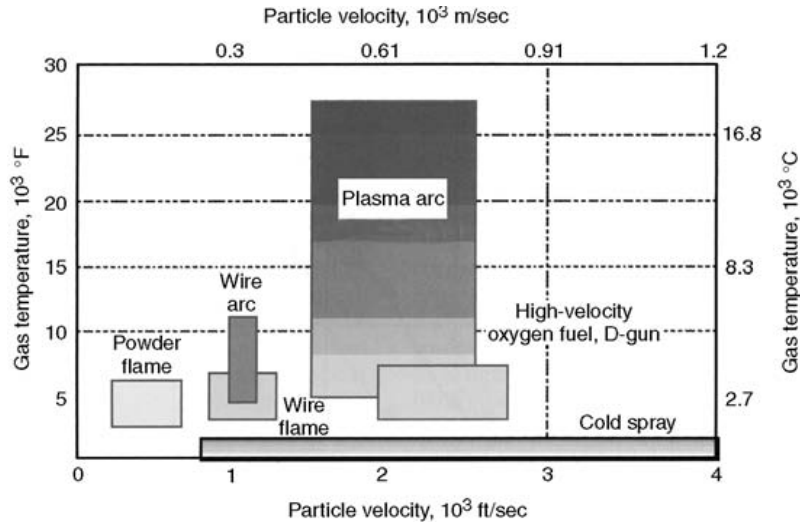
Figure 2.8: Comparison between thermal spray processes with respect to the
gas temperature and the particle/droplet velocity generated out of the gun [41].

2.3.2.1 High velocity oxy-fuel

In flame spray, the source of energy is a hot gas produced using a combusting fuel gas such as acetylene, kerosene or natural gas. Here, materials in the form of powder, rod or wire are introduced in the expanding hot flame, heated and expelled at high velocity toward the substrate [42]. Therefore, coatings are formed as described previously.

Among flame spray processes, the high velocity oxy-fuel (HVOF) technique (Figure 2.9) is widely used due to its ability to generate a relatively low gas temperature (~2800 °C) and a high gas velocity (~1800 m/s). In addition, the HVOF technique can be used to produce high quality coating with high deposition efficiency (>60 %), a high thickness (~mm), a low porosity level (<2 %) and a good adhesion (bond strength >70 N.m^{-2}) on a wide range of substrates [43].

The HVOF technique was developed in the 1980s by Browning Engineering Co and the first commercial HVOF spray system was the Jet Kote. Thereafter, other HVOF systems were developed based on the design of the nozzle while keeping the same operational principles. Over the years, the evolution of HVOF systems spans over three generations. In the first and second generation HVOF systems, the combustion pressure can vary between 3 and 5 bar. This can lead to a particle velocity of about 450 m.s^{-1} while in the third generation, the combustion pressure is higher (6 - 10 bar) as well as the particle velocity (600 - 800 m/s) [43].

2.3.2.1.1 Basic principles in a HVOF system

In a HVOF system, the materials to be sprayed are in powder form with a well-defined range of particle sizes. In such a system, oxygen is mixed in the combustion chamber with a combusting fuel (e.g. kerosene, natural gas or propane etc.). The ignition of the mixture leads to the formation of a hot and high-pressure gas that expands and flows toward the nozzle. The reaction between a hydrocarbon fuel (kerosene) and oxygen is represented by the following equation [44]:

$$\varphi C_n H_m + (n + \frac{m}{4}) O_2 = \sum_{i \in pr} \xi_i \qquad (2.5)$$

where ξ_i is the molar fraction of component i in the combustion product (pr), and φ is the equivalent ratio. The parameter φ is defined as: $\varphi = (Fuel/Oxidant)/(Fuel/Oxidant_{st})$ where st means stoichiometric.

Powder particles are introduced in the gas stream (at a precise location after the exit of the nozzle) for heating. The velocity of the expanding gas at the exit of the nozzle depends on the design. It can reach supersonic speeds with a converging/diverging nozzle [43].
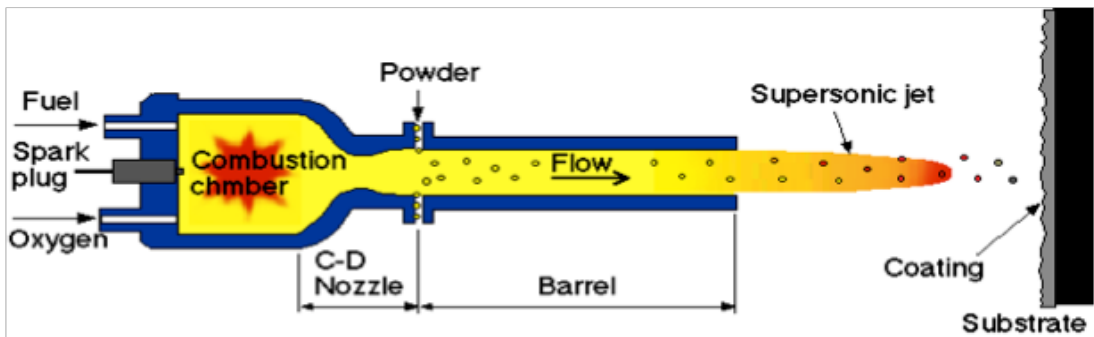
Figure 2.9: Schematic diagram the HVOF spray system in operation [45].

2.3.2.1.2 Gas and particle flow characteristics in the HVOF deposition process

Before impinging the substrate, powder particles interact with the gas flow. The coating-quality strongly depends on particle velocities and particle temperature before impact on the

substrate. Several models have been developed based on numerical simulations for the understanding of the gas dynamics in HVOF systems [45]. The combustion process in a HVOF gun is similar to that of a rocket suggesting that a one-dimensional model can be used to interpret the interaction between a particle and the gas flow. Therefore, the trajectory of a single particle of mass m_p in the gun is determined, using its equation of motion under the influence of the gas dynamic drag as follows [44]:

$$m_p \frac{dv_p}{dt} = \frac{1}{2} C_d \rho_g A_p (v_d\text{-}v_p) |v_d\text{-}v_p|$$ (2.6)

where v_p v_p is the particle axial velocity, v_d the drag velocity, A_p the projected area of the particle on the plane perpendicular to the flow direction, C_d the drag coefficient, and ρ_g is the density of the gas. Note that the term in the absolute sign represents the relative velocity between particles and the gas in a moving fluid. In HVOF systems, powder materials are in general non-spherical particles. Therefore, a new drag coefficient value as a function of the Reynolds number (Re), which accounts for the sphericity is used [43, 44].

The heating of powder particles can be described using the following heat conductivity equation [45]:

$$m_p C_p \frac{dT_p}{dt} = \pi d_p N_u k_g (T_g\text{-}T_p)$$ (2.7)

where C_p is the specific heat of the particle, T_g the gas temperature, T_p the particle temperature, d_p the particle diameter, k_g the thermal conductivity of the gas and N_u the Nusselt number (which is a function of the Reynolds and Prandtl numbers [45]).

2.3.2.2 Electric arc spray

In this process, two consumable wires (ideally from the same material) acting as electrodes are connected to a direct current (dc) power, and melting of the materials occurs when wires touch in the gun. Therefore, material droplets with size in the micron range can form at the tip of

the electrodes, and are atomized using a compressed air and propelled toward the substrate (Figure 2.10). The electric power is in the range of 5 to 10 kW and the arc voltage varies between 20 and 40 V. The size of the droplet increases with respect to the arc voltage. All electrically conductive materials can be sprayed using the arc spray process [46].
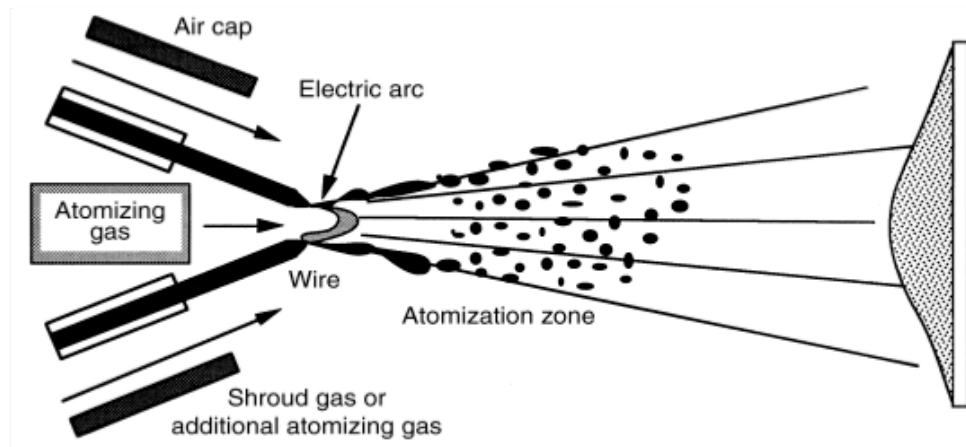
Figure 2.10: Schematic diagram of a side-view of the electric arc wire spray process [42].

2.3.2.3 Plasma spray

Plasma spray systems can be divided into two commonly used processes namely the air/atmospheric plasma spray (APS) and the vacuum plasma spray (VPS). In the APS process, the plasma is generated when an inert gas (e.g. argon) or a mixture of argon and hydrogen is heated by a dc arc. The VPS gun is basically a modified plasma torch which operates in a vacuum under a pressure range between 10 and 50 kPa. The working principle is similar for both processes, where powder particles are introduced in the plasma, heated and accelerated toward the workpiece (Figure 2.11). During the operation, the power of an APS gun can vary between 20 and 200 kW [42]. As shown in Figure 2.8, the gas temperature in plasma spray guns is well above the melting point of all materials which can be detrimental to some applications.
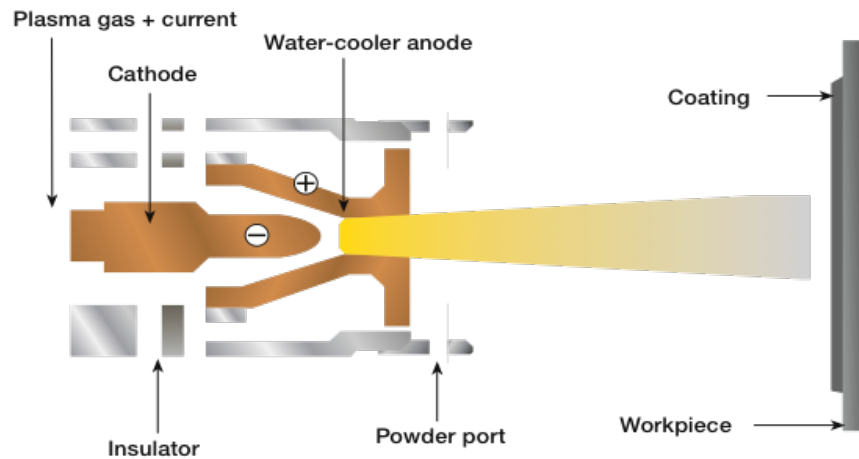
Figure 2.11: Schematic diagram of a side-view of a typical plasma spray system [47].

2.3.2.4 Cold pray

Cold spray is a relatively new technique in the family of thermal spray. It can allow the deposition of powder particles ranging from 1 to 50 μm in size. In this process, the gas temperature ranges from 0 to 900 °C and the temperature of particles at the exit of the gun is low (below the melting point of the material) compared to other thermal spray techniques (Figure 2.8). After heating, particles are accelerated toward a substrate with a velocity varying between 300 and 1200 m.s^{-1}, and particles deform plastically upon impinging the substrate (Figure 2.12). With cold spray, coatings are formed from the buildup of plastically deformed solid particles, thus minimizing the effect of high temperature oxidation, melting, evaporation or recrystallization [42].
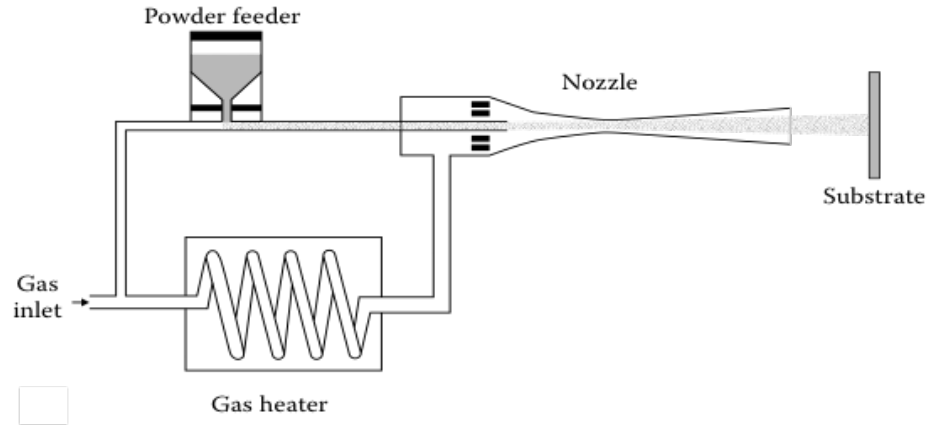
Figure 2.12: Schematic diagram of a side view of a cold spray system [48].

2.4   Characteristics of Fe₃Al-based composites

2.4.1   Mechanical surface response

Understanding a tribological process between at least two solid bodies is related to the type of interactions between tribological contacts. Therefore, the selection of materials for surface protection must be guided by a good understanding of such interactions. Upon the effect of loading or chemical reactions, the surface response can lead to severe deterioration.

2.4.1.1 Elastic response

For a material subjected to contact stresses (e.g.: tensile and compressive loadings), its mechanical behavior is characterized by the stress-strain curve. The typical stress-strain curve for brittle and ductile materials is presented in Figure 2.13 where stress (σ) is plotted as a function of the strain (ε). The elastic response from the material is represented by the linear portion of the curve. This behavior is reversible and is defined by Hooke's law,

$$\sigma = E\varepsilon \tag{2.8}$$

where E is the Young's modulus of the material.
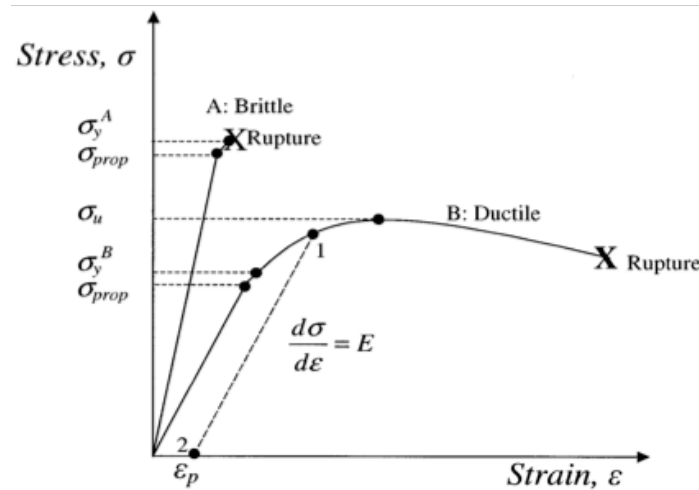
Figure 2.13: Typical stress-strain curve for brittle and ductile materials [49].

2.4.1.2 Plastic response

Plastic deformation (or a permanent deformation) takes place in the material when contact stresses induced by the effect of loading reaches a certain maximum. At this point, namely the elastic limit (also known as the material's yield strength), the material can no longer recover from such deformation. Indeed, above the elastic limit, the Hooke's law is no longer valid. This parameter is commonly obtained from the stress-strain curve by drawing a parallel line to the linear elastic portion that intercept the x-axis (Figure 2.13). The point of interception on the x-axis corresponds to ~0.2% of the strain whereas on the stress-strain curve the yield strength of the material can be obtained. In some cases (e.g.: coatings or engineered surfaces), the hardness represents the strength of the material since the yield strength of a surface is not practically easy to measure [50].

2.4.1.3 Fracture response

Fracture is a phenomenon that occurs when the contact stress applied on a material exceeds a certain limit. It is characterized by a sudden rupture of the material in an elastic or plastic deformation regime. For brittle materials, the fracture will occur with a little or no plastic deformation as illustrated by the point A in Figure 2.13. In the case of ductile materials, the rupture arises following a significant plastic deformation that lead to crack initiation at a local

point where stress is concentrated. These cracks propagate and reach a critical length where the rupture of the material occurs [50].

2.4.2 Wear

In tribology, the physical meaning of wear is well understood but a formulation of its definition, which includes all aspects of its meaning, does not exist. In general, a broad definition of wear includes the following concepts: the material loss from a surface, material transfer from one surface to another or movement of material within a single surface [51, 52]. Wear can be defined as the surface damage or material removal when at least two solid surfaces are in relative motion of rolling, sliding, or impacting [53]. In such case, the loss of material from a surface can be progressive. Wear can also be considered as a process in which surfaces are subjected to the material displacement with no net variation in volume or mass loss (change in surface topography).

The evaluation of the rate of wear is based on the real contact area of the surface under investigation. Archard and Hirst [54] showed that the rate of wear starts to be independent of the contact area when the variation of the contact surface conditions are minimized, and they demonstrated that the wear rate is proportional to the normal load. These rules of wear were supported by experimental studies in which various wear mechanisms were considered. The wear rate, K (mm^3/Nm), can be obtained from the following equation:

$$K = V/F*LK = V/F*LK = V/F \times L \tag{2.9}$$

where V (mm^3) is the volume of material loss or displaced, F (N) is the normal applied load and L (m) is the total sliding distance.

2.4.3 Type of wear mechanisms

In general, a wear process is driven by a mechanical, a chemical or a thermal (frictional heating) action that can take place individually or simultaneously between surfaces in relative motion. Surface interactions will lead to the alteration of surface morphology and/or properties or even to the material loss via various degradation modes.

A comprehensive classification of wear was proposed by Kragelsky in 1962 (Figure 2.14) [3]. In tribology, interactions between surfaces are critical at the level of surface roughness where

the nominal contact area is often defined. Under the influence of loading, asperities can be subjected to the elastic and/or plastic deformation, resulting to the generation of external particles. In some case, the surface with hard asperities will act as abrasive components. Moreover, at the tip of asperities, a difference in adhesion bond strength can also initiate material loss. Beside all these phenomena occurring because of surface interactions, the frictional heating of surfaces will likely accelerate the material loss [55].

Material removal due to the effect of wear is a common thing that exists between various wear degradation mechanisms. This phenomenon is unlikely to be caused by a specific wear mechanism instead of a combination of several modes that include abrasion, fatigue, adhesion and corrosion [53].
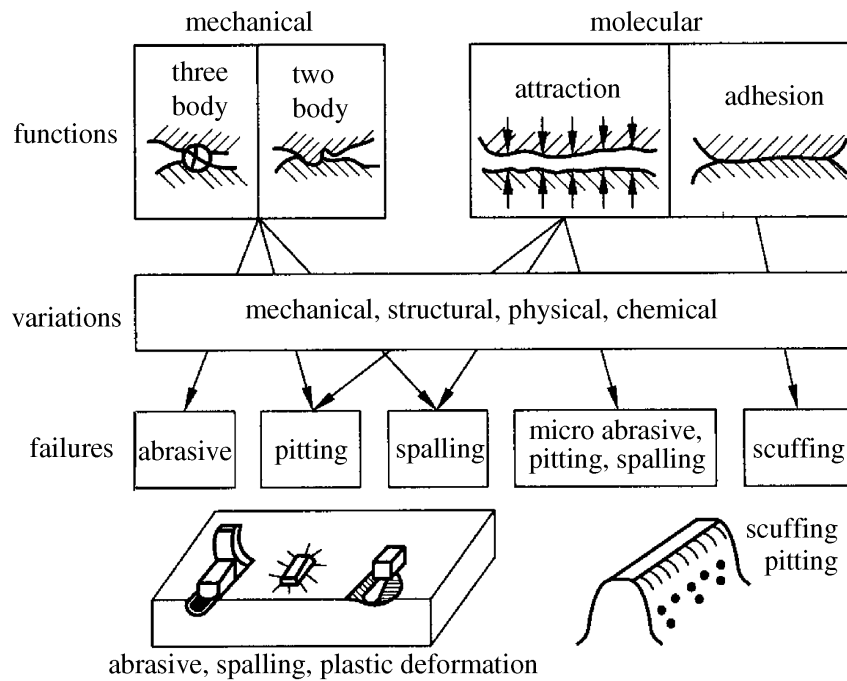
Figure 2.14: Wear classification proposed by Kragelsky [3].

2.4.3.1 Abrasive wear

In general, abrasive wear occurs in situations where plastic deformation or fracture can be initiated (Figure 2.15). The presence of hard asperities of one of the contacting surfaces or free hard particles entrapped between two surfaces in relative motion can result to a plastic deformation of the softer surface. Consequently, plowings are formed on the softer surface from a series of grooves. This process can lead to subsurface deformation where cracks can nucleate and

propagate in the material. In the case where the surface is brittle or exhibits a low fracture toughness, cracks initiate from the contact surface or defects (cracks, porosity, etc.) and materials can fail by brittle fracture [53]. In addition, the hard asperities of one surface can act as abrasive components.
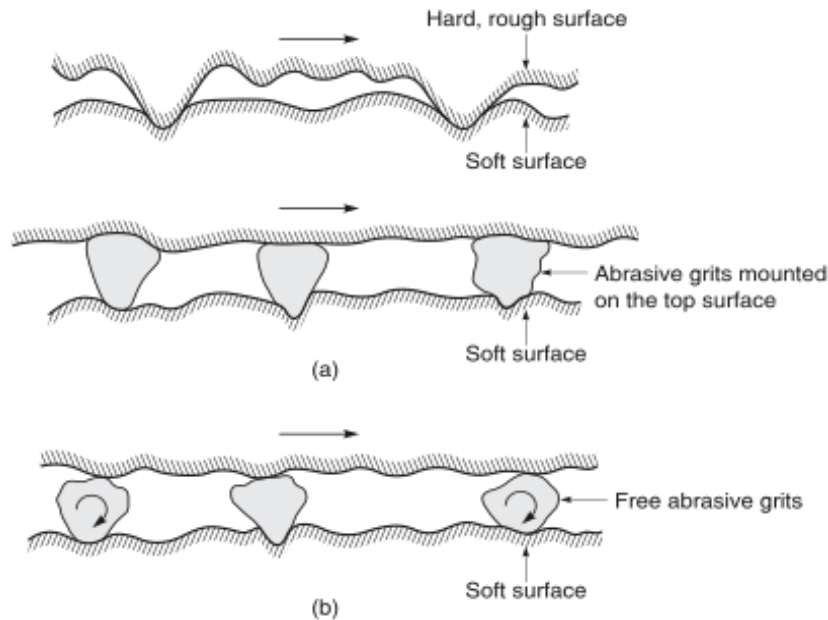
Figure 2.15: Schematic representation of different types
of abrasive wear mechanisms [53].

2.4.3.2 Adhesive wear

Material loss caused by adhesive wear is characterized by a transfer of materials from one mating surface to another. In this process, contact points between two surfaces (asperities) under normal pressure are sheared upon repeated sliding when the yield stress is exceeded [52]. The damage by adhesive wear can occur locally where the adhesive strength between a strong and a weak region of mating surfaces is lower than the breaking strength of these regions. In addition, material loss due to the accumulation or buildup of plastically sheared layers of material from asperities is also referred to as adhesive wear.

In general, the loss of the adhesion strength results to the detachment of wear fragments if the residual elastic energy of adherent fragment is higher than its cohesive strength in the material. In some situations, materials detached from mating surfaces via adhesive wear can be

beneficial if acting as solid lubricants, or detrimental if they contain hard particles that can act as abrasive components [53].

2.4.3.3 Fatigue wear

As described previously, abrasion or adhesion occurs primarily at the asperities of the two surfaces interact. However, in some situations asperities are not subjected to either adhesion or abrasion when they interact in a sliding context. Instead, they can be prone to plastic deformation due to contact stresses induced upon repeated loading and unloading. Therefore, a continuous deformation (until a certain stress limit is exceeded) can lead to crack nucleation at the surface and crack propagation in the subsurface. In the presence of defects in the material, these cracks can propagate much faster. Fatigue wear can also occur from a stress-dependent chemical reaction between the surface of the material and the corrosive medium [53].

2.4.3.4 Oxidative and corrosive wear

Material loss due to chemical or electrochemical reactions depends on the environment in which the action takes place. In ambient air, oxygen is the dominant corrosive agent and the resulting chemical reaction when sliding occurs in dry conditions between mating surfaces is referred to as oxidation. In ambient and dry conditions, the increase of the contact temperature at the tip of the asperities can accelerate the oxidation of sliding surfaces [52].

In wet conditions (presence of an electrolyte), chemical reactions take place due to a potential difference between two surfaces (or regions on the same surface), with a passage of an electric current, is referred to as the electrochemical corrosion. This type of corrosive wear frequently occurs in corrosive media that act as an ion conductor. In the presence of a current flow between a region at low potential (anode) and a region at high potentials (cathode), via an electrolyte, the material (metallic in most cases) at the anode dissolves producing ions and electrons. These electrons migrate from the anode to the cathode in order to reduce ions or oxygen in the electrolyte [53].

2.5 Enhancement of the tribo-mechanical properties of Fe$_3$Al

A suitable choice of material design and fabrication techniques usually results in a coating with unique microstructure and tailored tribo-mechanical properties [27]. As described

previously, changes in microstructure due to the solid-state phase transformation or the introduction of defects in the material, occurring during the Mechanical Milling (MM) process or the HVOF deposition, can provide the material with enhanced tribo-mechanical properties.

2.5.1   Strengthening by micro-alloying and grain refinement

A significant disordering of the iron aluminide structure resulting from the destruction of the long-range order of the cubic structure was observed when MM was used to process the Fe-40%Al alloy leading to an increase in the hardness [39]. In the form of a coating, MM materials with disordered structure tend to exhibit an increase in hardness. The disorder structure of the MM iron aluminide powder retained in coatings contributed for the higher hardness exhibited by the coatings compared to materials with ordered structure [40, 56]. Therefore, the higher hardness of such material with disordered structure is attributed to defect hardening in the coatings.

Grain refinement has been shown to have a positive impact on the toughness and ductility of iron aluminide alloys [56]. Similarly, FeAl coatings prepared with finer grains have been indicated to exhibit a higher hardness compared to larger powder particles. For thermal spray coatings, such a high hardness is attributed to the increased number of inter-splat boundaries [57]. However, a contradictory conclusion was reported from a similar study carried out by Grosdidier and colleagues [58]. These authors argued that large unmelted particles of MM FeAl powders, retained in the HVOF coating, were responsible for the high hardness. They also indicated that the hardness value of HVOF coatings increased with respect to the number of unmelted powder particles retained in the HVOF coatings (Figure 2.16). The use of different powder samples prepared under different milling and HVOF deposition conditions can result to such conflicting reports. In order to clarify this misunderstanding, it is imperative to perform a systematic study.
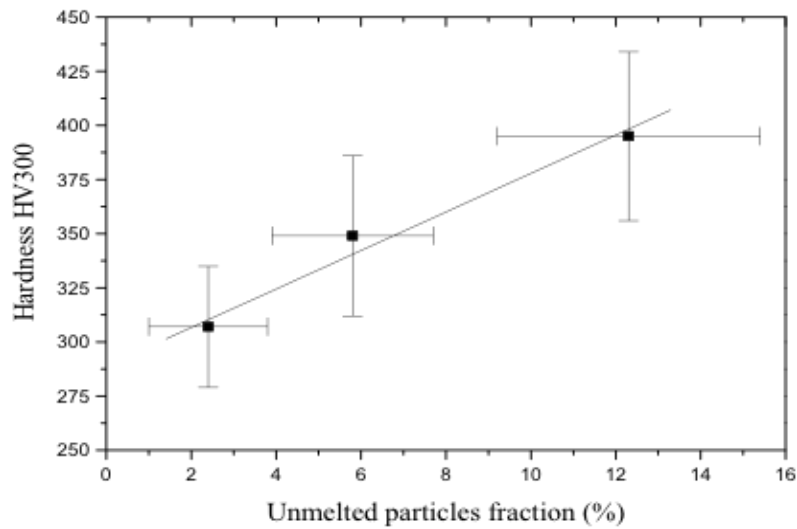
Figure 2.16: Evolution of the microhardness as a function of the amount
of unmelted milled powder particles retained in the HVOF coatings [58].

Solid solution strengthening via the addition of alloying elements is another way to improve the mechanical properties of iron aluminides. This happens through the insertion or replacement of atoms in the cubic structure of the FeAl or Fe_3Al. The formation of nanocrystalline Fe(Ti, Al) solid solutions were obtained by the MM of the mixture of Fe_3Al and Ti powders. The addition of Ti was beneficial in two ways; first, a positive influence on the hardness was observed since Ti tends to substitute for Fe in the cubic structure of the Fe_3Al; second the decrease of the grain size was noticed since the microstructure was refined by the hard Ti particles [59]. Grain refinement and grain boundary strength has also been achieved in iron aluminides with the addition of boron to avoid brittle intergranular fracture [15]. As discussed previously, iron aluminides exhibit poor mechanical properties characterized by the low cleavage strength and environmental brittleness due to hydrogen embrittlement in the presence of moisture. Improved ductility of iron aluminides has also been observed with the addition of C, Nb, and Ti into the Fe_3Al compound, resulting in a change in slip behavior of superlattice dislocation from planar slip to multiple slip process [60].

2.5.2 Strengthening by precipitation

Often, the energy provided to powder materials during the MM process is insufficient to initiate solid-state reactions. In other words, this energy is lower compared to the activation energy of some secondary phases (e.g.: ceramic materials). Therefore, heat treatment is used to bring the extra energy needed for such reactions to take place. MM combined with heat treatment has been used to prepare a wide range of MMC materials, for example iron aluminide-based composites reinforced with ceramic phases [61-65]. This fabrication approach is often referred to as *in situ* strengthening when the precipitation of secondary phases (ceramic materials in the context of this thesis) takes place within the matrix material during the fabrication process. This is a cost-effective manner to produce MMC leading to fine inclusions and a clean matrix/reinforcements interface. The resulting MMC coatings can thus exhibit enhanced tribo-mechanical properties.

Among ceramic materials used as secondary phases, carbides are commonly used. Krasnowski *et al.* obtained a nanocomposite material with TiC dispersion from a mixture of Fe, Al, Ti and C powders [66]. Nanoparticles of TiC formed within the metallic matrix during MM through a solid-state reaction between Ti and C [67]. Using a similar approach, Amiriyan *et al.* fabricated TiC-Fe$_3$Al composite coatings and showed that the hardness and the wear resistance of the composite increases with the TiC content. The enhancement of the mechanical properties was associated with the precipitation strengthening of the Fe$_3$Al matrix with TiC inclusions [61], whereas its high wear resistance was attributed to the load-carrying capacity of TiC particles [68]. Moreover, it has been shown that the coefficient of thermal expansion of the FeAl-TiC composite can be controlled to match that of various substrate materials by adjusting the TiC content [69].

A mixture of the Fe, Al, Ti and B powder was heat treated at high temperature in order to initiate combustion synthesis reactions (SHS reactions) between elementary powders. The resulting material was composed of fine TiB$_2$ particles dispersed in the FeAl matrix phase. The Vickers Hardness (HV) of the composites coating increases with the content of the secondary phases (TiB$_2$ or TiC) (Figure 2.17) [70].
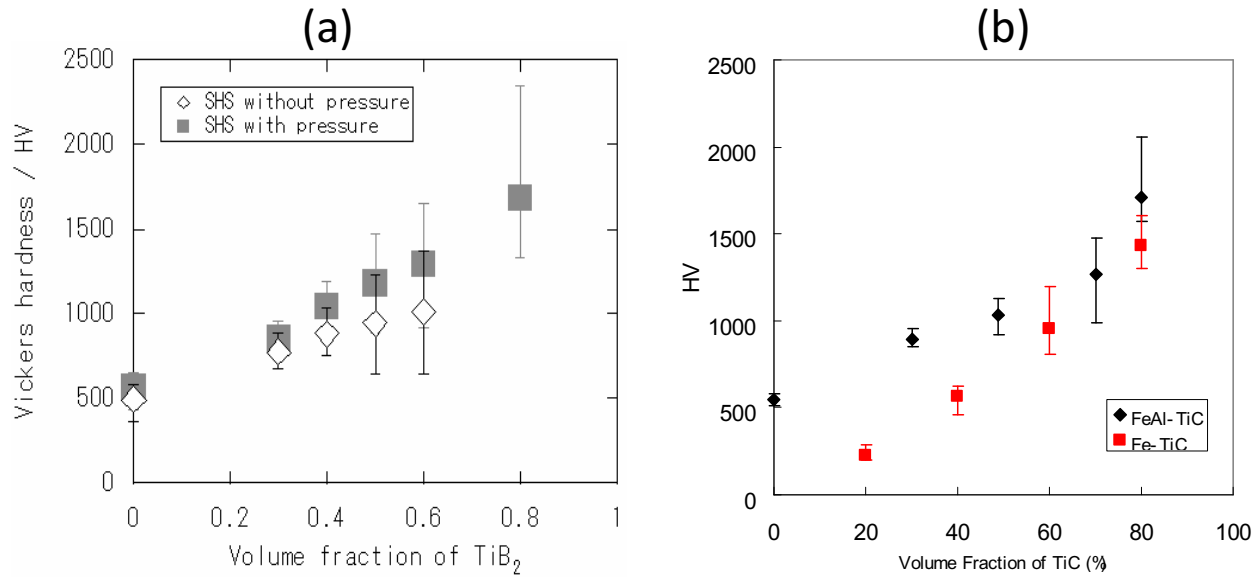
Figure 2.17: Vickers hardness (HV) of the FeAl alloy as a function of
the volume fraction of (a) TiB$_2$ and (b) TiC particles, adapted from [70].

The use of oxide phases has also been reported to provide enhanced tribo-mechanical properties to the iron aluminide matrix. Subramanian *et al.* fabricated and compared the mechanical properties of FeAl-based composites strengthened with alumina (Al$_2$O$_3$) particles [71]. The addition of alumina inclusions resulted in an increase in hardness and yield strength of the iron aluminide alloy. However, the authors suggested that an increase in the density (low porosity) and an increase of the bond strength between the matrix and *in situ* nanometric Al$_2$O$_3$ inclusions can yield further improvement such as high fracture toughness and high bend strength [72].

Boride phases have been formed in the iron aluminide matrix by the *in situ* precipitation process leading to enhance mechanical and tribological properties. Kim *et al.* [73] reported a high-bonding strength between the matrix and TiB$_2$ inclusions promoted by the clean matrix/reinforcement interface which resulted to a high hardness and a high elastic modulus. A significant increase of the fracture stress of the FeAl-TiB$_2$ composite was also observed.

2.5.3 Strengthening by particles

The addition of preformed hard ceramic materials into a soft matrix is another way to provide enhanced mechanical and wear properties. With this approach, carbide particles have been used to reinforce the iron aluminide matrix in order to improve its tribo-mechanical

properties [65, 74]. The wear behavior of the pure FeAl coating fabricated using the high velocity air fuel technique was compared with the composite FeAl-WC coating [75]. The addition of WC particles shows enhancement of the wear resistance of the FeAl. The presence of carbide particles in the FeAl matrix enhances the fracture toughness, bend strength and hardness of the composite material [27]. In addition, the ability of the WC inclusions to bear the high contact pressure during sliding wear also contributed to an increase of the wear resistance of the composite coating.

Huang *et al.* have reported that with the addition of 5 vol.% of WC, the hardness and Young's modulus of the Fe_3Al material substantially increase compared to the Co-based composite prepared under the same conditions (Figure 2.18) [76]. Knowing that the hardness of WC-Co materials follows the Hall-Petch consideration, the authors attributed the higher hardness of the WC-Fe_3Al composite material to the much finer grain size of the WC inclusions. In addition, the ability of the iron aluminide matrix to be worked hardened compared to cobalt can influence positively the mechanical properties of the Fe_3Al-based composite [77].
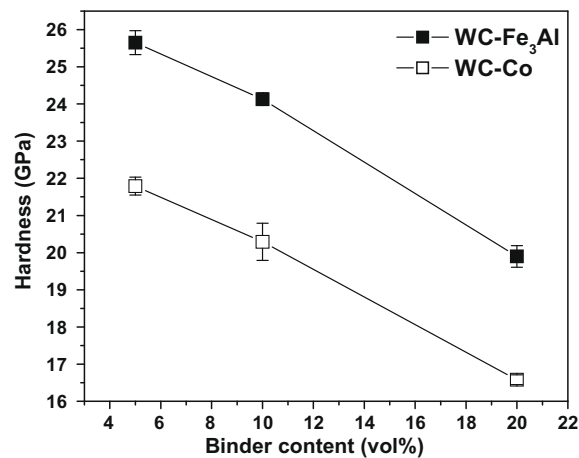
Figure 2.18: Hardness of WC-Fe_3Al and WC-Co materials as a
function of binder content, adapted from [76].

As indicated previously, iron aluminides are potential materials for high temperature applications where high resistance to oxidation and corrosion is required. Under these considerations, composite materials fabricated from the pure Fe_3Al reinforced with alumina (Al_2O_3) dispersions were used to provide additional attributes such as higher toughness at high

temperature [71]. However, the addition of Y_2O_3 particles to a Fe_3Al matrix via the MM process has shown only little effect on the hardness of the composite material [78].

The addition of preformed boride particles has also influenced the mechanical properties of the iron aluminide matrix. A significant improvement of the yield strength of the Fe_3Al material was observed with the addition of TiB_2 as well as SiC particles [79]. However, the elongation rate of the composite material was slightly lower compared to the matrix. The nanocrystalline composite of FeAl reinforced BN phases were prepared by Rosas *et al.* [80]. It has been demonstrated that the addition of BN particles contributes to refining the grains.

Strengthening the iron aluminide matrix by the addition of hard secondary phases has shown to be effective when enhancing the mechanical and tribological properties is required. However, certain aspects of the material design should be considered such as the volume fraction of inclusions. Schneibel *et al.* [27] have shown that a volume of about 20 to 80% of WC, TiB_2, TiC or ZrB_2 particles can be added to the iron aluminide matrix. Even though the addition of secondary phases can lead to improved mechanical and tribological properties of iron aluminides, only an optimum volume fraction of these inclusions is required [27, 71].

2.6 Enhancement of the corrosion properties of Fe₃Al

Iron aluminide alloys have been established as potential material for high temperature applications due to their ability to form protective aluminum oxide scales. However, the poor corrosion property of the iron aluminide at ambient temperature is a concern. The modification of the microstructure of the iron aluminide by micro alloying as well as the surface treatment in the case of coatings can provide an enhancement of corrosion properties.

2.6.1 Micro-alloying

Micro alloying is a process in which elements such as Cr, Ti, Nb, Mo, etc. added to a material using MM. They act as inhibitors for corrosion. In an oxidizing environment (e.g. liquid or gaseous) a material containing chromium will likely oxidize forming a passive layer in order to protect the surface of the material from the external environment. Taking advantage of this attribute, the addition of Cr and Ti into the iron aluminide induces a change of the electronic structure of the Fe_3Al atoms by the formation of solid solutions that leads to enhanced passivity. Other elements such as Ta or Mo can provide enhanced passivation to iron aluminide alloys by

the formation of an ordered structure on the surface of the material [81]. Combination of various elements has been shown to enhance the pitting and crevice corrosion of iron aluminide alloys. Kim and Buchanan [82] demonstrated that the presence of Cr and Mo will favor the formation of Al-rich passive layer containing MoO_3 and Cr_2O_3 which delays the absorption of chloride ions. The alloying of iron aluminide and carbon has shown to be beneficial for corrosion in aqueous electrolytes. However, Rao *et al.* have shown that in a 0.5 M sulphuric acid, the carbide phase was the preferential site for the corrosion attack [83]. Therefore, a large amount of C in the iron aluminide has been shown to be detrimental for the corrosion resistance of the alloy.

2.6.2   Surface engineering

Using the basic idea behind the self-protection of Cr containing materials in oxidizing environment, surface protection of coatings using multilayer structures has been developed. Often, coatings exhibit defects on the surface which are passageways for corrosion agents. For that reason, the addition of a topcoat on the coating is a way to delay the infiltration of corrosion agents. Topcoats such as DLC (diamond-like carbon) and CrN deposited by physical vapor deposition (PVD) have been used in multilayer structures. The amorphous structure of the DLC and its chemical inertness have been considered as the principal reason for the high corrosion resistance of DLC films [84]. The CrN film will instead form a passive protective layer [85, 86].

CHAPTER 3   EXPERIMENTAL METHODS

This section describes the materials, and the main experimental methodology applied in the context of this Ph. D. work. First, I will present details on the fabrication of powders and preparation of coatings for characterization. Secondly, I will describe the mechanical, the tribological and the corrosion characterization approaches used in the context of this thesis. Finally, I will present the techniques used to assess the morphology and the microstructure of powders and coatings.

3.1 Fe_3Al-based powder preparation

3.1.1   High-energy ball milling

All composite powders were prepared by mechanical milling (MM) using a horizontal rotary high-energy ball mill (HEBM) system (Zoz GmbH Simoloyer CM01 2 Liter) equipped with a stainless-steel jar and milling balls of 4.75 mm in diameter each; all composite powders were prepared under argon atmosphere in order to avoid undesired reactions. For all compositions of powder mixtures, the ball-to-powder weight ratio was 10:1. The milling system was operated at different motor velocities (200 and 1000 rpm) and different milling times (between 2 and 10 h) so as to provide the powder materials with different energies leading to different microstructures of the resulting powders.

In the context of this thesis, all starting materials were commercial powders provided by Hydro-Quebec (HQ). Two composite powder systems were studied. Each system contained different types of secondary phases dispersed in the iron aluminide matrix. In the first system, a stoichiometric mixture of hexagonal boron nitride (h-BN) and the pure iron aluminide (Fe_3Al) powders were ball-milled in order to favor solid-state reactions between powder materials. In this system, aluminum nitride (AlN) and iron boride (Fe_2B) are expected to form in an iron aluminide matrix. In the second system, the powder materials consisting of Fe_3Al, h-BN and Ti powders were ball-milled at high energy. In this case, the secondary phases of interest are TiN and TiB_2.

3.1.2   Heat treatment

In a MM process, new phases can form in the powder material mixture if the mechanical energy provided to the powder via collision is sufficiently higher than the activation energy. As

indicated previously, a structural change in such situations depends on the characteristics of powder materials and the milling parameters. Often, the energy transferred to powder materials is not enough to initiate solid-state reactions in the powder mixture leading to a resulting powder with metastable or stable phases. For that reason, it is necessary to provide the final powder with an extra energy needed for the reaction to complete using heat treatment.

In this Ph. D. project, the HEBM of initial powder materials was followed by the heat treatment of part of as-milled powders. The process was carried out in a furnace under vacuum (~10^{-6} mbar) at a temperature varying between 400 °C and 1300 °C. Powders were heated at 3 °C/min and cooling at 7 °C/min regardless of the system studied.

3.1.3   Particle size distribution

Powder materials were characterized before and after the HEBM process. Among, all characteristics of powders, the distribution of particle size was measured prior to powder deposition. The particle size distribution defines the efficiency of the deposition process and therefore influences the quality of the coatings. In this project, the particle size distribution of the powders studied was measured by laser diffraction spectroscopy using the Horiba LA-900 (Laser Scattering Particle Size Distribution Analyzer). During the measurement, a 633 nm laser beam passes and scatters through a cloud of powder particles suspended in a dispersant liquid. The intensity of the scattered light is converted to electrical signals, and the particle size distribution was calculated using the Mie scattering theory. This theory is appropriate for powders due to the wide range of particle sizes [87].

3.2   Fe$_3$Al-based coatings deposited by HVOF

All powders were deposited on stainless-steel (SS) 304 substrate using a Praxair TAPA J-P 8000 series high pressure high velocity oxy-fuel (HVOF) system under the conditions shown in Table 3.1. To improve adhesion of melted and semi-melted particles impinging on the surface, the substrates were grit blasted (to roughen the surface) using 60 grit alumina particles and cleaned with methanol. Before the deposition, powders were sieved and a suitable range of particle sizes was kept for ensuring a good deposition efficiency and a high quality of coatings. The particles impinging on the surface at a high impact velocity will deform, flatten and adhere on the rough surface of the substrate. A uniform coverage on the substrates was achieved by

scanning the HVOF gun, mounted on an ABB robot arm and controlled with a computer, in perpendicular directions. Deposits were formed from a buildup of solid, melted and semi-melted particles as described in Chapter 2.

Prior to further characterizations and analyses, HVOF deposits were cut into coupons and progressively grounded using silicon carbide polishing pads and mirror-finished using suspended diamond particles (3 and 1 μm). Samples were ultrasonically cleaned in acetone, and isopropanol for five minutes to remove the debris left on the surface as a result of polishing.

Table 3.1: HVOF deposition parameters used in this thesis for coating fabrication.

Spray parameters	Value
Standoff distance (cm)	38
Nozzle length (cm)	15
Nozzle diameter (mm)	11
Chamber pressure (kPa)	700, 710
Oxygen flow rate (slpm)	890, 897
Kerosene flow rate (l/h)	23.5
Equivalent ratio oxygen/kerosene	1.2, 1.1

3.3 Mechanical characterization

3.3.1 Indentation testing

Indentation is typically a method that consists of pushing an object with known geometry and properties into a material. Consequently, mechanical properties (hardness and Young's modulus) of tested materials can be evaluated. Indentation has evolved from the 10-step scratch hardness scale established by Friedrich Mohs for minerals, to the evaluation of hardness of metallic materials using spherical indenters (Brinell, Rockwell), and to the use of sharp pyramidal indenters (Vickers, Berkovich etc.).

During the indentation process, an indenter penetrates a material and the applied force is continuously monitored and recorded as a function of tip's penetration depth, and a load versus the indenter displacement curve is plotted (Figure 3.1). The loading segment of the curve

corresponds to the elasto-plastic response to the penetration of the indenter and the unloading part suggests that the material elastically recovers from the initial deformation (Figure 3.1b). Thus, the hardness and Young's modulus can be extracted using the methodology proposed by Oliver and Pharr [88] for elasto-plastic materials.
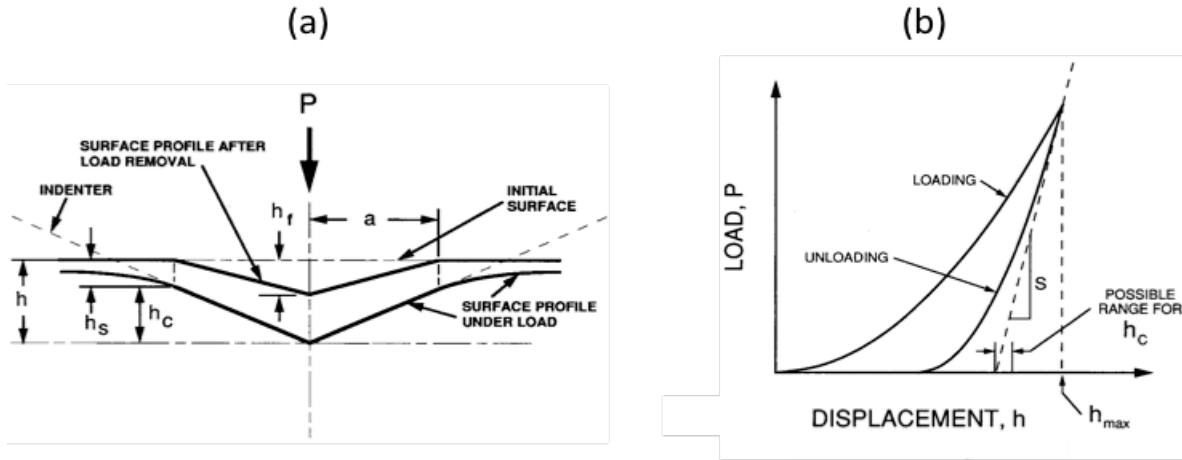
Figure 3.1: (a) Schematic representation of the cross-section of an indentation and (b) typical load versus the indenter displacement curve (adapted from [88]).

Hardness, expressed as $H = F/A$ where F is the applied load and A is the projected contact area, is often referred to as a measure of the resistance to the penetration of a body (indenter) with known geometry. Hardness is typically used for comparison, and its evaluation depends on its scale (macro, micro or nano) and the class of material (polymers, metals, ceramics, composite, etc.) studied. Hardness can also be evaluated from the residual impression left on the sample in accordance with the ASTM C1327-15 [89]. In the case of a Vickers indenter, the projected area can be evaluated using the geometrical description as illustrated in Figure 3.2. Therefore, the expression of the hardness (Vickers hardness) becomes $H = F/A = 1.8544 \, F/d^2$ [90]. This approach is also valid for the Berkovich tip because the area-to-depth is the same as for the Vickers tip.
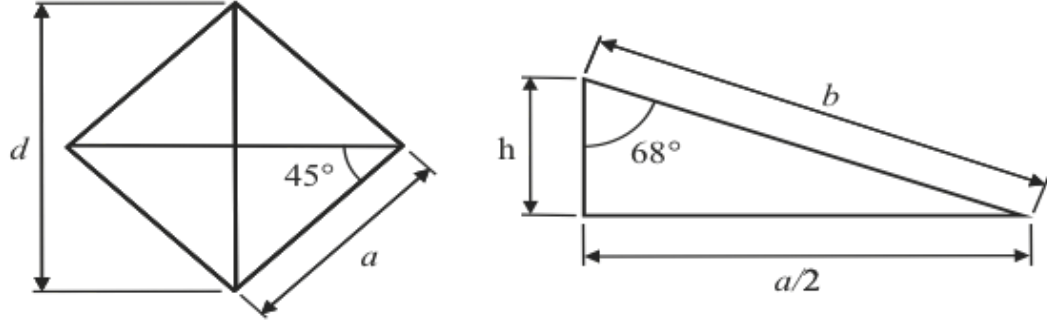
Figure 3.2: Schematic representation of a geometrical description of
the typical imprint of Vickers indenter, adapted from [90].

Regardless of the geometry of the indenter, the reduced modulus (E_r) can be obtained using the following equation:$E_r = S\pi^{1/2}/(2A$

$$E_r = S\frac{1}{2}\frac{\sqrt{\pi}}{\sqrt{A}} \tag{3.1}$$

where, A is the projected area on the surface of the sample and $S = dP/dh$ $S = dP/dh$ is the stiffness of the material at the maximum load (Figure 3.1). In addition, the reduced modulus is strongly dependent on the diamond tip geometry and the surface of the sample studied, and it is given by the following expression [88]:

$$\frac{1}{E_r} = \frac{(1-v^2)}{E} + \frac{(1-v_i^2)}{E_i} \tag{3.2}$$

where, EE is the indentation modulus to be measured, v the Poisson coefficient of the sample, E_i is the Young's modulus and v_i is the Poisson coefficient of the diamond tip.

In the context of this project where samples exhibit microstructure in which secondary phases are dispersed in a matrix, I have used Vickers and Berkovich indenters to evaluate the mechanical properties of the samples on the micrometer scale. Note that the HVOF samples are thick enough (few hundred microns) to avoid the effect of the substrate on indentation

measurements. Thus, the indentation parameters were chosen so that the volume of material plastically deformed under the indenter tip is confined in the HVOF coating.

To study the effect of individual phases in composite materials, the depth-sensing indentation (also called nanoindentation) technique with a Berkovich indenter was employed. The advantage of this technique is that the Berkovich diamond tip is sharp (as opposed to Vickers) and the mechanical properties are evaluated at very shallow depth.

A Micro-Combi tester (CSM, Peseux, Switzerland) was used to evaluate the microhardness of samples while the nanoindentation was performed using a Triboindenter (TI950 Hysitron Inc. Indianapolis, USA). During the indentation process, the load was linearly increased up to its maximum, kept constant at that maximum and then linearly decreased down to zero. Many indentations were performed on the cross-section and the top surface of coatings for statistical analysis purposes and the average hardness value and its standard deviation were calculated from these measurements.

3.3.2 Scratch testing

Scratch testing is a technique widely used to qualitatively and quantitatively characterize adhesion strength of a coating on a substrate. In this technique, a diamond tip typically (a 200 μm Rockwell C indenter) is drawn over the surface or the cross-section of the coating at constant speed. The applied force on the stylus can be constant, linearly increasing or decreasing. In general, the minimum applied load at which cracks appear with the detachment or removal of the coating from the substrate is used as the measure of adhesion of a coating. In the context of this project, the scratch test was performed on the cross-section of coatings because the minimum thickness of my samples was ~100 μm, and such test on the top surface could not yield any conclusive result. The appearance of the scratch damage (cracks, delamination, etc.) were used to qualitatively compare the adhesion strength of coatings on the substrate. Other useful information such as the cohesive bond strength between particles and/or splats can be extracted from this test.

3.4 Tribological characterization

3.4.1 Dry sliding wear test

A pin-on-disc tribometer is a laboratory test apparatus commonly used to evaluate friction and wear of materials due to its simple configuration and better control of experimental conditions. In this technique, a pin under a normal load, $F(N)$, is pressed perpendicularly on the top surface of a rotating sample (disc) as illustrated in Figure 3.3, and the tangential force (F_T) is continuously monitored and recorded. The dynamic coefficient of friction,

$$\mu = F_T/F \tag{3.3}$$

that maintains the sliding motion throughout the test can be plotted with respect to time, sliding distance or number of turns.

The wear rate, $K(mm^3 N^{-1} m^{-1})$ of the coatings was determined after the test from the volume of material loss or displaced, $V(mm^3)$. The product between the diameter of the wear track ring and its cross-sectional surface, measured by profilometry, was used to obtain V, and K was calculated using the expression,

$$K = V/F*L \tag{3.4}$$

where, L (m) is the total sliding distance.

In this Ph. D. project, the wear test was performed using a pin-on-disc tribometer operating in ambient conditions. The normal force was chosen between 5 and 40 N and the diameter of the wear track ring was fixed and the sliding velocity varied between 0.1 and 1 cm/s. The sliding distance was maintained at 1000 m and the counterpart material was an alumina (Al_2O_3) ball of 4.75 mm in diameter fixed at the end of a pin. The wear test conditions were selected in order to compare results with other systems studied at HQ [61, 91].
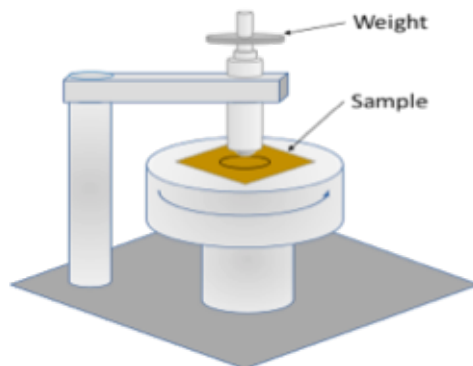
Figure 3.3: Schematic representation of a pin-on-disc tribometer.

3.5 Corrosion test

The corrosion behavior of materials in aqueous solution is typically studied using a three-electrode cell. In such a configuration, the sample is connected to the working electrode (WE) and its surface is in contact with the electrolyte (ionic conductor) in which the counter electrode (CE) (graphite rod or platinum wire) and the reference electrode (RE) are immersed. The Standard Calomel Electrode (SCE), which exhibits a potential of 0.242 mV with respect to the Standard Hydrogen Electrode (SHE), was used as the RE. These electrodes are connected to a potentiostat (equipped with a frequency analyzer) which controls and monitors the potential and current between the WE and the RE, and between the WE and the CE, respectively.

In the context of this thesis, the corrosion test was performed in three steps without changing the electrolyte solution. In the first step, the potential between the sample and the RE, namely the Open Circuit Potential (OCP), was monitored and recorded as a function of time in the absence of a driving force (current or potential). In the second step, the Electrochemical Impedance Spectroscopy (EIS) was performed over a frequency range of 10^{-2} Hz and 10^{5} Hz at OCP. Finally, the potentiodynamic polarization (pitting) test was carried out from 100 mV to 2000 mV above the OCP, with a scan rate of 1 mV/sec.

3.5.1 Electrochemical impedance spectroscopy

Electrochemical impedance spectroscopy is a technique frequently used to study the electrochemical kinetics of reactions that occurred at the material/electrolyte interfaces. In

experimental situations, the electrochemical impedance is measured by applying an excitation alternating voltage with small amplitudes -10 to +10 mV. The voltage signal (E_s) and its corresponding current (I) response, shifted in phase by ϕ with respect to E_s, can be expressed as a complex function using the Euler's relationship [92]:$E = E_0 exp(j\omega t)$

$$E_s = E_0 exp(j\omega t) \tag{3.5}$$

and

$$I = I_0 exp(j\omega t\text{-}\phi)I = I_0 exp(j\omega t\text{-}j\phi) \tag{3.6}$$

where E_0 and I_0 are the amplitude of the potential and current, respectively, and $\omega = 2\pi f$ is the angular frequency. The complex impedance, Z, can be obtained as:

$$Z = E_s/I = E_0/I_0 exp(\phi) = Z_0 exp(\phi) = Z_0 cos(\phi) + jZ_0 sin(\phi) = Z_{real} + jZ_{im}$$
$$Z = E/I = E_0/I_0 exp(\phi) = Z_0 exp(\phi) = Z_0 cos(\phi) + jZ_0 sin(\phi) = Z_{real} + jZ_{im} \tag{3.7}$$

where Z_0 is the amplitude of the complex impedance, Z_{real} and Z_{im} are the corresponding real and imaginary parts, respectively.

In EIS, the complex impedance Z, represented by the length of the vector Z, is used to interpret the "Nyquist plot" (Z_{real} in x-axis is plotted with Z_{im} in y-axis with ω varying from high to low frequencies) or the "Bode plots" (log of frequency in x-axis with Z_0 or ϕ in the y-axis) as illustrated in Figures 3.4a and 3.4b, respectively.
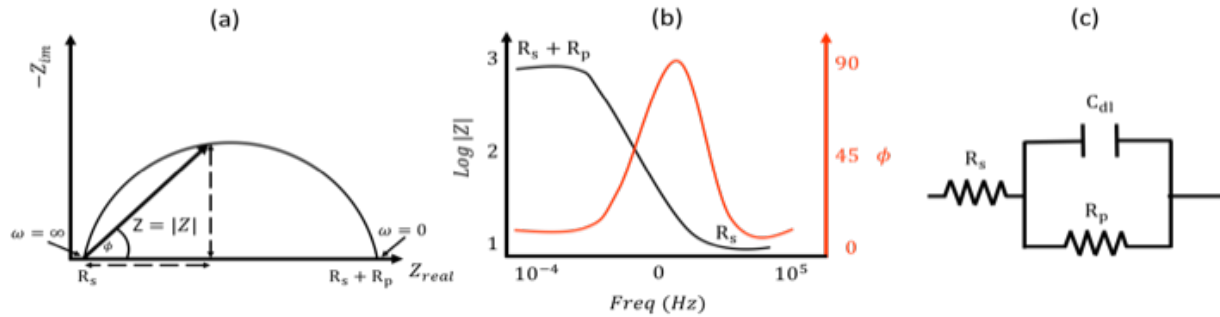
Figure 3.4: Schematic representation of the (a) Nyquist, (b) Bode plots,
and (c) the Randle circuit, adapted from [93].

In general, impedance data are analyzed by fitting an equivalent electrical circuit model with electric elements (resistor, capacitor, inductor, etc.) representing the different interfaces, created as a result of electrochemical activities [92]. An equivalent circuit of an electrochemical system is also called the "Randle circuit". An ideal case of such a circuit is illustrated in Figure 3.4c. R_s (resistance of the aqueous solution) represents the resistance to ionic migration in the electrolyte; C_{dl} represents the double layer capacitor and the charge accumulated at the interface between the WE and the electrolyte; R_p represents the resistance due to polarization. In such situations, the semi-circle in the Nyquist plot (Figure 3.4a) and the single peak in the Arg(Z) plot (Figure 3.4b) correspond to a single charge-transfer process [94]. In a situation where the system exhibits a double charge-transfer, ideal electrical elements can be inadequate to describe such complex impedance responses. Therefore, nonideal circuit elements such as the constant phase element (CPE), Q, or the Warburg (W) element can be considered. The expression of the CPE impedance is given by

$$Z_Q = Q(\omega t)^{-\gamma} \tag{3.8}$$

where the unit of Q is ($\Omega^{-1}sec^{\gamma}$) and the exponent γ lies between -1 and 1. The physical behavior of the CPE strongly depends on the value of the constant γ. For $\gamma = -1$, Q behaves like a pure inductance, for $\gamma = 0$, Q behaves like a pure resistor and if $\gamma = 1$, Q behaves like a pure capacitor.

Situations exist where γ is not an integer. For instance, if $\gamma = 0.5$, the CPE becomes the Warburg impedance [92].

3.5.2 Polarization tests

In an electrochemical cell, the reactions occurring at the WE electrode can initiate a passage of an electrical current in the system which causes a change in the WE potential. This phenomenon is referred to as polarization. The potential difference between the WE and the RE electrode is known as the overpotential (η) and defined as

$$\eta = E_p\text{-}E_{corr} \eta = E\text{-}E_{corr} \tag{3.9}$$

where E_p is the applied potential between WE and CE. An electrochemical system can be anodically or cathodically polarized and the response can be represented by a polarization curve as illustrated in Figure 3.5. This plot is also known as the Tafel plot. When $\eta = 0$, the corrosion potential is E_{corr} and the system is said to be at equilibrium. The corrosion current density (i_{corr}) can be obtained by extrapolating the linear portion of the anodic and cathodic curves and i_{corr} is determined by projecting the intercept of these lines on the x-axis (Figure 3.5).

In the anodic polarization, the overpotential, $\eta_a = E_p\text{-}E_{corr}$ is positive and this situation is associated with the oxidation (loss of electrons) of the WE and represented for a metal (*M*) by the following equation

$$M = M^{n+} + ne^- \tag{3.10}$$

where M^{n+} are ions from the dissolved metal in contact with the electrolyte. In the cathodic polarization, the overpotential $\eta_c = E_p\text{-}E_{corr} \eta_c = E\text{-}E_{corr}$ is negative implying that the applied potential is smaller than the corrosion potential. The reduction of dissolved oxygen, is the most probable cathodic reaction that can take place in an aerated solution as described by the equation [20]

$$O_2 + 2H_2O + 4e^- = 4OH^- \tag{3.11}$$

In the steady state conditions (the electrochemical system is at equilibrium), the anodic and the cathodic overpotential is given, respectively, by the following relationships [95]:

$$\eta_a = \beta_a log(i_a/i_{corr}) \tag{3.12}$$

and

$$\eta_c = -\beta_c log(i_c/i_{corr}) \tag{3.13}$$

where, i_a and i_c are the anodic and cathodic current densities, and β_a and β_c are the Tafel anodic and cathodic slopes, respectively. From the equations 3.12 and 3.13, the current density in each polarization condition can be given by the following relationship:

for the anodic polarization,

$$i_a = i_{corr} exp(2.303\eta/\beta_a) \tag{3.14}$$

and for the cathodic polarization,

$$i_c = i_{corr} exp(-2.303\eta/\beta_c) \tag{3.15}$$

When the system is moved from its equilibrium, the kinetics of the electrochemical corrosion is given by the Butler-Volmer equation expressed as follows:

$$i = i_{corr}[exp(2.303\eta/\beta_a)-exp(-2.303\eta/\beta_c)] \tag{3.16}$$

indicating that the corrosion current density measured on the WE electron depends on the potential.
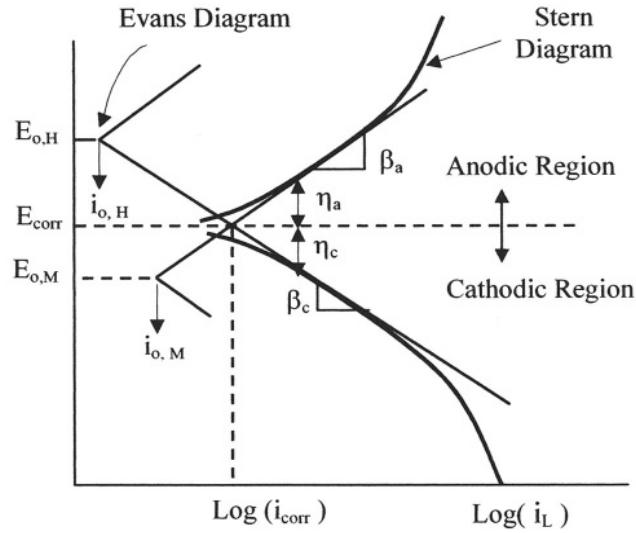
Figure 3.5: Schematic representation of the Tafel plot (polarization curve) [96].

3.6 Tribocorrosion characterization

The tribocorrosion behavior of coatings was studied using an apparatus in which the tribological contact was immersed in a 3.5 % NaCl electrolyte at ambient temperatures. The wear test was performed using a linear reciprocating pin-on-flat tribometer and the corrosion test was carried out in a three-electrode electrochemical cell. The working principle of the corrosion cell is similar to that described previously except that the CE was a platinum wire, and the surface of samples was horizontally positioned in the test apparatus.

The sliding wear test was performed using an Al_2O_3 ball of 4.75 mm in diameter as the counterpart. The Al_2O_3 ball was chosen for chemical inertness and its high hardness (20 GPa). The applied normal load (dead load) was 5 N corresponding to a minimum average Hertzian contact pressure of 1.26 GPa. A total number of 1800 cycles were performed using a sliding frequency of 1 Hz, and a fixed stroke length of 10 mm. The material loss of the sample was the difference between the weight of the sample before and after the tribocorrosion test using a high-precision scale.

In the tribocorrosion test, the sliding wear was performed with a constant potential between the WE and the RE, and the corrosion current was monitored before, during and after the wear test. In the first step, the OCP of the system was measured and recorded during 60 min before rubbing. This step was used to ensure the electrochemical stability of the surface of coatings. In

the second step, the sliding wear test was performed with the system polarized cathodically or anodically.

In the cathodic polarization, the applied potential was chosen below the corrosion potential of the Fe_3Al coating. In this situation, the surface of the coating is under cathodic protection and all anodic reactions are suppressed. During sliding, the corrosion current is measured and recorded as a function of time for a fixed number of cycles. For all coatings, the passivation time (time to form of a protective oxide layer on the surface of the coating) before and after the sliding wear test was 20 min. As a result, the total material loss (W_{total}) from the surface of the coating is due to the mechanical wear only (W_{mech}).

In the anodic polarization, the potential was chosen in such a way that it lies in the passivation region of the polarization curve of coatings. In this case, a potential of +250 mV with respect to the OCP was imposed to the system. Here, W_{total} is the sum of W_{mech}, static corrosion (W_{corr}) and the synergistic action of wear and corrosion (W_{syn}) as represented by the following equation [97]:

$$W_{total} = W_{mech} + W_{corr} + W_{syn} \tag{3.17}$$

where W_{total} can be obtained by weighting the sample after the tribocorrosion test while W_{corr} is calculated using Faraday's law as follows:

$$W_{corr} = (I_{corr} \times t \times M) / (z \times F) \tag{3.18}$$

where I_{corr} (A) is the current measured before rubbing, t (s) is the duration of the sliding wear test, M (g/mol) is the molar mass of the sample, z is the number of electrons transferred for the dissolution of one atom of the corroded material, and F is the Faraday constant (96 485 C/mol).

The term W_{syn} in equation (3.17) can be expressed as a sum of two components namely W_{syn-c} representing the material loss due to the effect of wear on corrosion, and W_{syn-w}, the material loss due to the effect of corrosion on wear. On the one hand, the W_{syn-w} component can be calculated using the Faraday's law where the current I_{corr} is the difference between the current measured before and during rubbing. On the other hand, the W_{syn-c} is calculated from equation (1) as follows:

$$W_{syn-c} = W_{total} - W_{corr} - W_{mech} - W_{syn-w} \tag{3.19}$$

The corrosion current was recorded for 20 min before and after rubbing to ensure its stability. The tribocorrosion measurement was obtained for a minimum of two tests under similar surface conditions (similar sample preparation).

3.7 Microstructural characterization

3.7.1 X-ray diffraction spectroscopy

X-ray diffraction (XRD) is commonly used for the crystallographic characterization of materials. The information obtained from XRD data includes the crystalline structure (phases) and the crystallographic orientation (texture). A Philips *X'pert* and a Brüker DISCOVER diffractometer using a copper source (Cu K$_\alpha$) in a $\theta/2\theta$ configuration was used to obtain the crystal structure of my samples. From the XRD diffractograms, one can identify the various crystalline phases in the materials by comparing with a suitable database. The average size of the crystallites (grain size) can be determined from the width at half maximum of the diffraction peaks and the Scherrer equation [98]. From the Bragg law,

$$\lambda = 2d \sin \theta \lambda = 2d_B \sin \theta \tag{3.20}$$

where, λ is the wavelength of the monochromatic light, d_B is the distance between two atomic planes and θ is the angle of diffraction, the crystal structure can be extracted. In the context of this project, the diffraction powder method (tiny crystal randomly oriented with respect to the incident beam) was applied to my samples. The diffraction data obtained using the Brüker DISCOVER diffractometer was used for phase quantification.

3.7.2 Differential thermal analysis

Differential thermal analysis (DTA) is typically used to determine the characteristic temperature range and enthalpy change of processes such as crystallization, melting or phase transformation in materials. In principle, the temperature difference between the sample and a reference material subjected to a controlled rate of heating or cooling, is recorded and plotted as a function of temperature or time. The temperature is measured with a thermocouple placed at the vicinity of the sample and the reference material, and the time is determined from the rate of cooling or heating. When a sample undergoes an exothermic transformation (heat is released) or

an endothermic transformation (heat is absorbed), a temperature change occurs. In the context of this thesis, the STA 449C Jupiter (NETZSCH-Gerätebau GmbH) and the SETSYS Evolution TGA-DTA-DSC (SETARAM Instrumentation) systems were used to study the thermal reactions of powders.

3.7.3   Scanning electron microscopy and electron dispersive x-ray

Scanning electron microscopy (SEM) is a commonly used surface analysis technique that uses signals generated from the interaction between electrons and matter. Electrons accelerated with sufficient energy bombard and interact (elastically or inelastically) with atoms at the surface of a sample. Such interactions generate several species that include:

- Backscattered electrons (from elastic collisions)

- Secondary electrons (from inelastic collisions), and

- X-ray (photons of different energy levels).

Each species is detected using a specific detector that provides an electric signal proportional to the number of species collected. Therefore, an image is formed by converting the signals using a visualization system. In the SEM, different observation modes can be obtained with respect to the type of species detected. In general, secondary electrons are low energy species that are generated from a volume of material near the surface. They provide the topographic information of the surface while the backscattered electrons that are sensitive to atomic number provide chemical information of phases in a material.

When the SEM is coupled with an X-ray spectrometer, the elemental chemical composition of materials can be obtained in a small volume using the energy dispersive spectroscopy (EDS). The X-ray spectra acquired by scanning the electron beam on the surface can be used to image the elements present in the samples.

A JEOL 7200 scanning electron microscope equipped with a field emission gun (FEG), the electron source, was used to observe the microstructure of my samples. In this SEM-FEG, samples were imaged at high resolution, and their chemical composition was determined by using an Inca X-max 80 Oxford EDS.

3.7.4   Scanning transmission electron microscopy

Scanning transmission electron microscopy (STEM) is a technique that can be used to achieve atomic resolution imaging and nanoscale analysis. In this technique, a beam of energetic electrons (~300 keV) is generated at the electron source and focused on a thin sample (~100 nm) using a combination of electromagnetic lenses. The electron probe (10 Å in size) is scanned over the sample in a raster pattern by exciting the scanning deflection coils. The scattered electrons are detected and their intensity plotted with respect to the probe position to form an image of the area scanned.

Similar to the SEM technique, incident electrons in STEM are subjected to elastic and inelastic interactions with atoms in the sample. Electrons can lose part of their energy, due to inelastic collision, before being transmitted. These electrons can provide useful information on the atomic composition of the sample using the Electron Energy Loss Spectroscopy (EELS) technique. In this work, this analysis has been used for selected samples to detect the presence of the ceramic particles in the as-milled powder mixtures.

CHAPTER 4   ARTICLE 1: EFFECT OF HIGH-ENERGY BALL-MILLING ON THE CHARACTERISTICS OF Fe₃Al-BASED HVOF COATINGS CONTAINING BORIDE AND NITRIDE PHASES

Fabrice Pougoum[a], Ludvik Martinu[a], Patrick Desjardins[a], Jolanta Klemberg-Sapieha[a,*]

Simon Gaudet[b], Sylvio Savoie[b], Robert Schulz[b]

[a] Groupe de recherche en physique et technologie des couches minces (GCM)

[b] Engineering Physics Dept., Polytechnique Montréal, Montréal, (QC) Canada, H3C 3A7

Materials Science Dept., Institut de recherche d'Hydro-Québec (IREQ), Varennes, (QC) Canada, J3X 1S1

* Corresponding author. Tel.: +1 514 340 5747; fax: +1 514 340 3218.

E-mail address: jolanta-ewa.sapieha@polymtl.ca (J. Klemberg-Sapieha).

Abstract

In the present work, we investigate the effect of boron nitride (BN) addition to Fe₃Al on the characteristics of ball-milled powders, and we study the influence of heat-treatment and subsequent milling of the powder mixtures on the microstructure and properties of coatings prepared by the high velocity oxy-fuel (HVOF) deposition process. The tribo-mechanical properties of the coatings were evaluated using indentation and pin-on-disc tribometry. Ball-milling of the Fe₃Al powder with BN and heat-treatment of the mixture lead to the formation of microstructures that contain BN, Fe₂B and AlN components. Further milling refines such microstructures and disperses the ceramic phases homogeneously within the metallic matrix. Thermal spraying of these powders results in hard coatings with microstructures similar to that of the powders. Compared to coatings obtained from a pure Fe₃Al milled powder, the coating hardness increases by ~40 % (from 5.6 GPa to 7.8 GPa), and the wear rate of 9×10^{-6} mm³/Nm decreases to 5×10^{-7} mm³/Nm when 30 mol.% of BN is added. The wear rate of the HVOF coatings further decreases to 2×10^{-7} mm³/Nm when the same powder is annealed and re-milled

at high energy for 10 h. The degradation mechanism appeared to be dominated by abrasive and fatigue wear.

Keywords: Iron aluminides, Metal ceramic composites, Mechanical milling, Sliding wear, Wear mechanisms, HVOF

4.1 Introduction

Iron aluminide alloys have received a great deal of attention over the past years due to their low cost, low density, relatively high melting point and good corrosion, oxidation and sulfidation resistance at high temperature [14]. These properties have made iron aluminide alloys suitable for applications in automotive, power generation, and petrochemical industries [99]. However, such materials exhibit poor ductility and low resistance to creep at room temperature. The brittleness of the iron aluminide alloys can be reduced by using a combination of thermomechanical processing and heat-treatment [16, 100]. Ternary addition such as chromium helps to reduce environmental embrittlement [23], while the addition of boron has shown to improve grain boundary strength and avoid intergranular fracture [15].

High strength and fracture toughness can be achieved by fine grain and dispersion strengthening [72, 101]. Krasnowski *et al.* reported an increase in the microhardness of nanocrystalline FeAl-TiN composites prepared by reactive milling of Fe, Al and Ti powders under nitrogen atmosphere, and they associated this effect to the fine matrix and TiN inclusions [102].

Iron aluminide alloys also exhibit poor wear performances that limit their structural applications [15]. It has been shown that dispersing hard metals and ceramic particles in the iron aluminide matrix can enhance the tribological properties [27, 102-104]. Xu *et al.* demonstrated that the addition of hard WC particles within the iron aluminide matrix increases the sliding wear-resistance of the un-reinforced Fe-Al coating [105]. Comparable abrasive behavior was observed between the WC-10 vol.% Co and the WC-40 vol.% FeAl composite materials as they exhibited similar hardness [77]. Amiriyan *et al.* showed that the dry sliding wear resistance of the Fe$_3$Al coating prepared by HVOF increased with the addition of *in-situ* precipitated TiC particles [61].

Several types of ceramic particles based on nitrides, carbides, and borides were found to be thermodynamically stable within the iron aluminide matrix [24, 104]. Compared to other nitrides and borides, AlN and Fe_2B have been less investigated as reinforcing agent in iron aluminides. Aluminum nitride exhibits high mechanical strength, and has a low thermal expansion coefficient [106]. Iron boride demonstrates high hardness, high fracture toughness and high chemical stability in iron aluminide [107, 108]. Avril *et al.* reported significant improvement of the tribological properties of the αFe (Cr)-based coating prepared by laser melting when Fe_2B was used as reinforcing components [109]. Thus, AlN and Fe_2B phases can be potential candidates for particle strengthening [110] and their effect on the microstructure and tribo-mechanical performance of Fe_3Al have not been previously investigated.

High energy ball-milling (HEBM) is a frequently employed process to produce composite materials with very fine microstructures in which a hard second phase can be uniformly dispersed within a metal matrix [111, 112]. In this method, the mixed powders are blended, cold worked, fragmented, and repeatedly welded to form homogeneous materials with a uniform distribution of stable and/or metastable phases. In the past years, iron aluminide alloys have been synthesized using this process [38, 80, 113-115]. It has been demonstrated that nanocrystalline alloys can be obtained through diffusion and formation of solid solutions using HEBM [38, 116-118]. Milling tools have been shown to be a crucial aspect of the degree of contamination and phase transformation during the fabrication of alloys [119]. The milling conditions such as revolution speed and time influence the degree of reaction, the size of the crystallite as well as the evolution of mechanical microstresses into the iron aluminide intermetallic [115, 116]. An iron aluminide-based nanocomposite with nanoparticles (20 nm in size) of BN was obtained after 35 h of ball-milling Fe, Al and BN powders [80] but the authors did not comment on the effects of the addition of BN on the mechanical and tribological properties of the iron aluminide.

To produce thick protective coatings on metal substrates, thermal spray processes are generally preferred over technologies such as chemical or physical vapor deposition [120, 121]. Compared to other thermal spray techniques, the high velocity oxy-fuel (HVOF) process offers a possibility to project powder particles at relatively low temperatures and very high speeds, up to three times the speed of sound. Therefore, dense coatings can be formed from the buildup of successive layers of rapidly quenched splats of partially melted or even unmelted particles [122].

The main objective of the present work is to enhance the mechanical and tribological properties of the Fe$_3$Al-based composite materials by the dispersion of nanoscale BN and *in-situ* precipitated AlN and Fe$_2$B particles in the iron aluminide matrix using the HEBM process and thermal treatment. The effect of heat-treatment on the microstructure and the tribo-mechanical characteristics of the HVOF coatings are systematically investigated.

4.2   Experimental Procedures

Pre-alloyed iron aluminide (Fe$_3$Al: FAS-100) 97.5 % pure with about 2 % of Cr from Ametek and boron nitride powder 98 % pure from Lower Friction were used in this study. The average particle sizes were 50 and 5 μm, respectively. Powder mixtures were prepared from 100, 90, 70 and 50 mol.% Fe$_3$Al ball-milled at high energy (1000 rpm) for 10 h with no BN, 10, 30 and 50 mol.% of BN and they are labeled as P1, P2, P4 and P5, respectively. For comparison, the composition of 70 mol.% of Fe$_3$Al and 30 mol.% of BN was milled at high energy for 2 h and labeled as P3. The powder mixture P4 was investigated in more detail in this work. The milling process was carried out under an argon atmosphere in a 2 liter high-energy mill (Zoz GmbH Simoloyer CM01). The ball to powder weight ratio was 10:1.

Following initial ball-milling, the powder composition P4 was heat-treated at 1300 °C for 2 h under vacuum (~ 10^{-6} mbar). The heating rate was 3 °C/min, and a cooling rate of 7 °C/min was used from 1300 to 500 °C. Part of the heat-treated powder was re-milled at low energy (200 rpm) for 5 min, and two other parts were milled at high energy (1000 rpm) for 2 and 10 h and they are labeled as AP4$_{5min}$, AP4$_{2h}$ and AP4$_{10h}$, respectively. All powders were sieved to obtain particle sizes between 20 and 50 μm for the HVOF deposition.

The HVOF coatings were prepared on austenitic (type 304) stainless steel (SS) substrates of dimensions 190 mm × 120 mm × 1.5 mm using kerosene fuel and oxygen gas for combustion. Before spraying, the substrates were sandblasted with alumina (grit 60) and cleaned with methanol. A Praxair J-P 8500 HVOF gun mounted on an ABB robot arm and controlled by a computer was used for deposition. Uniform coverage was achieved by scanning the gun in perpendicular direction at a speed of 10 cm/s for a total of fifteen passes. The gun was displaced by 10 mm between the line scans. The spray parameters shown in Table 4.1 were used for all coatings. Under these deposition conditions, the mean particle velocity measured using a DPV-2000 is about 800 m/s and the estimated particle residence time inside the gun is less than 200 μs.

Particle temperature varied between 1500 and 2200 °C. In the text, coatings are labeled with a letter "C" added in front of the abbreviated name of the corresponding powder.

Table 4.1: Parameters for high velocity oxy-fuel deposition experiments.

Spray parameters	Value
Standoff distance (cm)	38
Nozzle length (cm)	15
Nozzle diameter (mm)	11
Chamber pressure (kPa)	710
Oxygen flow rate (slpm)	897
Kerosene flow rate (l/h)	23.5
Equivalent ratio oxygen/kerosene	1.2

For further analysis, the deposits were cut into coupons of 2.5 cm × 2.5 cm in size. Before mechanical tests, the coupons were progressively polished using Al_2O_3 abrasive papers from 180 to 1000 grits, and then polished down to mirror finish using 15, 6 and 1 μm diamond suspensions. Finally, the samples were ultrasonically cleaned in acetone and isopropanol for 5 min, and the surface roughness was evaluated using profilometry. The porosity level and the volume fraction of ceramic phases were estimated from the cross-section of sprayed coatings using image analysis software.

The powders and coatings were characterized using a Phillips X'Pert X-ray diffractometer (XRD) equipped with a Cu Kα radiation at 50 kV and operated in the θ-2θ configuration. The average crystallite size, d, of the Fe_3Al phase was estimated using the Scherrer formula $d = \lambda/(\varpi.cos\theta)$ at the principal peak of Fe_3Al around 41 °. This rough estimate does not take into account the microstrain contribution: here λ is the X-ray wavelength and ϖ is the line broadening at half maximum intensity. The XRD data were used to quantify the phases present in the composite powders after heat-treatment.

Surface morphology of the coatings was analyzed at 10 kV using a 7200 JEOL field emission scanning electron microscope (SEM) equipped with energy dispersive X-ray

spectroscopy (EDS Inca X-max 80 Oxford). The working distance was varied between 10 and 21 mm. Powder particles were prepared with the focused ion beam and observed at 10 kV under a Hitachi HD2700 scanning transmission electron microscope (STEM) equipped with an Enfina Gatan electron energy loss spectroscopy (EELS). The thermal stability of the milled powders was investigated using a differential thermal analyzer (DTA) from Netzsch STA 449C at a heating rate of 10 °C/min using an alumina crucible and an argon atmosphere.

In order to evaluate the nano-hardness of the composite materials in powder form, the powder particles were embedded in a non-conductive resin and polished down to mirror finish using 15, 6 and 1 μm diamond suspensions. Nanoindentation experiments have been carried out using a Hysitron Triboindenter with a Berkovich indenter. Indentations were performed at the center of a cross-sectional surface of selected powder particles of 50 μm in diameter. The load was linearly increased up to a maximum load of 2 mN with a dwell-time of 5 secs, and the maximum penetration depth was 300 nm. For the HVOF coatings, nanoindentation was performed on both the surface and the cross-section of the coatings over a grid of 5×5 points, evenly spaced by 3 μm. The micro-hardness of the coatings and of the alumina ball was measured using a CSM Micro-Combi tester equipped with a Berkovich indenter. The applied load was linearly increased up to a maximum of 3 N, kept constant for 15 s and linearly decreased. The maximum penetration depth was ~6 μm.

The average micro-hardness was obtained using the Oliver and Pharr method [123] from a minimum of 100 indentations for the coatings and 10 indentations for the alumina ball.

The tribological properties of coatings with respect to alumina ball (micro-hardness of 20 GPa) were measured according to ASTM-G99 using a pin-on-disc apparatus in dry conditions (relative humidity: 30 – 40 %) at room temperature. The diameter of the wear track rings was 6 mm, and a new alumina ball (4.75 mm in diameter) was used for each test. The total sliding distance was 1000 m, and the linear speed was 7.86 cm/s. The applied normal force was 5 N and the wear rate, K, was calculated using the formula $K = V/F{\times}L$, where V is the total volume of material removed, F the normal force, and l the sliding distance. The testing parameters (alumina ball, load, sliding length) are those suitable for the comparison of metal-based coatings considered for the repair of hydroelectric generation equipment as described in [61]. These sliding conditions are chosen in a way to obtain high "sensitivity" with respect to the coatings' microstructure,

composition and thickness. The average cross-sectional surface of the ring was obtained from 20 measurements at different positions of the wear track. The error bars on the average hardness and wear rate are the standard deviation from the measurements. In order to assess the wear mechanism, SEM analysis of the wear track was performed, and worn and unworn regions of HVOF coatings were analyzed using EDS.

4.3　Results

4.3.1　Microstructure of the composite powders

4.3.1.1 X-ray diffraction

The XRD patterns of the Fe_3Al and BN powders before milling, and those of a mixture of the Fe_3Al and BN powders milled at high energy for 2 h (P3 trace) and 10 h (P4 trace) are compared in Figure 4.1. The Fe_3Al and BN diffractograms reveal sharp and well-defined peaks of the Fe_3Al and BN phases, respectively. Particularly, the peak at 44.11 ° in the Fe_3Al diffractogram exhibits a shoulder on the right side that coincides with a broad peak of BN. After 2 h of milling, the peaks of the BN phases are no longer visible in the diffractogram P3, while the Fe_3Al peaks broadened and their intensity decreased. The Fe_3Al peaks are slightly shifted towards lower 2θ angles compared to the un-milled powder suggesting that the composition of the matrix material had changed. Upon milling for 10 h, the Fe_3Al peaks continued to broaden and their intensity decreases further.
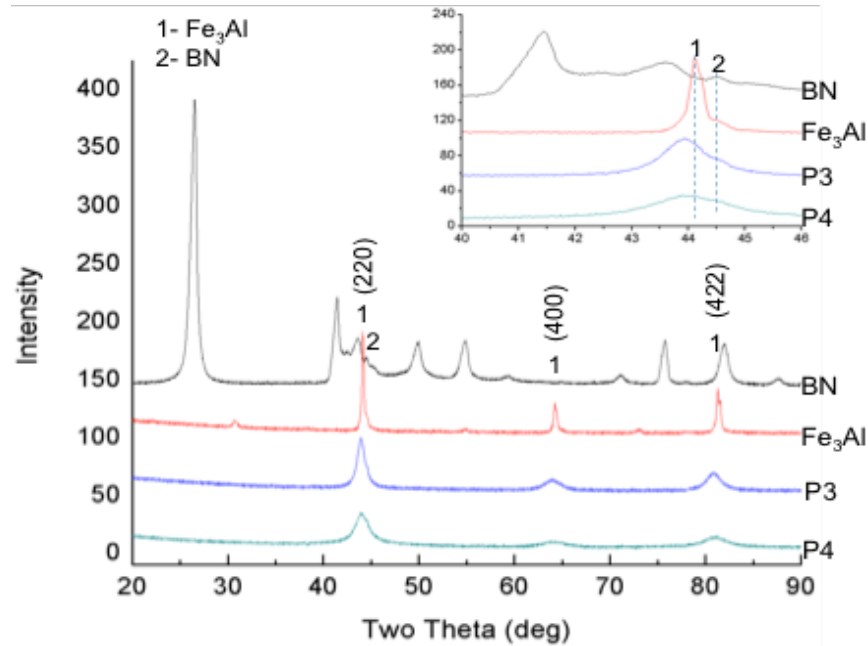
Figure 4.1: XRD patterns of the Fe₃Al and BN mixed powder, P3: Fe₃Al and BN powder mixture milled for 2 h, and P4: Fe₃Al and BN milled for 10 h.

The XRD patterns of the mixture of Fe₃Al and BN powders milled for 10 h (P4 trace) and that of the as-milled powder heat-treated at 1300 °C for 2 h in vacuum and re-milled at low energy for 5 min (AP4₅ₘᵢₙ trace), and at high energy for 2 h (AP4₂ₕ trace) and 10 h (AP4₁₀ₕ trace) are compared in Figure 4.2. After heat-treatment and re-milling for 5 min, the diffractogram shows evidence of sharp and well-defined peaks of the AlN and FeB₂ phases. As expected, the peaks of the Fe₃Al are sharper and their intensity is higher compared to the as-milled powder (P4 trace). All peaks decrease in intensity and become broad when the heat-treated powder was re-milled for 2 h (AP4₂ₕ trace). These features become significant after 10 h of re-milling (AP4₁₀ₕ trace). Upon subsequent re-milling, some ceramic peaks disappear from the diffractograms. A quantitative analysis carried out on the XRD data of the heat-treated powder re-milled for 2 h reveals that the composite powder contains approximately 59 wt.% of Fe₃Al, ~9 wt.% of AlN and 32 wt.% of Fe₂B.
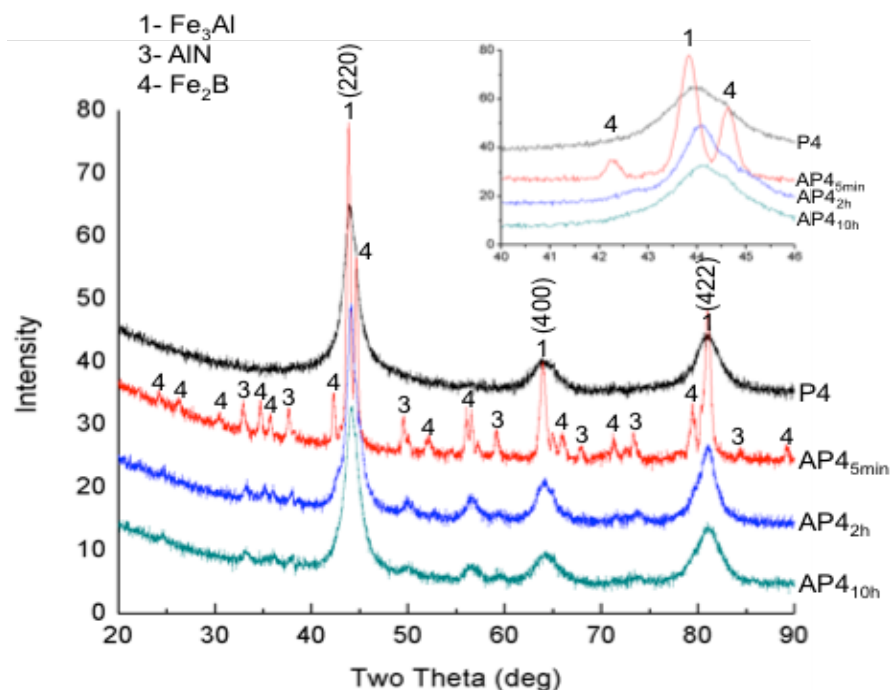
Figure 4.2: XRD patterns of: P4, powder mixture of Fe_3Al and BN milled for 10 h (as-milled powder); AP4$_{5min}$, as-milled powder annealed and re-milling for 5 min; AP4$_{2h}$, as-milled powder annealed and re-milled for 2 h, and AP4$_{10h}$, as-milled powder annealed and re-milled for 10 h.

4.3.1.2 Differential thermal annealing

The DTA curve of the mixture of Fe_3Al and 30 mol.% of BN milled for 10 h is compared in Figure 4.3 to that of the un-milled Fe_3Al powder. The curve of the as-milled powders exhibits two broad exothermic peaks at approximately 562 and 723 °C. A sharp endothermic peak is visible at about 1224 °C indicating that melting has occurred in the material during the ball-milling process. On the contrary, the curve of the un-milled Fe_3Al powder shows no evidence of exothermic or endothermic peaks. This indicates that no phase transformation or melting has occurred.
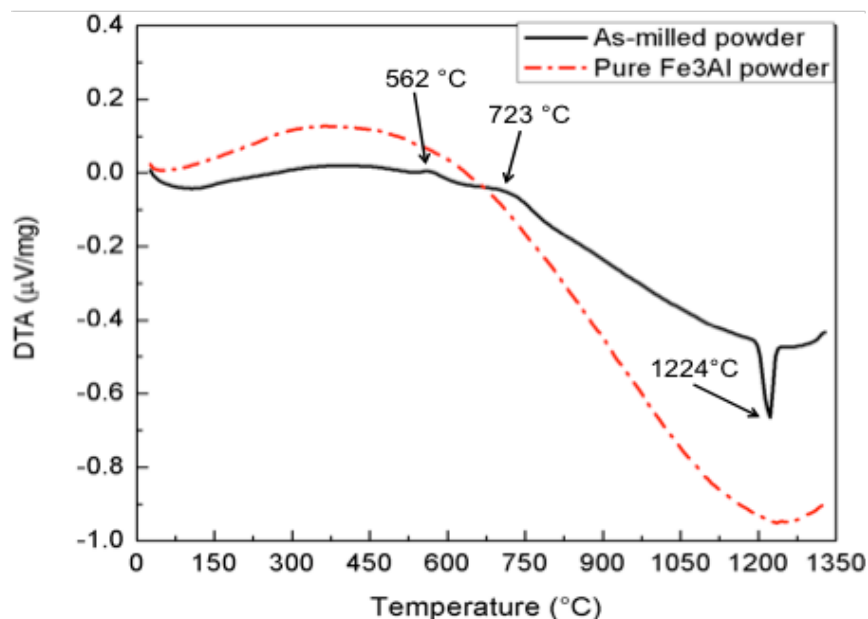
Figure 4.3: DTA curve of the Fe$_3$Al powder milled at high energy for 10 h with 30 mol.% of h-BN is compared to that of the un-milled Fe$_3$Al powder.

4.3.1.3 STEM and EELS observations

STEM micrograph and EELS composition maps of a powder particle of the Fe$_3$Al milled at high energy for 10 h with 30 mol.% of BN is shown in Figure 4.4. Figure 4.4a presents a "sandwich-like" microstructure where different components (gray and light-gray features) are superimposed. This structure results from the high-energy collision experienced by the powder particles in the HEBM process. The EELS mapping revealed a correlation between Boron and Nitrogen suggesting that BN phases with thicknesses of about 30 nm (initial BN particle size is 5 μm) are still present, highly deformed and well dispersed in the iron aluminide matrix after 10 h of milling.
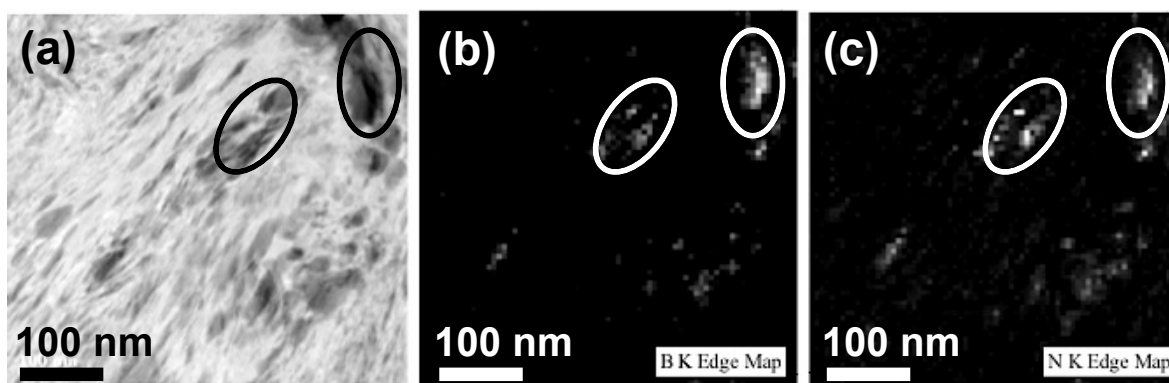
Figure 4.4: STEM micrograph of the powder particle from the mixture of the Fe₃Al powder milled at high energy for 10 h with 30 mol.% of h-BN, and EELS mapping of (b) Boron and (c) Nitrogen.

4.3.2 Characteristics of the composite powders

The characteristics of the powders are summarized in Table 4.2 in which the composition of the elementary powders was chosen to promote different contents of the second phases in the metal matrix. The nano-hardness (average of 100 indentations) initially increases with the BN content in Fe_3Al and with the milling time. However, for 50 mol.% of BN the large amount of BN has probably diminished the physical properties of the composite materials. The Fe_3Al powder milled at high energy for 10 h with 30 mol.% of BN exhibits the highest average nano-hardness.

After initial milling of the Fe_3Al powder with 30 mol.% of BN for 10 h, heat-treatment and subsequent re-milling were performed. The characteristics of the heat-treated powders re-milled at low energy for 5 min and at high energy for 2 h and 10 h are given in Table 4.2. Interestingly, after reaching a maximum value just after heat-treatment the nano-hardness of the re-milled powders decreases with the re-milling time suggesting the influence of soft interfaces and porosities in the re-milled powders on the mechanical properties of the heat-treated powders.

Table 4.2: Composition of elemental powder mixtures and characteristics of as-milled and heat-treated and re-milled powders.

		Composition		Milling time (h)	Fe_3Al crystallite size estimation, d (nm)	Fe_3Al lattice constants (Å)	Mean nano-hardness (GPa)
		Fe_3Al (mol.%)	BN (mol.%)				
Pure powders		-	h-BN	-	16	-	-
		Fe_3Al	-	-	42	5.793 ± 0.001	4.9 ± 0.9
As-milled powders	P1	100	-	10	35	5.793 ± 0.001	5.3 ± 1.1
	P2	90	10	10	12	5.803 ± 0.016	9.2 ± 1.7
	P3	70	30	2	14	5.817 ± 0.003	7.7 ± 1.9
	P4	**70**	**30**	**10**	**10**	**5.827 ± 0.002**	**10.4 ± 2.0**
	P5	50	50	10	12	5.812 ± 0.001	8.3 ± 1.9
Heat-treated powders	AP4	-	-	5 min	29	5.816 ± 0.005	16.2 ± 4.7
	AP4	-	-	2	14	5.811 ± 0.024	15.4 ± 6.7
	AP4	-	-	10	10	5.802 ± 0.005	12.4 ± 3.1

4.3.3 Microstructure of the HVOF coatings

4.3.3.1 X-ray diffraction analysis

The particle size distribution, the morphology of the P4 powder prior to HVOF spraying and the XRD diffractograms of the HVOF coatings prepared from the powders described in section 4.3.1 are shown in Figure 4.5. In Figure 4.5a, the particle size after sieving exhibits a uni-modal Gaussian distribution. This size range and the quasi-spherical shape of the powder particles (Figure 4.5b) are suitable for HVOF deposition. The diffraction patterns of the coatings in Figure 4.5c are quite similar to that of the corresponding powders (see Figure 4.2). After spraying the mixture of the Fe_3Al powder milled for 10 h with 30 mol.% of BN, the spectrum of the broad and low intensity peaks of the Fe_3Al matrix is observed on the CP4 curve. On the other hand, sharp peaks of Fe_3Al, AlN and Fe_2B phases are observed for coatings prepared from the heat-treated and re-milled powders. Peak widths and positions are not significantly different from

that of the powder; this suggests that no significant transformation of the microstructure of the powders occurred under the deposition conditions described in Table 4.1.

4.3.3.2 SEM and EDS observations

The effect of h-BN addition on the microstructure of the milled iron aluminide is shown in Figure 4.6 where the coating made from pure milled Fe_3Al is compared to that containing the BN phases. The coating fabricated from pure Fe_3Al presents a significant amount of large unmelted particles (Figure 4.6a) as opposed to typical splats in composite coatings (Figures 4.6b, c and d) prepared from the powders containing boron nitride. The coatings containing BN powders exhibit uniform light-gray regions that represent the metal matrix in which large splats and small ones with a range of contrast are observed. Modification of microstructures and compositions by the addition of the boron nitride phase has most likely affected the overall characteristics of the iron aluminide matrix. In particular, the coating prepared from 50 mol.% of BN (Figure 4.6d) shows a porosity level of about 5.2 % compared to other coatings: 1.9 % for CP1, 2.5 % for CP2 and 2.1% for CP4.
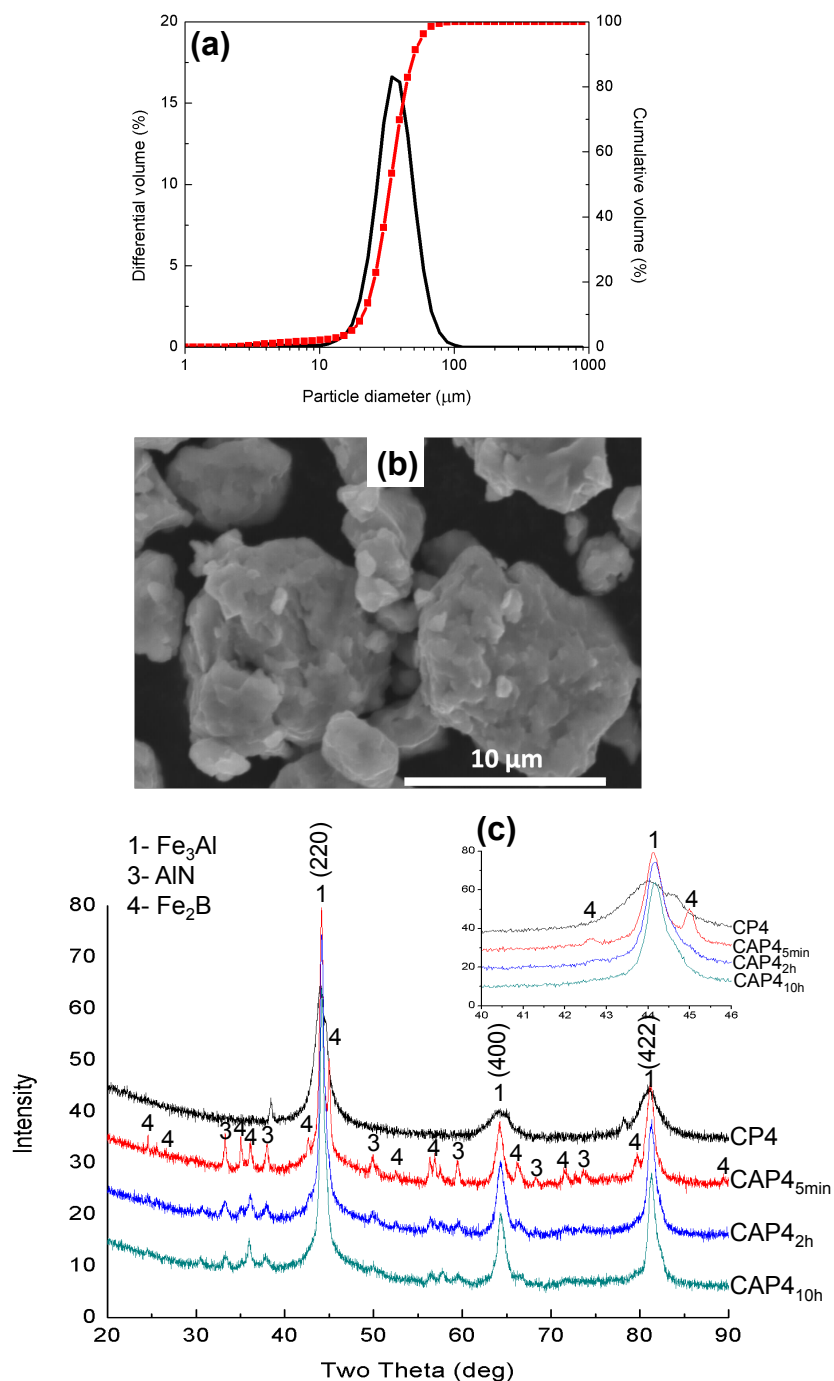
Figure 4.5: (a) Particle size distribution, (b) morphology of the P4 powder particles and (c) X-ray diffractograms of HVOF coatings prepared from the Fe_3Al powder milled for 10 h with 30 mol.% of BN: CP4, as-milled powder, CAP4$_{5min}$ heat-treated and re-milling for 5 min, CAP4$_{2h}$ heat-treated and re-milled for 2 h, and CAP4$_{10h}$ heat-treated and re-milled for 10 h.
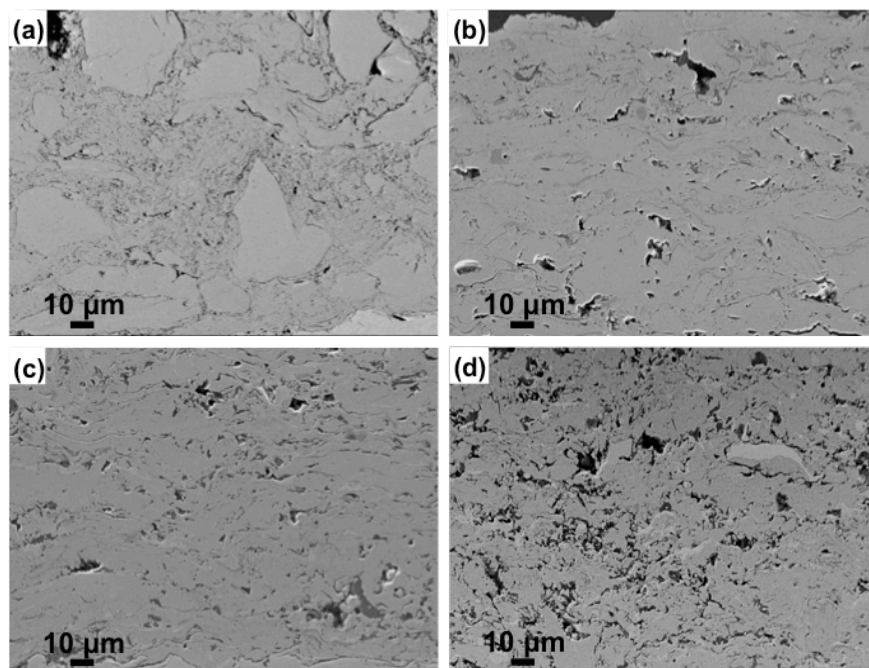
Figure 4.6: SEM micrographs of the cross-section of the HVOF coatings made from the Fe$_3$Al powder milled for 10 h with (a) no BN, (b) 10, (c) 30 and (d) 50 mol.% of BN.

The SEM micrograph of the HVOF coatings prepared from the mixture of Fe$_3$Al and 30 mol.% of BN powders milled at high energy for 10 h is compared in Figure 4.7 to the as-milled powder heat-treated and re-milled. The coating prepared from the untreated powder shows a typical HVOF microstructure as described above, whereas coatings prepared from heat-treated powders reveals precipitates (white and dark features) dispersed within the matrix (Figures 4.7b-d). The precipitates are almost spherical, and they occupy a volume fraction of about 20 to 32 % in the coating. Image analysis of the cross-section of the coatings showed that the mean size of the precipitates in the CAP4$_{5min}$ coating decreases from 1.2 ± 0.1 µm to 800 ± 60 nm for CAP4$_{2h}$ and to 435 ± 30 nm for CAP4$_{10h}$ as the re-milling time increases.
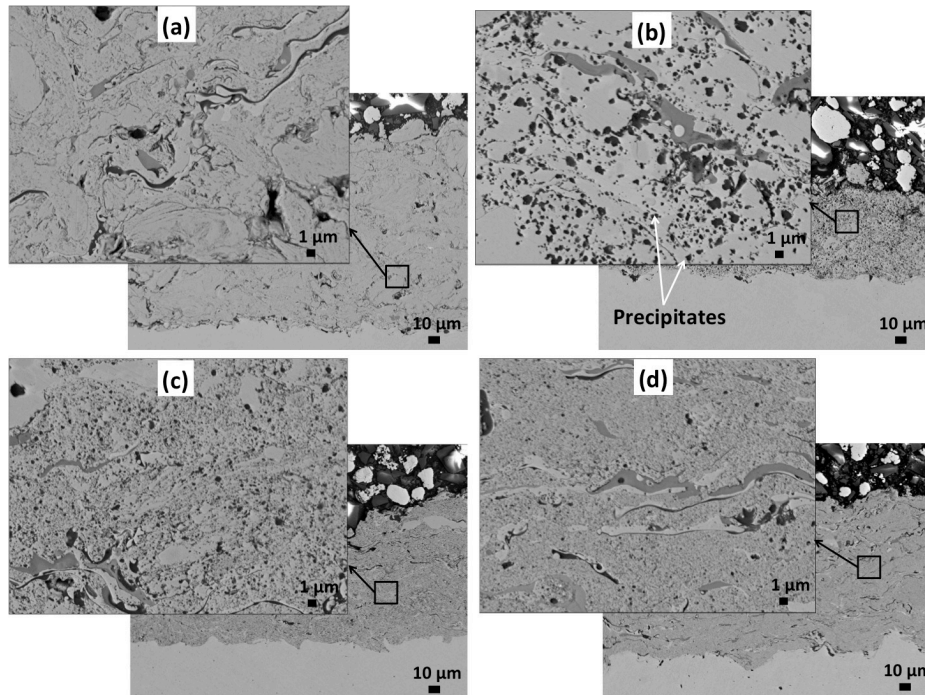
Figure 4.7: SEM micrographs of the cross-section of HVOF coatings prepared from the Fe$_3$Al powder milled for 10 h with 30 mol.% of BN: (a) as-milled powder (b) heat-treated and re-milling for 5 min, (c) heat-treated and re-milled for 2 h, and (d) heat-treated and re-milled for 10 h.

The EDS analysis performed on the cross-section of the HVOF coating prepared from the heat-treated powder re-milled at high energy for 2 h is shown in Figure 4.8. Interestingly, the EDS mapping revealed a correlation between oxygen and aluminum suggesting that Al$_2$O$_3$ formed from the oxidation of aluminum during the deposition process, while a correlation between aluminum and nitrogen indicates the presence of AlN phases in the metal matrix. Evidence of iron boride phases is not clear from the EDS mapping.
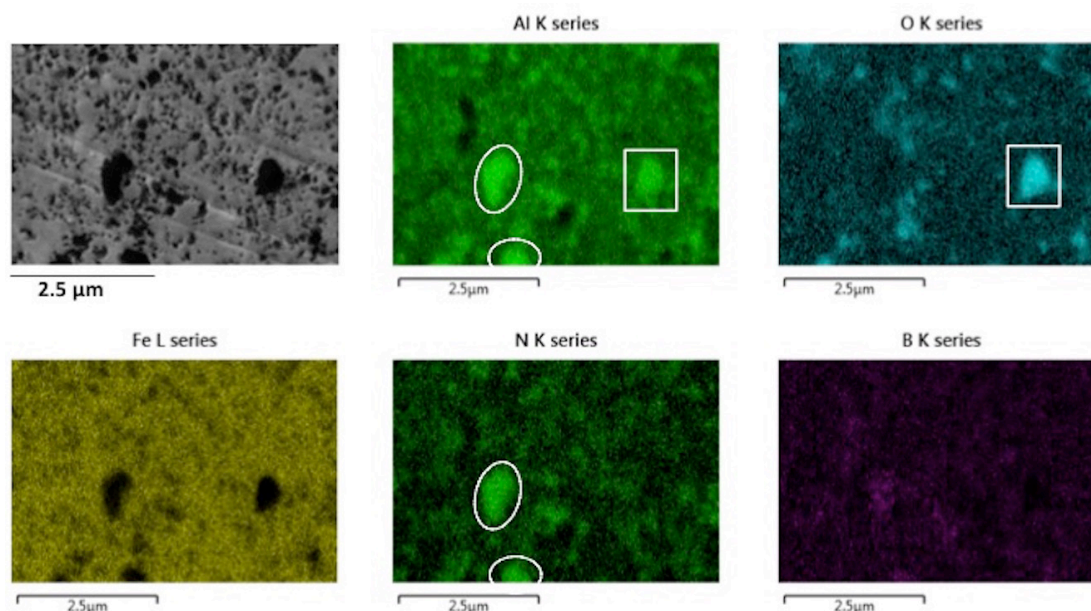
Figure 4.8: SEM micrograph of a cross-section of the HVOF coating prepared from the mixture of Fe₃Al powder milled with 30 mol.% of BN, heat-treated and re-milled for 2 h, and EDS mapping of aluminum, oxygen, iron, nitrogen and boron.

4.3.4 Tribo-mechanical characteristics of the HVOF coatings

4.3.4.1 Wear rate and hardness

The effect of BN addition on the wear rate, *K*, and micro-hardness, *H*, of the HVOF coatings is shown in Figure 4.9a. After polishing, the thickness of the HVOF coatings varies between 60 and 100 μm, which is larger compared to the maximum wear (~7 μm) depth reached for all tests. The wear rate of the 304-type stainless steel (~9×10^{-5} mm³/Nm) substrate is reduced by one order of magnitude (~9×10^{-6} mm³/Nm) when the Fe₃Al coating made from pure iron aluminide milled powder (95 μm thick) is applied. The addition of BN phases in the iron aluminide matrix decreases *K* by one order of magnitude while increasing *H* (5.6 GPa without BN) by up to ~40 % in the case of the 30 mol.% of BN. The lowest *K*, 5×10^{-7} mm³/Nm, and the highest *H*, 7.8 GPa, are obtained for a coating prepared from the Fe₃Al powder milled at high energy for 10 h with 30 mol.% of BN (CP4 coating).

In Figure 4.9b, the values of *K* and *H* of the CP4 coating (98 μm thick) are compared to the HVOF coatings prepared from heat-treated and re-milled powders. The value of *K*, of the

CAP4$_{5min}$ coating (60 μm thick) significantly increases by a factor of 6 and *H* decreases by 50 % compared to the CP4 coating. On the contrary, when the heat-treated powders were further re-milled for 10 h, the value of *K* decreased up to ~2 × 10^{-7} mm^3/Nm and *H* increased to ~9 GPa. The effects of BN addition in the Fe$_3$Al and heat-treatment combined with re-milling were noticeable on the mechanical and tribological characteristics of the HVOF coatings.
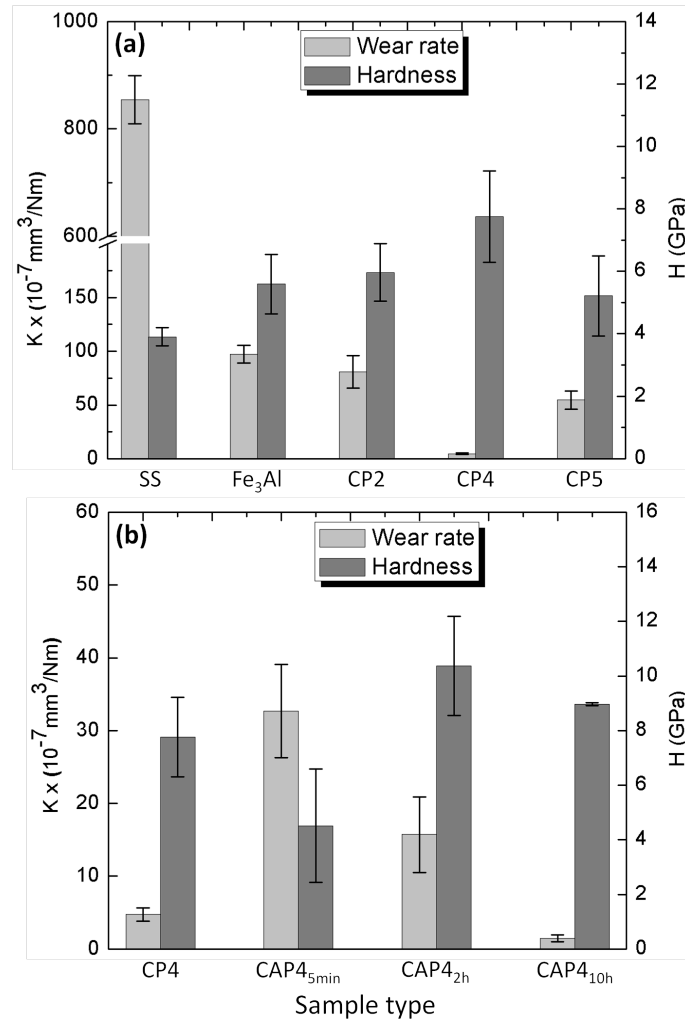
Figure 4.9: Micro-hardness and wear rate of HVOF coatings compared to the stainless steel substrate 304 (a) Effect of BN additions to the Fe$_3$Al powders, and (b) effect of heat-treatment and re-milling of Fe$_3$Al milled for 10 h with 30 mol.% of BN.

SEM micrographs of the worn surfaces of the CP1, CP2, CP4 and CP5 coatings after a sliding distance of 1000 m with a 5 N normal load, are shown in Figure 4.10. The width of the wear track of the CP1, CP2 and CP5 coatings is large compared to that of the CP4 coating (Figures 4.10a-d). Scratches and wear debris that are visible inside the wear tracks result from the

rough interaction between the surface of the coating and the Al_2O_3 ball. Particularly, the worn surfaces of CP2 and CP5 materials show debris of a size smaller than 30 μm and large pieces of worn material are found inside the wear tracks. These features are indication of the severity of the interaction between the surface of the coatings and the hard counterbody.
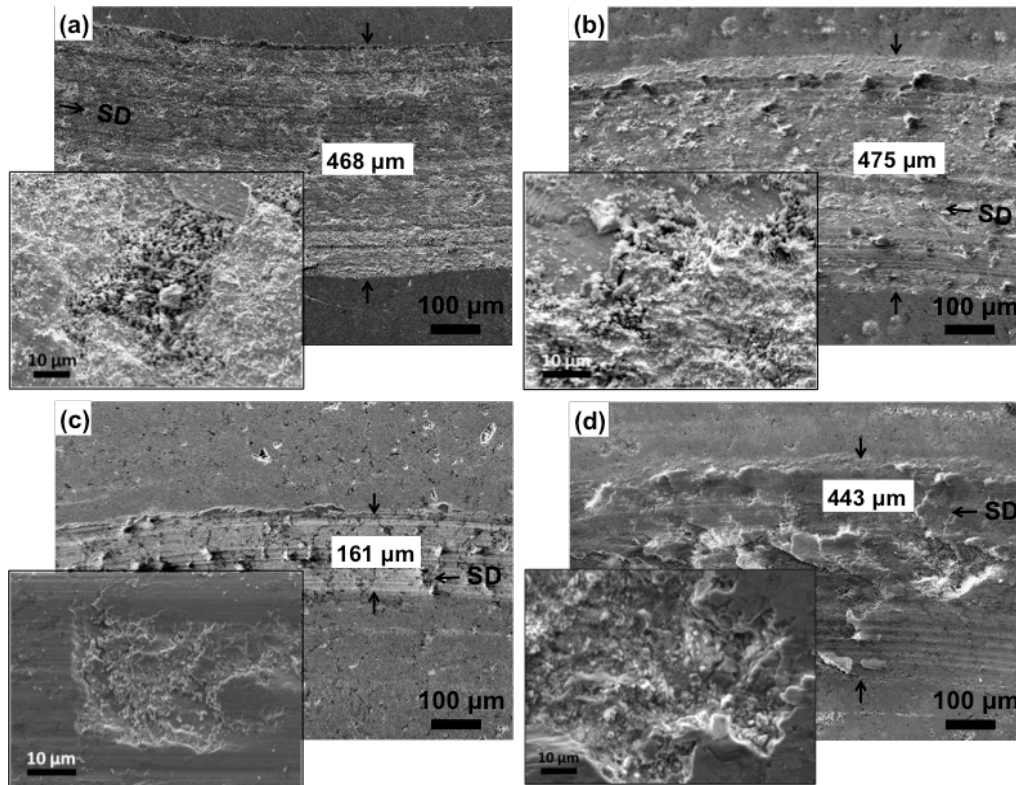
Figure 4.10: SEM micrographs of the wear track after wear tests for the HVOF coatings prepared from the Fe_3Al powder milled for 10 h with: (a) no BN (CP1) (b) 10 mol.% of BN (CP2) (c) 30 mol.% of BN (CP4), and (d) 50 mol.% of BN (CP5). SD indicates sliding direction.

Figure 4.11 shows SEM micrographs of the worn surfaces of the $CAP4_{5min}$, $CAP4_{2h}$ and $CAP4_{10h}$ coatings and the EDS analysis inside and outside the wear track of the $CAP4_{5min}$ coating. Inspection of the wear tracks reveals significant differences between the wear behaviors of these coatings. The wear tracks of the $CAP4_{5min}$ and $CAP4_{2h}$ coatings are large compared to $CAP4_{10h}$. The wear track of the $CAP4_{5min}$ is covered with worn materials and shows micro-cracks (Figure 4.11c) as opposed to the $CAP4_{2h}$ and $CAP4_{10h}$ coatings where grooves of micro plowing with localized debris of about 30 μm and ~10 μm in size, respectively, can be seen. Examination of the curves of the EDS performed on the worn and unworn regions of the $CAP4_{5min}$ coating (Figure 4.11d) reveals evidence of oxygen inside the wear track compared to the unworn region

suggesting that oxidation has taken place during the wear test. Moreover, no significant difference is noticed in the intensity of the Al peak regardless of the region examined while Fe is lower in the worn region indicating that aluminum oxide has probably formed during wear tests performed in ambient air. Moreover, oxides may originate from the degradation of the Al_2O_3 ball.
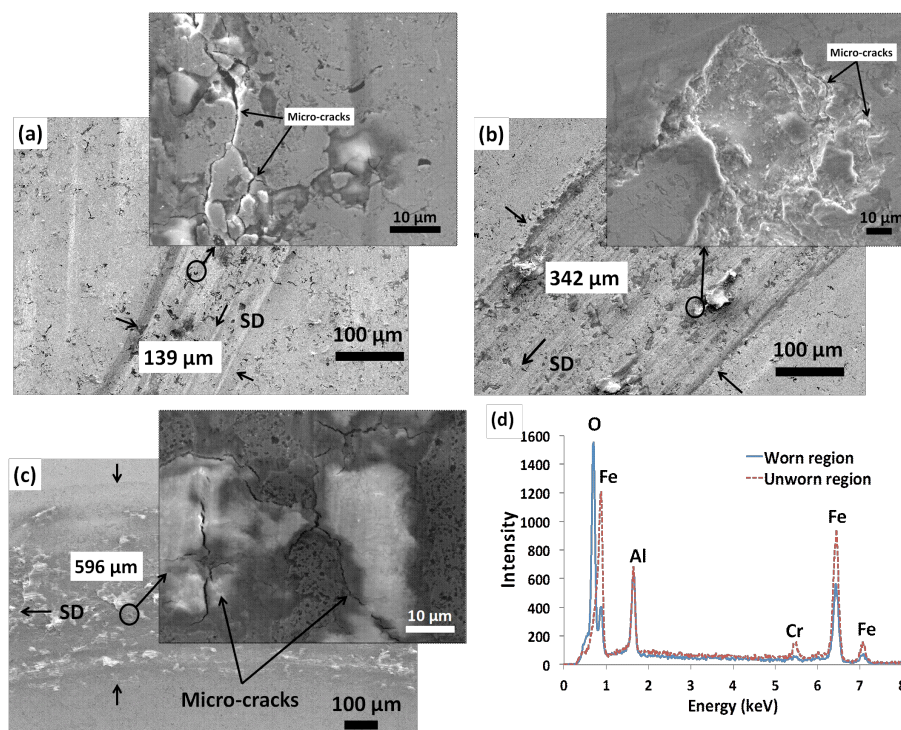
Figure 4.11: SEM micrographs of the wear track after wear tests of various HVOF coatings prepared from the Fe_3Al powder milled for 10 h with 30 mol.% of BN, heat-treated and re-milled for: (a) 10 h (CAP4$_{10h}$) (b) 2 h (CAP4$_{2h}$) and (c) 5 min (CAP4$_{5min}$), and (d) EDS analysis of the worn and unworn regions of the CAP4$_{5min}$ coating. SD means sliding direction.

4.4 Discussion

4.4.1 Microstructure of the milled powders

Figure 4.1 revealed no clear evidence of BN peaks on the diffractogram obtained after 2 h of milling. This observation can be attributed to the severe plastic deformation that occurred during the HEBM process where the hexagonal structure of boron nitride was severely modified, thus prompting extreme broadening of the BN peaks. A similar observation was made by Rosas *et al.* [80] where the absence of the h-BN peaks in the XRD diffractograms was associated with

the atomic difference between FeAl and BN. However, Figure 4.4 reveals a "sandwich-like" microstructure, and the EELS mapping shows a correlation between boron and nitrogen in the powder particle of Fe_3Al milled at high energy with BN. This is an indication that no significant reaction has occurred between the h-BN and the Fe_3Al during the milling process.

The shift of the left side of the Fe_3Al peaks towards lower 2θ angles is believed to be related to the formation of an Fe (Al, B, N)-based random solid solution as indicated by the increase of the lattice constant (Table 4.2) of the cubic Fe_3Al from 5.793 Å before milling to 5.817 Å and 5.827 Å after 2 h and 10 h of milling, respectively. On the contrary, the unit cell of the heat-treated powder contracts by 0.4 % after 10 h of re-milling, which is also associated with the formation of a Fe (Al)-based solid solution after AlN and iron boride phases were precipitated. The expansion or the contraction of the unit cell can be attributed to the formation of substitutional or interstitial solid solutions [124]. Further analysis is needed to identify more precisely the species (B and/or N) involved in the formation of such solid solutions. In addition, modifications of the composition of the Fe_3Al upon milling and changes in the degree of chemical order can influence the XRD peak position of Fe_3Al since the lattice constant of the pure Fe_3Al (5.792 Å) slightly increases to 5.793 Å after 10 h of milling.

The broadening of the peaks with the milling time observed in the XRD diffractograms (Figures 4.1 and 4.2) of the as-milled and heat-treated powders is believed to be a result of the reduction of the crystallite size (Table 4.2) and the possible introduction of defects into the structure [80, 125]. Particularly, the initial crystallite size of pure Fe_3Al (42 nm) decreases down to 14 nm and to 10 nm after 2 h and 10 h of milling with 30 mol.% of BN, respectively. Similarly, the crystallite size of the heat-treated powders decreases from 29 nm when the powder was re-milled at low energy (200 rpm) for 5 min down to 10 nm after 10 h at high energy (1000 rpm). The heating temperature (1300 °C) employed was sufficient to form large ceramic particles in the as-milled powders [98, 126]. Upon re-milling, powder particles were repeatedly deformed, cold-welded, and fractured leading to a decrease in particle size. As the milling time was extended, severe plastic deformation and fragmentation became significant and dominant leading to further refinement. The disappearance of some XRD ceramic peaks in Figure 4.2 can be related to the extreme broadening of these peaks caused by the refinement of the ceramic particles (Figure 4.7d) [98]. The crystallite size of Fe_3Al of the as-milled powders decreases as

the BN content increases in the powder mixtures suggesting that the large amount of hard and brittle BN phases accelerates the refinement of the microstructure of the as-milled powders.

Heat-treatment was employed with the intent to precipitate nitride and boride phases within the metal matrix taking advantage of the microstructure of the milled powders where all components are present and likely to react. The XRD analysis performed on the heat-treated and re-milled powders revealed evidence of AlN and Fe_2B phases.

The differential thermal analysis of the Fe_3Al powder milled at high energy for 10 h with 30 mol.% of BN was used to investigate the mechanism of formation of the AlN and Fe_2B ceramic phases in the iron aluminide matrix. The first exothermic peak observed at ~562 °C is attributed to the precipitation of AlN phases as its heat of formation (Table 4.3) is very large compared to that of Fe_2B suggesting that there is a strong driving force for its formation. XRD analysis performed (not shown) after heat-treatment above 562 °C confirms the presence of AlN. The second exothermic peak is associated with the precipitation of Fe_2B phases as nitrogen has reacted with the aluminum, and boron is free to react with iron.

Table 4.3: Characteristics of the ceramic materials.

Ceramic materials	Heat of formation (kJ/mol)	Vickers hardness (GPa)	Melting temperature (°C)
AlN	-318 [127]	14.6	2200
Fe_2B	-67.4 [128]	17.7	1410

The endothermic peak seen at ~1224 °C is attributed to the melting of the milled product. Based on the previous discussion, a model for the microstructural and compositional changes of the powder during heat-treatment can be proposed. In the early stage of the heat-treatment of the Fe_3Al powder milled for 10 h with 30 mol.% of BN, the reaction can be described by the following equation:

$$0.7Fe_3Al + 0.3BN \Rightarrow 0.3AlN + 2.8(Fe_{0.75}Al_{0.14}B_{0.11})$$

(4.1)
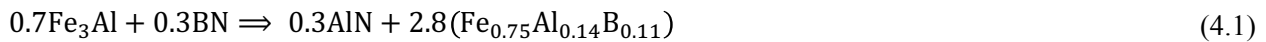
The second term on the right-hand side of equation (4.1) describes the solid solution formed once the aluminum has reacted with nitrogen to form AlN. The subsequent reaction that takes place at higher temperatures can be described using the following equation:

$$2.8(Fe_{0.75}Al_{0.14}B_{0.11}) \Longrightarrow 0.3Fe_2B + 1.9(Fe_{0.79}Al_{0.21}) \qquad (4.2)$$
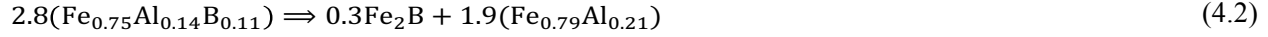
Formation of the products of equation (4.2) can be explained from the ternary phase diagram of the Fe-Al-B system at 1000 °C (Figure 4.12a) [129] where the composition of the $Fe_{0.75}Al_{0.14}B_{0.11}$ solid solution is indicated. At that particular composition, the Fe_2B phase is expected to form in the Fe(Al)-based matrix as discussed previously. By analogy to the Fe-B binary system shown in Figure 4.12b [130], the liquidus temperature of a $0.3Fe_2B + 1.9(Fe_{0.79}Al_{0.21})$ mixture is expected to be lower [131] compared to that of a mixture of the same Fe_2B ceramic content in an Fe matrix due to the presence of aluminum as shown in Figure 4.12b.

The complete transformation of the mixture

$$0.7Fe_3Al + 0.3BN \text{ into}$$

$0.3AlN + 0.3Fe_2B + 1.9(Fe_{0.79}Al_{0.21})$ would give weight fractions of AlN, Fe_2B and iron aluminide of 8.6, 25.6, and 65.85 %, respectively. This estimation is close to that obtained from the XRD analysis discussed previously considering the fact that some aluminum oxides are also present in the composite materials.
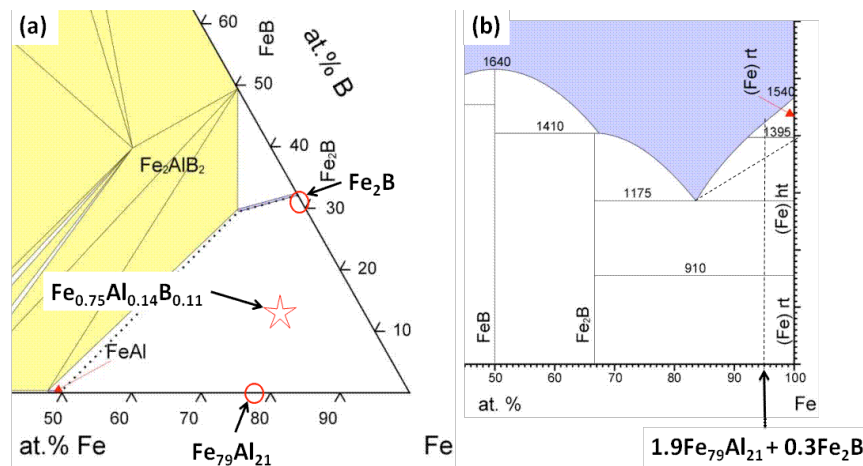
Figure 4.12: Fe-Al-B and Fe-B phase diagrams used to illustrate the composition of the $Fe_{0.75}Al_{0.14}B_{0.11}$ powder mixture. Adapted from [129] and [130].

4.4.2 Mechanical properties of the milled powders

The effect of powder composition and milling time on the mechanical properties of the milled powders are compared in Table 4.2. It has been shown that the hardness can be controlled by the volume fraction of secondary phases in the iron aluminide matrix [27]. After 10 h of milling, the crystallite size of the Fe_3Al phase is similar regardless of the powder composition. The average nano-hardness (8.3 GPa) of the Fe_3Al powder milled for 10 h at high energy with 50 mol.% of BN is lower compared to 10 mol.% (9.2 GPa) and 30 mol.% (10.4 GPa), respectively. These peculiar trends can be related to the large amount of BN that probably reduces the ability of the powder particles to cold-weld during milling, thus promoting fragmentation, which led to a brittle behavior and to a loss of strength and toughness. As expected, the nano-hardness increases with the milling time, which is believed to be a consequence of progressive hardening with time as the powder mixture is exposed to repeated cold-welding and severe plastic deformation. Therefore, particle fragmentation and grain refinement have led to an increase of the number of interfaces between the matrix and inclusions, thus limiting and/or stopping indentation crack growth as expected for nanocrystalline materials [132, 133]. The highest nano-hardness is achieved for the optimum concentration of 30 mol.% of BN in the Fe_3Al.

Compared to the as-milled powders, the nano-hardness of the heat-treated and re-milled powders is higher as presented in Table 4.2 probably due to the presence of ceramic phases (AlN and Fe_2B) that occupy a volume fraction between 20 and 32 % in the material. The large standard deviation (± 3.1 to ± 6.7 GPa) calculated from the nano-indentation data of heat-treated powders indicates a large degree of inhomogeneity in the microstructure as opposed to the as-milled powders (± 1.1 to ± 2.0 GPa). These observations clearly show that the average nano-hardness of the heat-treated powders is a response from individual phases present in the material (precipitation hardening) as opposed to a response from the as-milled powders where solid solution hardening is the dominant strengthening mechanism. This analysis is supported by the distribution of nano-hardness in Figure 4.13. The heat-treated powder indicates two or three groups of nano-hardness as opposed to a broad peak from the as-milled powder.
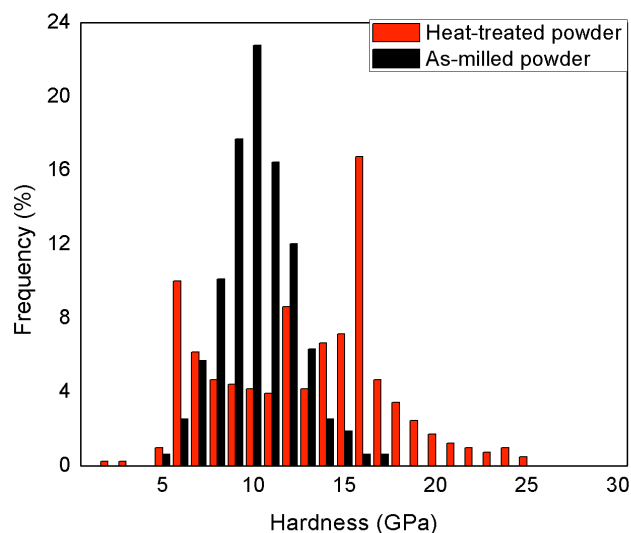
Figure 4.13: Distribution of nano-hardness values of the mixture of Fe₃Al and 30 mol.% of BN milled at high energy for 10 h compared with that of the same powder heat-treated at 1300 °C for 2 h and re-milled for 10 h.

4.4.3 Mechanical and tribological properties of the HVOF coatings

The XRD diffractograms of the HVOF coatings in Figure 4.5c show similar phases and features compared to the corresponding powders presented in Figure 4.2 suggesting that no significant phase transformation occurred during the deposition process. The retention of the microstructure of the powders in the HVOF coatings can be attributed to the short residence time (<2 μs) of the powder particles in the gun and the short thermal spike associated with the process [122]. Grosdidier *et al.* in [134] made similar observations on iron aluminide powder and associated them with lower particle temperatures achievable by HVOF. However, the X-ray diffractogram of the CP5 coatings compared in Figure 4.14 to the CP1, CP2 and CP4 coating reveals evidence of ceramic phases formed in the HVOF gun when the BN content is sufficiently high. This observation suggests that the spraying conditions described in Table 4.1 may not be optimum to induce significant reactions between the reactants in the P4 powder. Nevertheless, SEM micrograph of the CP4 coating in Figure 4.6c reveals features with a range of contrast within the iron aluminide matrix that are believed to be ceramic precipitates.
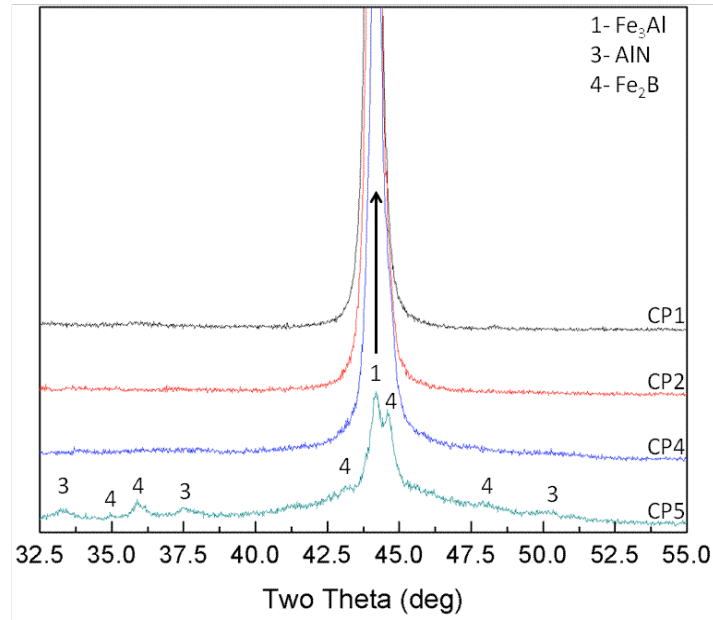
Figure 4.14: X-ray diffractograms of the HVOF coatings prepared from the as-milled powders.

The micro-hardness of the HVOF coatings (see Figure 4.9a) shows a similar trend to the nano-hardness of the corresponding powders discussed previously (Table 4.2). However, these observations are strongly dependent on the size of the indentation. Under micro indentation at 3N, a large volume of material is displaced compared to the nano indentation at 2 mN. The increase in micro-hardness of the HVOF coatings prepared from pure Fe_3Al ball-milled for 10 h with BN powder is associated with the nanocrystalline structure of the powders retained in the coatings. The hardness of the milled powders is enhanced by fine grains, solid solution strengthening, and by hardening via heat-treatment as discussed above. Moreover, the presence of oxides (Al_2O_3) and AlN particles (Figure 4.8) offers extra strength to the iron aluminide matrix.

The micro-hardness of the HVOF coating prepared from the Fe_3Al milled at high energy for 10 h with 30 mol.% of BN, heat-treated and mildly re-milled at low energy decreases by 50 % compared to the untreated powder (Figure 4.9b). Heat-treatment at such high temperature (1300 °C) is believed to have decreased the overall mechanical properties [98] of the matrix as a result of melting. After milling the heat-treated powder for 2 h and 10 h at high energy, the overall micro-hardness of the HVOF coatings approaches ~9 GPa.

The wear rate (K, ~9 × 10^{-5} mm^3/Nm) of the substrate decreases by one order of magnitude when the Fe_3Al coating is used. The addition of the hard h-BN provides additional improvement.

High micro-hardness (7.8 GPa) and high wear resistance (5×10^{-7} mm^3/Nm) are achieved for the CP4 coating compared to the CP2 and CP5 coatings. The poor wear performance of the CP2 and CP5 materials is associated with their poor mechanical properties described above. In addition, the CP5 coating exhibits a higher level of porosity compared to other materials. The highly fractured surface of the CP5 coating (Figure 4.10d) may be related to the special composition of this material with a large ceramic content and its high level of porosity.

The wear performance under the selected tribological conditions seems to be defined by the micro-hardness of the HVOF coatings. The larger wear tracks in Figures 4.10b and 4.10d, and the features observed are believed to be associated with the lower micro-hardness and the brittle behavior of the corresponding coatings. The width of the wear track of the CP4 coating (Figure 4.10c) is ~3 times smaller compared to other coatings suggesting that 30 mol.% of BN is optimum under the chosen tribological conditions.

The wear rate of the CAP4$_{5min}$ coating, ~3 $\times$ 10^{-6} mm^3/Nm, significantly increases as compared to the CP4, 5×10^{-7} mm^3/Nm for which the powder was untreated as shown in Figure 4.9b. This result seems surprising at first glance since the AP4$_{5min}$ powder exhibits the highest mean nano-hardness (Table 4.2) and its microstructure is preserved in the HVOF coating as discussed previously. However, the micro-hardness of the coating is low (Figure 4.9b) and examination of the wear track of the CAP4$_{5min}$ (inserted micrograph of Figure 4.11c) indicates the presence of cracks around large particles suggesting that the matrix-ceramic interface bond is weak and may be preferential sites for crack initiation and propagation. Moreover, the size and the distribution of the precipitates may not be adequate for providing good tribological properties. In Figure 4.9b, the CAP4$_{2h}$ coating (79 μm thick) exhibits the highest hardness but its wear rate is higher compared to CAP4$_{10h}$ (98 μm thick). This observation is related to the differences in the degradation mechanism of the coatings. The width of the wear track of the CAP4$_{10h}$ coating is 2.5 times smaller than that of the CAP4$_{2h}$. Although the precipitates are uniformly dispersed in the matrix after 2 h of re-milling, their size is much larger compared to 10 h (see Figure 4.7). The relatively large precipitates in the CAP4$_{2h}$ coating prompted a much faster material removal compared to CAP4$_{10h}$ coating. The CAP4$_{10h}$ coating prepared from precipitate strengthening exhibits a 13 % increase in hardness and a 50 % decrease in wear rate compared to the CP4 coating prepared from solid solution strengthened Fe$_3$Al matrix as discussed previously.

4.4.4   Wear mechanism

4.4.4.1 Fatigue and delamination

Observation of the top surface of the wear track in Figures 4.10 and 4.11 reveals the presence of various tribo-features such as micro-cracks, parallel grooves and scratches in the direction of sliding. These features seem to indicate the fatigue degradation mechanism [53, 135]. In addition, SEM micrographs of the longitudinal cross-sections of the wear track of the pure Fe_3Al coating shown in Figure 4.15 illustrate the degradation mechanism mode. In Figure 4.15a, the cross-section perpendicular to the sliding direction reveals micro-cracks below the region of contact of the worn surface of the coating. The initiation of micro-cracks inside particles is due to repeated stresses induced by the hard asperities of the alumina ball (20 GPa) (see Figure 4.15a). When the shear stress generated at a certain depth is maximum, cracks grow and propagate rapidly as shown on the longitudinal cross-section parallel to the sliding direction (Figure 4.15b) where a large crack can be seen within an unmelted particle of Fe_3Al. Thus, the top surface of the Fe_3Al coating primarily degrades via spallation/delamination.
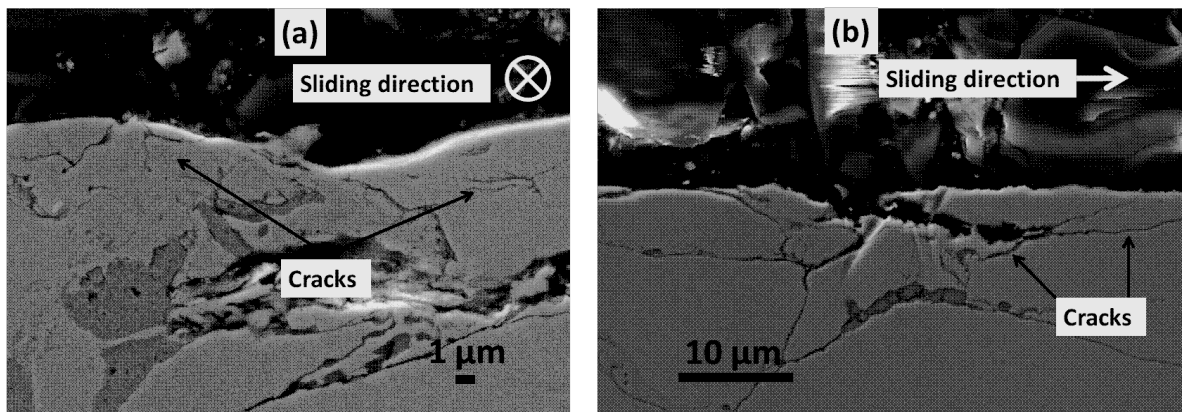
Figure 4.15: SEM micrographs of cross-sections (a) perpendicular and (b) parallel to the tangential force of the wear track of the pure Fe_3Al coating.

4.4.4.2 Abrasion

The presence of debris in the wear tracks (Figures 4.10b-d and 4.11a-c) and parallel grooves and scratches in the direction of sliding (Figures 4.10b, 4.11b) are indications that material removal is, to a large extent, governed by abrasion [53]. In Figure 4.16, the SEM micrograph of the cross-section of the wear track of the CP5 coating shows that cracks due to

stress concentration propagate rapidly through splats and/or porosity and coating material is worn. It is believed that the hard asperities at the surface of the composite coatings were deformed upon interactions with the Al_2O_3 ball and materials including hard ceramic particles were removed. The hard particles from the generated debris act as abrasive particles between the surface of the composite coatings and the Al_2O_3 ball.

Amiriyan *et al.* [61] identified similar degradation mechanisms as discussed above for the pure Fe_3Al and Fe_3Al-TiC coatings tested under comparable dry sliding conditions at a lower sliding speed (between 0.04 and 0.1 m/s).
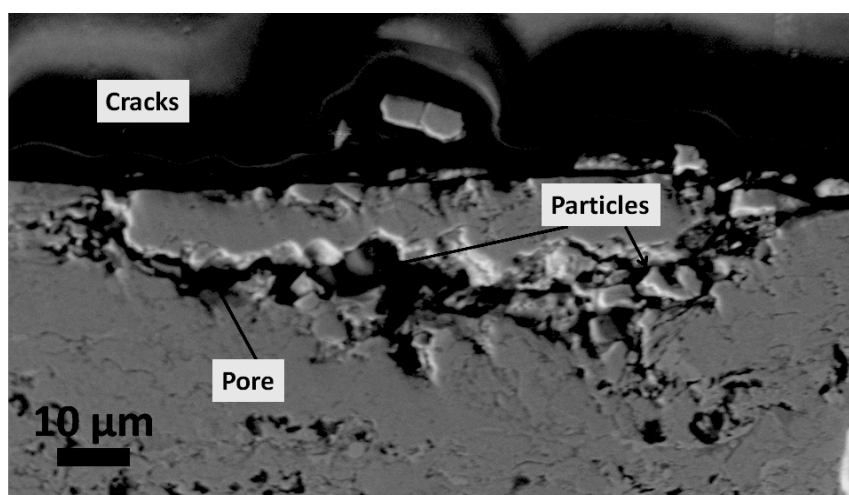
Figure 4.16: SEM micrograph of a longitudinal cross-section of the wear track of the CP5 composite coating perpendicular to the sliding direction.

4.4.4.3 Oxidation

The EDS analysis of the wear track of the $CAP4_{5min}$ coating (Figure 4.11d) indicates the presence of a significant amount of oxygen compared to the unworn surface. From the peak intensity of Fe and Al, it is believed that aluminum oxide forms superficially in the wear track as a result of oxidation. In Figure 4.17a, inspection of the SEM micrograph of the region of contact of the counterbody after rubbing on the surface of the coating shows that the Al_2O_3 ball is worn. The traces of aluminum and oxygen from debris of the counterbody are likely to be observed in the wear tracks. The EDS analysis of the contact of the ball (Figure 4.17b) revealed coating

materials (Fe) transferred to the alumina. This is an indication that coating material losses also occur via adhesive wear.
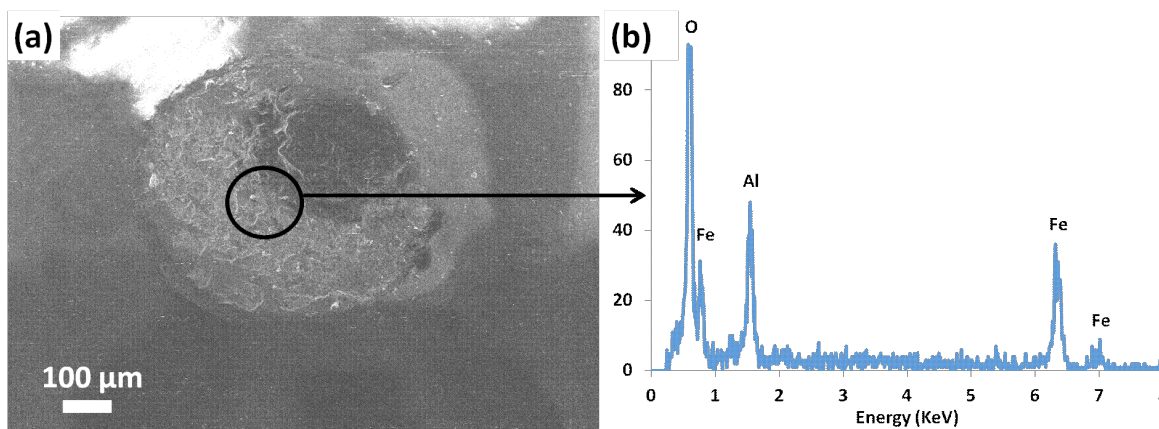
Figure 4.17: (a) SEM micrograph and (b) EDS analysis of the contact of the Al_2O_3 ball after sliding on the surface of the HVOF coating prepared from the as-milled powder containing 50 mol.% of BN.

4.5 Conclusion

High-energy ball-milling was successfully used to fabricate Fe_3Al-based composite materials with nano-scale BN inclusions. Heat-treating this powder mixture led to the formation of AlN and Fe_2B ceramic particles in the iron aluminide matrix. Re-milling the powders significantly reduces the size of the precipitates in the material.

Following HVOF deposition of the powder mixture, it has been found that the microstructure of the feedstock materials was preserved in the coating to a large extent.

Detailed mechanical analysis of both the powders and of the HVOF coatings has revealed that the micro-hardness of the pure milled Fe_3Al sprayed coating was increased by ~40 %, and its initial wear rate ~9×10^{-6} mm^3/Nm was decreased by one order of magnitude when 30 mol.% of BN was added to Fe_3Al. Grains refinement, solid solution and particle strengthening are believed to be the main reason for the observed improvements. A homogeneous dispersion of ultra-fine and hard particles throughout the metal matrix by re-milling the heat-treated powder mixture was found to provide the best tribological performance.

Particular insights have been gained when analyzing the HVOF coating wear mechanisms. The worn Al_2O_3 counterbody and the presence of particles and scratches inside the wear track

suggest that abrasion is the predominant wear degradation mechanism. Detailed inspection of the cross-section of the coating has revealed micro-cracks below the contact zone due to repeated stresses induced by the hard Al_2O_3 ball on the coating, suggesting that the fatigue mechanism also contributed to the coating failure during testing.

4.6 Acknowledgments

CHAPTER 5   ARTICLE 2: WEAR PROPERTIES OF Fe₃Al-BASED HVOF COATINGS STRENGTHENED WITH *IN-SITU* PRECIPITATED NITRIDE AND BORIDE PARTICLES

Fabrice Pougoum[a], Ludvik Martinu[a], Jolanta-Ewa Klemberg-Sapieha[a,*]

Sylvio Savoie[b], Robert Schulz[b]

[a]Engineering Physics Department., Polytechnique Montréal, Montréal, QC, Canada H3C 3A7

[b]Materials Science Department. Institut de recherche d'Hydro-Québec (IREQ), Varennes, QC, Canada, J3X 1S1

* Corresponding author.

E-mail address: jolanta-ewa.sapieha@polymtl.ca (J.-E. Klemberg-Sapieha).

Abstract

Iron aluminide coatings reinforced with *in-situ* precipitated TiN, TiB₂ and Fe₂B particles were synthesized from Fe₃Al, BN and Ti powders using a combination of high-energy ball milling and high velocity oxy-fuel (HVOF) process. In the present work, we investigate the effect of the BN/Ti contents on the microstructure and characteristics of the HVOF coatings and we discuss their tribological properties. The microstructure and composition of powders and coatings were investigated using X-ray diffraction, differential thermal analysis and optical and scanning electron microscopies. The wear rate was evaluated by tribometry in a pin-on-disc configuration, and the mechanical properties were obtained using indentations. X-ray analysis of the coatings prepared from the as-milled powders revealed evidence of TiN, TiB₂ and Fe₂B peaks. The microhardness (4.3 GPa) and the wear resistance (3×10^{-4} mm³/Nm) of the coating prepared from the pure Fe₃Al powder were increased 3.3 times and by about three orders of magnitude, respectively, when 70 wt% of Fe₃Al was milled with 10 wt% of BN and 20 wt% of Ti. Fatigue and abrasive wear was found to be the predominant degradation mechanism during sliding against an alumina ball of the pure Fe₃Al and composite HVOF coatings, respectively. Adhesive

wear also contributed to the material loss as confirmed by EDS analysis that revealed a transfer of the coating material to the counterpart.

5.1 Introduction

Iron aluminide alloys with tailored tribo-mechanical properties have been extensively studied as potential candidates to replace bulk steels or hard chromium coatings due to their low density and low cost of manufacture. They exhibit good corrosion-, oxidation- and sulfidation-resistance at high temperature [14]. These materials are suitable for applications in power generation, petrochemical and automotive industries owning to their interesting metallurgical properties [136]. At room temperature, iron aluminide alloys exhibit poor ductility (<5 %), low resistance to creep and poor wear performance that restrict their use for structural applications [15, 137]. It was demonstrated that these drawbacks can be improved through solid solution or precipitation strengthening [15, 19, 36, 138].

Among different mechanical alloying processes, the high-energy ball milling (HEBM) technique is convenient to produce metal-ceramic composite materials in a powder form [139]. In this technique, powder particles are blended, cold worked, fragmented and repeatedly welded giving rise to materials with fine and homogeneous microstructure. The resulting materials often contain stable and/or metastable phases within a metallic binder with clean matrix/reinforcement interfaces.

In many wear applications where severe environmental conditions are experienced such as high temperature corrosion, solid particle and cavitation erosion or abrasion, thick protective coatings are suitable [122]. To produce thick (hundreds of μm up to mm) coatings on metal substrates, thermal spray processes are preferred over technologies such as chemical or physical vapor deposition used to fabricate films with a thickness below 30 μm [120]. Compared to other thermal spray techniques, the high velocity oxy-fuel (HVOF) process can be used to achieve relatively low particle temperature and high speed (~800 m/s). Thus, dense coatings with low porosity and less prone to oxidation can be obtained [122].

Borides and nitrites have been less frequently considered as reinforcing components for iron aluminide alloys compared to other refractory materials such as carbides and oxides. Titanium diboride (TiB_2) is a wear-resistant material that exhibits high hardness, high elastic modulus and high toughness. Compared to TiB_2, titanium nitride (TiN) exhibits higher melting temperature and demonstrates lower physical performance [140]. Both ceramic materials are thermodynamically stable in iron aluminides [24], and they can be considered as potential reinforcing components for metal matrices [27, 140]. The effect of single ceramic particles on the mechanical and wear properties of bulk iron aluminide alloys has been already studied [102, 104, 141]. Alman *et al.* have demonstrated that the addition of 40 up to 70 vol% of TiB_2 particles using arc melting decreased the wear rate of Fe_3Al by one order of magnitude. They reported that the solid particle erosion resistance of FeAl is higher when TiB_2 particles are used compared to TiC [142]. The micro-hardness of bulk iron aluminide alloys was increased with the addition of TiN particles with a size 20 nm [102]. It is believed that a combination of TiN and TiB_2 particles as reinforcing components in iron aluminides can yield alloys with high fracture toughness and unique ductility.

The main objective of this work is to enhance the tribo-mechanical performance of the Fe_3Al-based composites reinforced via *in-situ* precipitation of borides and nitride particles. The effect of the BN/Ti contents on the mechanical and wear properties of the iron aluminide-based HVOF coatings are investigated in detail.

5.2 Experimental methods

5.2.1 Powder preparation

Powder mixtures were prepared from 100, 78, 70, 57 and 37 wt% of Fe_3Al (97.5 % pure with ~2 % of chromium from Ametek) with 0, 14, 20, 28 and 41 wt% of Ti (99.4 % pure from Alfa Aesar), and 0, 8, 10, 15 and 22 wt% of BN (98 % pure from Lower Friction), and labeled as M100, M40, M30, M20 and M10, respectively. The initial mean particle sizes of BN, Fe_3Al and Ti powders were 5, 50 and 150 μm, respectively, and the ball-to-powder weight ratio was 10:1. The powders were ball milled at high energy (1000 rpm) for 10 h under an argon atmosphere using a Zoz GmbH Simoloyer CM01 2 Liter high-energy mill with stainless steel jar and milling

balls. For comparison, the powder mixture M30 was ball milled at high energy for 1 h and 4 h, and labeled as M30-1h and M30-4h, respectively.

5.2.2 HVOF coating preparation

The ball milled composite powders were sprayed onto sandblasted stainless steel 304 type substrates using a Praxair J-P 8500 HVOF gun mounted on an ABB robot arm and controlled by a computer. The deposits were cut into coupons prior to the tribo-mechanical characterization. Details of the preparation of the composite coatings and of the samples are described elsewhere [36]. The coatings are labeled with a letter "C" added in front of the abbreviated name of the corresponding powder. For example, CM100 for the coating prepared from the pure Fe_3Al powder ball milled for 10 h.

5.2.3 Microstructural analysis

All powders and HVOF coatings were examined using a Phillips X'Pert X-ray diffractometer equipped with a Cu Kα radiation source operated at 50 kV and applied in the θ-2θ configuration. The X-ray diffraction data were used to determine and quantify the phases formed in the HVOF coatings.

Microstructure of the HVOF coatings was assessed from the observations of polished cross-sections using a 7200 JEOL scanning electron microscope (SEM) equipped with energy dispersive X-ray spectroscopy (EDS, Inca X-max 80 Oxford) with a 10 kV electron beam. For better resolution, the specimens were observed and analyzed at a distance of 15 mm from the detector. The porosity level was estimated using image analysis of the polished cross-sectional surface of the HVOF coatings.

The thermal stability of the as-milled powders was investigated using a SETSYS Evolution TGA-DTA/DSC (from SETARAM Instrumentation) at a heating rate of 10 °C/min. The milled powders were held in an alumina crucible under an argon atmosphere. Part of the M20 composite powders was heat-treated at different temperatures (450, 550, 740 and 900 °C) under vacuum ($\sim$$10^{-6}$ mbar) and rapidly quenched in air. The heating rate was 10 °C/min up to the desired temperature.

5.2.4 Indentation

The indentation measurements on the HVOF coatings were performed using a CSM Micro-Combi tester. The microhardness was evaluated with a Berkovich tip, and the applied load was linearly increased up to a maximum of 3 N, kept constant for 30 seconds, and then linearly decreased. The average microhardness was obtained from a minimum of 200 indentations randomly conducted on the polished surface or cross-section of the coatings using the Oliver and Pharr method [123]. The error bars on the average hardness values represent standard deviation from the 200 indentation measurements.

5.2.5 Scratch test

The scratch tests were performed on polished cross-sectioned HVOF coatings using a CSM Micro-Combi tester equipped with a diamond Rockwell C indenter with a radius of 200 μm. The scratch test started in the substrate and ended in the resin. The scratch length was fixed at 1 mm, and the constant normal load was 10 N. The appearance of defects within the fractured cross-section was used to classify the HVOF coatings.

5.2.6 Pin-on-disc

The wear rate of the HVOF coatings were measured according to ASTM-G99 using a pin-on-disc configuration in the dry conditions at room temperature with a relative humidity between 20 and 40 %. The diameter of the wear track ring was 9 mm, and a new alumina (Al_2O_3) counterpart of 4.75 mm in diameter was used for each test. Alumina and the sliding test conditions were chosen to compare results with previously reported experiments [36]. The total sliding distance, L, was 1000 m, and the linear speed was 15.7 cm/s. The applied normal force, F, was 10 N, and the wear rate, K, was calculated using the formula $K = V/F*L$ $K = V/F \times L$, where V is the total volume of coating material loss. The average cross-sectional surface of the ring was obtained from a minimum of 20 measurements at different positions of the wear track ring, and the error bars on the average wear rate are the standard deviation from these measurements. The SEM micrographs of the top and cross-sectional surfaces of the wear track were analyzed in order to assess the degradation mechanisms of the HVOF coatings. EDS analysis of the worn and unworn surfaces of the coatings and counterpart were performed to obtain more insight into the material loss mechanism.

5.3   Results and discussion

5.3.1   Microstructure of the composite powders

Figure 5.1 presents the X-ray diffractograms of the elementary powders (Fe_3Al, BN and Ti) compared with the mixture of 78, 70, 57 and 37 wt% of Fe_3Al milled for 10 h with with 14, 20, 28 and 41 wt% of Ti, and 0, 8, 10, 15 and 22 wt% of BN. After one hour of ball milling, all peaks broadened and weakened compared to that of the elementary powders (Figures 5.1a and 5.1b). Broadening and weakening becomes more important as the milling is prolonged to 4 h (see the diffractogram for the M30-4h sample) due to a decrease of the crystallite size and presence of defects induced by the high-energy collisions of the powder particles.

Following 10 h of milling, the left side of the principal peak of Fe_3Al is slightly shifted toward lower 2θ angles indicating a change of its composition prompted by the formation of random Fe-based solid solutions. On the contrary, the titanium peaks remain unshifted regardless of the initial composition of the mixture (see Figure 5.1c) suggesting that asymmetric diffusion occurred upon ball milling. Compared to the unmilled powders, weakening and broadening of the Ti peaks indicate that part of Ti particles has been severely deformed and their size was significantly decreased. The iron aluminide peak at ~44.2 ° in the diffractograms exhibits a right shoulder that coincides with Ti and broad BN peaks. This right shoulder remains evident after 10h of milling irrespective of the initial composition of the powder mixtures suggesting that its presence is a contribution from the un-shifted Ti and Fe_3Al peaks. The contribution from the broad BN peak is not significant as we describe below.

As ball milling evolved, the BN peaks rapidly disappeared in the diffractograms except for M10 where a weak peak is evident at ~26 ° due to a larger amount of BN in the mixture. The rapid disappearance of the BN peaks in the diffractograms in Figures 5.1b and 5.1c is associated with the destruction of the BN crystal structure and its low scattering power. Moreover, the microstructure of the M10 and M20 mixtures exhibits amorphous-like features between 33 ° and 46 ° after 10 h of milling. These features are associated with the amorphization of the powder mixture upon HEBM. It has been reported that upon mechanical treatment, amorphization of h-BN particles occurred when the nanocrystallites are less than several nanometers in size [35].
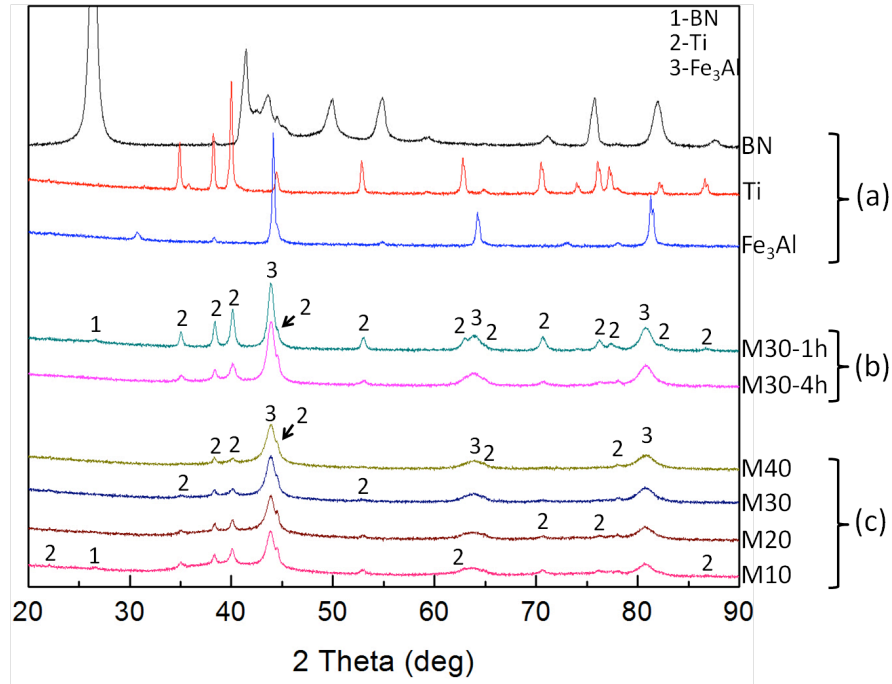
Figure 5.1: X-ray diffractograms of (a) initial powders, (b) powder mixtures of 70 wt% of Fe_3Al milled for 1 h and 4 h with 10 wt% of BN and Ti of 20 wt%, and (c) powder mixtures of 78, 70, 57 and 37 wt% of Fe_3Al milled for 10 h with 14, 20, 28 and 41 wt% of Ti and 8, 10, 15 and 22 wt%, respectively.

The absence of new phases after 10 h of HEBM suggests that the milling time and/or the mechanical energy provided to the powder particles were not sufficient to initiate solid-state reactions between reactants in the mixtures regardless of the composition of the powder. In fact, there are conflicting reports on the synthesis of TiN/TiB_2 composite powders via the HEBM of Ti and h-BN powders. Shim *et al.* obtained the TiN/TiB_2 composite powders in a single step. The TiN and TiB_2 phases were formed after 2 h of milling [143]. On the contrary, a two-step process was reported in [144] and [145]. The authors primarily observed the formation of TiN phases within 30 to 70 h of milling, and subsequent heat-treatment was employed to form TiB_2 phases. It is evident that mechanical energy and/or milling time are critical in the formation of TiN and TB_2 phases.

After ball milling, the powders were sieved and particle with sizes between 20 and 50 μm were kept for the HVOF spraying. The morphology and the distribution of the particle sizes are shown in Figure 5.2. SEM micrographs of the as-milled powder reveal that the shape of the

powder particles is irregular and the morphology exhibits a typical "sandwich-like" microstructure. In Figure 5.2a, the M30 powder particles seem to be compact as opposed to M10. The distribution of sizes of the as-milled powder particles exhibits a Gaussian-type unimodal distribution with an average particle diameter of about 35 µm except for the M10 powder which shows a bimodal distribution (Figure 5.2b). The average diameter of the M10 powder particles is 5 and 40 µm with respect to the modes. This peculiar trend seems to indicate that smaller particles of the as-milled M10 powder are loosely bonded to larger ones due to the large amount of h-BN and Ti that has not favored cold-welding during the HEBM process.
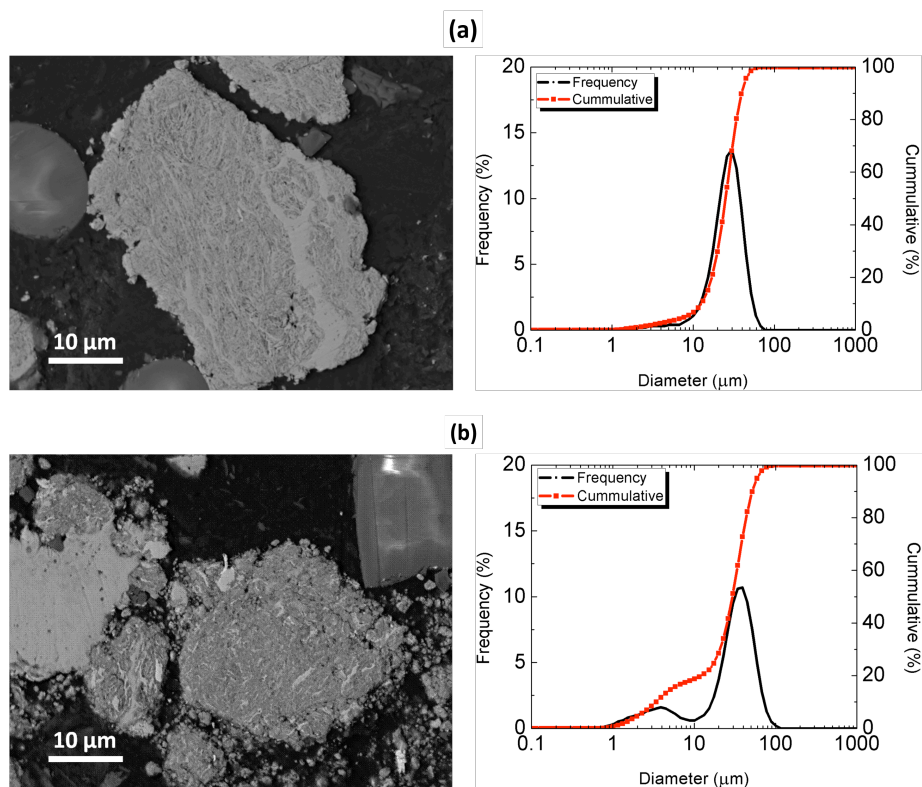
Figure 5.2: SEM micrographs and powder particle size distribution of two mixtures: (a) 70 wt% of Fe_3Al and 10 wt% of BN and 20 wt% of Ti, and (b) 37 wt% of Fe_3Al and 22 wt% of BN and 41 wt% of Ti milled at high energy for 10 h.

5.3.2   Microstructure of the HVOF coatings

X-ray diffractogram of the HVOF coating prepared from the pure Fe_3Al powder milled for 10 h at high-energy is compared in Figure 5.3 to those of the coatings prepared from the as-milled powders described in section 5.3.1. The presence of TiN, TiB_2 and Fe_2B peaks in the

diffractograms of the HVOF coatings prepared from the as-milled powder provides an evidence that phase transformation has occurred during the deposition. Ball milling of the mixture of Fe$_3$Al, BN and Ti led to the formation of a powder with a microstructure in which all reactants are close to each other and likely to react. It has been demonstrated that the decrease of the particle sizes of Ti and BN down to nanoscale using the HEBM process favors the reaction between the components [144]. In general, decreasing the particle size leads to a reduction of the diffusion paths and it increases reaction activities and interface areas [146]. Although the powder particles were subjected to a short thermal spike and their residence time in the HVOF gun was short (<200 μs) [122], ceramic phases can be formed under the deposition conditions described in [36]. It is worth mentioning that no significant ceramic formation was observed in our coatings when a mixture of Fe$_3$Al and h-BN powders was ball milled without Ti and sprayed under similar HVOF deposition conditions. This means that Ti significantly influences the phase evolution of the composite powders.
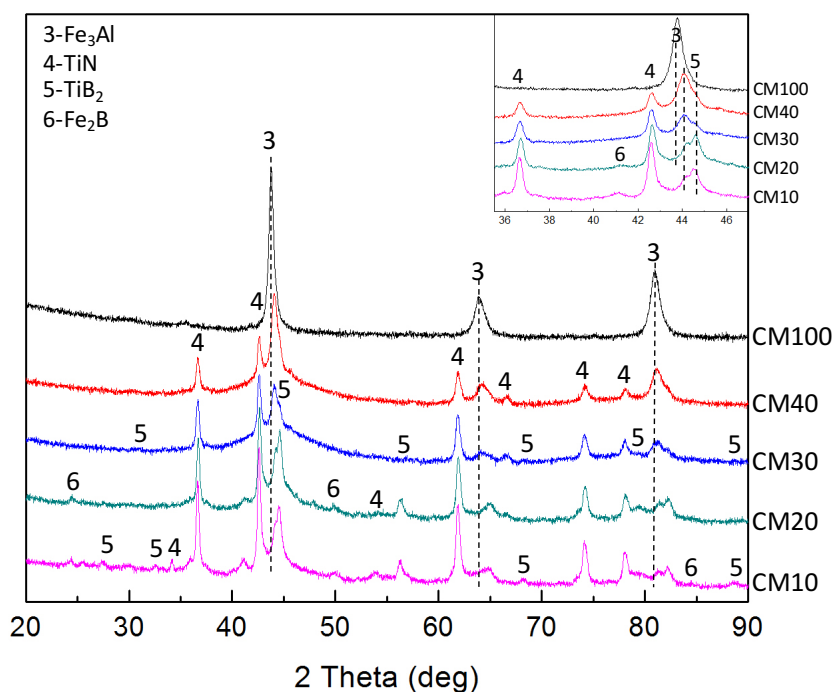
Figure 5.3: X-ray diffractograms of HVOF coatings prepared from the pure Fe$_3$Al powder compared to those prepared with composite powders. A section (from 36 to 46 °) of the diffractograms is presented in the inserted graph.

DTA characteristics of the as-milled powders shown in Figure 5.4 can be used to understand powder behavior upon heat treatment. In Figure 5.4a, the DTA curves reveal two broad exothermic peaks that occurred at about 550 and 740 °C irrespective of the powder mixtures, suggesting the nucleation/precipitation of new phases. The first peak has been associated mainly with the formation of TiN since the X-ray diffractogram of the M20 powder shown in Figure 5.4b reveals evidence of TiN peaks when the powder mixture was annealed at 550 °C. The second exothermic peak is attributed to the formation of both TiB_2 and Fe_2B phases: when the temperature was increased to 800 °C, TiB_2 and Fe_2B peaks become evident. Thermodynamically, Ti is more likely to react first with N than with B since the heat of formation of TiN (-338 kJ/mol) is more negative than that of TiB_2 (-281 kJ/mol) [147]. From the thermodynamic point of view, Fe_2B (-67.4 KJ/mol [148]) is unlikely to form before TiN and TiB_2 because of the low driving force for its formation.
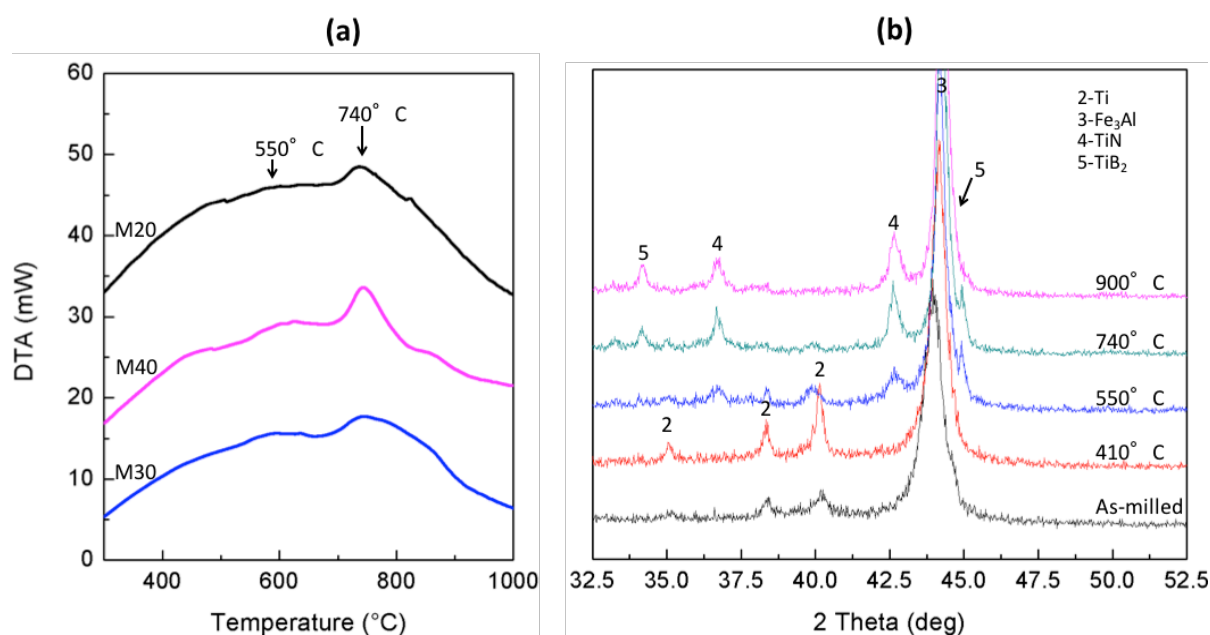
Figure 5.4: a) DTA curves of as-milled powders and b) X-ray diffractograms of the as-milled M20 powder heat-treated at various temperatures up to 1000 °C and quenched in air.

The X-ray diffractograms of the CM40 and CM30 coatings reveal broad and weak peaks of iron aluminide compared to that of CM100. The increase of intensity of the TiN and TiB_2 peaks with respect to the amount of BN/Ti can be related to the content of precipitated ceramic materials in the matrix as presented in Table 5.1.

Table 5.1: Composition of the elementary powders of the
mixtures, and characteristics of the HVOF coatings.

		Composition									
		Starting powders (wt%)			Phases (wt%)					Scratch appearance	Porosity level (%)
		Fe$_3$Al	BN	Ti	Fe$_3$Al	FeAl	TiN	TiB$_2$	Fe$_2$B		
As-milled powders	M100	100	-	-							
	M40	78	8	14							
	M30	70	10	20							
	M20	57	15	28							
	M10	37	22	41							
HVOF coatings	CM100				100	-	-	-	-	Poor	2.2 ± 0.1
	CM40				59	-	28	13	-	Good	2.4 ± 0.1
	CM30				46	-	36	18	-	Good	2.5 ± 0.2
	CM20				-	10	44	34	12	Poor	4.7 ± 0.1
	CM10				-	8	58	25	9	Poor	5.8 ± 0.2

In particular, for the CM10 and CM20 coatings, the Fe$_2$B peaks are visible in the diffractograms as the iron aluminide peaks are significantly weakened and shifted toward higher 2θ angles. This change of composition is attributable to the loss of Fe in the iron aluminide crystal structure through the formation of Fe$_2$B phases.

5.3.3 Mechanical and tribological properties of HVOF coatings

The microhardness (*H*) of the HVOF coatings prepared from the as-milled Fe$_3$Al powder (CM100) is compared in Figure 5.5 with the coatings prepared from the composite powders. The *H* value of 4.3 GPa for the CM100 coating increased 3.3 times when BN and Ti were added. Compared to other compositions, the M30 seems to contain the optimum BN/Ti content.

Interestingly, the microhardness of the HVOF coatings does not increase continuously with the BN/Ti contents. This observation was also previously made by Schneibel *et al.* for various iron aluminide-based alloys [27]. The authors showed that the mechanical properties do not improve linearly with the volume fraction of the secondary phases.

The presence of oxides (Al_2O_3) originated from the oxidation that occurred during spraying can offer extra strength to the coatings. Such mechanical improvement can be associated with the microstructure of the coatings.
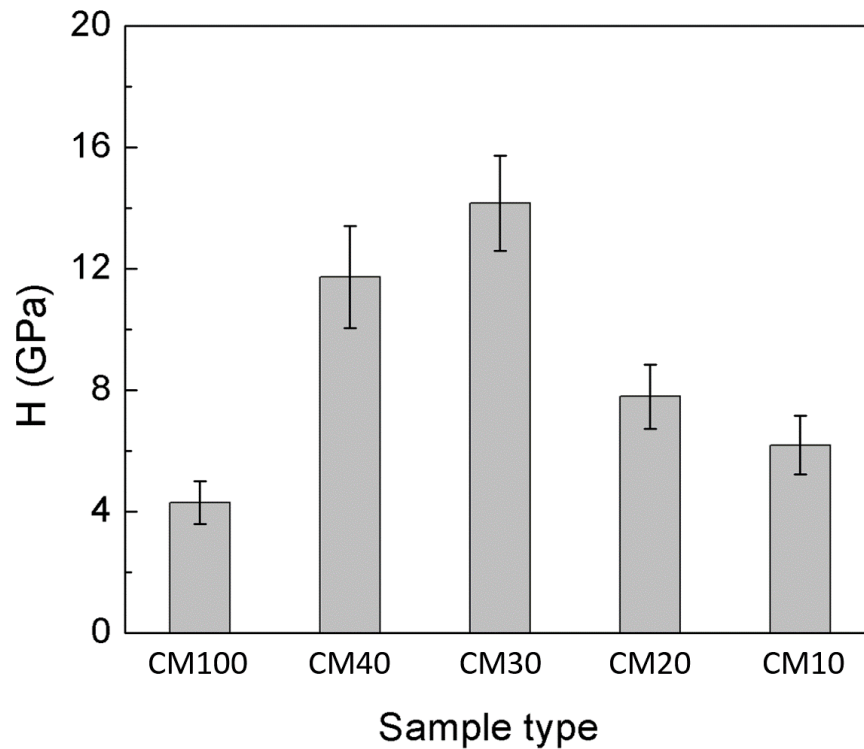
Figure 5.5: Microhardness of the HVOF coatings.
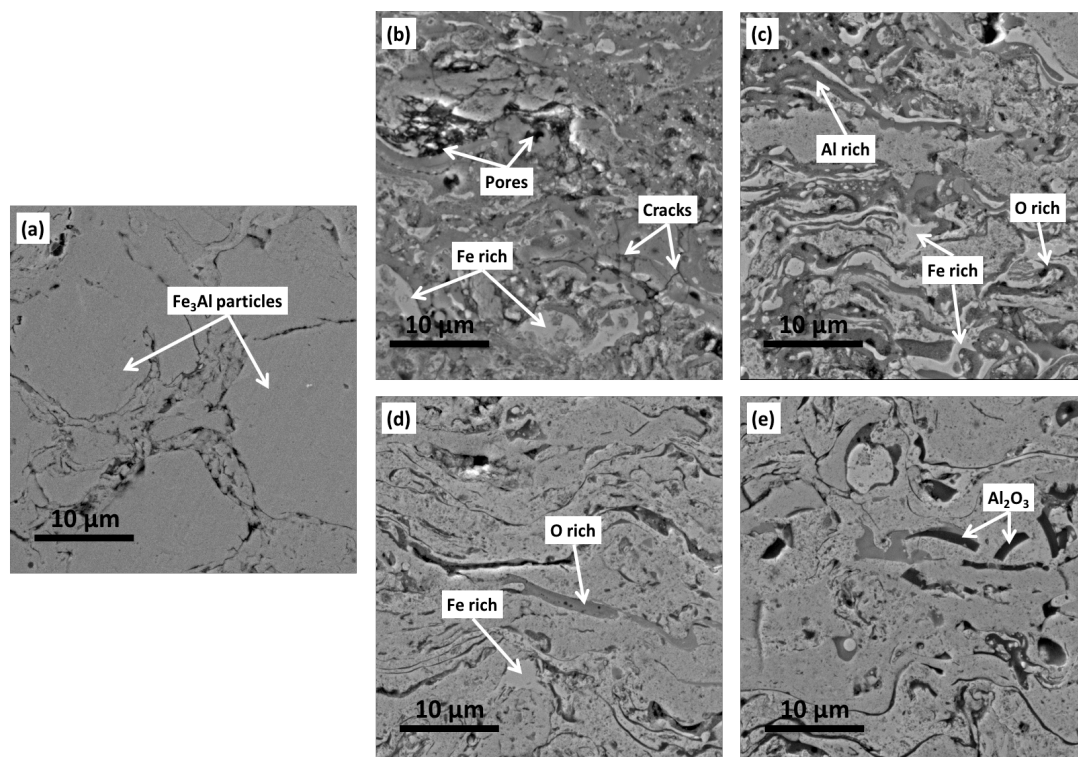
Figure 5.6: Cross-section SEM micrographs of the HVOF coatings prepared from (a) pure Fe₃Al powder milled for 10 h, and from the as-milled powders of (b) 78 wt% of Fe₃Al and 8 wt% of BN and 14 wt% of Ti, (c) 70 wt% of Fe₃Al and 10 wt% of BN and 20 wt% of Ti, (d) 57 wt% of Fe₃Al and 15 wt% of BN and 28 wt% of Ti, and (e) 37 wt% of Fe₃Al and 22 wt% of BN and 41 wt% of Ti.

In Figure 5.6a the CM100 coating shows unmelted rounded particles as opposed to the typical HVOF microstructure seen for other coatings (Figures 5.6b – 5.6e). The melted powder particles in which fine and hard ceramic precipitates are dispersed in an iron aluminide matrix is beneficial to the mechanical properties [58]. These fine dispersions increase the number of interfaces in the material that can help to delay or stop the propagation of cracks initiated via indentation compared to unreinforced and unmelted particles of the CM100 coating. The CM10 and CM20 coatings exhibit lower H compared to the CM30 and CM40. First, both CM10 and CM20 coatings (Figures 5.6b and 5.6c) show fewer light-gray regions that were identified to be the Fe(Al) matrix. These regions display dark inclusions that are Ti-rich and believed to be the ceramic precipitates formed during HVOF deposition. Second, the CM10 and CM20 coatings exhibit micro-cracks and higher porosity level (5 – 6 %) compared to other coatings as detailed in Table 5.1. The presence of cracks and porosities are believed to be a consequence of the brittle

nature of the M10 and M20 powder particles rich in BN and Ti as described above (Figure 5.2b). The brittle behavior was inherited from that of the powders. This type of microstructures and defects can be detrimental to the mechanical properties of the CM10 and CM20 coatings.
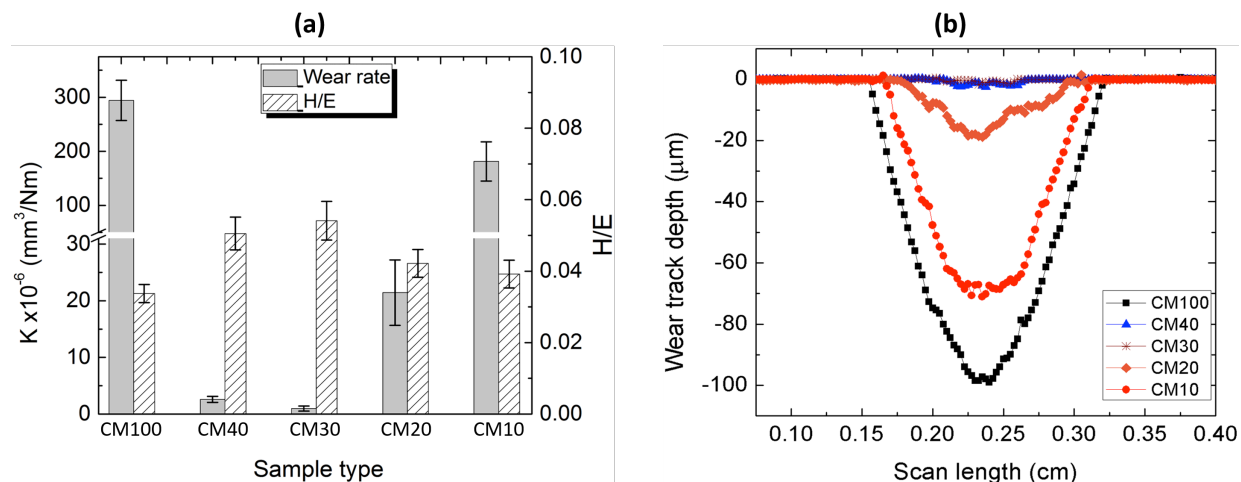
Figure 5.7: Comparison of the wear characteristics of the HVOF coatings:
a) wear rate and elasticity index, and b) wear track depth profiles.

Figure 5.7 presents the wear rate, elasticity index and wear track profiles of the HVOF coatings after the wear test under dry conditions. In analogy to the mechanical properties, the wear rate of the HVOF coating prepared from the pure Fe_3Al powder milled for 10 h is significantly enhanced when BN and Ti are added as shown in Figure 5.7a. The wear resistance of the CM100 coating (3×10^{-4} mm^3/Nm) was increased by nearly three orders of magnitude (8×10^{-7} mm^3/Nm) when ceramic inclusions are added. The mechanical properties of the coatings seem to define the wear behavior since the hardest coating exhibits the lowest wear rate (see Figures 5.5 and 5.7a). In addition, the hardest coating displays the highest H/E suggesting that it is prone to show elastic behavior compared to other coatings as can be seen in Figure 5.7a. Thus, the surface of the hardest coating is capable of absorbing and dissipating energy from contact pressure induced by the hard Al_2O_3 ball during the wear test. It has been demonstrated that porosity can affect the mechanical properties of coatings, thus influencing its elastic/plastic behavior [149]. The hardest coating exhibits the lowest wear track depth. The profiles of the worn region are not smooth which is an indication that the wear features such as debris, grooves or holes can be found inside the wear track.

The CM30 and CM40 coatings exhibit a relatively high wear resistance compared to other coatings. Despite a larger amount of the BN/Ti contents (15/28 and 22/41 wt%) in the CM10 and CM20 coatings, their poor wear performance is associated with their poor mechanical properties as described above. In addition, poor particle cohesion and coating adhesion on the 304 stainless steel substrate were observed for CM10 and CM20 that also exhibit pores and cracks. The observations in Figure 5.8a indicate that after scratch test, cracks are initiated within the coating and at the substrate/coating interface, and they propagate perpendicularly to the scratch direction. Particles show weak cohesion bonds, and delamination of the coating follows. On the contrary, the CM30 and CM40 coatings show good particle bonding since they exhibit no cracks or delamination (Figure 5.8b).
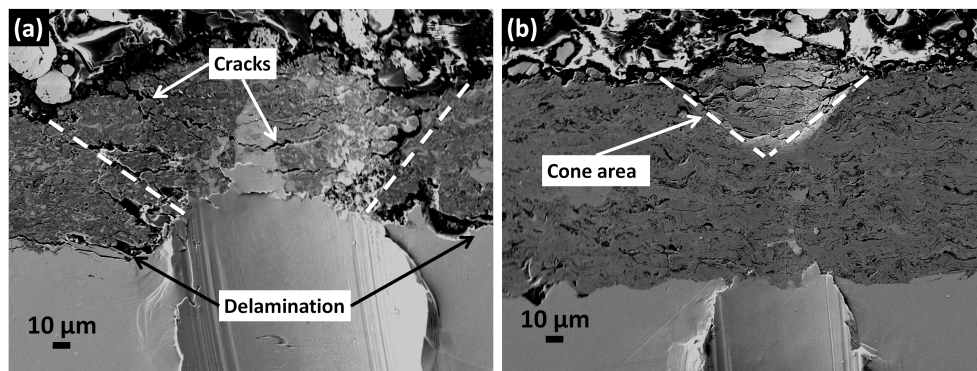
Figure 5.8: SEM micrographs of the HVOF coating cross-sections fractured after the scratch test: (a) poor (CM10) and (b) good (CM30) adhesion/cohesion behavior.

5.3.4 Degradation mechanisms of the HVOF coatings

5.3.4.1 Fatigue and delamination wear

In Figure 5.9 SEM micrographs of the top surface of the wear track of the HVOF coatings after wear test reveal various tribo-features such as holes, debris, micro-cracks and parallel grooves. These features are characteristic of strong interactions between the surface of the HVOF coatings and of the hard asperities with the Al_2O_3 counterpart. In Figures 5.9a and 5.9b, the presence of micro-cracks near holes inside the wear track is an indication that the surface of the coating degraded via fracture (dislocation fracture) [135, 150].
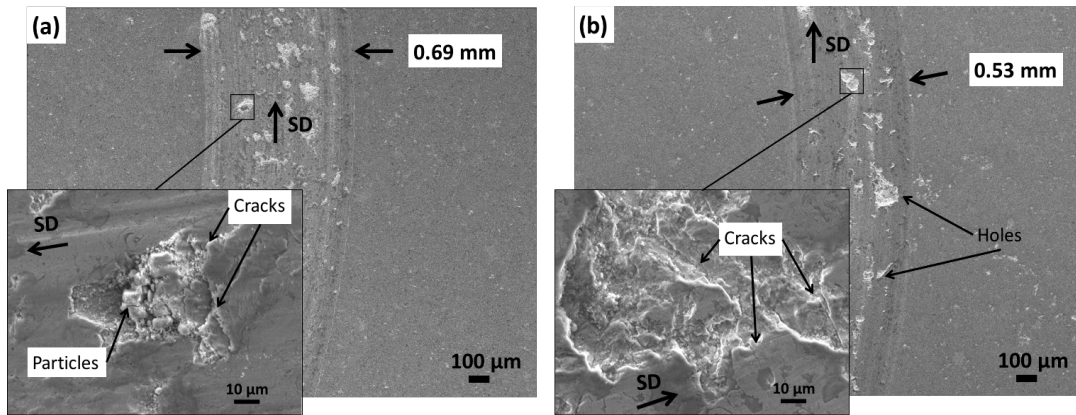
Figure 5.9: SEM micrographs of the wear tracks of two different
HVOF coatings: (a) CM40, and (b) CM30.

The tensile and compressive stresses repeatedly induced by the hard asperities of the Al_2O_3 ball at the surface led to the generation of cracks from defects on the surface and sub-surface. The inspection of the cross-sectional surface of the wear track of the CM100 coating perpendicular to the sliding direction shown in Figure 5.10a reveals that cracks (indicated by arrows) initiate and propagate within unmelted particles. To some extent, these cracks grow and reach the surface of the coating as revealed by the SEM micrograph of the cross-sectional surface parallel to the sliding direction (Figure 5.10b). As a consequence, the surface of the CM100 coating is prone to fracture and delamination.
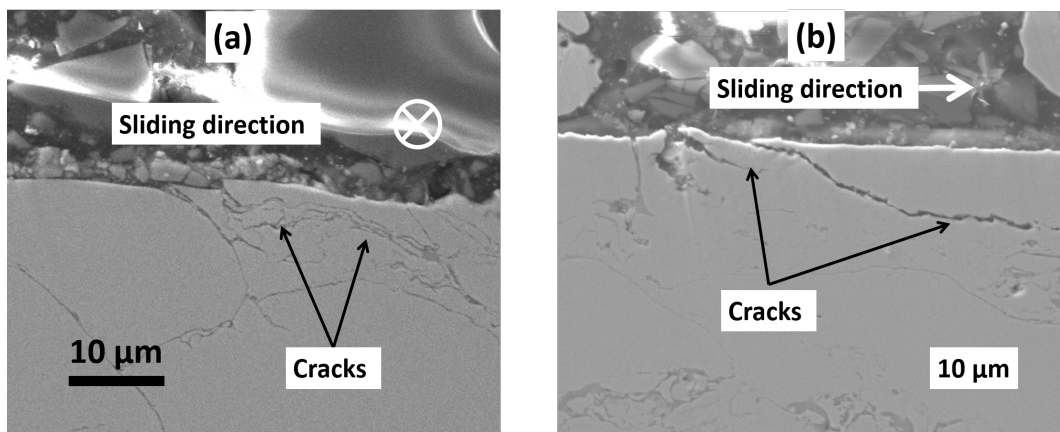
Figure 5.10: SEM micrographs of the cross-sections (a) perpendicular and (b)
parallel to the tangential force of the wear track of the CM100 coating.

In the case of composite coatings, the wear mechanism is similar. The cracks initiated in the sub-surface rapidly propagate to the surface via the defects in the coating as shown in Figures

5.6b to 5.6e leading to material removal. This behavior is linked to the fact that inter-splat boundaries and porosities are weak links in the HVOF coatings in agreement with [122].

5.3.4.2 Abrasive wear

In Figures 5.11a and 5.11b, the presence of parallel grooves inside the wear track and debris is an indication that the surface of the coating was damaged by abrasive wear. The surface of the coating is plastically deformed by the hard asperities of the Al_2O_3 ball and materials are displaced in the direction of sliding. The coating materials removed via plastic deformation and/or fatigue wear as described above contained hard secondary phases. These hard materials trapped between the Al_2O_3 counterparts and the surface of the coating act as abrasive components. Catastrophic failure of the CM10 and CM20 coatings occurred since they contain a higher ceramic content (Table 5.1) and their fragile microstructure favored removal of a large amount of material. The size of the debris inside the wear track of the CM10 and CM20 coatings is smaller than 10 µm.
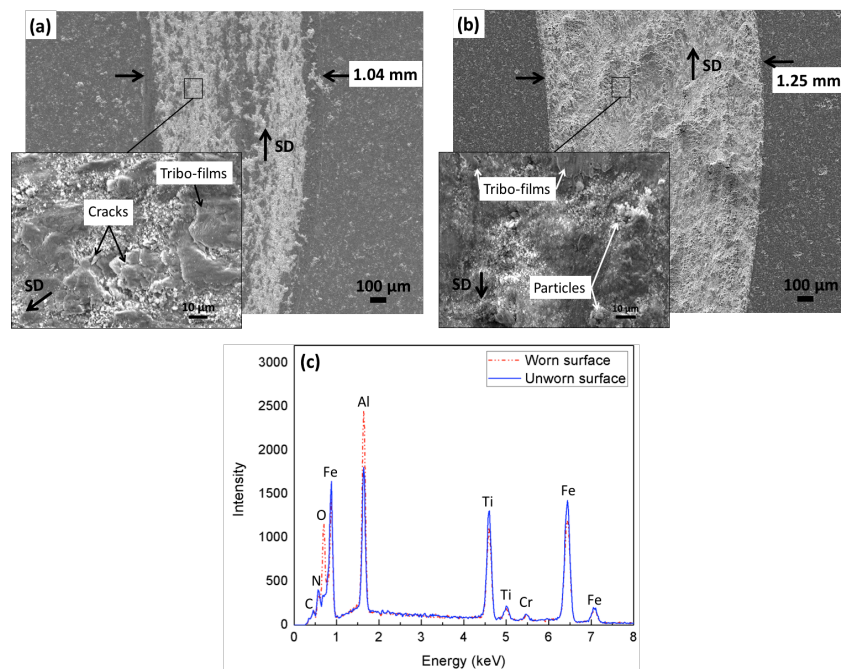
Figure 5.11: SEM micrographs of the top surface of the wear track of (a) CM20 and (b) CM10 HVOF coatings, and (c) EDS analysis of the worn and unworn surfaces of the CM20 coating.

5.3.4.3 Oxidative and adhesive wear

The top surface of the wear tracks reveals discontinued tribo-films formed inside the worn area after rubbing (see Figures 5.11a and 5.11b). Chemical inspection using EDS has shown that these tribo-films are O-rich. However, the CM10 and CM20 have demonstrated poor tribological performance suggesting that the discontinuity of the tribo-films could not help to reduce wear. In Figure 5.11c, the EDS analysis shows a significant amount of oxygen and aluminum in the worn surface compared to the unworn area, whereas the content of Fe and Ti decreased. Based on our results, we believe that O and Al originate from the worn Al_2O_3 ball (Figures 5.12a and 5.12b). Upon rubbing under a relatively high contact pressure, fresh coating surfaces exposed to the ambient air (humidity between 20 and 40%) can oxidize. In addition, it has been shown that in dry sliding conditions, oxide formation can be a consequence of increasing contact surface temperature [105]. Furthermore, the oxide inclusions that formed during HVOF spraying in the oxygen-rich regime described in [36] can appear at the surface during the wear test.

Chemical analysis performed on the contact surface of the counterpart body after sliding on the polished surface of the composite coatings shows evidence of coating materials (Fe and Ti) transferred onto the Al_2O_3 ball (Figure 5.12c). This is an indication of material loss via adhesive wear [150]. Therefore, it can be concluded that adhesive wear contributed to material removal in this system and under the sliding wear test conditions used.
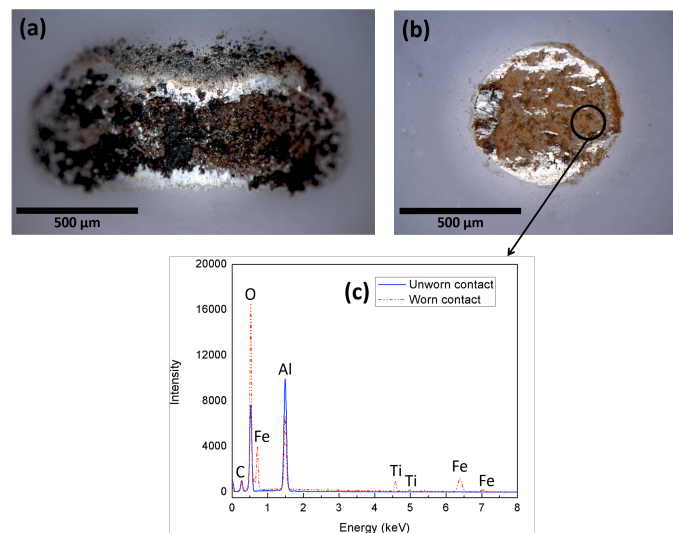
Figure 5.12: Optical microscope images of the counter surface of (a) CM100 and (b) CM30 coatings, and (c) EDS analysis of unworn and worn surfaces of the Al_2O_3 ball after the wear test.

5.4 Conclusion

Fe_3Al-based coatings reinforced with *in-situ* TiN, Fe_2B and TiB_2 precipitates were fabricated using a combination of high-energy ball milling and high velocity oxy-fuel processes. The microstructure of the as-milled powders evolved during the HVOF spraying as confirmed by X-ray analysis of the coatings that revealed evidence of nitride and boride phases in the iron aluminide matrix.

The microhardness of the HVOF coating prepared from the pure Fe_3Al was increased 3.3 times and its initial wear rate 3×10^{-4} mm^3/Nm, was decreased by about three orders of magnitude when 10 wt% of BN and 20 wt% of Ti were added to Fe_3Al powder and milled at high-energy for 10 h. We found a close relationship between the microhardness and the wear behavior of the HVOF coatings.

Inspection of the wear tracks of the pure Fe_3Al coating revealed the presence of micro-plowing, micro-crack, wear-debris, and localized hole formation suggesting that repeated tensile and compressive stresses induced by the hard Al_2O_3 counterpart led to material removal by fatigue wear. For composite coatings, abrasive wear was shown to be the predominant degradation mechanism since the hard ceramic particles from the coating materials acted as abrasive components during the wear test. EDS analysis of the contact area on the counterpart body provided evidence of coating materials transfer indicating that adhesive wear has played a role in material loss.

5.5 Acknowledgments

CHAPTER 6   ARTICLE 3: WEAR BEHAVIOR OF Fe₃Al-TIN-TIB₂ HVOF COATINGS: A COMPARATIVE STUDY BETWEEN IN SITU AND EX SITU POWDER PROCESSING ROUTES

Fabrice Pougoum[a], Ludvik Martinu[a], Jolanta-Ewa Klemberg-Sapieha[a,*]

Sylvio Savoie[b], Robert Schulz[b]

[a]Engineering Physics Department., Polytechnique Montréal, Montréal, QC, Canada H3C 3A7

[b] Materials Science Department. Institut de recherche d'Hydro-Québec (IREQ), Varennes, QC, Canada, J3X 1S1

[*] Corresponding author.

Email address: jolanta-ewa.sapieha@polymtl.ca (J. -E. Klemberg-Sapieha)

Abstract

In the present study, the tribological properties of High Velocity Oxy-Fuel (HVOF) coatings prepared from Fe₃Al-based composite powders were investigated. The iron aluminide matrix of the composite powders was reinforced with TiN and TiB₂ particles made using two different processing routes: a) an *in situ* method where fine ceramic particles were formed in the matrix by the reaction between Ti and BN, and b) an *ex situ* method where preformed coarse TiN and TiB₂ particles were added to the matrix. The tribo-mechanical performance of the coatings was assessed using indentations and pin-on-disc wear tests. Compared to *ex situ* samples*,* the Fe₃Al-based coatings strengthened with *in situ* ceramic particles exhibit higher microhardness and wear resistance regardless of the sliding velocity. The presence of voids, cracks and scratches/grooves in the wear track of the *in situ* coatings and the coating material transferred to the corresponding counterpart suggest that coatings with fine reinforcing particles fail predominantly via delamination and adhesive wear mechanisms. In the case of the *ex situ* coatings, the presence of a significant amount of hard ceramic particles within the wear track indicates that abrasive wear plays a dominant role in the degradation mechanism. Oxidation wear also contributed to material removal at high sliding velocity since transfer materials inside the

wear track contain a high oxygen content compared to the unworn region regardless of the coating type.

Keywords: Metal ceramic composites; ball milling; In situ/Ex situ powder synthesis; iron aluminides; HVOF; Wear

6.1 Introduction

Metal matrix composites (MMC) have been widely recognized as materials of interest for wear protection due to their special microstructure and excellent mechanical properties [151]. The combination of the metallic matrix and the secondary phases give rise to enhanced properties of the resulting material [152]. MMC are promising potential candidates for replacing conventional bulk steels or hard chrome in many areas of applications such as aerospace, automotive, hydroelectricity or manufacturing industries [12].

Among potential matrix candidates, special attention has been given to low-cost and low-density materials such as iron aluminides. These materials are environmentally friendly and demonstrate good corrosion and oxidation resistance at high temperature [23]. However, their poor mechanical and tribological performances have restricted their use in the fields where wear-resistance is particularly important. It has been shown previously, that the modification of microstructure of iron aluminides leads to improvement of mechanical properties [15, 18].

Iron aluminides are thermodynamically compatible with several borides, carbides, nitrides and oxides [24, 36]. The iron aluminide (Fe_3Al) MMC including ceramic inclusions exhibit unique microstructure and excellent mechanical properties such as high hardness, high strength and high fracture toughness [27, 140].

High-Energy Ball Milling (HEBM) is widely used to manufacture MMC materials [111, 153]. In this process, powder particles are plastically deformed, fragmented and repeatedly cold-welded in order to form materials with fine and homogeneous microstructure in which secondary phases are uniformly dispersed. The technique allows one to manufacture composites with a relatively defect-free matrix/reinforcement interfaces [111].

Thermal spray techniques are often used for producing thick coatings that exhibit interesting wear resistance characteristics [154]. In many applications subjected to hostile environmental conditions, thick protective coatings are preferred compared to thin films prepared

using PVD or CVD for extended lifetime protection. Among the fabrication techniques, High Velocity Oxy-Fuel (HVOF) deposition can be used to obtain dense protective coatings on different types of substrates [155]. In the high-pressure HVOF process, such as the one used in this work, oxygen and kerosene are mixed and ignited to form a hot and high-pressure gas into which powder particles are injected. The particles are heated and expelled at about three times the speed of sound toward the substrate, and coatings are formed from the successive buildup of melted or semi-melted splats [155].

Ball milling followed by subsequent heat treatment has been used to prepare Fe_3Al-based composite powders reinforced with *in situ* formed ceramic particles. Specifically, it has been demonstrated that the microstructure and the mechanical properties of the hybrid Fe_3Al/(AlN, Fe_2B) powders could be preserved during the HVOF deposition [36]. Improved tribo-mechanical properties of these coatings were attributed to the fine dispersion of *in situ* precipitated AlN and Fe_2B particles within the Fe_3Al matrix. Using an *ex situ* approach, Peng *et al.* [101] have shown that the room temperature toughness and flexural strength of the ball milled then hot-pressed Fe_3Al-based composite were improved by the addition of preformed ZrO_2 particles. The low thermal expansion mismatch between the Fe_3Al matrix and the coarse ZrO_2 particles, and the stress-induced transformation of ZrO_2 particles were reported to be particularly beneficial [101].

Both *in situ* and *ex situ* approaches lead to enhanced mechanical and tribological properties of Fe_3Al-based composites. However, little has been done to sufficiently identify which fabrication route can effectively enhance the tribo-mechanical properties of such materials.

In the present work, we compare the microstructure and the mechanical properties of the Fe_3Al-based composite coatings prepared using powders with *in situ* strengthened and *ex situ* preformed ceramic particles namely titanium nitride and titanium diboride. The wear behavior of the HVOF coatings are compared and discussed with respect to different sliding test conditions.

6.2 Materials and Experimental Methods

6.2.1 Powder preparation

In the *in situ* approach, the initial powder mixture consisted of 70 wt% of pre-alloyed iron aluminide (Fe_3Al: 97.5 % pure with ~2% of Cr from Ametek), 10 wt% of boron nitride (BN: 98% pure from Lower Friction) and 20 wt% of titanium (Ti: 99.4 % pure from Alfa Aesar). The mean

particle size of BN and Ti was 5 and 150 μm, respectively. This powder mixture was milled for 10 h using the HEBM technique, and is labeled M30 in the following text. More details on the fabrication of the composite powders are described in [37].

Following the initial HEBM, the as-milled M30 powder; was heat-treated in a furnace at 1000 °C for 2 h under vacuum (10^{-6} mbar) to form TiN and TiB_2 particles in the matrix; it is labeled AM30 in the following text below. The heating rate was 7 °C/min, and a cooling rate of 4 °C/min was used from 1000 °C to 500 °C. Thereafter, the heat-treated powder was re-milled at high energy (1000 rpm) for 5 h; it is labeled In-M30. This fabrication approach is referred to as the *in situ* synthesis route because the hard ceramics (TiN and TiB_2) are formed during the powder fabrication process. The re-milling time of 5 h was chosen in order to obtain a reasonable amount of powder (after sieving) with an average particle size between 20 and 50 μm which is adequate for the HVOF deposition.

During the *ex situ* approach, X-ray diffractograms of the AM30 samples were used to evaluate the amount of TiN and TiB_2 materials in the composite powder. An equivalent amount of preformed titanium nitride (TiN: 99.8 % pure) and titanium diboride (TiB_2: 99.5 % pure) particles from Alfa Aesar was ball milled at high energy (1000 rpm) with the Fe_3Al powder. The initial size of the TiN and TiB_2 particles was <10 μm and 44 μm, respectively. The powder mixture is labeled Ex-M30 in the following text. To monitor the evolution of the Ex-M30 particle size as a function of milling time, a small amount of powder (~1 g) was collected every hour and analyzed using the Horiba LA 900 Particle Size Analyzer. The HEBM of the Ex-M30 powder was stopped (after 4 h) when the average particle size of the as-milled powder was identical to that of the In-M30 powder (i.e. 30 – 40 μm).

6.2.2   Coating preparation

The HVOF coatings were fabricated using a Praxair J-P 8000 HP-HVOF system mounted on an ABB robot arm and controlled by a computer using the deposition conditions described in Table 1. The composite powders were deposited onto flat 304 stainless steel substrates previously sandblasted using 60 grits alumina particles and cleaned with methanol. The HVOF gun was scanned at a speed of 10 cm/s for a total of ten passes. The gun was displaced by 10 mm after each pass. The coatings are labeled with a "C" in front of the names of the corresponding powder.

For example, In-CM30 is referred to the HVOF coating prepared from the In-M30 composite powder. More details on the HVOF coating process can be found in [36]

Table 6.1: Experimental conditions for HVOF deposition.

Spray parameters	Value
Standoff distance (cm)	38
Nozzle length (cm)	15
Nozzle diameter (mm)	11
Chamber pressure (kPa)	700
Oxygen flow rate (slpm)	890
Kerosene flow rate (l/h)	23.5
Equivalent oxygen/kerosene ratio	1.1

6.2.3 Microstructural analysis

X-ray diffractograms of composite powders and of their corresponding HVOF coatings were obtained using a Brüker D8 DISCOVER diffractometer in a $\theta/2\theta$ configuration. The diffractometer, operated at 40 kV and 40 mA, was equipped with a copper source (λ: 1.5406 Å), a Gobel mirror, a divergent slit of 0.6 mm and a LynxEye detector set with soller slit (2.5 °). The diffractograms were acquired from 20° to 90 ° in 2θ, with a step size of 0.051 ° and a time per step of 0.5 sec. The phase quantification was obtained by Rietveld refinement using Topas 4.2 software (Brüker AXS).

Surface morphology and chemical composition of the powders and the HVOF coatings were obtained on polished cross-sectional surfaces using a 7200 JEOL scanning electron microscope (SEM) equipped with energy dispersive X-ray spectroscopy (EDS Inca X-max 80 Oxford) operating at 15 kV.

6.2.4   Mechanical characterization

The depth-sensing indentation measurements on the surface and on the cross-section of the HVOF coatings were performed using a Triboindenter (TI950 Hysitron) equipped with a Berkovich diamond tip calibrated with a quartz standard. Matrices of 20 x 20 points evenly spaced by 5 μm were used with a trapezoidal load function: the load was linearly increased up to a maximum of 2 mN for 5 sec, kept constant for 2 sec, and linearly decreased for 5 sec. The maximum penetration depth was about 150 nm. Measurements were obtained from two distinct and randomly chosen regions of the polished surfaces of the specimen (because of the heterogeneity of the coating), and a minimum of 300 indents was considered for statistical analysis. The nanoindentation technique was chosen in order to measure the mechanical properties of the individual phases of the coatings in a small volume.

In order to evaluate the influence of several phases on the mechanical properties of the coatings, the microindentation method was used as well. The volume of interaction of material under microindentation is much higher than in nanoindentation. For microhardness measurements, a CSM Micro-Combi tester equipped with a Berkovich diamond tip was used, and the applied load was linearly increased up to a maximum of 3 N, kept constant at 3N for 30 sec, then linearly decreased. The maximum penetration depth was ~5 μm. Note that the HVOF coatings were thick enough (few hundreds μm) to avoid the influence of the substrate. The average microhardness value, H, was obtained from a matrix of 25×25 points evenly spaced by 150 μm conducted on the polished surface of the coatings using the Oliver and Pharr method [123]. The error bars on the average H values are the standard deviation from a minimum of 200 indentation measurements.

6.2.5   Sliding wear tests

A pin-on-disc tribometer operated in dry conditions at room temperature with a relative humidity between 45 and 50 % was used to measure the wear rate of the HVOF coatings according to ASTM-G99. The normal load (F) was fixed at 5 N, and the sliding distance was maintained at 1000 m. The sliding velocity (v_s) was varied between 20 and 60 cm/s. The diameter of the wear track ring was 9 mm, and a new alumina (Al_2O_3) ball of 4.75 mm in diameter was used for each test. These test conditions were chosen in order to adequately assess

the wear behavior of the HVOF coatings and to compare results with previous studies [36, 37]. During the wear test, the tangential force, F_T, was continuously recorded and the friction coefficient, μ, was obtained from $\mu = F_T/F$. The average value of μ was obtained from the stable segment of the friction coefficient curves.

The wear rate, K, was calculated using the formula $K = V/F{\times}LK = V/F*L$, where V is the total volume of material removed or displaced upon interaction between the hard Al_2O_3 ball and the coating. The average cross-sectional surface of the ring was obtained from a minimum of 20 measurements at different positions of the wear track ring, and the error bars on the average wear rate are the standard deviation from these measurements.

The wear mechanisms of the HVOF coatings were identified from the morphology of the top surface and longitudinal cross-section of the wear track. Moreover, the SEM micrographs and EDS analysis of the wear track and the worn contact of the counterpart provided additional information necessary for the assessment of the degradation mechanisms.

6.3   Results and Discussion

6.3.1   Microstructure of the composite powders

Figure 6.1 presents X-ray diffractograms of the as-milled (M30) and of the as-annealed (AM30) powders prepared from a mixture of 70 wt% of Fe_3Al (ICDD: 00-045-1203), 10 wt% of BN and 20 wt% of Ti powders ball milled for 10 h. The presence of TiN (ICDD: 00-038-1420) and TiB_2 (ICDD: 04-010-8470) peaks in the diffractogram of the AM30 composite powder is an evidence that phase transformation occurred in the powder during heat-treatment. The evolution of the microstructure of the M30 powder mixture during HEBM and the formation mechanism of the TiN and TiB_2 phases in an Fe_3Al matrix are discussed in [37].
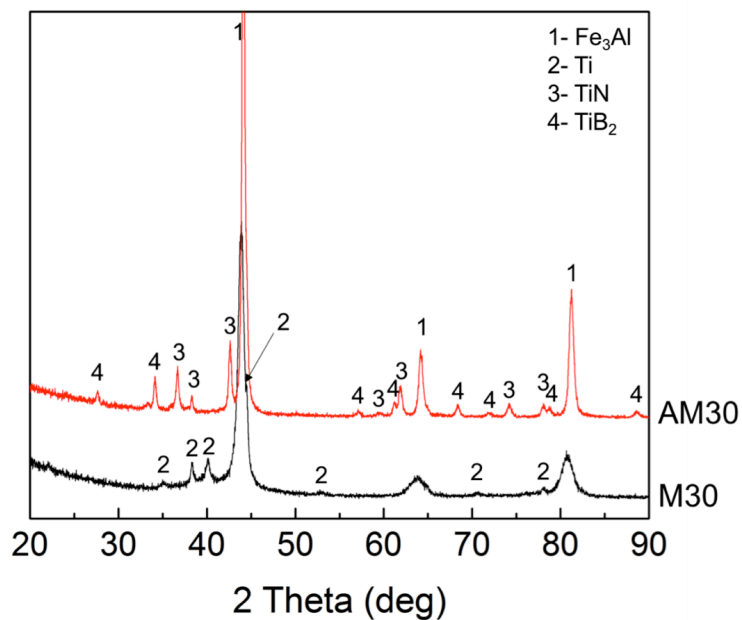
Figure 6.1: X-ray diffractograms of the as-milled (M30) and heat-treated powder mixture (AM30) of 70 wt% of Fe_3Al ball milled for 10 h with 10 wt% of BN and 20 wt% of Ti.

Rietveld analysis of the AM30 diffractogram reveals that about 15 wt% of TiN and 15 wt% of TiB_2 phases were formed *in situ* within 70 wt% of Fe_3Al matrix during thermal treatment.
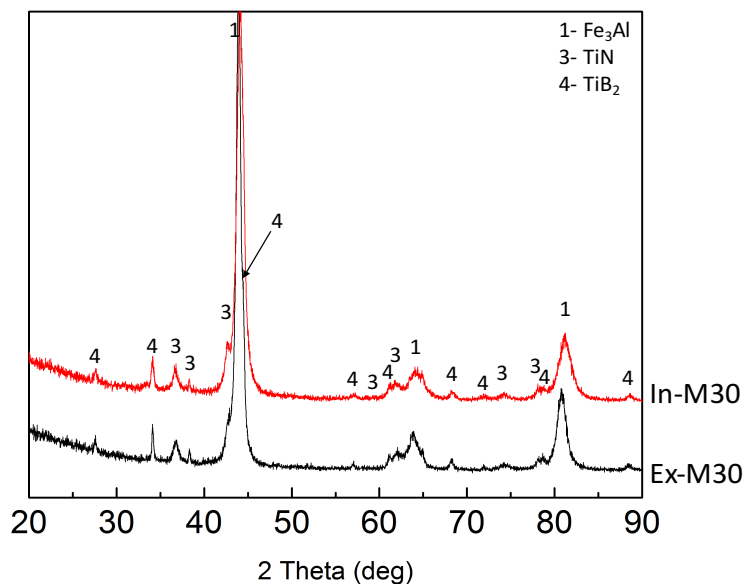
Figure 6.2: X-ray diffractograms of the composite powders prepared from Fe_3Al matrix reinforced with *in situ* and *ex situ* formed TiN and TiB_2 particles.

Using this information, an *ex situ* sample with the same amount of preformed ceramic particles was prepared. In Figure 6.2, the X-ray diffractogram of the AM30 composite powder re-milled for 5 h at high energy (In-M30) is compared to that of the Ex-M30 powder mixture prepared from pre-alloyed Fe_3Al ball milled for 4 h with preformed TiN and TiB_2 (commercial powder) particles. Both samples have about the same amount of ceramics. The diffractograms reveal no differences between the structure of the Ex-M30 and In-M30 composite powders except, perhaps, for the width of the different peaks, indicating a different size of the crystallites in each sample.

The morphology and particle size distribution of the In-M30 and Ex-M30 powder samples are presented in Figure 6.3. The cross-sectional surface of powder particles reveals that the In-M30 composite contains very small ceramic inclusions (<300 nm) homogeneously dispersed within the Fe_3Al matrix (Figure 6.3a). On the contrary, the Ex-M30 powder contains larger ceramic particles (<3 μm), and they are randomly distributed in the Fe_3Al matrix (Figure 6.3b). Both composite powders have about the same particle size distribution after sieving prior to the HVOF deposition (Figure 6.3c).
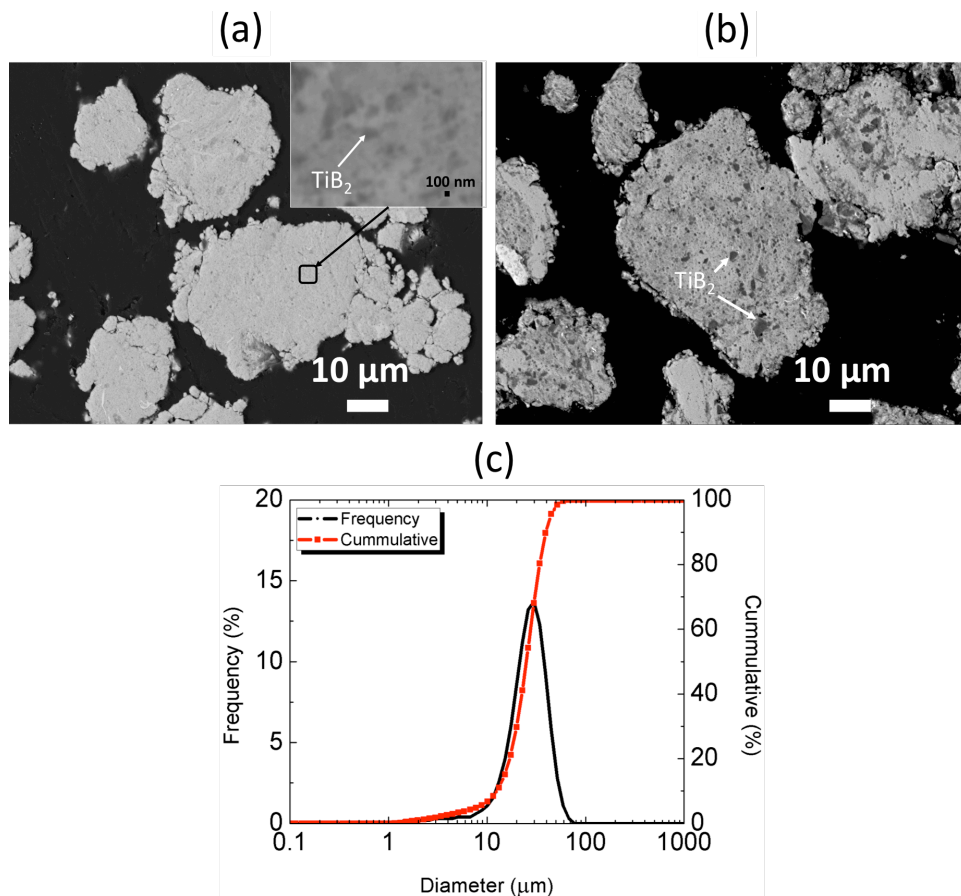
Figure 6.3: SEM micrographs of the cross-sectional surface of powders: (a) Fe_3Al milled for 10 h with 10 wt% of BN and 20 wt% of Ti and heat-treated at 1000 °C for 2 h and re-milled for 5 h, (b) Fe_3Al milled for 4 h with preformed TiN and TiB_2 powders, and (c) the corresponding particle size distribution of powders prior to HVOF deposition.

6.3.2   HVOF coatings

6.3.2.1 Microstructure

Figure 6.4 presents X-ray diffractograms and SEM micrographs of HVOF coatings prepared from the In-M30 and Ex-M30 composite powders. It can be seen in Figure 6.4a that the phase composition (crystallography) of composite powders was preserved during HVOF deposition. This observation can be attributed to the thermodynamic stability of the ceramic phases and the chosen deposition conditions (Table 6.1). Moreover, the peaks due to the ceramic phases TiN and TiB_2 are better defined and the full width at half maximum of the peaks is smaller which is comparable to the corresponding powders shown in Figure 6.2. This indicates

that reduction of defects and crystal growth took place during HVOF deposition [98]. The disappearance or broadening of the peaks due to ceramic phases arise as a result of internal strains developed in the powder particles by rapid heating and cooling (solidification) [156].

SEM micrographs of the coating cross-section reveal significant differences. In Figure 6.4b, the In-CM30 coating exhibits a microstructure in which very small ceramic precipitates (see the encircled region) are homogeneously dispersed in the Fe_3Al matrix. At high magnification, this microstructure is similar to that of the corresponding powder shown in Figure 6.3a. On the contrary, the Ex-CM30 coating shows large reinforcing particles randomly distributed in the Fe_3Al matrix (Figure 6.4c). The inter-particle distance is higher in the Ex-CM30 coating compared to In-CM30.
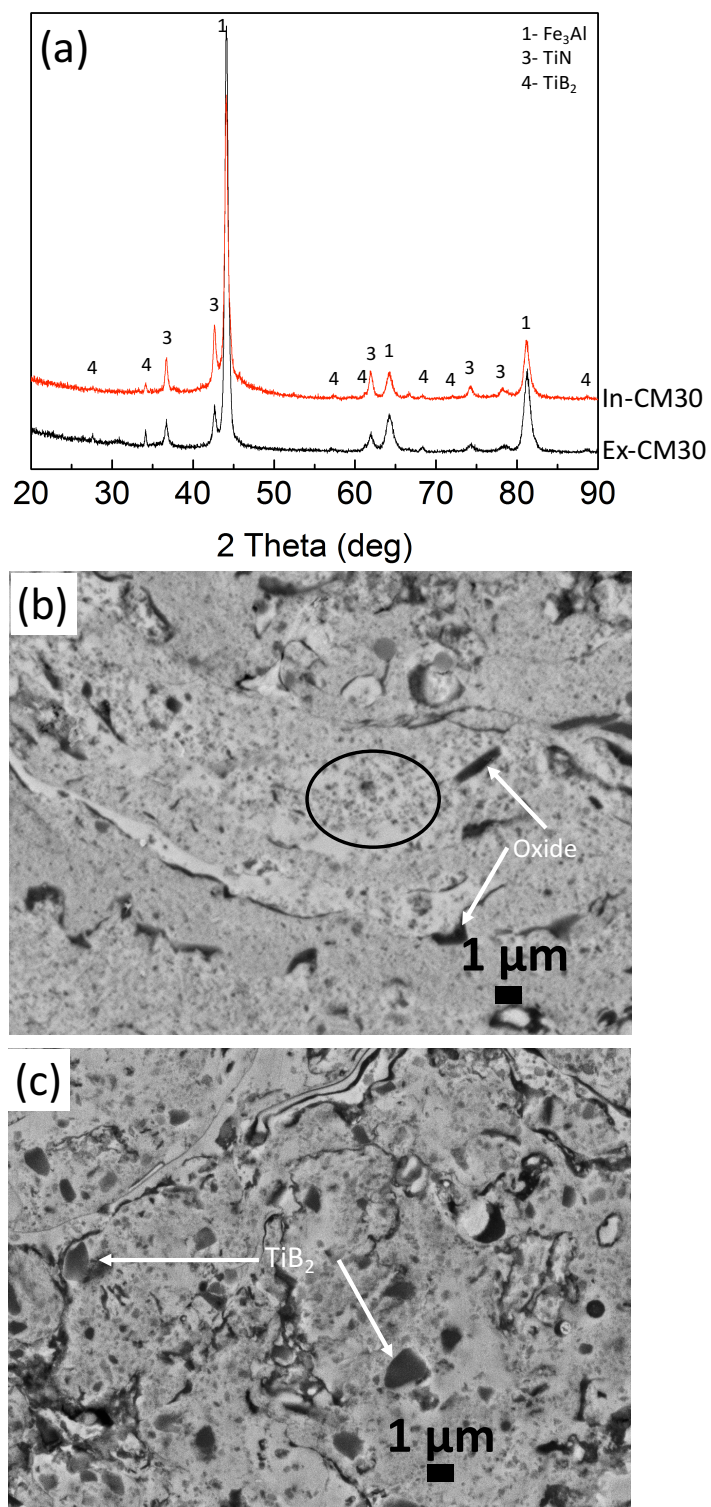
Figure 6.4: (a) X-ray diffractograms of the HVOF coatings prepared from Fe_3Al-based composites reinforced with *in situ* precipitated and *ex situ* formed TiN and TiB_2 particles, and SEM micrographs of cross-sectional surface of (b) In-CM30, and (c) Ex-CM30 HVOF coatings.

6.3.2.2 Mechanical properties

The mechanical properties of a composite depend on the amount, size and distribution of secondary phases in the material as well as the characteristics of internal interfaces. The microhardness (*H*) values for the In-CM30 and Ex-CM30 coatings are compared in Figure 6.5. The *H* value of In-CM30 (9.3 GPa) is about 34 % higher compared to Ex-CM30 (6.5 GPa). This result can be attributed to the microstructure of the coatings described above. When the sizes of the ceramic particles are in the nanometer range, the relative area of interfaces between the matrix and reinforcing components increases. Inter-particle distances are small; this can help to delay and/or stop crack propagation during indentation. On the contrary, large portions of the soft Fe_3Al matrix decrease the mechanical properties of the Ex-CM30 coating as reflected by the lower H value of the Ex-CM30 coating. Note that the microhardness of the HVOF coating prepared from unreinforced Fe_3Al was found to be 4.3 GPa [37].

The distribution of the microhardness values for the In-CM30 and Ex-CM30 coatings is shown in Figure 6.6a. Both coatings display a Gaussian-type unimodal distribution with an average *H* value of ~9.3 and ~6.5 GPa for In-CM30 and Ex-CM30, respectively. In Figure 6.6b, the distribution of the elastic modulus, *E*, obtained from microindentation measurements, shows a similar behavior (i.e., unimodal distribution) as in the case of the *H* values. The average *E* value is higher in the case of the In-CM30 coating reflecting the fact that the stiffness is higher when the size of the reinforcing particles is small (number of grain boundaries increases).
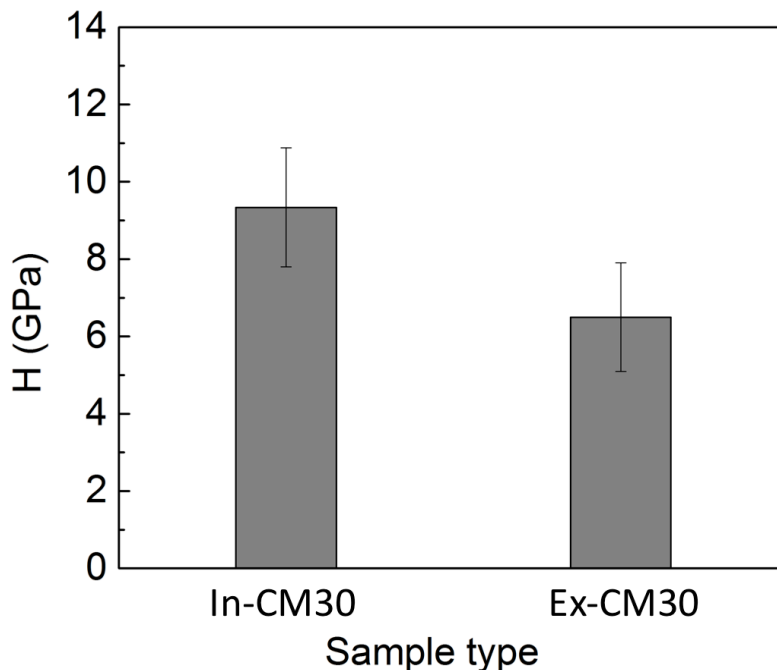
Figure 6.5: Comparison of the microhardness of the coatings.

For comparison, the nanohardness values presented in Figure 6.6c exhibit a much broader and unimodal distribution in the case of the In-CM30 coating, whereas a distinct bimodal distribution is observed for the Ex-CM30 sample. To some extent, this observation indicates that the microstructure of the In-CM30 coating is homogeneous on the nanoscale compared to the Ex-CM30 coating. In the former coating, the effect of individual phases is less apparent as opposed to the latter one where the nanoindentation response from the soft Fe_3Al matrix and the hard-secondary phases is noticeable. However, a clear bimodal distribution of E is not observed in the case of the Ex-CM30 coating probed by nanoindentation (Figure 6.6d). This could be due to the fact that E measured by nanoindentation depends on a much larger volume of material and as a result, the measurement reflects mechanical properties of a large volume compared to the size of the imprint. However, the width of the distribution of E for the Ex-CM30 coating is much larger when measured by nanoindentation compared to microindentation indicating the fact that inhomogeneity in the Ex-CM30 coating are better observed with small tip size. As in the case of microindentation, E value of the In-CM30 coating measured by nanoindentation is higher compared to the Ex-CM30 sample which, as mentioned before, indicates that the Fe_3Al matrix reinforced by a distribution of fine ceramic inclusion is much stiffer.

Figure 6.6e shows a typical micro-indent imprint on a polished surface of the Ex-CM30 coating. The size of this imprint ($\sim$1050 μm^2) is at least 100 times larger than the maximum size of reinforcing particle ($<$10 μm^2) and, as a result, microindentation represents average mechanical properties. On the other hand, the size of the nano-indent imprint ($\sim$0.1 μm^2) is smaller than the average size of the ceramic inclusions in the Ex-CM30 sample; for this reason, nanoindentation can help to distinguish the properties of both phases. Therefore, in the Ex-CM30 coating, where inclusions are randomly dispersed and the inter-particle distance is larger, individual phases are likely to be probed during nanoindentation. On the contrary, the nanoindentation response for *in situ* coatings is a contribution from the Fe_3Al matrix and of the ceramics inclusions in a small volume of the material. Thus, the broad distributions are a consequence of the small imprint, small inter-particle distances, and uniform dispersion of inclusions in the matrix of *in situ* coatings.

Considering that ceramic contents are about the same in both coatings, these results suggest that the size and distribution of reinforcing agents in a material have a large effect on their mechanical properties.
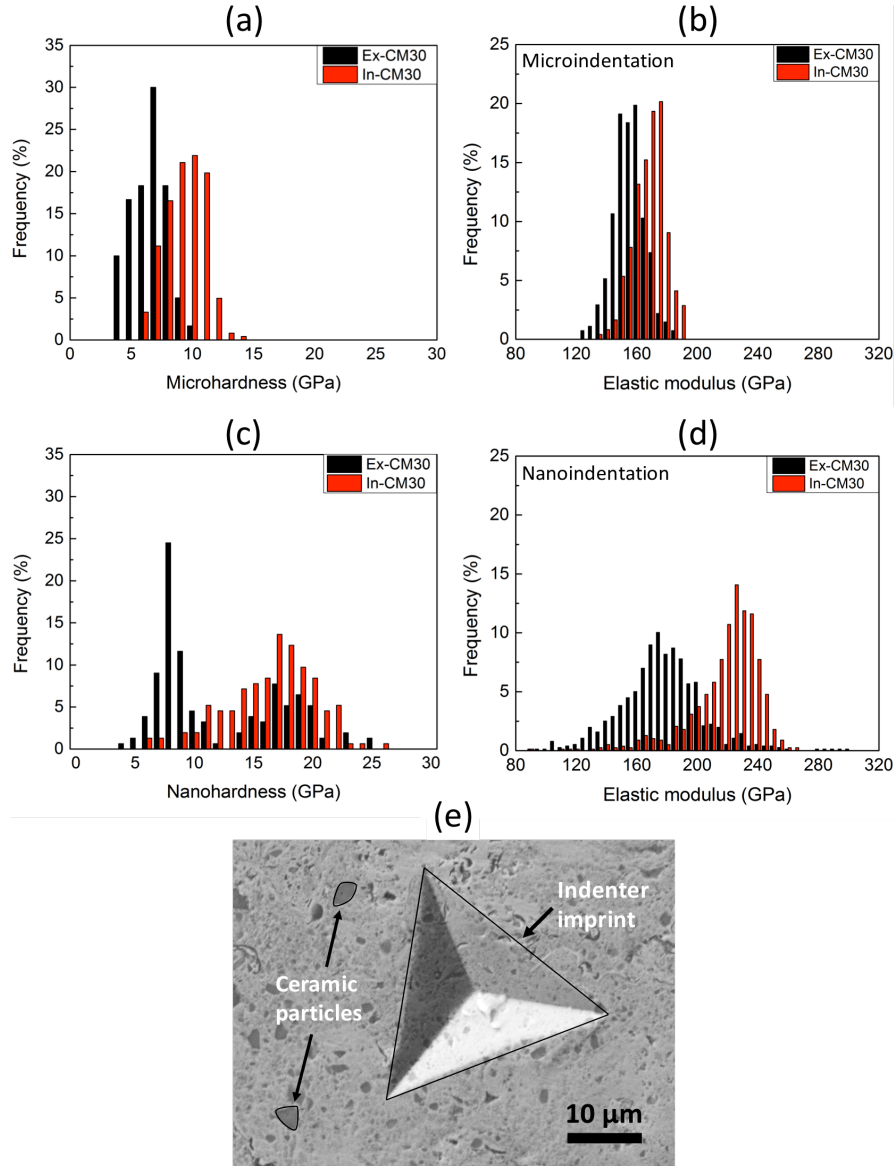
Figure 6.6: Distribution of hardness and elastic modulus values obtained from microindentation: (a) microhardness and (b) elastic modulus; and from nanoindentation: (c) nanohardness and (d) elastic modulus of HVOF coatings. (e) is a micrograph of a micro-indent imprint on a polished surface of the Ex-CM30 coating.

6.3.2.3 Wear behavior

The coefficient of friction, μ, of the In-CM30 and Ex-CM30 coatings at different sliding velocities, v_s, as a function of sliding distance is presented in Figure 6.7. After a rapid increase, up to 0.7 at the start of the test, the value of μ of the In-CM30 sample tends to slowly decrease in

time and it finally reaches a value of 0.6 for $v_s = 40$ cm/s (Figure 6.7a). For other sliding velocities conditions, the value of μ seems to fluctuate around its average (~0.6) until the end of the wear test. For Ex-CM30 coatings, μ shows less variation and remains stable after the initial rise (Figure 6.7b) regardless of v_s. However, the average value of μ (~0.7) is slightly higher at $v_s = 40$ cm/s compared to other v_s where μ varies between ~0.65 and 0.6. Interestingly, the In-CM30 and the Ex-CM30 coatings exhibit marginally lower value of μ (0.6) at 60 cm/s. The error (standard deviation), obtained from μ data of three tests is approximately 0.02.

These behaviors of μ with v_s and with the sliding distance could be associated with changes occurring at the surfaces of the coating and of the counterpart as the wear test progresses.
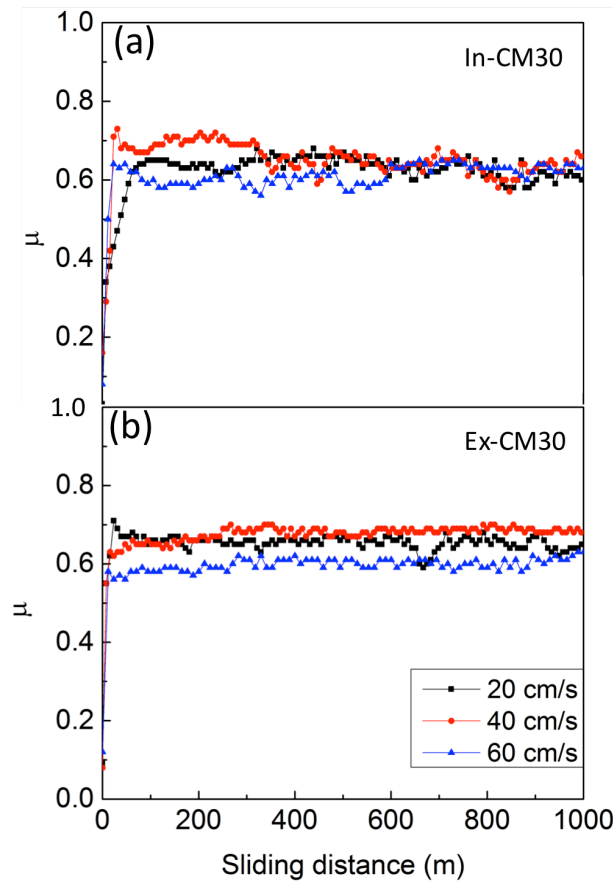
Figure 6.7: Coefficient of friction of the In-CM30 and Ex-CM30 coatings with respect to v_s as a function of the sliding distance.

Figure 6.8 presents the wear rate, K, as a function of v_s of the In-CM30 and Ex-CM30 coatings. K of the In-CM30 coating is lower regardless of the v_s. This observation is in agreement with the fact that the In-CM30 coating (H = 9.3 GPa) is harder than the Ex-CM30 sample (H = 6.3 GPa). Thus, the wear resistance of the HVOF coatings scales with the microhardness. This behavior has also been observed in similar coating systems and under similar wear test conditions, where the unreinforced Fe_3Al coating (H = 4.3 GPa) exhibited a K = 3×10^{-4} mm^3/Nm$K = 3 \times 10^{-4}\ mm^3 N^{-1} m^{-1}$ at v_s = 15 cm/s [37]. As discussed above, the In-CM30 coating exhibits a better resistance to crack propagation because of the multiple interfaces within its microstructure. On the contrary, the large areas of unreinforced Fe_3Al matrix in Ex-CM30 seems to weaken the mechanical strength of the coating and favor fast material removal during wear tests. Moreover, a faster wear process might be expected if large ceramic particles detach from the coatings and are entrapped between sliding surfaces [36].
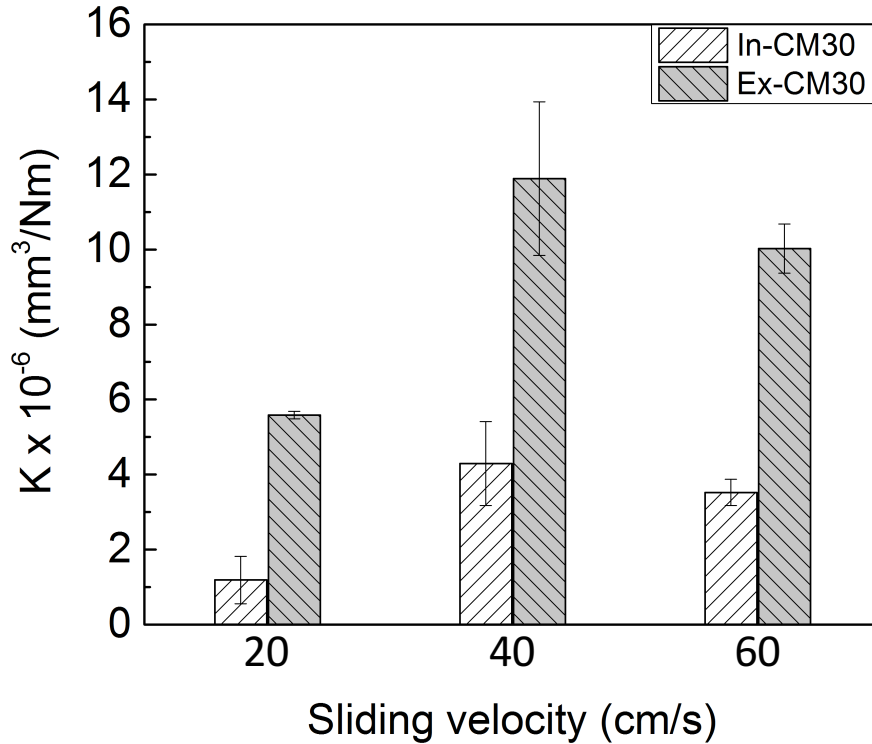
Figure 6.8: Wear rate as a function of sliding speed of the In-M30 and Ex-M30 coatings.

K increases when v_s changes from 20 to 40 cm/s suggesting that the wear mechanisms change as well (Figure 6.8). It has been shown that the increase of K with respect to v_s can be attributed to the delamination of the surface layer [157]. Inspection of the wear track of both coatings after the wear test at 40 cm/s reveals the presence of voids and debris irrespective of the coating (Figure 6.9). This suggests that worn materials likely remained inside the wear track and influenced the friction behavior. As shown in Figure 6.9a, the size of the particles inside the wear track of the In-CM30 coating is smaller compared to Ex-CM30 (Figure 6.9b).

At $v_s = 60$ cm/s, K decreases regardless of the coating type. Often, the increase of v_s can lead to an increase of the contact temperature between two surfaces in relative motion [55]. Consequently, oxidation of the contact surface is likely to occur at high v_s, and the oxide may act as a solid lubricant to protect surfaces from further material removal [53]. Thus, the average value of μ of the In-CM30 and Ex-CM30 coatings at $v_s = 60$ cm/s is marginally lower (~0.6) compared to other v_s values (Figure 6.7). Note that the wear rate at $v_s = 60$ cm/s decreases at the same rate compared to $v_s = 40$ cm/s regardless of the HVOF coating. The friction behavior described above suggests that both coatings experienced distinct degradation mechanisms as suggested by their different wear performances shown in Figure 6.8.
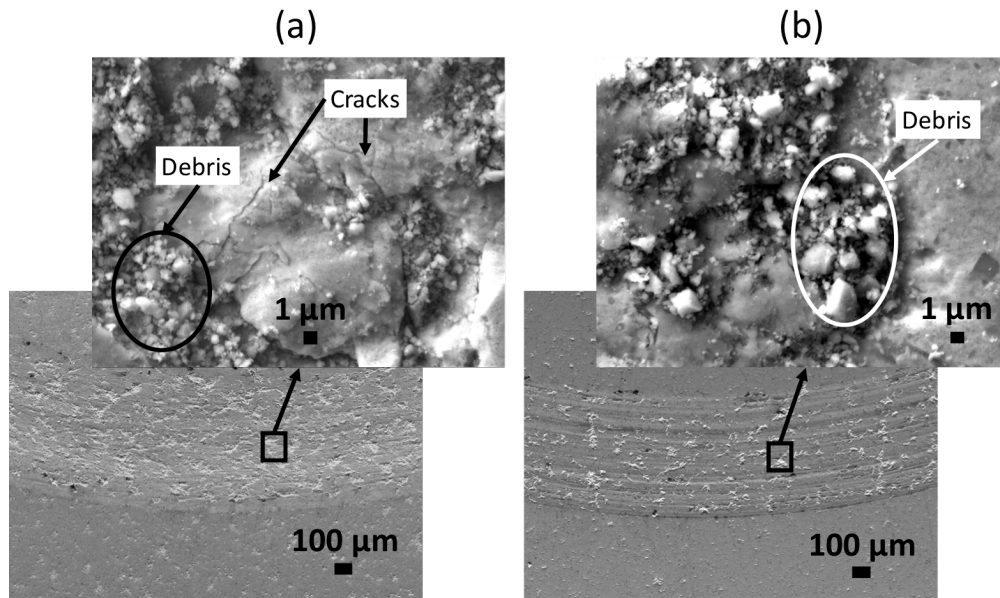
Figure 6.9: SEM micrographs of the top surface of the wear track of

(a) In-CM30, and (b) Ex-CM30 coatings at $v_s = 40$ cm/s.

6.3.2.4 Wear mechanisms

All the wear mechanisms described below, responsible for the degradation of the In-CM30 and Ex-CM30 HVOF coatings were present in both coating systems during wear tests. However, some wear mechanisms were predominant in the *in situ* coatings namely adhesive and delamination wear compared to abrasive and oxidation wear in the *ex situ* coatings. These mechanisms of material loss will be separately described in the following sections.

6.3.2.4.1 In situ coatings

6.3.2.4.1.1   Adhesive wear

SEM micrographs and the EDS compositional maps of the worn contact of the Al_2O_3 ball shown in Figure 6.10 reveal evidence of the worn region and the coating materials (e.g. Fe and N) transferred to the counterpart. These observations suggest that the coating and the counterpart materials have been transferred from one to the other during sliding and rubbing. This is an indication that beside other degradation mechanisms, adhesive wear also influenced the wear behavior of the In-CM30 coating.
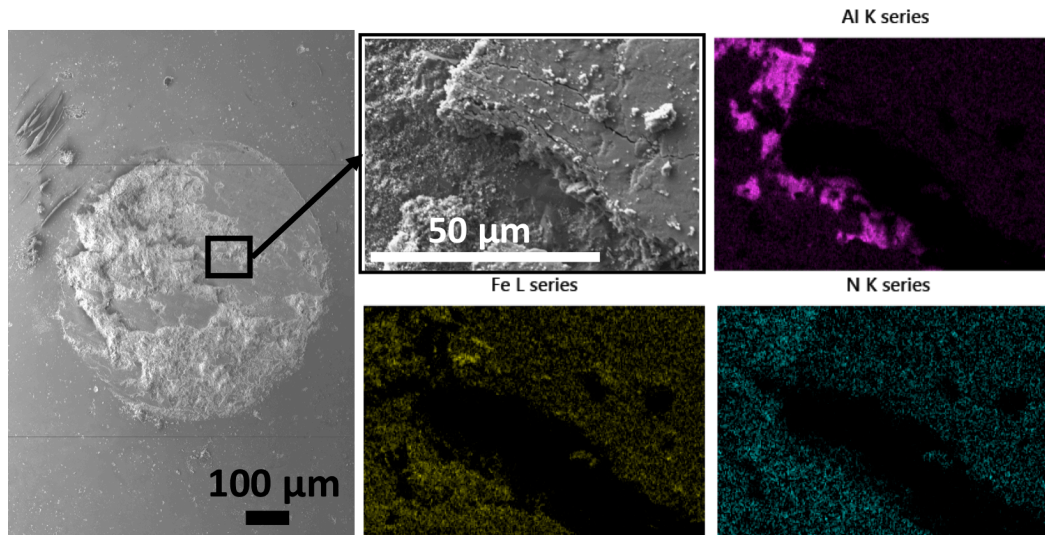
Figure 6.10: SEM image and EDS compositional maps of the worn Al_2O_3 ball after the wear test of the In-CM30 coating at $v_s = 40$ cm/s.

6.3.2.4.1.2 Delamination wear

Inspection of the top surface of the worn region of the In-CM30 coating reveals evidence of isolated voids inside the wear track (Figures 6.9a and 6.11a). It is likely that the exposure of the surface of the sample to cyclic tensile and compressive stresses induced by the hard Al_2O_3 ball during the wear test initiated cracks near defects in the contact area . A magnified SEM image of a void reveals the presence of cracks and debris which is an indication that the coating material was removed via delamination between the splats (Figure 6.11a). The cracks generated at the surface could propagate in the subsurface via weaker links (splat boundaries and porosities), and coating would fracture as shown in the encircled regions of the longitudinal cross-sectional surface of the In-CM30 coating (Figure 6.11b). Therefore, delamination with the formation of voids on the surface of the coatings follows when the shear stress is maximum in these regions. Random distribution of these voids within the wear track suggests that material removal on the surface of the In-CM30 coating was irregular.
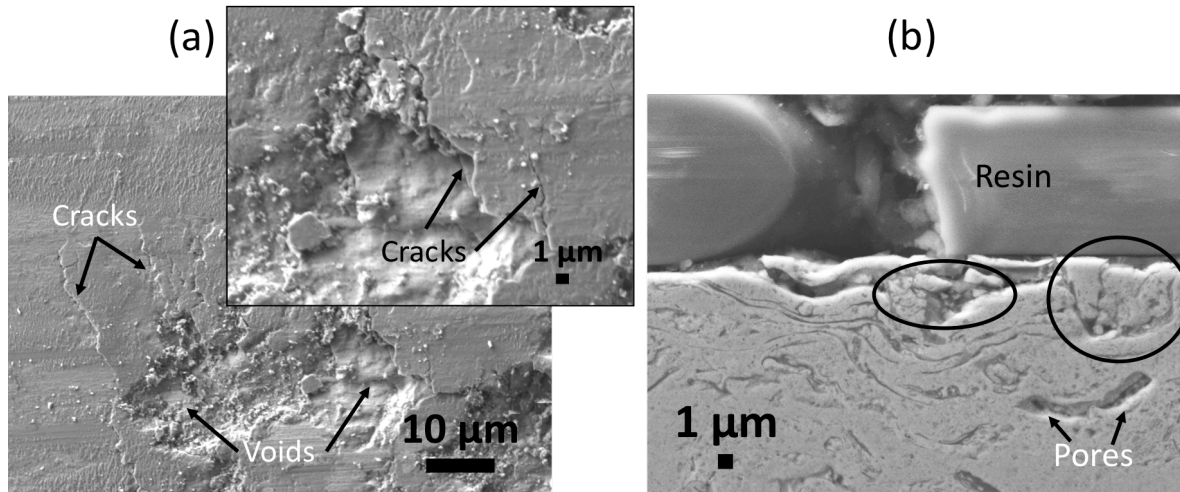
Figure 6.11: SEM micrographs of (a) the top surface of the wear track, and (b) the longitudinal cross-sectional surface of the wear track of the In-CM30 coating at $v_s = 40$ cm/s.

6.3.2.4.2 Ex situ coatings

6.3.2.4.2.1 Abrasive wear

The top surface of the wear track of the Ex-CM30 coating presented in Figure 6.9b reveals presence of parallel grooves and scratches. These features are also seen in the case of In-CM30 coatings but they are less pronounced (Figure 6.9a). Particles as large as ~3 μm are present inside the wear track of the Ex-CM30 coating. The size of these particles is similar to that of the preformed ceramic particles dispersed in the Fe_3Al matrix (Figure 6.4c). In addition, detailed inspection of the wear track of the Ex-CM30 coating shows fractured or loose TiB_2 particles with sharp edges as shown in Figure 6.12. The particles found inside the wear track in Figure 6.9b can originate from materials removed from the surface of the coating or from debris of the worn Al_2O_3 ball (Figure 6.13a).
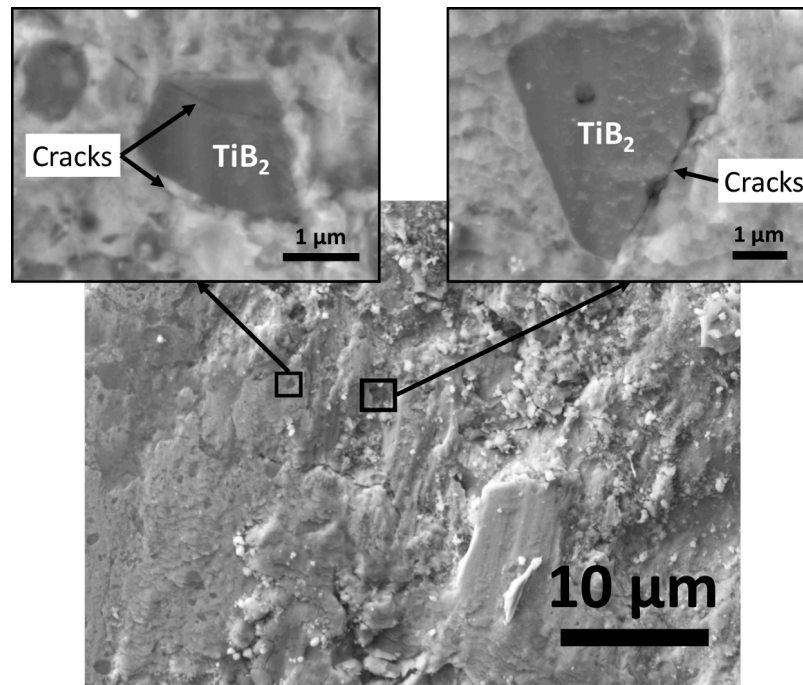
Figure 6.12: SEM micrograph of the top surface of the wear track of the Ex-CM30 coating at $v_s = 40$ cm/s showing fractured and loose TiB_2 particles detached from the matrix.

When the fractured particles with sharp edges get loose and entrapped between the surface of the Ex-CM30 coating and that of the Al_2O_3 ball they act as abrasive components and severe damage of the coating can be observed. This suggests that three-body abrasive wear is likely the main reason for the poorer wear performance of the Ex-CM30 coating since larger portions of unreinforced Fe_3Al matrix exposed to these particles can be subjected to high shear stresses. It has been shown that third-body particles with sharp edges can induce severe damage when they are entrapped between two surfaces in relative motion [53].

Abrasive wear likely contributed to the material loss since the analysis of the worn contact region of the Al_2O_3 ball also reveals large cracks and sharp asperities as shown in Figure 6.13a. The interaction between these asperities and the surface of the coating result in the removal of materials and formation of grooves inside the wear track as presented in Figure 6.13b.
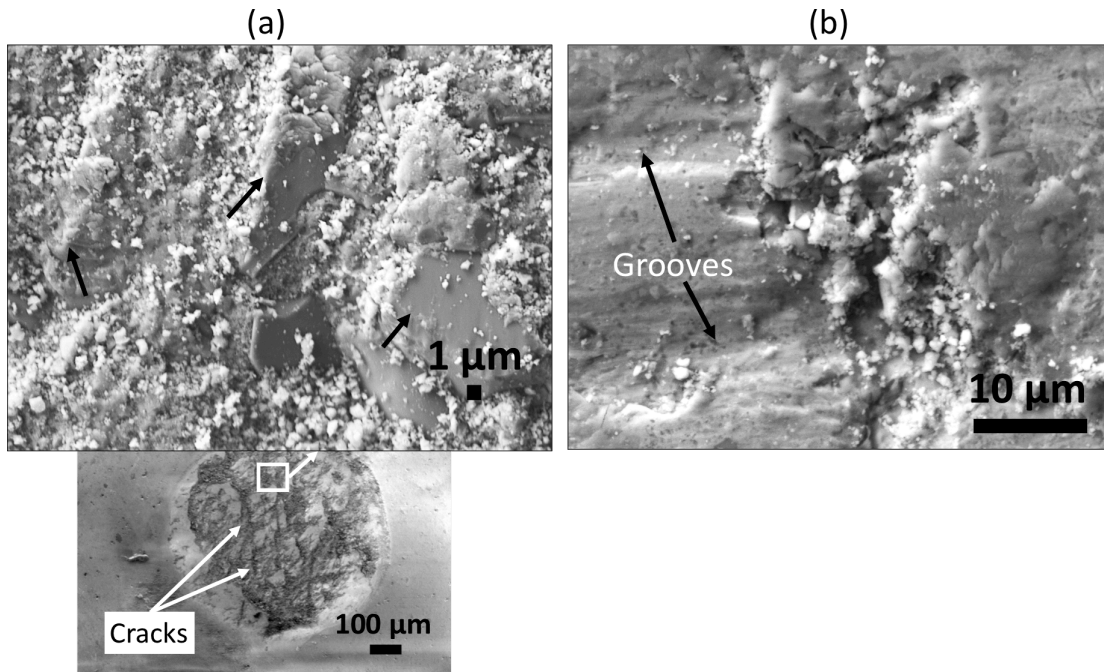
Figure 6.13: SEM micrographs of (a) the contact region of the worn Al_2O_3 counterpart showing cracks and large asperities (black arrows indicate the tip of the asperities), and (b) the top surface of the wear track of the Ex-CM30 coating showing grooves/scratches after a wear test at $v_s = 40$ cm/s.

6.3.2.4.2.2   Oxidation wear

Figure 6.14 presents an SEM image of the top surface of the wear track after a wear test at $v_s = 60$ cm/s and the chemical composition of the worn and unworn regions of the Ex-CM30 coating. The presence of transfer materials inside the wear track indicates that chemical changes (oxidation of the contacts) occurred between the surface of the coating and that of the Al_2O_3 ball. The amount of oxygen inside the wear track (region 1) is higher compared to the outside (region 2) suggesting that oxidation of the wear track has likely occurred. As discussed above, this phenomenon can be beneficial in tribology to lower the coefficient of friction and consequently to decrease the wear rate [55] as shown in Figure 6.8.
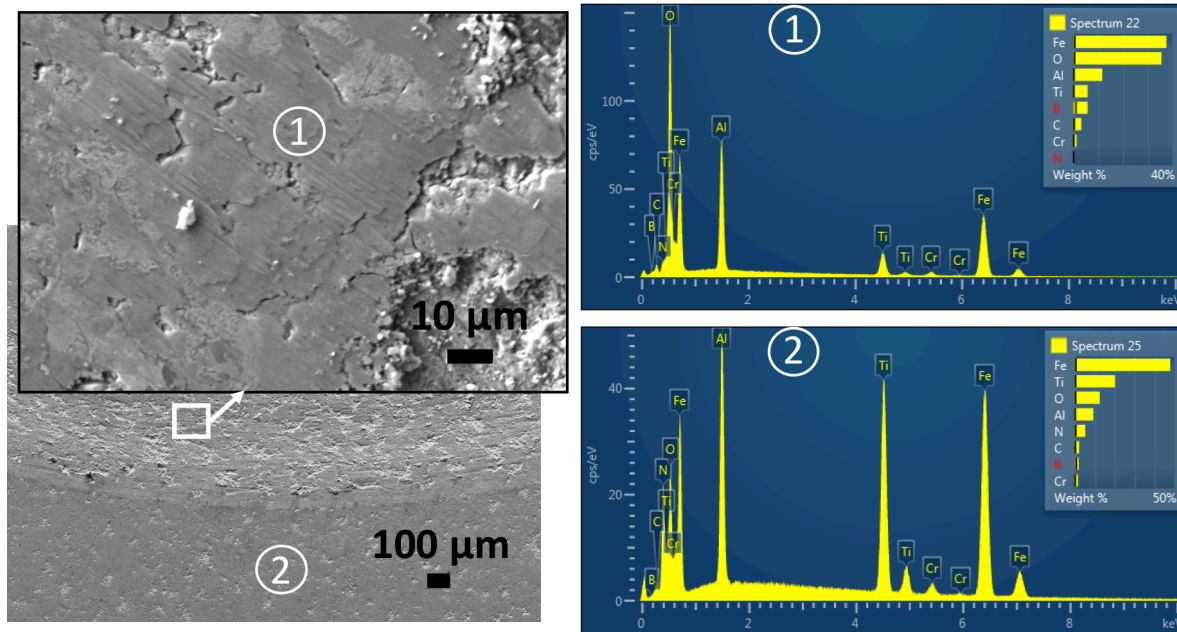
Figure 6.14: SEM micrograph of the top surface and EDS analysis of the worn (1)

and unworn (2) regions of the Ex-CM30 sample after a wear test at $v_s = 60$ cm/s.

6.3.3 Conclusion

Iron aluminide-based MMC coatings prepared using the *in situ* and *ex situ* fabrication routes were reinforced with fine and large ceramic particles (TiN and TiB$_2$), respectively, using the HEBM and HVOF techniques.

The HVOF coating fabricated from the *in situ* composite powder exhibits higher microhardness compared to the *ex situ* materials. The distribution of nano- and microhardness values showed that the homogeneity of the microstructure influenced the mechanical performance of the HVOF coatings. The MMC coatings fabricated using powders prepared via the *in situ* approach exhibit a higher wear resistance compared to the *ex situ* ones, regardless of the sliding velocities.

Detailed inspection of the wear track of the *in situ* coatings revealed voids, debris and presence of cracks at the surface and subsurface of the coatings suggesting that delamination was the primary wear mechanism. It was found that adhesive wear also contributed to material removal since the EDS analysis revealed coating materials transferred to the counterpart. In the case of the *ex situ* coatings, the presence of scratches, grooves and debris with a size similar to

that of the hard-ceramic particles inside the wear track indicates that abrasive wear was the predominant mechanism of material removal.

6.3.4 Acknowledgments

CHAPTER 7 ARTICLE 4: TRIBO-MECHANICAL PROPERTIES OF Fe₃Al-BASED PVD/HVOF DUPLEX COATINGS

Fabrice Pougoum[a], Jincheng Qian[a], Zhifeng Zhou[b], Kwok Yan Li[b], Ludvik Martinu[a], Jolanta-Ewa Klemberg-Sapieha[a,*], Sylvio Savoie[c], Robert Schulz[c]

[a] Engineering Physics Department., Polytechnique Montréal, Montréal, QC, Canada, H3C 3A7

[b] Mechanical and Biomedical Engineering, Dept., City University of Hong Kong, 83 Tat Chee Avenue, Kowloon, Hong Kong, China

[c] Materials Science Department. Institut de recherche d'Hydro-Québec (IREQ), Varennes, QC, Canada, J3X 1S1

[*] Corresponding author.

Email address: jolanta-ewa.sapieha@polymtl.ca (J. -E. Klemberg-Sapieha)

Submitted to the journal of Wear

Abstract

In this work, the tribo-mechanical properties of several duplex (thin-on-thick) coatings were evaluated under different loading conditions. The coating systems consisted of a 304-stainless steel (SS304) substrate or the same steel previously coated with a layer of iron aluminide (Fe₃Al) based material using the high velocity oxy-fuel (HVOF) technique, onto which a thin film of CrN or DLC (diamond-like carbon) was deposited using the physical vapor deposition (PVD). The mechanical properties of coatings were investigated by indentation, and their wear performances were evaluated using a pin-on-disc tribo-system in ambient conditions under applied loads between 5 N and 15 N. Wear mechanisms of coatings were assessed by examining the morphology of top surfaces and cross-sections of wear tracks, and by analyzing the counterpart material using scanning electron microscopy, energy dispersive and Raman spectroscopies. Results show that the addition of a top coat significantly enhances the wear resistance of the SS304 substrate and of the HVOF coatings due to the excellent tribological properties of DLC and CrN films. Moreover, the PVD/HVOF/SS304 coating systems exhibit excellent wear properties when compared to PVD/SS304 coatings alone due to the high load bearing capacity of the HVOF layers. The wear resistance of such systems increases with the hardness of the HVOF layer. The DLC/HVOF/SS304 duplex coatings show the best tribo-

mechanical performance due to their very low coefficient of frictions and good bond strengths between layers. On the contrary, the relatively poor tribological performance of the CrN/HVOF/SS304 duplex coatings can be attributed to the brittle nature of the CrN film. The main degradation mechanisms for the DLC-based duplex coatings were adhesive wear and plastic deformation, while in the case of the CrN-based duplex system, brittle fractures and oxidation wear were predominant. In both coating systems, abrasive wear has also contributed to the material loss.

Keywords: Thin-on-thick coatings; PVD/HVOF duplex coating; DLC and CrN films; Wear, Iron aluminides, SS304

7.1 Introduction

Stainless steels (SS) are used in many applications owing to their good corrosion resistances, their machinability, their appearance and durability. However, they are relatively soft and they often exhibit poor wear properties in applications where high load is required. The poor tribo-mechanical properties of SS as well as their high cost have motivated the use of engineered coatings that exhibit superior tribological properties for protection in hostile environments (e.g., tribological contacts or corrosion agents).

Traditionally, relatively thick coatings are used to protect materials in applications where harsh and hostile environmental conditions exist. For instance, thick coatings fabricated by thermal spray techniques such as the high velocity oxy-fuel (HVOF) are often used. HVOF coatings can exhibit high density (<2 % porosity) and excellent mechanical and wear properties [43]. Moreover, a wide range of materials (ceramics, polymers, composites, metals, etc.) can be deposited using thermal spray techniques.

In the past, iron aluminide alloys have been extensively studied due to their light-weight and low production costs. The good oxidation resistance of iron aluminides at high temperature has been a reason for the use of these materials in the area of energy generation [11]. However, there are some concerns about their mechanical properties at low temperature. Low ductility and strength in ambient conditions are drawbacks, and as a result, various microstructural modifications have been proposed to improve room temperature properties and increase their applicability, especially in tribology [15].

Recently, it has been shown that the wear resistance of the SS 304 (SS304) substrate can be significantly improved by the addition of Fe_3Al-based composite coatings using the HVOF technique [36, 37, 158]. The coefficient of friction (μ) of such coatings is still high ($\mu \sim 0.7$) [159] and, therefore, reducing it would improve wear properties even more [160]. Multilayer structures, consisting of a thick layer and a wear- and corrosion-resistant thin film with low μ on top, have been considered in applications where superior tribological properties are required. In such systems, the thick layer supports the load and the thin film acts as a functional coating and protective barrier against the environment. Such systems can yield tribo-mechanical properties that are unachievable by a single layer.

The thick layer can be obtained by nitriding the bulk substrate [161, 162], but such nitrided layers are usually thin and brittle. Duplex coatings consisting of thick HVOF coatings and thin films fabricated by physical vapor deposition (PVD) have been modelled, developed and evaluated for their tribological performance [163, 164]. The thick HVOF layer reduces contact stresses in the substrate during repeated loading and unloading, and the top coat decreases μ and consequently influences the wear behavior of the duplex system [162]. Among potential materials appropriate for the top layer, DLC and CrN films have been suggested due to their low μ (below 0.4 for CrN and below 0.1 for DLC) [28, 97, 162, 165].

In this work, two coating systems namely PVD/SS304 and PVD/HVOF/SS304 were investigated with two different types of HVOF layers showing different mechanical properties. The PVD layer consisted of a magnetron sputtered DLC or CrN thin film. The objective of this work was to evaluate and compare the tribo-mechanical properties of such systems. The influence of the mechanical properties of the HVOF layer and of the type of the PVD film on the wear rate was studied at different applied loads up to 15 N. The wear mechanisms of coatings were also investigated and discussed.

7.2 Experimental methodology

7.2.1 Preparation of PVD/HVOF duplex coatings

7.2.1.1 HVOF deposition

All thick coatings were deposited from ball milled powders using a high pressure high velocity oxy-fuel (HVOF) technique (Praxair TAFA JP 8000 series). Two types of HVOF coatings with different compositions and mechanical properties were used in this work, namely Fe_3Al and Fe_3Al-TiN-TiB_2, which were synthesized from the pure iron aluminide (Fe_3Al) and a mixture of Fe_3Al, BN and Ti powders, respectively. These two types of powders were both prepared by ball milling at high energy (1000 rpm) for 10 h using a high-energy mill (Zoz Simoloyer CM01 2L) apparatus. Prior to the HVOF deposition, the stainless-steel 304 (SS304) substrate was grit blasted with alumina particles (grit 60) to roughen the surface with the purpose of improving the mechanical bonding of impinging molten or semi-molten particles. More details about the fabrication of the Fe_3Al and the Fe_3Al-TiN-TiB_2 coatings can be found in the references [36] and [37], respectively.

Before the physical vapor deposition (PVD) and the mechanical characterization of fabricated coatings, the bare SS304 substrate and the HVOF/SS304 coatings were cut into coupons of 25 mm × 25 mm in size, and polished. The coupons were grounded with silicon carbide pads (grit 320 to 4000) and mirror finished with diamond suspension solutions (3 and 1 µm). All coupons were ultrasonically cleaned in acetone and isopropanol for 5 min to remove debris left during the polishing process.

7.2.1.2 PVD deposition

CrN and DLC layers were deposited on top of the HVOF coatings and of the bare SS304 substrates by magnetron sputtering using a closed field unbalanced magnetron sputtering system (UDP650/4, Teer Coatings Ltd, UK). with a target 380 mm × 175 mm. All substrates were cut into coupons of 2.5 cm × 2.5 cm and polished using SiC pads (grit 320 to 4000) and diamond suspension solutions (3, 1 and 0.1 µm). Prior to deposition, the substrates were sputter-cleaned in an Ar plasma for 30 min at a bias of -450 V for adhesion promotion. The background pressure of the deposition system was <2.7 × 10^{-4} Pa.

The CrN films were deposited by reactive sputtering using two Cr targets facing each other. The Cr targets were powered by a DC power supply at a constant current of 4 A. The sputtering process was carried out using a gas mixture of N_2: Ar (1:1) at a pressure of 0.4 Pa. A 200 nm thick Cr interlayer has been applied to enhance adhesion. DLC films were DC sputtered at a constant current of 4 A in an Ar atmosphere at a pressure of 0.17 Pa. In order to improve adhesion a compositionally graded interlayer consisted of 200 nm of Cr followed by a 400 nm CrC_x layer. During all the depositions, the substrate holder rotated at 10 rpm; the substrates were biased at −80 V; and the substrate temperature was maintained at ~200 °C. The schematic structures of the thin-on-thick PVD/HVOF duplex coatings are shown in Figure 8.1. More details about the sputtering processes for CrN and DLC can be found in references [166] and [167], respectively.
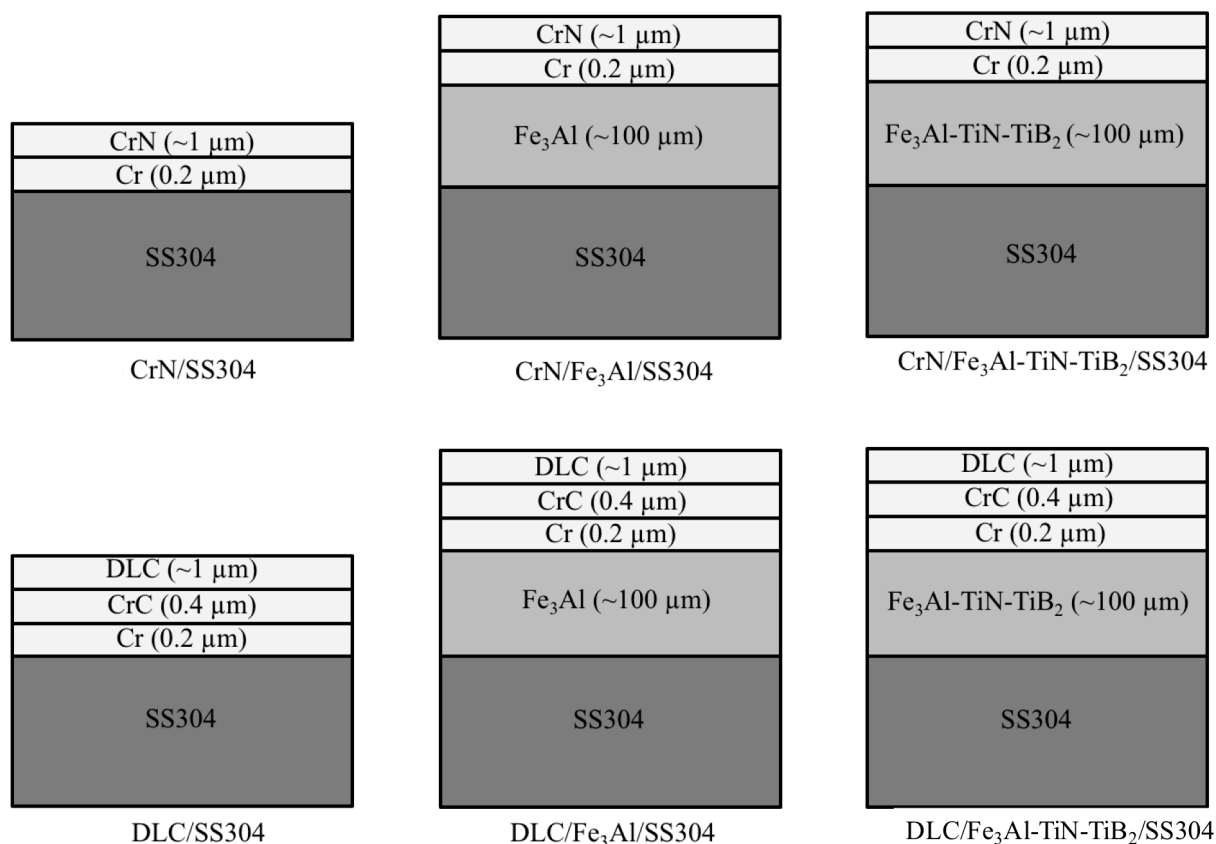
Figure 7.1: Schematic representation of the structure of the thin-on-thick PVD/HVOF duplex coatings studied in this work.

7.2.2 Mechanical characterization

7.2.2.1 Indentation tests

The mechanical properties, namely hardness (H) and elastic modulus (E), of the SS304 substrate, HVOF thick coatings, and PVD thin coatings were evaluated by the indentation techniques. The microhardness of the HVOF coatings was measured using a CSM Micro-Combi tester equipped with a pyramidal Berkovich diamond tip. The normal force was linearly increased up to its maximum (3 N), kept constant for 30 sec and then linearly decreased to obtain a load-displacement curve from which the H and E values were extracted using the Oliver and Pharr method [88]. More details about the indentation methodology of HVOF coatings can be found in [37]. The mechanical properties of DLC and CrN thin films on HVOF coatings, were measured by depth-sensing nanoindentation using a Triboindenter (TI950 Hysitron) also equipped with a pyramidal Berkovich diamond tip. The maximum load applied was 5 mN, and the H and E values were obtained using the Oliver and Pharr method as well [88].

7.2.2.2 Scratch test

The adhesion bond strength of PVD films on SS304 substrate, Fe_3Al and Fe_3Al-TiN-TiB_2 coatings was evaluated by scratch test using a CSM Micro-Combi tester equipped with a 200 μm Rockwell C diamond tip. The normal force was linearly increased from 0 to 30 N and the diamond tip was drawn on the coating surface at a constant speed of 10 mm/min over a scratch length of 5 mm.

7.2.3 Tribological characterization

The tribological behavior of coatings was studied using a tribo-system in a pin-on-disc configuration under ambient conditions (~25 °C) with a relative humidity varying between 45 % and 50 %. Different normal loads (F) varying from 5 to 15 N were applied on an alumina (Al_2O_3) ball (hardness: 20 GPa) of 4.75 mm in diameter to study the effect of the mechanical properties and load carrying capacity of the HVOF coatings on the tribological performance of the duplex coatings. A new ball was used in each experiment to ensure repeatability of the wear tests. During the pin-on-disc wear tests, the diameter of the wear track ring was fixed at 7.5 mm, the sliding velocity was maintained at 20 cm/s, and the sliding distance (L) was kept at 1000 m.

The coefficient of friction (μ) was calculated using the equation: $\mu = F_T/F$, where F_T is the tangential force measured during the test. The average value of μ for each wear test was obtained from a stable segment of the friction coefficient curve (preferably toward the end of the test). In some cases, the wear test had to be stopped after an abrupt increase of the value of μ was observed. The wear rate, K, was obtained from the expression: $K = V/(F \times L)$, where V is the volume of material loss and/or displaced which was calculated by multiplying the diameter of the wear track ring and the surface area of its cross-section, measured by profilometry. The value of K was determined by averaging the results obtained from a minimum of two tests.

7.2.4   Microstructure and surface characterization

The surface morphology of coatings and wear tracks was obtained from cross-sections using a JEOL 7200 series Scanning Electron Microscope (SEM) equipped with a field emission gun as electron source. The analysis of the chemical composition of debris and worn regions of the wear track was performed using an Inca X-max 80 Oxford energy dispersive spectroscopy (EDS) system. Prior to the SEM analysis of cross-sections of wear tracks, a thin layer of titanium was deposited on the top surface of duplex coatings in order to protect surfaces and reduce the effect of rounding edges of interfaces during polishing. The Raman spectra of the as-deposited DLC coating and of the wear tracks obtained with different loads were recorded using a RM3000, InVia Reflex-Raman from Remishaw with an excitation wavelength of 514 nm.

7.3   Results and discussion

7.3.1   Microstructural analysis

The microstructure and morphology of the thick Fe_3Al and Fe_3Al-TiN-TiB_2 coatings have been described in detail in reference [37]. For the present study, representative SEM micrographs of the cross-section of the CrN/Fe_3Al/SS304 and DLC/Fe_3Al/SS304 duplex coatings are presented in Figure 7.2. In Figure 7.2a, the CrN/Fe_3Al/SS304 coating exhibits a uniform CrN film thickness of about ~1 μm including the bond coat. In the case of the DLC/Fe_3Al/SS304 coating, the thickness is slightly higher of ~1.5 μm (Figure 7.2b). In both duplex systems, the Cr-based interlayer can be distinguished.
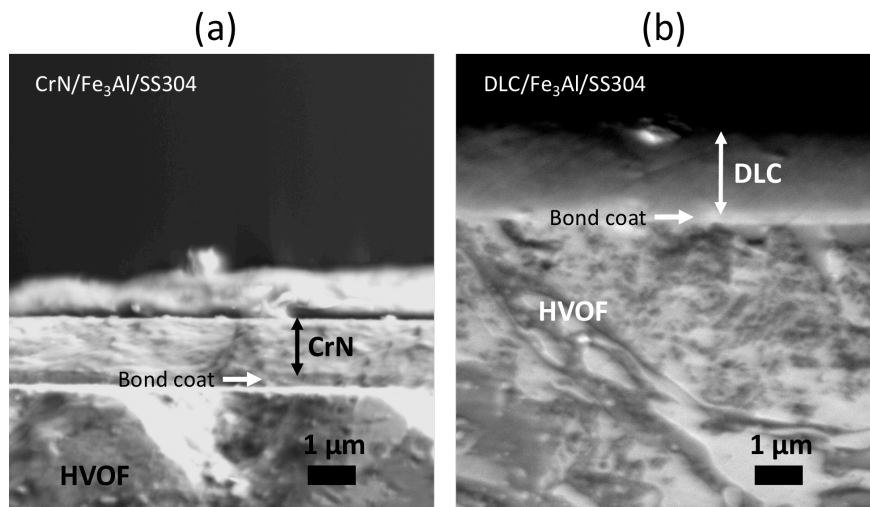
Figure 7.2: SEM micrographs of the cross-section of the duplex coatings: (a) CrN/Fe$_3$Al/SS304 and (b) DLC/ Fe$_3$Al/SS304.

7.3.2 Mechanical characterization

7.3.2.1 Mechanical properties

The hardness (H), the Young's modulus (E) and the ratio of the H/E of the SS304 substrate, the HVOF coatings, obtained by microindentation, and the sputter-deposited CrN and DLC top coats, determined using nanoindentation, are presented in Table 7.1. For the substrate and thick coatings, the H value and the ratio of the H/E increase in the following order: SS304 < Fe$_3$Al < Fe$_3$Al-TiN-TiB$_2$. The higher H of the Fe$_3$Al-TiN-TiB$_2$ coating is due to the presence of nanometer size ceramic precipitates (< 100 nm) homogenously dispersed in the Fe$_3$Al matrix as reported previously [159]. The variation trend in E does not follow that in H. The Fe$_3$Al coating shows the lowest E value among the three samples, which is most likely related to the presence of porosity. It has been shown that porosity has a detrimental effect on the elastic modulus of nanocrystalline materials [168]. Meanwhile, the Fe$_3$Al-TiN-TiB$_2$ coating shows the highest E value as a result of a low porosity level compared to the Fe$_3$Al coating and due to the presence of fine ceramic inclusions within the matrix [159]. For the sputter-deposited top coats, the CrN exhibits a higher H (19 GPa) and E (230 GPa) values compared to the DLC film. However, the higher ratio of the H/E of the DLC top coat indicates its high resistance to plastic deformation as opposed to the CrN film.

Table 7.1: Mechanical properties of individual layer of the thin-on-thick structures.

	Samples	H (GPa)	E (GPa)	H/E
Microindentation	SS304	1.3 ± 0.04	175 ± 7	0.007
	Fe_3Al/SS304	4.3 ± 0.8	131 ± 9	0.033
	Fe_3Al-TiN-TiB_2/SS304	12.6 ± 1.4	217 ± 10	0.064
Nanoindentation	CrN/SS304	19 ± 1.3	230 ± 11	0.083
	DLC/SS304	14 ± 1.8	150 ± 9	0.093

7.3.2.2 Adhesion

Scratch tests under increasing load were performed on all six types of coating structures illustrated in Figure 7.1. Figure 7.3 presents the SEM micrographs of their top surface after the scratch tests. Regardless of the type of the top coat, it can be seen that the width and the volume of the scratch track decrease as the hardness of the underneath layers increases. In the case of the PVD/SS304 system, the coating is subjected to severe plastic deformation. With increasing applied normal force, the severity of such deformation increases, which leads to the failure of the top thin films as revealed by the regions 1 and 3 in Figures 7.3a and 7.3b, respectively. The HVOF coatings show less plastic deformation compared to the SS304 substrate, which can be attributed to their high stiffness. For all PVD/HVOF duplex coatings in Figure 7.3, no delamination was observed, which reveals a good adhesion strength between the PVD thin films and the HVOF thick layers (see regions 2 and 4 in Figures 7.3a and 7.3b, respectively). These observations also suggest that in such duplex coating systems, the applied normal force is uniformly distributed over the surface of the structure during loading via the thick and hard HVOF layers.
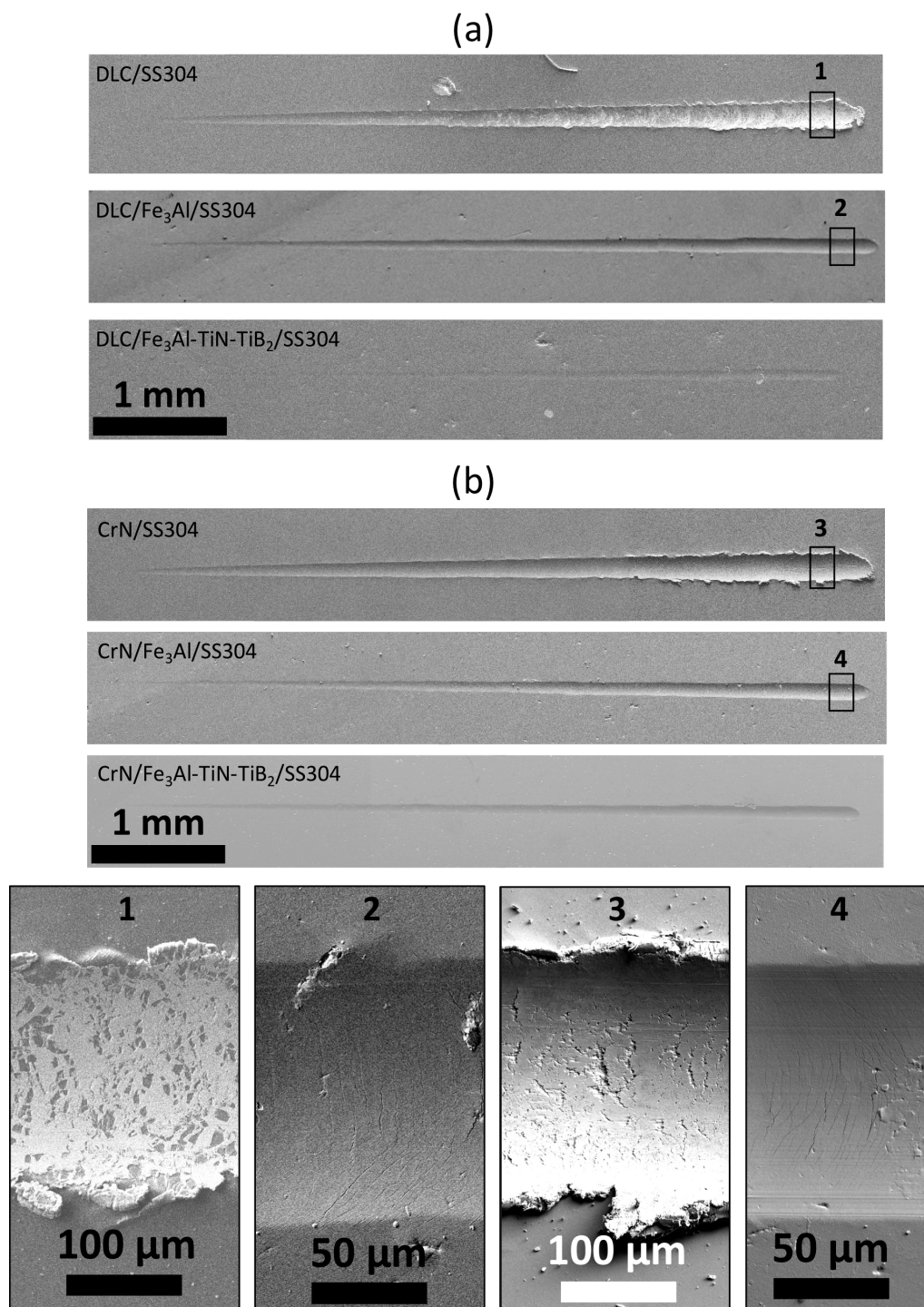
Figure 7.3: SEM micrographs showing the top surface of scratch tracks on (a) DLC-coated and (b) CrN-coated samples. The bottom micrographs represent a magnification of the regions toward the end of the scratch track indicated above.

7.3.3 Tribological characteristics

7.3.3.1 Coefficients of friction

Figure 7.4 presents the coefficient of friction, μ, as a function of the sliding distance under different applied normal loads for different coating systems. For the CrN-based coatings shown in Figures 7.4a, 7.4a' and 7.4a", μ increases rapidly at the initial stage of the wear test, and it then reaches a stable value afterwards. Under a normal load of 5 N, μ stabilizes between 0.3 and ~0.4, which is a typical μ value for CrN films [169]. When the normal load increases to 10 N or 15 N, an abrupt increase of μ from ~0.4 to ~0.7 can be observed after a sliding distance of ~50 m, except for the $CrN/Fe_3Al/SS304$ coating under a load of 10 N. Such rapid increase of μ is indicative of a failure of the CrN film; the steady value of μ reached afterward is similar to that of the SS304 substrate [36], and of the Fe_3Al or the Fe_3Al-TiN-TiB_2 coatings alone tested under similar wear conditions [159] (Table 7.1). In the case of the $CrN/Fe_3Al/SS304$ coating, μ remains at about 0.3 till the end of the test at 10 N suggesting that the CrN film was subjected to little or no damage. The difference in the ratio of the H/E between the CrN top coat and the Fe_3Al seems to be optimum to avoid cracking and debonding.

In the case of the DLC-based duplex coatings (Figures 7.4b, 7.4b' and 7.4b"), the values of μ obtained under different loads vary between ~0.04 and ~0.09 for all coatings which are much lower compared to the CrN-based coatings. These values are typical for hydrogen-free DLC films obtained under dry sliding wear conditions in ambient atmosphere [170]. In addition, no failure was observed after 1000 m long wear tests for all of the DLC-coated samples, that is attributed to the excellent tribological performance of the DLC material in agreement with the published data [162, 171]. Particularly, the $DLC/Fe_3Al/SS304$ system exhibits a very low μ of ~0.04 under a load of 5 N (Figure 7.4b). This very low μ was maintained even for longer sliding distances (~2000 m). Such ultra-low value of μ for DLC films after a long sliding distance has been reported in [171] for similar test conditions (same Al_2O_3 counterpart and sliding distance). This observation has been attributed to the formation of a tribofilm on the surface of the counterpart during sliding due to the unique combination of chemical, physical, and mechanical interactions at the interface between the DLC film and Al_2O_3 ball [170].
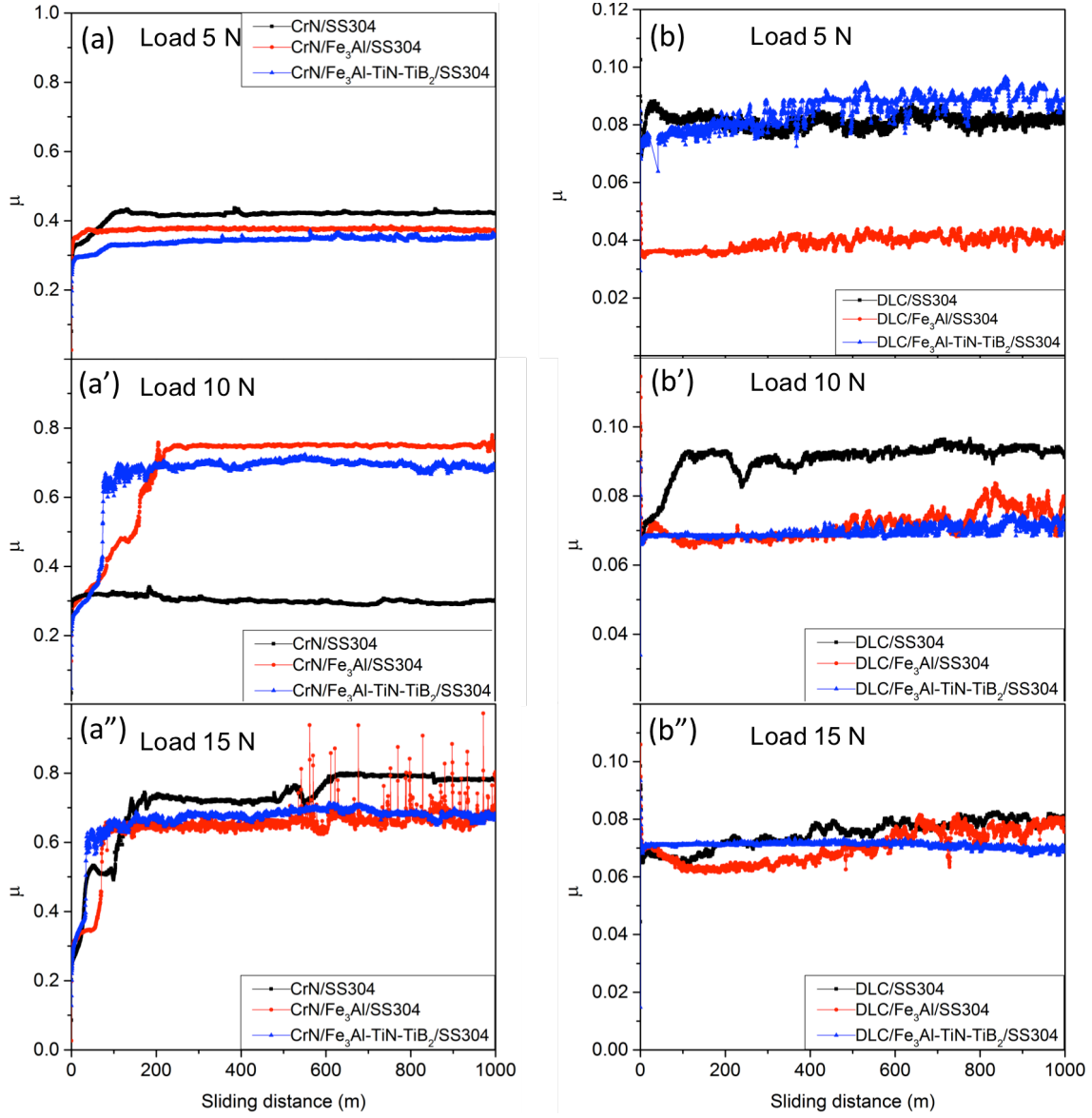
Figure 7.4: Evolution of μ of coating as a function of time under
different loads: 5 N load (a, b), 10 N (a', b'), and 15 N (a", b").

7.3.3.2 Wear rate

The wear rate, K, of the DLC- and CrN-based samples under different normal loads are compared with the SS304 substrate, and the Fe_3Al and Fe_3Al-TiN-TiB$_2$ coatings in Figure 7.5. Under a load of 5 N, the wear rate of the SS304 substrate decreased from 8.5×10^{-5} mm^3/Nm to 9.7×10^{-6} mm^3/Nm and 2.6×10^{-7} mm^3/Nm with the addition of the Fe_3Al and Fe_3Al-TiN-TiB$_2$

coatings, respectively, as shown in Figure 7.5a. The wear properties of the SS304 substrate and the Fe$_3$Al and Fe$_3$Al-TiN-TiB$_2$ coatings are presented in Table 7.2.
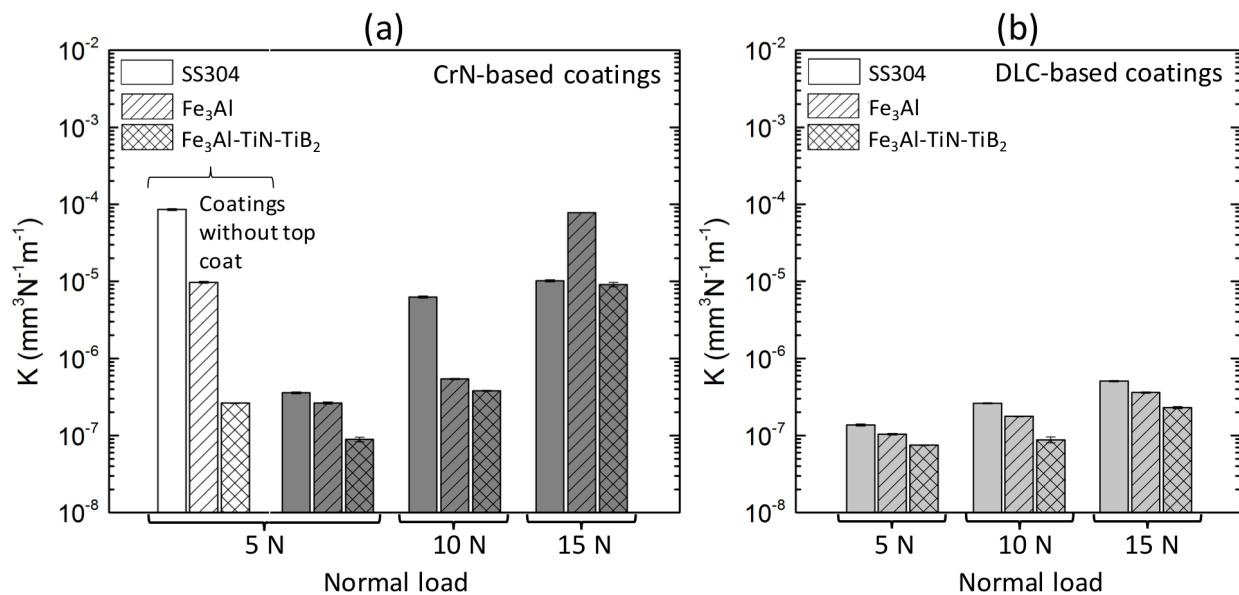
Figure 7.5: Wear rate of the CrN (a) and DLC (b) coated SS304 substrate and Fe$_3$Al and Fe$_3$Al-TiN-TiB$_2$ layer using 5 N, 10 N and 15 N applied loads.

Table 7.2: Wear properties of substrate and HVOF coatings obtained under the conditions: Al$_2$O$_3$ ball as counterpart, 5 N load and 15-20 cm/s in an ambient atmosphere.

Sample	K (mm^3/Nm)	μ	Wear mechanisms
SS304	8.5×10^{-5}	0.7 - 0.8	Adhesive [36]
Fe$_3$Al/SS304	9.7×10^{-6}	0.6 - 0.7	Fatigue, delamination [37]
Fe$_3$Al-TiN-TiB$_2$/SS304	2.6×10^{-7}	0.6	Abrasive, adhesive [37, 159]

The addition of a CrN top layer increases the wear resistance of the SS304 substrate and of the Fe$_3$Al and Fe$_3$Al-TiN-TiB$_2$ coatings by several orders of magnitude under 5 N loads (Figure 7.5a). At higher normal loads, K is higher as well. The increase is relatively large when changing the load from 5 to 10 N in the case of CrN/SS304, and from 10 to 15 N in the case of

CrN/Fe$_3$Al/SS304. However, the value of K increases gradually as a function of load in the case of CrN/Fe$_3$Al-TiN-TiB$_2$/SS304. The wear rate decreases as the hardness of the interlayer increases in the following order: SS304 < Fe$_3$Al < Fe$_3$Al-TiN-TiB$_2$ except at the 15 N load where a large increase of K (one or two orders of magnitude) is observed for the CrN/Fe$_3$Al/SS304 and CrN/Fe$_3$Al-TiN-TiB$_2$/SS304 coatings. The poor wear resistance at such high loads in the CrN-based systems is related to the failure of the CrN film that led to the abrupt increase of μ at the early stage of the wear test (Figures 7.4a' and 7.4a").

Compared to the CrN-based samples, the DLC-based coatings exhibit a higher wear resistance (Figure 7.5b). Under the same loading conditions, the values of K for DLC-based samples decrease as the hardness of the underneath layer increases in the following order SS304 < Fe$_3$Al < Fe$_3$Al-TiN-TiB$_2$. This observation is attributed to the excellent tribological properties of the DLC film and its ability to exhibit low μ regardless of the underneath layer and loading conditions (Figures 7.4b, 7.4b' and 7.4b").

Indeed, the wear rate is related to the volume of material removed or displaced during the test as represented by the wear track depth. In Figure 7.5b, K slightly increases with the normal load irrespective of the coating structure. In addition, inspection of the line profiles of the cross-section of the wear tracks for DLC-based duplex coatings obtained after the wear test at 5, 10 and 15 N loads reveals that the wear track depth increases with the normal load (Figure 7.6). Moreover, the depth slightly decreases as the hardness of the HVOF coating increases. In the case of the DLC/SS304 coating, the pileup on both sides of the wear track as revealed by the positive line profile, reflects the deformation of the SS304 substrate upon repeated loading and unloading conditions during sliding. This indicates a strong plastic deformation of the SS304 substrate, and most likely the good adhesion strength between the DLC film and the substrate. The pileup is not observed in the cases of DLC/Fe$_3$Al/SS304 or DLC/Fe$_3$Al-TiN-TiB$_2$/SS304 coatings regardless of the applied load. In the case of the PVD/HVOF duplex systems, plastic deformation is less severe due to the high hardness of HVOF interlayers compared to the SS304 substrate. Moreover, the wear track depth of the DLC/Fe$_3$Al/SS304 and DLC/Fe$_3$Al-TiN-TiB$_2$/SS304 coatings under 15 N is about 1 μm as opposed to ~1.5 μm for the DLC/SS304 coating. This observation is in agreement with the scratch results in Figure 7.3, where the width and the volume of the scratch track are higher for the SS304 substrate compared to HVOF coatings. The line profiles for the

CrN-based coatings are not presented because the top coat was completely removed after the wear test at 10 N and 15 N.

Under similar wear conditions, the value of K is lower for DLC-based coatings compared to the CrN-based ones. The superior wear performance of the DLC-based coatings can be explained by the fact that during the wear test, the DLC film undergoes structural transformation that leads to the formation of a tribofilm on the counterpart material which helps to reduce friction.
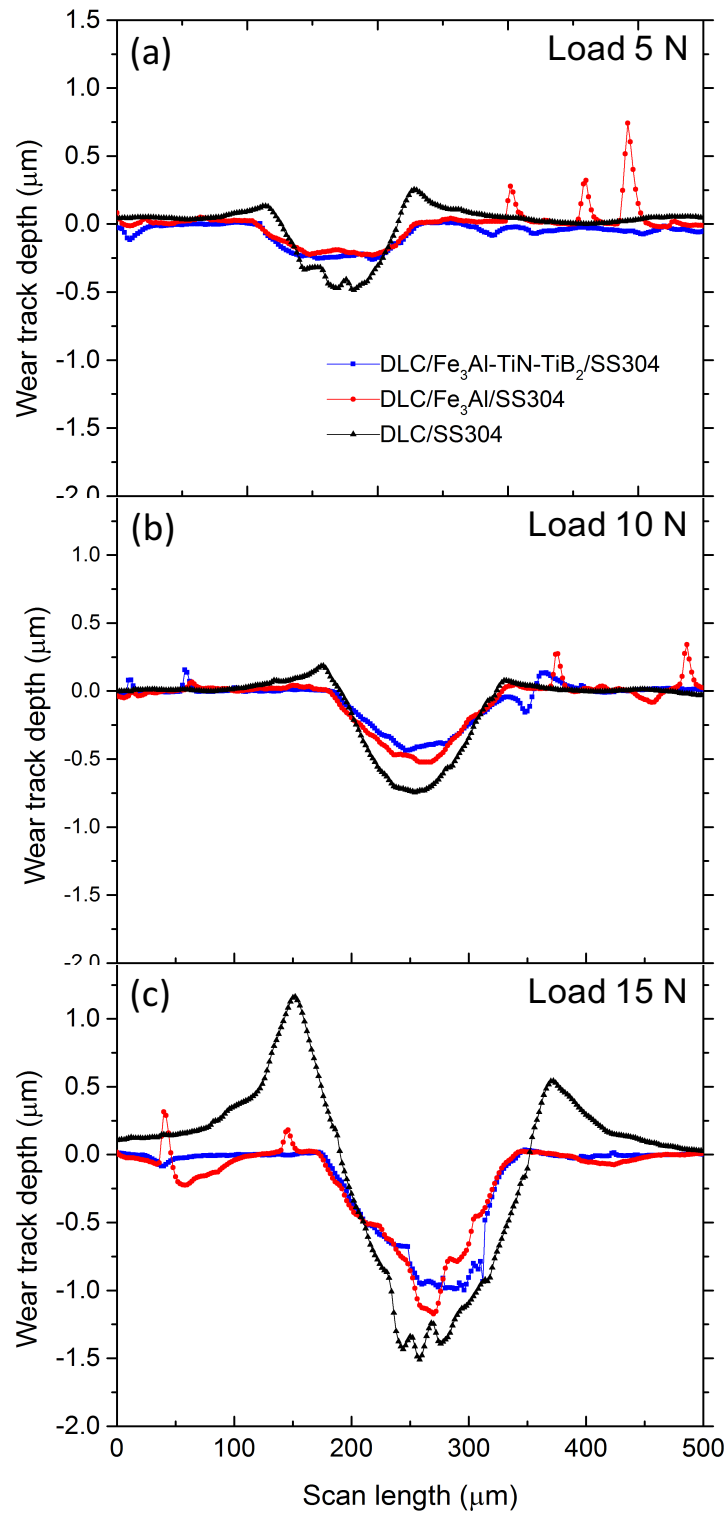
Figure 7.6: Line profiles of the wear track of DLC-based coatings tested under different normal loads (a) 5 N, (b) 10 N, and (c) 15 N.

7.3.4 Wear degradation mechanisms

7.3.4.1 CrN coatings

The SEM micrographs of the CrN-based coating surfaces after the wear tests under different loading conditions are presented in Figure 7.7. The thin CrN film on a soft SS304 substrate exhibits significantly lower tribological performances compared to the duplex coatings. The wear track of the CrN/SS304 coating tested under 5 N exhibits parallel and curved cracks oriented mostly perpendicular to the sliding direction (Figure 7.7a), that can be attributed to the relative brittle behavior of the CrN film and the soft nature of the SS304 substrate. In order to inhibit debonding or cracking, the thin and hard CrN film should not exhibit too different mechanical properties (H, E and H/E ratio) compared to those of the substrate [172]. By comparing the properties of individual layers presented in Table 7.1, it can be observed that there exists a very large difference between the CrN film and the SS304 substrate. This may be the reason for the initiation and propagation of cracks in the film upon repeated loading and unloading conditions. On the other hand, no cracks are evident at low load in the case of duplex coatings with the Fe_3Al and Fe_3Al-TiN-TiB_2 interlayer (Figures 7.7b and 7.7c). It was shown above that the hard and thick HVOF coating helps to distribute the contact stresses on the surface of the thin-on-thick coating. Therefore, the reduction of localized stresses and more similar mechanical properties between top and bottom layers likely inhibited crack formation in these multilayer systems.

For the CrN/HVOF/SS304 coatings (Figures 7.7b, 7.7c and 7.7d), there is evidence of grooves parallel to the sliding direction, appearance of short needle-like debris perpendicular to the sliding direction, and of small spherical-like particles outside the wear track. These features indicate that abrasive wear has contributed to the material loss. As the applied load increases from 5 N to 10 and 15 N, the contact pressure increases and these features become more significant leading to catastrophic failure of the CrN film as described above. The SEM micrographs of the surface of the wear tracks of coatings where the top coat has been completely worn down are not presented.
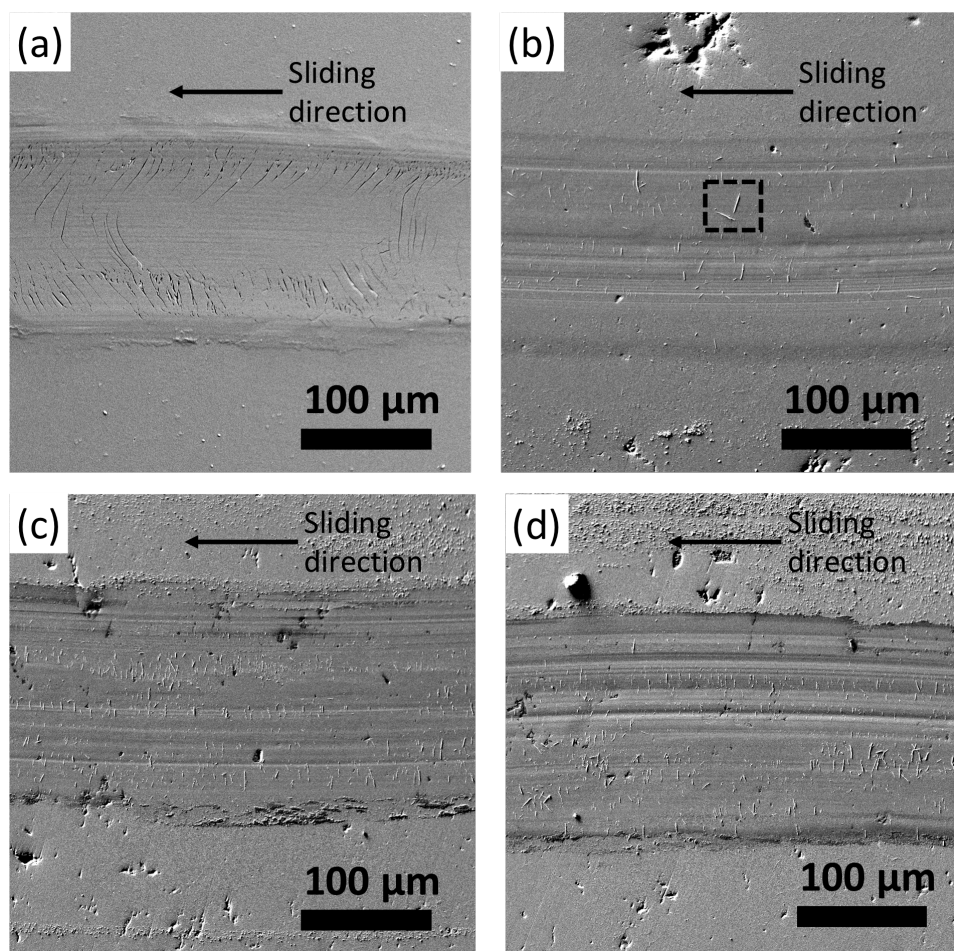
Figure 7.7: SEM micrographs of the surface of the wear track of the (a)
CrN/SS304, (b) CrN/Fe$_3$Al/SS304 and (c) CrN/Fe$_3$Al-TiN-TiB$_2$/SS304 samples
tested at 5 N load, and (d) CrN/Fe$_3$Al/SS304 sample tested at 10 N load.

The EDS analysis of the needle-like debris found inside the wear track of the CrN/Fe$_3$Al/SS304 coating after the wear test under 5 N is presented in Figure 7.8. The EDS maps reveal that the debris are composed of Cr, O and C suggesting that the interaction between the CrN film and the hard Al$_2$O$_3$ ball in ambient atmosphere leads to oxidation of the top coat. Carbon originates from the fabrication of the CrN films [173]. In addition, the absence of aluminum in the debris indicates that the Al$_2$O$_3$ ball was not damage during the wear test under these wear conditions. Therefore, the main mechanisms responsible for the material loss in the case of CrN-based coatings are brittle fracture and oxidation wear with a non-negligible contribution from abrasive wear.
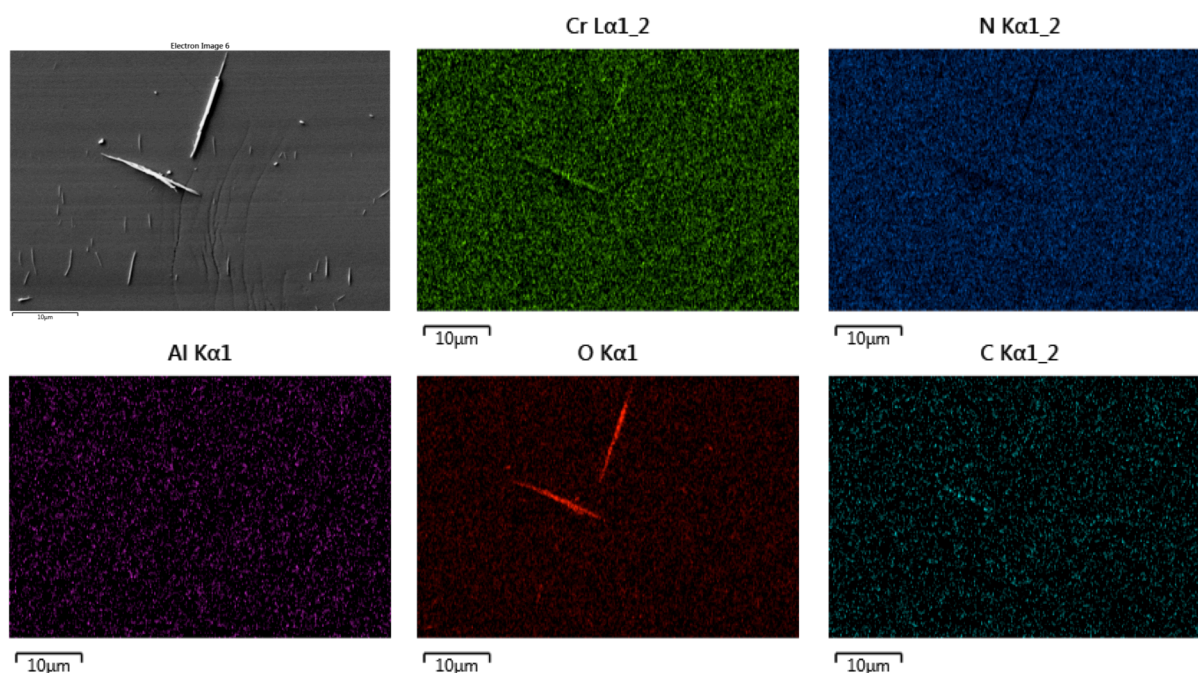
Figure 7.8: EDS mapping of debris found inside the wear track of the CrN/Fe$_3$Al/SS304 coating after the wear test under a load of 5 N.

7.3.4.2 DLC coatings

Figure 7.9 presents SEM micrographs of the surface of wear tracks of DLC-based coatings after the tests at different applied loads. In the case of the DLC/SS304 coating, the width of the wear track significantly increases with the load as expected from the soft and ductile SS304 substrate (Figures 7.9a, 7.9b and 7.9c). Plastic deformation is preponderant in these cases as indicated by the line profile (Figure 7.7a). The wear tracks exhibit parallel grooves at 5 N and 10 N with no evidence of debris. At 15 N, parallel cracks oriented at about 45 ° from the sliding direction are observed on both sides of the track.

In the case of the DLC/Fe$_3$Al/SS304 and DLC/Fe$_3$Al-TiN-TiB$_2$/SS304 coatings, the change in the width of the wear track with the applied load is less significant due to the hard HVOF interlayer. As the load increases, the grooves inside the wear track become more pronounced especially in the case of the DLC/Fe$_3$Al/SS304 system, and a significant amount of debris is observed on both sides of the wear track (Figures 7.9a', 7.9b' and 7.9c'). This suggests that abrasive wear plays a major role in the degradation mechanisms of the DLC/HVOF/SS304 coatings.
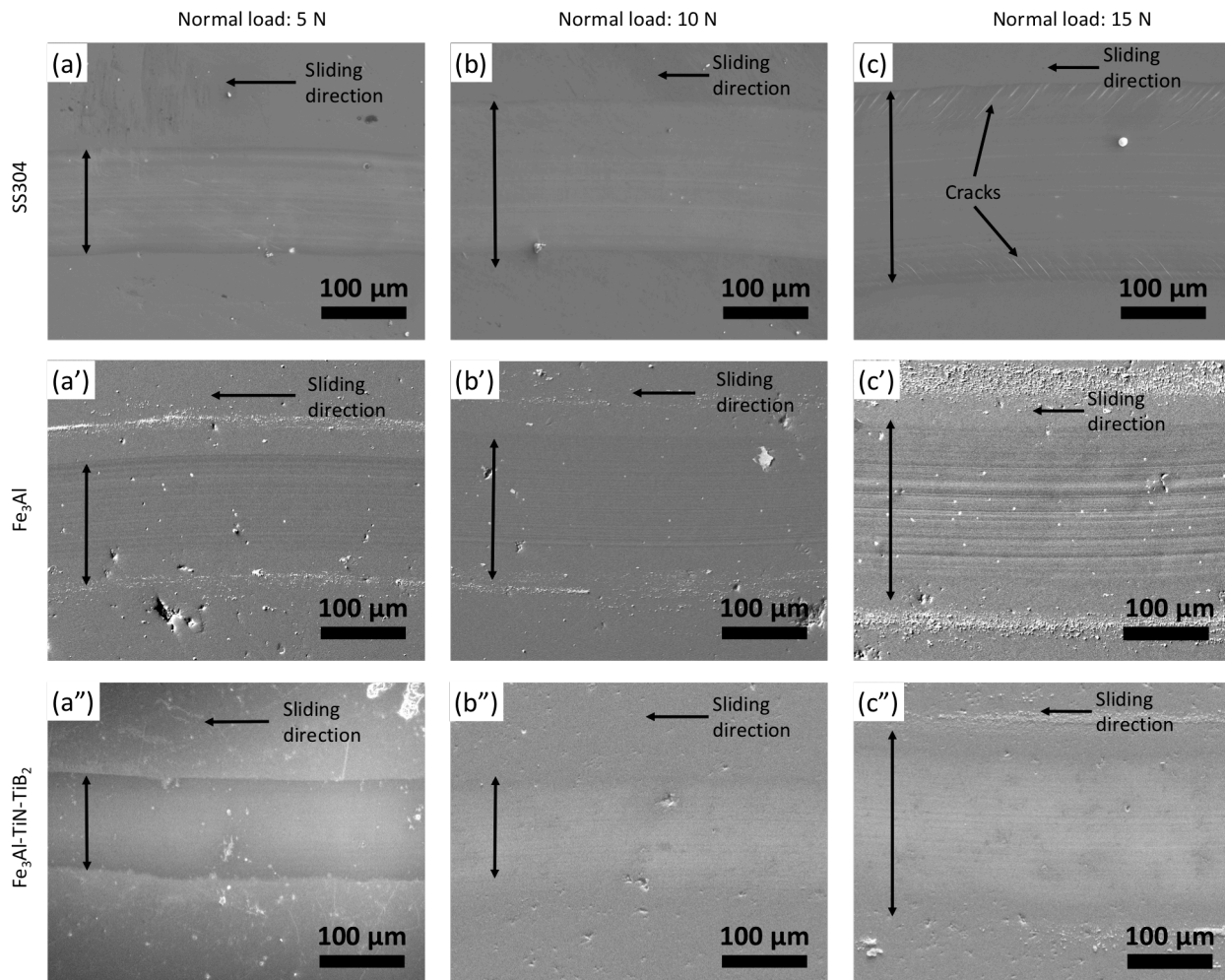
Figure 7.9: SEM micrographs of the surface of the wear track of DLC-based coatings after the wear test at 5 N (a, a', a"), 10 N (b, b', b"), and 15 N (c, c', c") with different underlayers: SS304, Fe_3Al/SS304 and Fe_3Al-TiN-TiB_2/SS304.

Figure 7.10 presents SEM micrographs of the cross-section of the wear track of the DLC/SS304 coating after a wear test performed at 15 N. In Figure 7.10a, the width of the wear track is highlighted by the dash lines and the magnification of the interface near the center of the track (Figure 7.10b) shows an undulated interface caused by the grooves in the wear track described previously. This feature is a consequence of the severe deformation by plastic flow that occurred in the SS304 substrate, and not in the DLC film, during the wear test. The good adhesion between the DLC film and the substrate, and the large difference between the mechanical properties of the DLC film and the SS304 substrate seem to be the reasons for

cracking. In Figure 7.10c the high magnification of the SEM micrograph of the interface reveals no observable difference in the coating thickness in the wear track compared to the unworn area. The integrity of the DLC film seems to be preserved after a wear test at 15 N despite the severe plastic deformation taking place in the soft SS304 substrate.
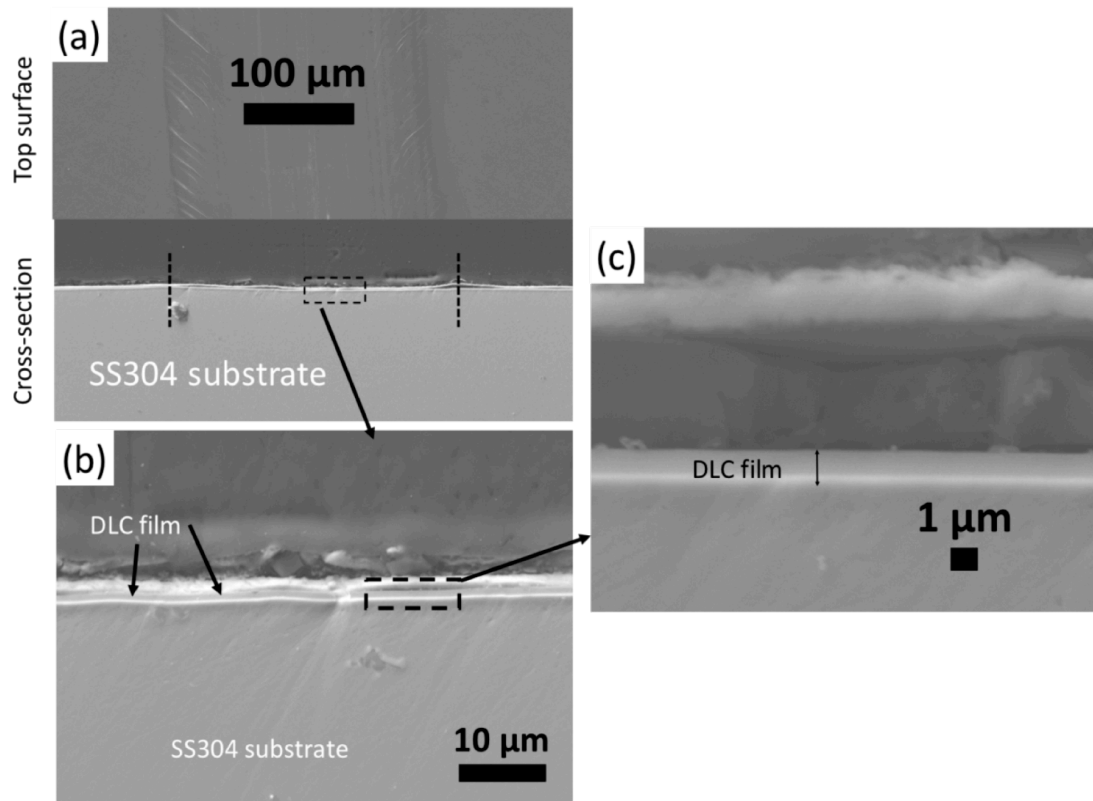
Figure 7.10: SEM micrographs of the cross-section of the wear track of the DLC/SS304 coating after the wear test performed at 15 N: (a) surface and cross-section of the wear track perpendicular to the sliding direction, (b) higher magnification of a section in the middle of the wear track and (c) high magnification image of the DLC top coat.

Since the wear track depths of these coatings are comparable to the thickness of the DLC layer (e.g. between 1 μm and 1.5 μm (Figure 7.6)), these observations suggest that plastic deformations play a dominant role in the degradation of these DLC-based coatings. As before, the DLC on a soft SS304 substrate represents the worst scenario where severe deformations lead to crack formation in the carbon film as a result of the mismatch of the mechanical properties between the DLC film and the SS304 substrate. As for the case of the CrN/SS304 coating where

brittle fractures were the main degradation mechanism, in the case of DLC/SS304, plastic deformations are preponderant degradation mechanisms. The DLC film on hard Fe_3Al and Fe_3Al-TiN-TiB_2 interlayers exhibits significantly better wear-resistant properties especially compared to the CrN films. For instance, the DLC/Fe_3Al-TiN-TiB_2/SS304 system reaches a K value as low as ~8×10^{-8} mm^3/Nm at 5 N.
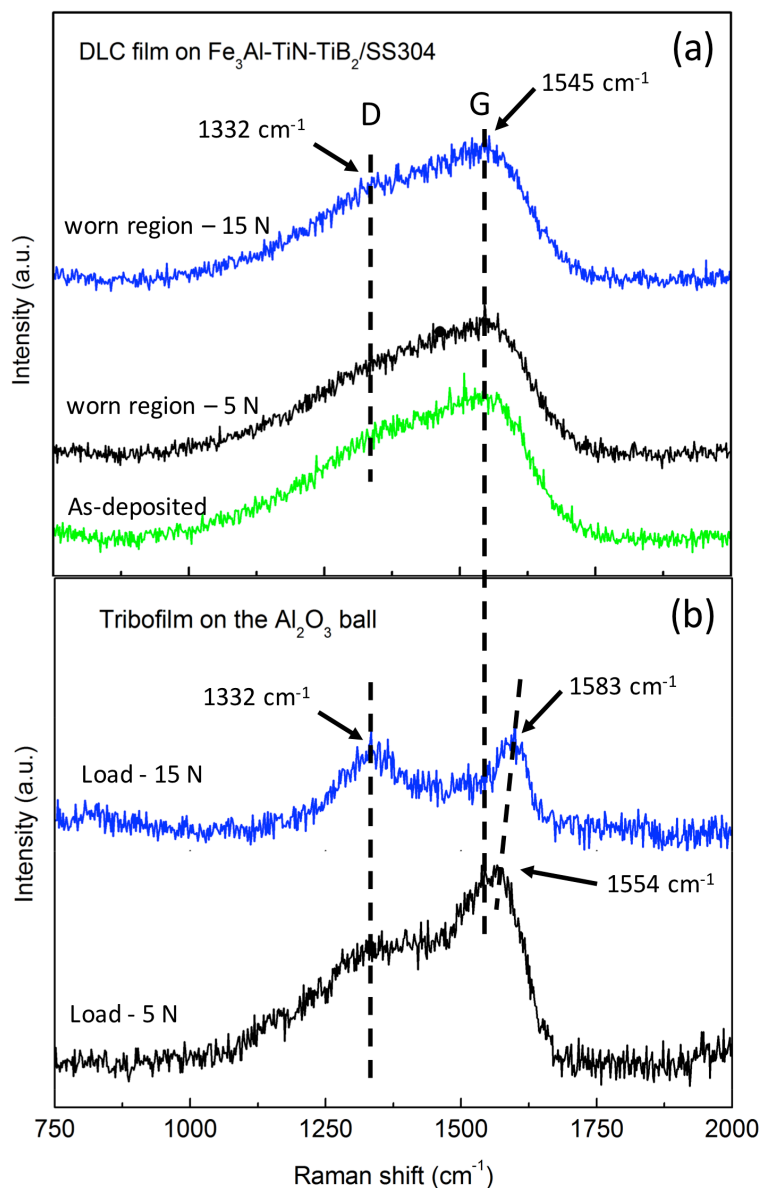
Figure 7.11: (a) Raman spectra from the unworn and worn regions of the DLC/Fe_3Al-TiN-TiB_2/SS304 coating tested under different loading conditions. (b) Corresponding Raman spectra obtained from the Al_2O_3 ball after the wear tests under at 5 and 15 N.

In Figure 7.11, the Raman spectrum of the unworn surface of the DLC/Fe$_3$Al-TiN-TiB$_2$/SS304 coating is compared to the worn surfaces obtained after wear tests performed at 5 N and 15N loads; Raman spectra from the contact surface on the corresponding Al$_2$O$_3$ ball are also shown. In Figure 7.11a, the spectra of the worn and unworn regions of the coating are similar. The graphite-like (G) peak at about 1545 cm^{-1} and the diamond-like (D) peak around 1332 cm^{-1} have the same intensities, and no peak shift is observed irrespective of the applied load. This indicates that no observable structural transformation occurred inside the wear track during the wear test. On the other hand, a comparison of the Raman spectrum of the as-deposited DLC film and the counterpart reveals that the G peak is slightly shifted to higher frequencies (Figure 7.11b). This observation suggests that the DLC film undergoes structural transformations under strain and/or thermal effects when transferred to the counter material [171]. As the applied load increases from 5 N to 15 N, the G peak decreases in intensity and the D peak becomes better defined reflecting the effect of a variation of the sp^2/sp^3 ratio in the tribofilms [174].

7.3.5   Conclusions

The tribo-mechanical properties of CrN and DLC duplex coating systems were investigated under different loading conditions. The coating structure consisted of a thin film of CrN or DLC deposited, using PVD, on (i) a SS304 substrate, and (ii) a SS304 substrate previously coated with a layer of Fe$_3$Al or Fe$_3$Al-TiN-TiB$_2$ materials prepared by HVOF.

The wear resistance at low load of the SS304 substrate and the HVOF/SS304 systems was significantly enhanced with the addition of a CrN or a DLC top layer. This performance was attributed to the excellent tribological and friction properties of these PVD top layers. In addition, the wear resistance of CrN- or DLC-based coatings increased with the hardness of the interlayer in the following order: SS304 (1.7 GPa) < Fe$_3$Al (4.2 GPa) < Fe$_3$Al-TiN-TiB$_2$ (12.3 GPa) indicating the high load carrying capacity of the thick and hard HVOF interlayer compared to the SS304 substrate.

Compared to CrN, the excellent wear resistance of the DLC-based coatings at high loads is attributed to the good bonding between DLC film and the HVOF coatings, its ability to preserve its structural integrity and to form a tribofilm on the counterpart during the wear test which acts as a solid lubricant to reduce the coefficient of friction. DLC films on hard HVOF interlayers are the best coating systems in term of wear resistance with a wear rate as low as 8×10^{-8} mm^3/Nm

for the DLC/Fe$_3$Al-TiN-TiB$_2$ coating system at 5 N. On the other end, CrN-based coatings fail catastrophically at high loads due to their brittle nature. It was found that the large difference between the mechanical properties (*H, E, H/E*) of the top coat and the underlying substrate or interlayer leads to poor tribological performances.

At low load, CrN/SS304 coatings exhibit brittle fractures but no evidence of debris. When the normal load increases, abrasion and oxidation predominantly act as main wear mechanisms, particularly for CrN/HVOF/SS304 coating systems. The degradation mechanism that led to wear in the case of DLC/SS304 coatings is plastic flow deformation followed by crack formation and propagation due to the cyclic loading and unloading condition. At high loads, abrasive wear is observed from particle removal.

7.3.6   Acknowledgments

CHAPTER 8 ARTICLE 5: STUDY OF CORROSION AND TRIBOCORROSION OF Fe₃Al-BASED DUPLEX PVD/HVOF COATINGS AGAINST ALUMINA IN NaCl SOLUTION

Fabrice Pougoum[a], Jincheng Qian[a], Zhifeng Zhou[b], Kwok Yan Li[b], Ludvik Martinu[a], Jolanta-Ewa Klemberg-Sapieha[a,*], Sylvio Savoie[c], Robert Lacasse[c], Estelle Potvin[c], Robert Schulz[c]

[a] Engineering Physics Department., Polytechnique Montréal, Montréal, QC, Canada, H3C 3A7

[b] Mechanical and Biomedical Engineering, Dept., City University of Hong Kong, 83 Tat Chee Avenue, Kowloon, Hong Kong, China

[c] Materials Science Department. Institut de recherche d'Hydro-Québec (IREQ), Varennes, QC, Canada, J3X 1S1

[*] Corresponding author.

Email address: jolanta-ewa.sapieha@polymtl.ca (J. -E. Klemberg-Sapieha)

Abstract

In this study, we assess the corrosion and tribocorrosion of duplex (thin-on-thick) coating systems formed by thin CrN or DLC layers sputter deposited on top of thick Fe₃Al layers thermal sprayed on 304-type stainless steel (SS304) substrates using the high velocity oxy-fuel (HVOF) technique. The corrosion behavior of coatings was evaluated in a 3.5 % NaCl aqueous solution using a three-electrode cell, and the tribocorrosion assessment was carried out in an apparatus in which the contact of the reciprocating pin-on-flat tribometer was immersed in the aqueous solution. The microstructure and surface morphology of the coatings were analyzed using X-ray diffraction, scanning electron microscopy and energy dispersive spectroscopy. Results show that the corrosion resistance of the Fe₃Al coating increased by approximately 1 and 3 orders of magnitude with the addition of a CrN and DLC top layers, respectively. The electrochemical impedance spectroscopy analysis revealed that the poor corrosion behavior of the Fe₃Al coating can be attributed to the presence of defects (porosity, cracks and inter-splat boundaries) in the HVOF layer that favor infiltration of the electrolyte and formation of corrosion products. The tribocorrosion results show that the addition of DLC and CrN layers is particularly beneficial when the duplex system is subjected to wear tests during cathodic polarization. However, in the

anodic regime, defects formed at the surface by the wear process are detrimental since the electrolyte infiltrates the top layer and causes the dissolution of the Fe_3Al interlayer. In this situation, material losses are due to synergistic effects of wear and corrosion.

Keywords: Fe_3Al; Thin-on-thick, PVD/HVOF duplex coatings; Corrosion; Tribocorrosion, Electrochemical impedance spectroscopy

8.1 Introduction

Iron aluminide alloys have been considered as potential candidates for high temperature applications due to their ability to form protective aluminum oxide (Al_2O_3) scales at the surface. The good corrosion and oxidation resistance at high temperature makes iron aluminides suitable for applications in automotive industry (e.g. exhaust pipes and tubes) [11]. Moreover, iron aluminide alloys offer other benefits such as low density and low cost which make them attractive as base materials to form metal matrix composites. However, its poor room temperature corrosion and poor wear properties in hostile environments remain a concern.

Over the years, aqueous corrosion resistance of iron aluminides (Fe_3Al, FeAl) has been the subject of particular attention. Various approaches, based on the modification of microstructure with the addition of different inhibitors such as Cr, Mo, Nb, Ti etc., have been employed to improve their room temperature corrosion resistance [175-177]. In addition, thick and dense coatings of these materials have been considered as potential protective layers against harsh environments, where severe tribological, chemical or electrochemical conditions prevail [158, 178].

The field of thermal spray covers a wide range of techniques commonly used to fabricate thick and dense coatings; among them, the High Velocity Oxy-Fuel (HVOF) deposition offers many benefits such as high particle velocity and relatively low particle temperature. Such characteristics of powder particles can lead to coatings with low porosity (< 2 %), large thickness (0.3 - 1.0 mm) and excellent mechanical properties [155].

The poor corrosion resistance of nanocrystalline iron aluminide HVOF coatings in a 0.5 M aqueous solution of H_2SO_4 at room temperature was attributed to localized attacks at inter-splat boundaries and/or around unmelted particles [179]. Zhao *et al.* reported that pores, micro-cracks and the typical lamellae structure of thermal spray deposits can be detrimental for the corrosion

resistance of HVOF-based coatings [180]. These defects are prone to favor infiltration of the liquid electrolyte in the coatings. Moreover, previous wear studies showed that the deterioration of the surface of Fe_3Al-based HVOF coatings takes place by material removal due to crack propagation in the subsurface via defects (i.e. porosity and inter-splats boundaries) [36, 37, 159].

Different coating structures and designs have been explored in order to reduce material removal at the surface, and to stop or delay infiltration of electrolyte and formation of corrosive products into thermal spray coatings [162, 164, 181, 182]. Zhao *et al.* have proposed to seal the pores [180], while studies have shown that improved corrosion and better wear performance of thermal spray coatings can be achieved by the addition of a top corrosion resistant layer prepared by physical vapor deposition (PVD) or chemical vapor deposition (CVD) techniques [164, 183].

In such a multi-layer structure, often referred to as duplex or thin-on-thick coating, the HVOF layer acts as a load-bearing-interlayer to avoid localized plastic deformations of the substrate during wear tests. Thick HVOF interlayers can be used to uniformly distribute contact stresses when the surface is subjected to repeated loading and unloading. The top PVD layer behaves like a barrier between the HVOF coating and the external environment. Among potential materials for the top layer, DLC and CrN films deposited by PVD have been extensively studied for their corrosion resistance in chloride containing solutions [84, 184-186]. It has been shown that on a metallic substrate (e.g. Ti6Al4V, stainless-steels, etc.), the amorphous structure of the DLC film and its chemical inertness are beneficial for the corrosion resistance, while CrN can form a thin passive layer of chromium oxide on the surface. Beside their good corrosion attributes, DLC and CrN are well-known for their excellent resistance to dry sliding wear due to their high hardness and ability to exhibit low coefficient of friction (< 0.1 for DLC and < 0.3 for CrN films) [183]. However, there is no study, in the literature, of the influence of the CrN or DLC films by PVD on the corrosion and tribo-corrosion behavior of the Fe_3Al coatings prepared by HVOF.

In continuation of our previous studies on thick Fe_3Al-based HVOF coatings for tribological property investigation [36, 37, 159] and in view of the merit of DLC and CrN thin films, the objective of this work is to study the effect of sputter-coating CrN and DLC layers on top of HVOF Fe_3Al coatings on corrosion performances in a chlorine containing NaCl solution. The corrosion behavior and the degradation mechanisms of the PVD/HVOF thin-on-thick system

are studied using Electrochemical Impedance Spectroscopy (EIS) and the simultaneous action of wear and corrosion was investigated.

8.2 Materials and Experimental Methods

8.2.1 Preparation of the HVOF coatings

Fe_3Al iron aluminide powders (97.5 % purity with ~2 % of Cr and an initial particle size of 150 μm) from Ametek were ball-milled for 10h at high-energy (1000 rpm) using a Zoz Simoloyer CM01 apparatus in order to refine the microstructure and reduce the particle size to an appropriate value for thermal spray.

After milling, the Fe_3Al powders were deposited on 304-type stainless steel (SS304) substrates (190 mm × 120 mm × 2.5 mm) using a TAFA JP 8000 series high pressure HVOF gun from Praxair. Prior to the deposition, the substrate was grit-blasted with alumina (Al_2O_3) particles (grit 60), and rinsed with methanol. Such pre-treatment helped to roughen the surface, to improve adhesion of the impinging melted or semi-melted powder particles. Details of the ball milling process, HVOF deposition parameters and coating preparation can be found in reference [36].

8.2.2 PVD deposition of CrN and DLC thin films

CrN and DLC layers were deposited on top of the HVOF coatings and on the bare SS304 substrates by magnetron sputtering using a closed field unbalanced magnetron sputtering system (UDP650/4, Teer Coatings Ltd, UK) with up to four 380 mm × 175 mm target. All substrates were cut into coupons of 2.5 cm × 2.5 cm and polished using SiC pads (grit 320 to 4000) and diamond suspension solutions (3, 1 and 0.1 μm). Prior to deposition, the substrates were sputter-cleaned in an Ar plasma for 30 min at a bias of -450 V for adhesion promotion. The background pressure of the deposition system was $<2.7 \times 10^{-4}$ Pa.

The CrN films were deposited by reactive sputtering using two Cr targets facing each other. The Cr targets were powered by a DC power supply at a constant current of 4 A. The sputtering process was carried out using a gas mixture of N_2: Ar (1:1) at a pressure of 0.4 Pa. A 200 nm thick Cr interlayer was deposited to enhance adhesion. DLC films were sputtered from pure graphite targets at a constant current of 4 A in an Ar atmosphere at a pressure of 0.17 Pa. In order to improve adhesion, an interlayer consisting of 200 nm of Cr followed by a 400 nm CrC_x layer

was used. During all the depositions, the substrate holder rotated at 10 rpm; the substrates were biased at −80 V; and the substrate temperature was maintained at ~200 °C. More details about the sputtering processes for CrN and DLC can be found in references [166] and [167], respectively.

8.2.3 Corrosion tests

The corrosion tests were carried out in a 3.5 % NaCl aqueous solution at room temperature (~25 °C) using a three electrode-cell described in reference [97]. The sample was positioned vertically and its surface was in contact with the electrolyte. The coating was chosen to be the working electrode (WE) while a graphite rod (6 mm diameter) was the counter electrode (CE). The reference electrode (RE) was a Saturated Calomel Electrode (SCE of 242 mV vs standard hydrogen electrode), and the area of the specimen exposed to the solution was 0.79 cm^2. The electrochemical measurements including open circuit potential (OCP), electrochemical impedance spectroscopy (EIS) and polarization were performed using a potentiostat (Autolab PGSTAT302 Echochemie) equipped with a frequency response analyzer.

The surface of the coating was stabilized in the electrolyte for 60 min to reach a stable OCP value. The OCP values for all coatings were obtained from the stable segment of the OCP curve.

Following the OCP measurement, the EIS was performed at OCP with a frequency varying between 10^5 Hz and 10^{-2} Hz using an AutoLab frequency response analyzer program (FRA, Eco Cemie B.V. Utrecht).

The potentiodynamic polarization tests were carried out from cathodic to anodic polarization at a rate of 5 mV/s. The breakdown potential is defined by the potential at which an irreversible increase of current occurs.

8.2.4 Tribocorrosion tests

The tribocorrosion behavior of coatings was studied by performing the wear tests using a reciprocating ball-on-flat tribometer where the sliding contact was fully immersed in a 3.5 % NaCl aqueous electrolyte at room temperature (~25 °C). The corrosion tests were performed in a three-electrode-type electrochemical cell in which the coating served as the WE; a platinum wire was used as the CE, and a SCE was used as the RE electrode. In this configuration, the surface of coatings was horizontally positioned.

An alumina (Al_2O_3) ball (4.75 mm in diameter) was used as the wear counterpart due to its high hardness (20 GPa) and its chemical inertness. A normal load (dead load), F, of 5 N was applied corresponding to a minimum average Hertzian contact pressure of 1.26 GPa. The wear tests were performed under wet conditions with a total number of 1800 cycles using a sliding frequency of 1 Hz and a fixed stroke length of 10 mm. The material's loss of the coating was calculated by measuring its weight difference before and after the tribocorrosion test using a high precision scale.

The tribocorrosion test was performed in several steps. In the first step, the OCP of the system was measured and recorded during 60 min before rubbing. This step was used to ensure the electrochemical stability of the surface of the coating. In the second step, the system was polarized cathodically or anodically, and the sliding wear test was performed. In both cases, the test was conducted at a fixed potential between the WE and the RE, and the corrosion current was monitored before, during and after the wear test. In the cathodic polarization, the applied potential was -800 mV, which was below the corrosion potential of the Fe_3Al coating. Note that under cathodic protection, anodic reactions are suppressed (no corrosion takes place). In the anodic polarization, a potential of +250 mV with respect to the OCP of the coating was applied. This potential lies in the passive region of the polarization curve of coatings. During sliding, the corrosion current was measured and recorded as a function of time for a fixed number of cycles. The corrosion current was recorded for 20 min before and after rubbing to ensure its stability. The coefficient of friction (μ) was calculated using the equation: $\mu = F_T/F$, where F_T is the tangential force measured during the test. In this context, a minimum of two tribocorrosion tests was performed under similar surface conditions (similar sample preparation) to validate the measurements and ensure reproducibility of the results.

8.2.5 Surface characterization

The structural characteristics of coatings were obtained using a Phillips X'Pert X-ray diffractometer (XRD) in a $\theta/2\theta$ configuration operating at 50 keV and 40 mA. The diffractometer was equipped with a copper source ($\lambda = 1.5406$ Å) with a fixed divergent slit of 1.5 mm. The diffractograms were acquired from 20 ° to 90 ° with a step size of 0.02 ° and a time per step of 2 sec.

The morphology and the chemical composition of the coating surface and cross-section before and after exposure to the electrolyte were characterized using a JEOL 7200 series Scanning Electron Microscope (SEM) equipped with a field electron gun as electron source, and an Inca X-max 80 Oxford Energy Dispersive Spectroscopy (EDS) system.

8.3 Results and discussion

8.3.1 Microstructure of the deposited coating systems

Figure 8.1 presents SEM micrographs of surfaces and cross-sections, and the X-ray diffractograms of the coatings studied in this work. The surface of the Fe_3Al coating reveals some porosity and defects (Figure 8.1a) while its cross-section shows melted and un-melted particles and pores (Figure 8.1a'). These features likely originated from the deposition process as described in reference [36]. For the Fe_3Al HVOF coating, a thickness of 120 μm was obtained after the deposition. Prior to the deposition of the CrN and DLC films, coupons of the Fe_3Al HVOF coating were polished. Fe_3Al layer with an average thickness of 100 μm and a relative surface roughness below 100 nm were obtained.

In the case of the $CrN/Fe_3Al/SS304$ and the $DLC/Fe_3Al/SS304$ samples, the top surface exhibits some defects (bumps and pits) which may come from the polished surface of the Fe_3Al sublayer (Figures 8.1b and 8.1c). The SEM micrographs of the cross-section of the duplex coatings (Figures 8.1b' and 8.1c') show that the CrN and DLC films are dense and uniform; the thicknesses, including the bond layers, are approximately 1 and 1.5 μm for CrN and DLC films, respectively.

The XRD diffractograms of the Fe_3Al HVOF coating (Figure 8.1a") reveals peaks from the pure iron aluminide. For the $CrN/Fe_3Al/SS304$ coating (Figure 8.1b"), well-defined peaks due to CrN phases were observed, and the left shoulder of the peak at ~43 ° is attributed to the Fe_3Al phase. In the case of the $DLC/Fe_3Al/SS304$ coating (Figure 8.1c"), no diffraction peaks due to DLC were observed since the DLC layer is amorphous. The diffraction peaks observed are from the Cr phase from the interlayer. The XRD patterns from the Fe_3Al and Cr phases overlap in the diffractograms in this case.
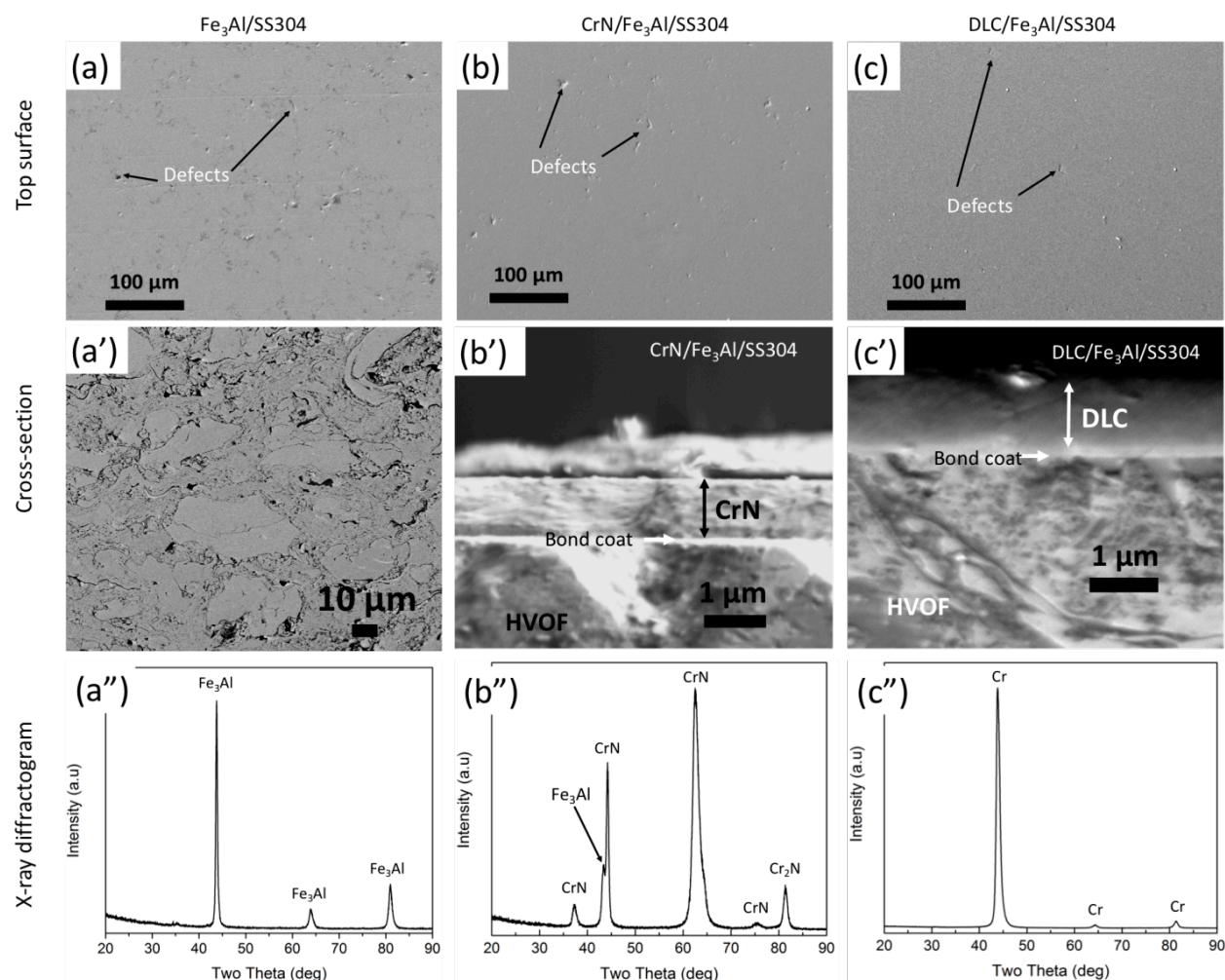
Figure 8.1: SEM micrographs of the coating (a, b, c) surface and (a', b', c') cross-section, and (a", b", c") X-ray diffractograms of Fe$_3$Al, CrN/Fe$_3$Al/SS304 and DLC/Fe$_3$Al/SS304 coatings.

8.3.2 Corrosion characterization

8.3.2.1 Open circuit potential (OCP)

Figure 8.2 presents the evolution of the OCP of the coatings exposed to a 3.5 % NaCl aqueous solution as a function of time. In most cases, the value of the OCP slightly decreases before stabilization indicating that the electrochemical evolution of the surface of the coating has reached a steady state. However, a sharp voltage drop was observed after around 600 sec for the CrN/Fe$_3$Al/SS304 duplex sample which indicated some instability in this system. This behavior may be related to the presence of defects and the breakdown of the CrN top protective layer after

this period of time. The OCP for the uncoated SS304 substrate and Fe$_3$Al coatings increased when a top layer of CrN or DLC was added. The increase of the OCP is relatively small in the case of the SS304 substrate, which indicates only marginal differences in the corrosion resistance performances of these materials. In contrast, a large shift of the OCP toward anodic potential was observed for the Fe$_3$Al coating when coated with a CrN or DLC film. This means that the PVD layers delayed the corrosion of Fe$_3$Al upon exposure to the electrolyte, and led to a large improvement of its corrosion resistance.
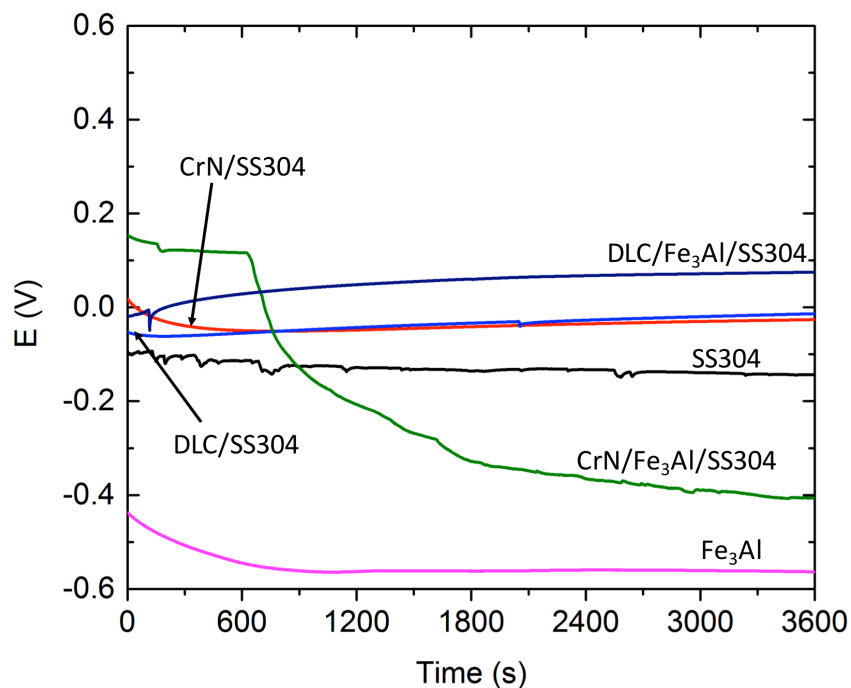
Figure 8.2: Evolution of the OCP of the SS304 substrate and of the pure Fe$_3$Al coatings as a function of time, in comparison with the duplex coatings.

8.3.2.2 Electrochemical impedance spectroscopy (EIS)

The EIS data of the Fe$_3$Al-based duplex coatings are presented in Figure 8.3 in the form of Bode and Nyquist plots [187]. In Figure 8.3a, the logarithm of the amplitude of the impedance, log |Z|, and the negative argument of the complex impedance Z (phase shift between the current and the potential), -Arg(Z) are plotted as a function of the logarithm of the frequency (f), log f.
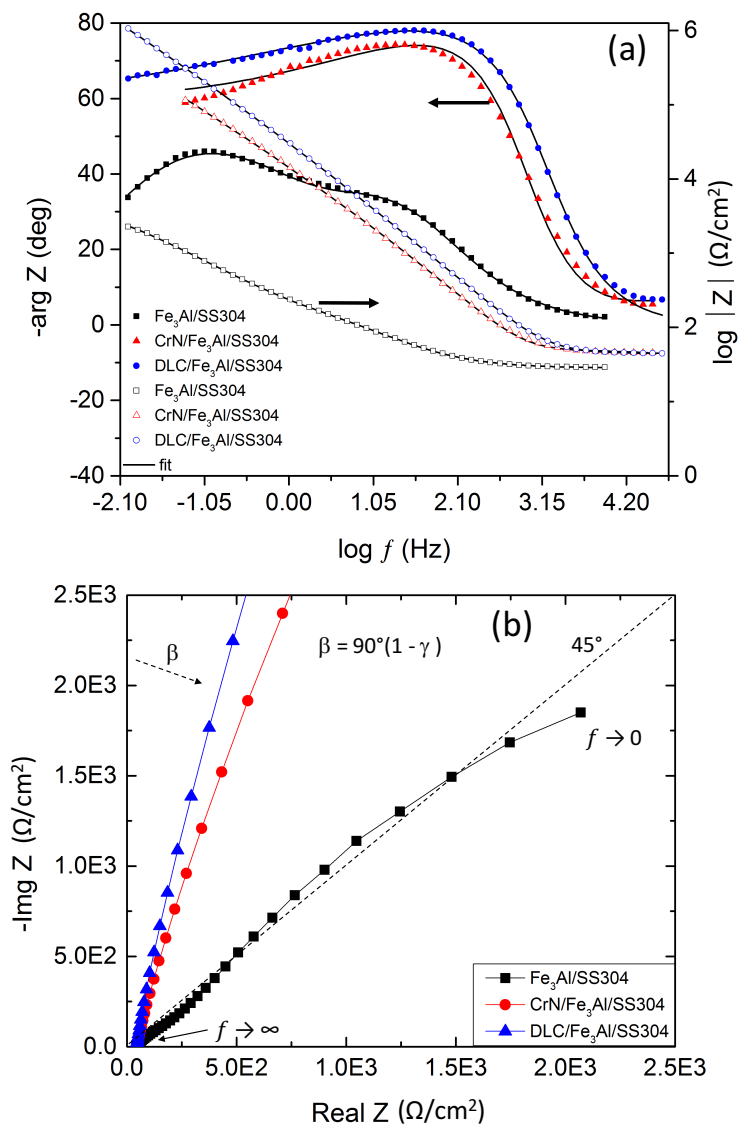
Figure 8.3: EIS data of the Fe$_3$Al, CrN/Fe$_3$Al/SS304 and DLC/Fe$_3$Al/SS304 coatings represented in the form of (a) Bode, and (b) Nyquist plots.

The -Arg(Z) curves for the CrN/Fe$_3$Al/SS304 and DLC/Fe$_3$Al/SS304 coatings shifts rapidly from low values near 0 ° at high frequencies to high values approaching 80 ° (close to 90 °) at low frequencies, and stay fairly high as we move towards dc conditions. The corresponding log |Z| curves of these coatings show basically two straight lines one horizontal at high frequencies, and one inclined with a negative slope at low frequencies with a breakpoint between 1 and 10 kHz. The corresponding Nyquist plots presented in Figure 8.3b show almost vertical straight lines with relatively small angles with respect to the y axis for the PVD-coated samples. This behavior is typical for Bode and Nyquist plots of a simple electrical circuit consisting of a

resistance (R) in series with a capacitor (C). Therefore, these coating systems are mainly characterized by a single time constant ($\tau = RC$).

The $-Arg(Z)$ curve for the Fe$_3$Al/SS304 coating shows a significantly different behavior. Two maxima, one between 10 and 100Hz, and the other between 0.01 and 0.1 Hz are distinguishable. The corresponding impedance curve (log $|Z|$) shows a gradual slow increase with decreasing frequency. At low frequencies, the impedance of the duplex coatings is about three orders of magnitude higher than that of the Fe$_3$Al/SS304 system reflecting the much higher resistance of the DLC and CrN layers compared to the intermetallic Fe$_3$Al coating. These observations indicate that the Fe$_3$Al/SS304 system is characterized by more than one τ. The existence of multiple time constants in this case is also reflected on the corresponding Nyquist plot where a fairly well-defined capacitive loop is observed at low frequency, while at high frequency the curve approaches the origin at an angle of about 45 °.

The total impedance of an electrode consists of the contributions of the electrolyte (resistance of the solution R_s), the electrode-solution interface (double layer capacitance C_{dl} and charge transfer resistance R_{ct}), and the electrochemical reaction taking place on the surface or within the electrode when the electrolyte is able to penetrate the coating via defects.

For a coating consisting of multi-layers, the impedance can be represented by an equivalent electrical circuit consisting of a series of resistances and capacitances in parallel such as those shown in Figure 8.4, each block corresponding to one layer in the coating [93].
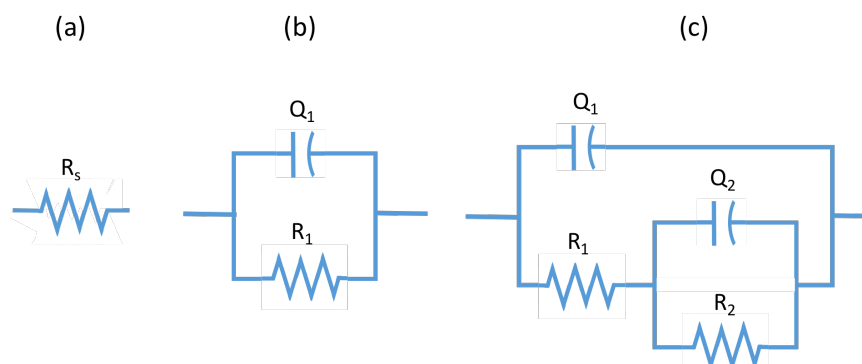
Figure 8.4: Equivalent electrical circuits representing: (a) the solution resistance, (b) the CrN or DLC layer, and (c) the Fe$_3$Al HVOF coating.

According to [93], the case of the $CrN/Fe_3Al/SS304$ and $DLC/Fe_3Al/SS304$ systems would be represented by an equivalent electrical circuit consisting of a linear combination of the circuits of Figures 8.4a, 8.4b and 8.4c in series, while the $Fe_3Al/SS304$ system would be represented by a linear combination of Figures 8.4a and 8.4c. R_1 is the charge transfer resistance (R_{ct}), Q_1 is the double layer capacitance (C_{dl}) at the surface, while R_2 and Q_2 are components associated with the subsurface or internal structure of the electrode (pores and inter-splats boundaries). These components may also represent a diffusion process when the reaction is diffusion limited. In this case, a Warburg impedance is often introduced instead of R_2 and Q_2 [187].

In solid state electrodes, because of the surface roughness and dispersion of dielectric constants in the material, the behavior cannot be represented by a connection of simple R/C elements. Therefore, the capacitance is often expressed in terms of a constant phase element Q (CPE) whose impedance is given by $Z_Q = 1/ Y_0(j\omega)^\gamma$, where $\omega = 2\pi f$ and Y_0 (F/cm^2 $s^{\gamma-1}$) is a constant and γ is related to the angle of rotation of a purely capacitive line on the complex plane plots: $\beta = 90°$ ($1 - \gamma$) (see Figure 8.3b) [187]. When $\gamma = 1$ ($\beta = 0$, straight vertical line in the complex plane), the CPE behaves as a pure capacitor. When $\gamma = 0$ ($\beta = 90°$, horizontal line in the complex plane), the CPE is a simple resistance, and when $\gamma = 0.5$ ($\beta = 45°$), the CPE is equivalent to a Warburg element which represents the impedance of a Faradaic reaction in the presence of semi-infinite linear diffusion [187].

In our case, the CrN and DLC layers are very dense and almost defect free. They block the infiltration of electrolyte fairly well and, as a result, the equivalent circuit of the underlying Fe_3Al layer (Figure 8.4c) is masked by the top layer. Therefore, in a first approximation, the equivalent circuit of the $CrN/Fe_3Al/SS304$ and $DLC/Fe_3Al/SS304$ systems can be represented by Figures 8.4a and 8.4b only. Moreover, since R_1 (the charge transfer resistance) is very high for these coatings as indicated before, the equivalent circuit of the duplex coating consists simply of the solution resistance in series with the CPE element Q_1.

Table 8.1 shows the values of the fits of the impedance data with the equivalent electrical circuits described above. For the $CrN/Fe_3Al/SS304$ and $DLC/Fe_3Al/SS304$ systems, the values of Q_1 of 1.0×10^{-5} F/cm^2 and 6.7×10^{-6} F/cm^2, respectively, are relatively small compared to that of the $Fe_3Al/SS304$ coating. This suggests that the surfaces of these duplex coatings are smooth, and the effective surface areas with the electrolyte are small. The time constant τ_1 of 2.2 and 3.4 kHz

correspond to the break points between the horizontal and inclined lines in the log $|Z|$ versus log f curves as discussed above. The values of γ_1 of about 0.9 in both cases indicate nearly ideal capacitive behavior. The angle $\beta = 90\,°(1 - 0.9)$ in the Nyquist plots is about 10 °.

The value of Q_1 and Q_2 for the $Fe_3Al/SS304$ system is several orders of magnitude higher compared to the double layer capacitances of the duplex coatings. This is due to the very high effective surface area of the HVOF coating caused by its porous structure. The electrolyte can migrate into the coating via pores and inter-splats boundaries. The intercepts of the capacitive loop shown in the Nyquist plot of Figure 8.3b is about 5.1 $k\Omega.cm^2$ ($R_s + R_1 + R_2$) at low frequency, and about 230 $\Omega.cm^2$ ($R_s + R_1$) at high frequency. The value of γ_2 is close to 0.5 (α is ~45 °) which means that this constant phase element is similar to an infinite Warburg impedance. Therefore, diffusion processes are most likely relevant in the corrosion of the $Fe_3Al/SS304$ coating.

Table 8.1: Characteristics of the fitted models for the EIS data of
coatings immersed in a 3.5 % NaCl aqueous solution.

Coatings	R_s ($\Omega.cm^2$)	Q_1		R_1 ($\Omega.cm^2$)	Q_2		R_2 ($\Omega.cm^2$)	τ_1 (kHz)	τ_2 (kHz)
		Y_{o1} (F/cm^2)	γ_1		Y_{o2} (F/cm^2)	γ_2			
CrN/Fe$_3$Al/SS304	45	1.0×10^{-5}	0.9	$> 10^9$				2.2	-
Est. Error (%)	0.6	3.1	6.4						
DLC/Fe$_3$Al/SS304	44	6.7×10^{-6}	0.9	$> 10^9$				3.4	-
Est. Error (%)	0.8	11.6	1.1						
Fe$_3$Al/SS304	28	6.4×10^{-4}	0.7	2.0×10^2	1.3×10^{-3}	0.6	4.9×10^3	0.008	0.001
Est. Error (%)	0.5	5.7	1.3	7.5	2.7	1.4	3.3		

8.3.2.3 Potentiodynamic polarization tests

The polarization curves of the SS304 substrate and the Fe$_3$Al coating are compared to their corresponding duplex coatings in Figure 8.5, and the resulting corrosion characteristics (i.e. corrosion potential, E$_{corr}$, and corrosion current density, i$_{corr}$) are summarized in Table 8.2. The E$_{corr}$ value of the SS304 substrate (-0.24 V) is higher compared to the Fe$_3$Al coating (-0.71 V). For duplex coatings, the top CrN and DLC layers raised E$_{corr}$ of the Fe$_3$Al coating up to approximately -0.34 V and -0.09 V, respectively. The lower E$_{corr}$ of the CrN/Fe$_3$Al/SS304 coating compared to the OCP value in Figure 8.2 can be associated with the surface instabilities in this system as indicated above. The i$_{corr}$ of the Fe$_3$Al coating decreases by one and three orders of magnitude with the addition of the CrN and DLC top layers, respectively.
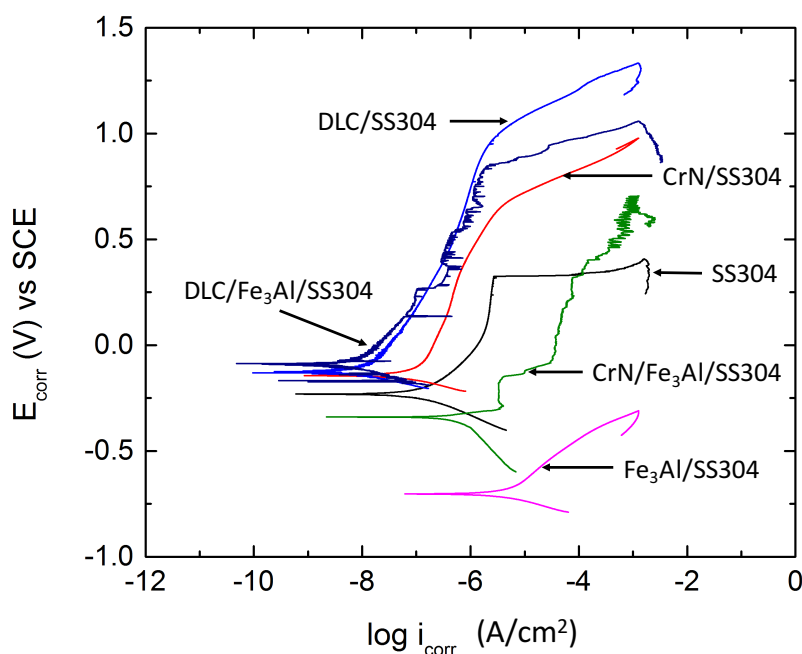
Figure 8.5: Polarization curves of coating systems and of the substrate.

The Fe$_3$Al system which exhibits a microstructure with a large number of defects (porosities and inter-splat boundaries) seems to be unable to produce a protective oxide layer on the surface. The low E$_{corr}$ value is an indication that the Fe$_3$Al material starts to corrode immediately when exposed to the NaCl solution. A passive region is not observed in the polarization curve. On the contrary, the SS304 substrate shows a wide passive region associated to a protective oxide layer which inhibits surface corrosion. The polarization curve of the

PVD/SS304 and PVD/Fe$_3$Al/SS304 systems also exhibit a passive region. It has been shown that a protective oxide layer forms on CrN films when immersed in chlorine-based solutions. The Cr bond coat may also play a beneficial role by acting as a diffusion barrier and by blocking the migration of species [84, 188].

Table 8.2: Corrosion characteristics obtained after a polarization test in a 3.5 % NaCl aqueous solution.

Coating	E_{corr} (V)	i_{corr} (A/cm^2)
SS304	-0.24	1×10^{-7}
SS304/CrN	-0.15	1×10^{-7}
SS304/DLC	-0.13	1×10^{-8}
Fe$_3$Al	-0.71	2×10^{-5}
CrN/Fe$_3$Al/SS304	-0.34	1×10^{-6}
DLC/Fe$_3$Al/SS304	-0.09	1×10^{-8}

8.3.2.4 Degradation mechanisms

SEM micrographs of the surface of the SS304 substrate and of the Fe$_3$Al coating after the corrosion test are shown in Figure 8.6. The surface morphology of the SS304 substrate shows localized corrosion pits (Figure 8.6a). In general, these pits form after the break down of the passive oxide layer as chlorine ions (Cl$^-$) diffuse into the layer initiating cracks on the surface. The perforation of the oxide film leads to a rapid increase of the corrosion current density as shown in the polarization curve of the SS304 coating (Figure 8.5).
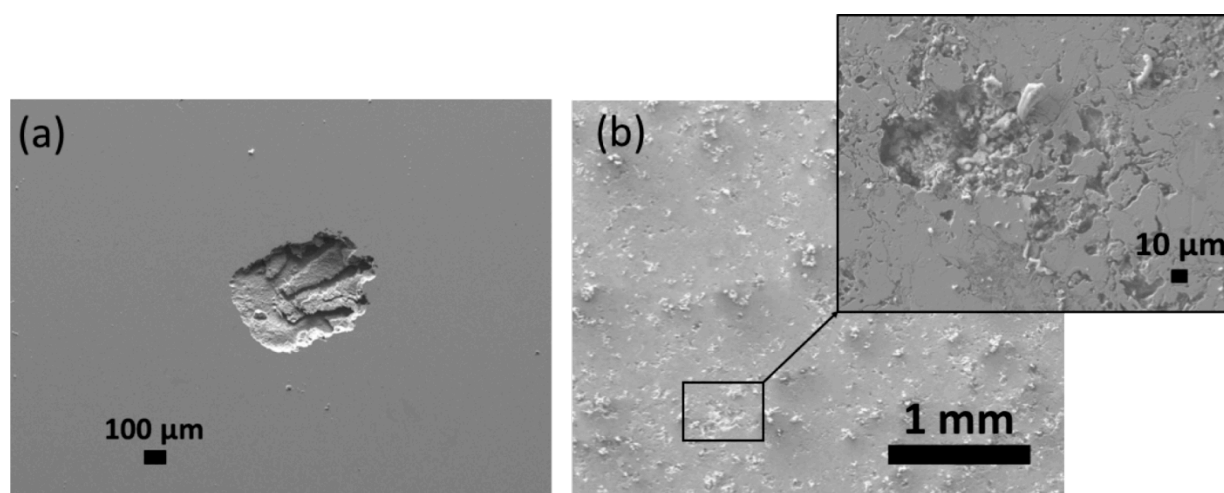
Figure 8.6: SEM micrograph of the surface of the (a) SS304 substrate and (b) Fe₃Al HVOF coating obtained after the corrosion test in a 3.5 % NaCl solution.

In the case of the Fe₃Al coating shown in Figure 8.6b, the surface morphology reveals the presence of corrosion products surrounding defects (cracks, porosities, inter-splat boundaries, oxides). This observation suggests that the corrosion of the Fe₃Al material started in the vicinity of defects. The extent and random distribution of corrosion products confirms that the surface was not protected by a passive oxide film, in conjunction with the presence of inhomogeneity on the surface and subsurface (Figures 8.1a and 8.1a'). Surface inhomogeneity may also create micro-galvanic cells which can aggravate the corrosion process.

Figure 8.7 presents SEM micrographs of the surface of the CrN and DLC coatings after polarization tests. In all cases, the surface morphology shows the presence of pits. Near them, the protective films are removed, and cracks are observed. The size of the pits is typically around 100-150 μm in diameter. DLC and CrN films are well-known for their chemical inertness and excellent corrosion resistance. However, in duplex systems, the films deposited by PVD still exhibit defects (pinholes, porosity, cracks) that can be regarded as passageways for the solution to reach the sublayer or substrate. The corrosion resistance of these coating systems is therefore highly related to surface defects and quality of the top coat.
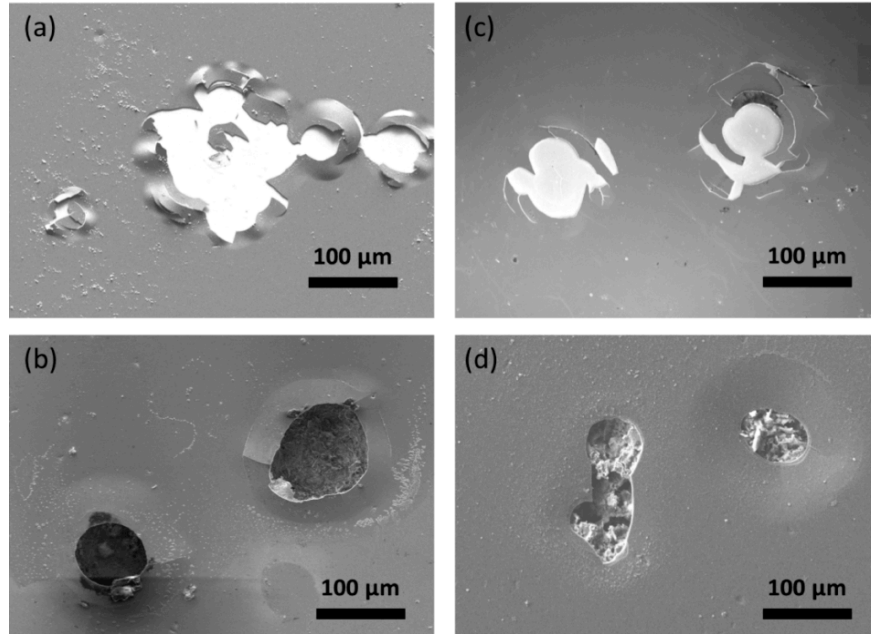
Figure 8.7: SEM micrograph of the surface of coatings obtained after the polarization test in a 3.5% NaCl aqueous solution: (a) CrN/SS304, (b) CrN/Fe$_3$Al/SS304, (c) DLC/SS304 and (d) DLC/Fe$_3$Al/SS304.

8.3.3 Tribocorrosion of the single layer and duplex coatings

We have evaluated the wear tests performed under both cathodic and anodic polarization conditions. For the cathodic polarization, the system was subjected to cathodic protection, i.e., the anodic reactions were suppressed. As a result, the total material loss (W_{total}) from the surface of the coating is principally due to mechanical wear only (W_{mech}), whereas in the case of an anodic polarization, W_{total} is the sum of three components, namely W_{mech}, static corrosion (W_{corr}) and the synergistic action of wear and corrosion (W_{syn}) as represented by the following equation [97]:

$$W_{total} = W_{mech} + W_{corr} + W_{syn} \tag{8.1}$$

where W_{total} can be obtained by weighing the coating after the tribocorrosion test, while W_{corr} is calculated using the Faraday's law:

$$W_{corr} = (I_{corr} \times t \times M) / (z \times F) \tag{8.2}$$

where I_{corr} (A) is the corrosion current measured before rubbing, t (s) is the duration of the sliding wear test, M (g/mol) is the molar mass of the coating, z is the number of electrons transferred

from the dissolution of one atom of the corroded material, and F is the Faraday constant (96485 C/mol).

The term W_{syn} in equation (8.1) can be expressed as a sum of two components:

$$W_{syn} = W_{syn-c} + W_{syn-w} \tag{8.3}$$

where W_{syn-c} represents the material loss due to corrosion during rubbing and W_{syn-w} is the material loss by wear during the tribocorrosion test. The W_{syn-c} component can be calculated as before using the Faraday's law but in this case, I_{corr} is the mean current measured during rubbing. Finally, W_{syn-w} is calculated from equations 8.1 and 8.3 as follows:

$$W_{syn-w} = W_{total} - W_{corr} - W_{mech} - W_{syn-c} \tag{8.4}$$

The total mass loss and its components for the $Fe_3Al/SS304$, $CrN/Fe_3Al/SS304$ and $DLC/Fe_3Al/SS304$ coating systems are presented in Table 8.3.

Table 8.3: Total weight loss and its various contributions, and the coefficient of friction of the coatings after the tribocorrosion test.

Samples	Weight loss due to mechanical wear, W_{mech} (mg) (cathodic polarization)	Total weight loss, W_{total} (mg) (anodic polarization)	Weight loss due to corrosion, W_{corr} (mg)	Synergistic contribution to W_{total}, W_{syn} (mg)	
				W_{syn-c}	W_{syn-w}
$Fe_3Al/SS304$	0.9	2.3	0.3	0.2	0.9
$CrN/Fe_3Al/SS304$	0.6	5.2	0.03	0.97	3.6
$DLC/Fe_3Al/SS304$	0.2	7.9	0.002	0.9	6.798

8.3.3.1 Cathodic polarization (-800mV vs SCE)

Under the cathodic polarization condition, W_{mech} represents the total mass loss due to the mechanical interaction between the surface of the coating and the Al_2O_3 ball. The W_{mech} values for the $CrN/Fe_3Al/SS304$ and $DLC/Fe_3Al/SS304$ duplex coatings are 0.6 mg and 0.2 mg, respectively, which are lower than that of the pure Fe_3Al coating (0.9 mg). This indicates that the mechanical wear under wet conditions is reduced, respectively, by a factor of 1.5 or 4.5 when a CrN or DLC top layer are added.

SEM micrographs of the surface of the wear track of coatings, after the tribocorrosion tests under cathodic polarizations are shown in Figure 8.8. Inspection of the uncoated Fe_3Al surface reveals cracks, voids and parallel grooves (Figure 8.8a) that result from severe interactions with the Al_2O_3 ball due to repeated contact stresses induced by the hard Al_2O_3 ball during the reciprocal movement [36]. During the wear test, cracks propagate to the subsurface, and the coating material is removed via delamination. In Figure 8.8b, the surface of the wear track of the CrN/Fe_3Al/SS304 sample also shows grooves parallel to the sliding direction, but no cracks have been observed. In contrast, the top surface of the DLC/Fe_3Al/SS304 coating system is smooth with no groove as seen in Figure 8.8c; this can be attributed to the good elastic properties of the amorphous DLC film.

Figure 8.8: SEM micrographs of the surface of the wear track obtained after a tribocorrosion test in a 3.5 % NaCl solution under cathodic polarization of (a) Fe_3Al/SS304, (b) CrN/Fe_3Al/SS304, and (c) DLC/Fe_3Al/SS304 coatings.

8.3.3.2 Anodic polarization (+250mV vs SCE)

The evolution of I_{corr} and the coefficient of friction (μ) during the tribocorrosion test under the anodic polarization is shown in Figure 8.9. During the OCP measurement, no current is recorded for 3600 s for all coatings. Before the onset of the wear test, the current increases until a plateau is reached (~0.11 A) for the Fe_3Al coating during the subsequent 1200 s, whereas a weak signal ($<10^{-6}$ A) is recorded for the duplex coatings during the same period of time. This observation is an indication that during the OCP measurements, little or no oxide layer has been formed to protect the surface of the pure Fe_3Al coating, while the CrN/Fe_3Al/SS304 and the DLC/Fe_3Al/SS304 coating surface is better protected by a passive layer.

When rubbing starts, the current gradually drops for the Fe_3Al coating until the end of the wear test. Such evolution of the current during rubbing indicates a tendency of the surface to

passivate either by the formation of an aluminum oxide from the Al exposed to the solution, the closing of pores by the mechanical action of the counter body or from the oxidation of the SS304 substrate after significant infiltration of the electrolyte in the coating. The marginal decrease observed on the coefficient of friction of the Fe_3Al coating (Figure 8.9b) reflects changes occurring on the surface and the influence of the electrolyte and third body in the contact area. From the start of the wear test, an increase of the current is measured after 200 s for the $DLC/Fe_3Al/SS304$ and 400 s for the $CrN/Fe_3Al/SS304$ coatings. This observation suggests that the thin protective layer on the surface of the $CrN/Fe_3Al/SS304$ coating breaks down after 400 s due to interactions with the hard Al_2O_3 ball. An increase of μ is recorded when this event takes place.

In the case of the $DLC/Fe_3Al/SS304$ coating, the chemical inertness of the DLC film is the reason for the ultra-low current with little or no effect on μ as shown in Figure 8.9b. Thereafter, one can notice a slight increase of the current up to approximately 0.004 A and 0.009 A for the $DLC/Fe_3Al/SS304$ and $CrN/Fe_3Al/SS304$ coatings, respectively. In these cases, the slow increase of the current may be related to the gradual increase of the area exposed to the electrolyte which occurs when the wear track is formed and the slow degradation of the protective layer. As the wear test evolves, the width of the wear track increases leading to an increase of I_{corr} (Figure 8.9a). When the wear test stops, a gradual decrease of the current is observed for all coatings; this can be associated with the re-passivation of the surface leading to the reduction of active areas.
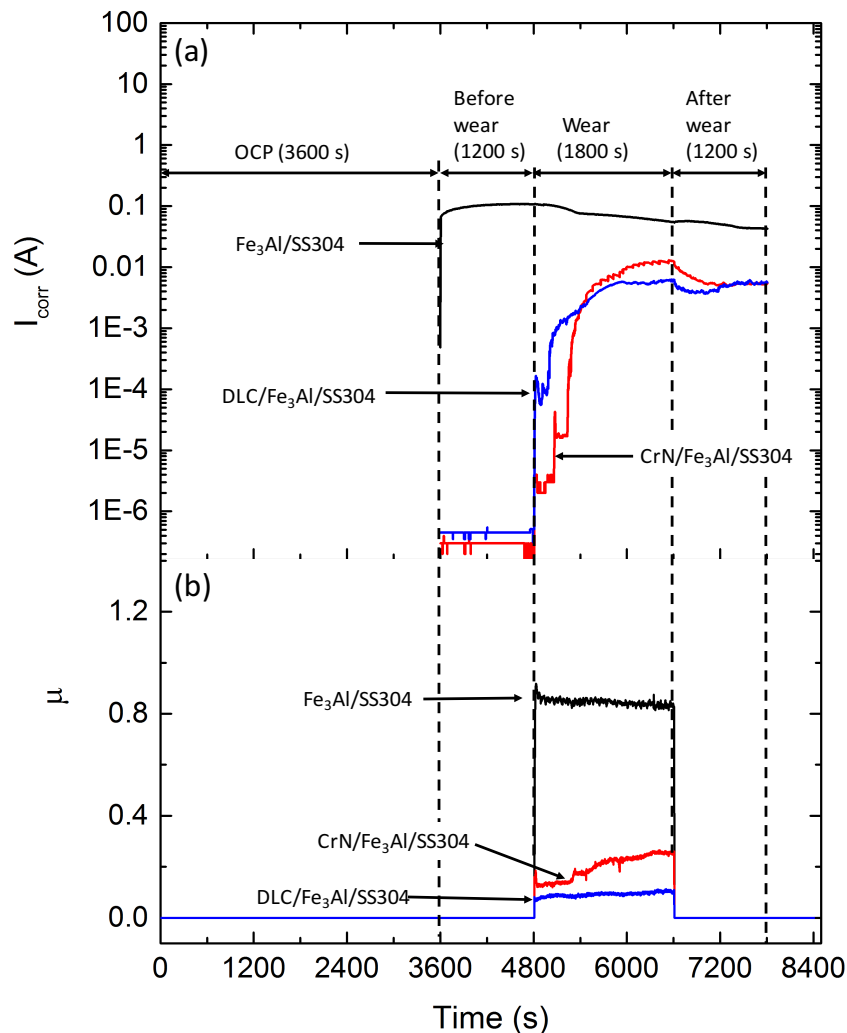
Figure 8.9: Evolution of the corrosion current (a) and the coefficient of friction (b) as a function of time during the tribocorrosion test of all coatings performed under anodic polarization.

For the anodic polarization, W_{total} is a combination of the mass loss due to corrosion, mechanical wear, and a synergistic contribution of both effects as described by the equation (8.1). Therefore, W_{total} for all samples is higher than their corresponding W_{mech}, as presented in Table 8.3. The W_{total} values of duplex coatings are higher than that of the Fe$_3$Al coating suggesting that under the anodic polarization conditions used in this work, the CrN and DLC layers do not sufficiently protect the Fe$_3$Al coating when corrosion and wear act simultaneously. When W_{corr} and W_{syn} are compared (Table 8.3), it can be seen that W_{corr} which ranges from 0.1 - 0.001 mg is a small fraction of W_{total} [189]. Therefore, the major contribution to the mass loss originates from synergistic effects between wear and corrosion. By comparing the weight loss due to corrosion, it can be seen that W_{syn-c} is comparable to W_{corr} in the case of Fe$_3$Al/SS304 but much higher for the

duplex coatings. This is an indication that rubbing has a strong influence corrosion rates in the case of the duplex coatings.
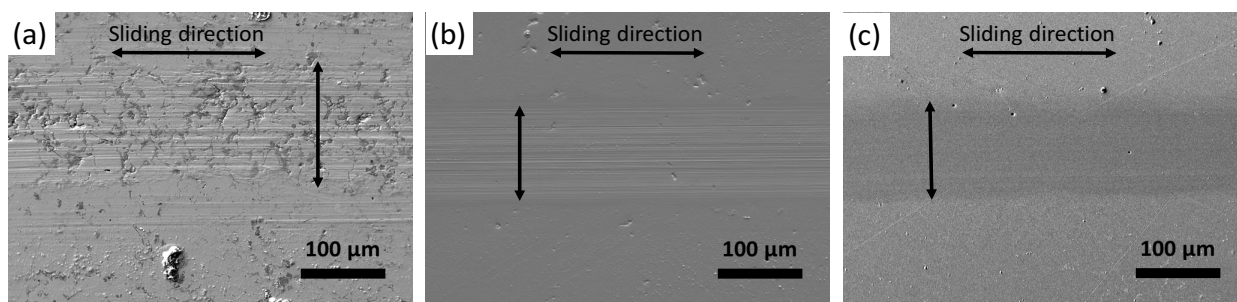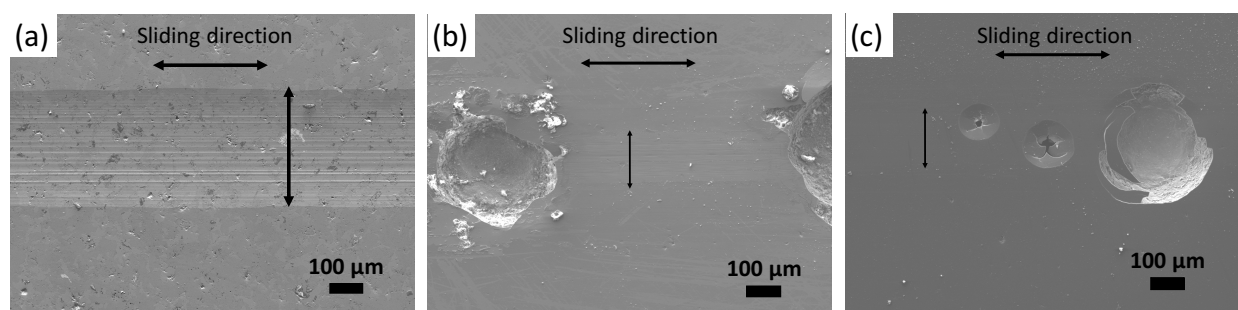

Figure 8.10: SEM micrographs of the surface of the wear track obtained after a tribocorrosion test in a 3.5 % NaCl solution under anodic polarization of: (a) $Fe_3Al/SS304$, (b) $CrN/Fe_3Al/SS304$, and (c) $DLC/Fe_3Al/SS304$ coatings.

The difference between the W_{syn-w} components of the three samples is relatively large. For duplex coatings, W_{syn-w} is significantly higher compared to W_{mech} which means that the mechanical wear is substantially aggravated by the corrosion process and the presence of corrosion products. During rubbing, the oxide layer formed is destroyed and as a result, new fresh surfaces are accessible by the electrolyte. This increases the electrochemical activities of the surface. Moreover, the repeated formation and destruction of the protective oxide layer inside the wear track likely leads to the generation of wear debris that acted as abrasive components inside the wear track and accelerate material removal. Finally, in the case of the duplex coatings, strong galvanic couples consisting of $DLC-Fe_3Al$ and $CrN-Fe_3Al$ (see Figure 8.2) are being formed on the surface during the tribocorrosion tests. These local defects accelerate corrosion and lead to the formation of pits at the surface.

SEM images obtained from the wear track of coatings under the anodic polarization are presented in Figure 8.10. Inspection of the surface reveals the presence of parallel grooves inside the wear track of the $Fe_3Al/SS304$ coating (Figure 8.10a) compared to the $CrN/Fe_3Al/SS304$ and the $DLC/Fe_3Al/SS304$ duplex coatings (Figures 8.10b and 8.10c, respectively) where large pits are observed.

In the case of the pure Fe_3Al HVOF coating, the total mass loss comes from significant contributions of the wear and corrosion processes. For duplex coatings, the severe damage is related to the fact that the mechanical action of the wear process breaks down the passive film

while inducing cracks in the PVD layer. The electrolyte infiltrates the interface between the PVD film and the Fe$_3$Al coating. This leads to the formation of strong galvanic couples between the CrN or DLC component and the Fe3Al sublayer. As a result, the subsurface is subjected to severe pitting corrosion that weakened the coating structure and generated large voids upon continuous loading and unloading.

8.3.4 Conclusion

The corrosion behavior of the Fe$_3$Al-based HVOF coating evaluated in a 3.5 % NaCl aqueous solution was compared to the duplex CrN/Fe$_3$Al/SS304 and the DLC/Fe$_3$Al/SS304 coatings. The single layer Fe$_3$Al coating exhibits a poor corrosion resistance, while the addition of CrN and DLC layers shifts the corrosion potential from -0.7 V for the Fe$_3$Al coating to -0.34 V and -0.09 V for the duplex coatings respectively (Table 8.2). This leads to a decrease of the corrosion rates by formation of a protective barrier against the corrosive electrolyte.

The corrosion current density of the uncoated Fe$_3$Al coating decreases by one and three orders of magnitude with the addition of CrN and DLC films, respectively. The poor corrosion resistance of the Fe$_3$Al coating is related to the presence of defects that favor infiltration of the electrolyte within the coating, thus contributing to the rapid dissolution of the iron aluminide material. The electrochemical impedance spectroscopy investigation revealed that the PVD layers tend to act as a protective capacitive barrier between the electrolyte and the Fe$_3$Al coating.

The tribocorrosion studies of coatings subjected to cathodic polarization show that the DLC and CrN top layers help in reducing material removal during wear. However, the simultaneous action of wear and corrosion in a 3.5 % NaCl aqueous solution under anodic polarization conditions leads to severe damages once the protective top layer of DLC and CrN has been broken by the hard Al$_2$O$_3$ counterpart. This leads to the formation of strong CrN-Fe$_3$Al and DLC-Fe$_3$Al galvanic couples. Thus, the major contribution to the total material loss is the contribution due to synergistic effects of wear and corrosion and more specifically, the mass loss by wear during rubbing as a result of galvanic corrosion.

8.3.5 Acknowledgments

CHAPTER 9   GENERAL DISCUSSION

This chapter provides a summary and a general discussion of the results presented in the last five chapters. In the first section, I summarize the main findings and discuss how they have fulfilled the objectives defined in Chapter 1. The following section discusses the main contribution of this research to the development of iron aluminide alloys for wear applications. The chapter concludes with ideas and interests that can be explored to further enhance the tribo-mechanical properties of the materials developed in this thesis.

9.1   Summary of the main results

The concept of structural modification by the addition of hard secondary phases in a metal matrix via mechanical ball-milling was used in this thesis as the principal tool to enhance the mechanical and wear properties of iron aluminide (Fe_3Al). In this context, two composite powder systems were considered: the first system consisted of an Fe_3Al matrix in which AlN and Fe_2B phases formed *in situ* within the matrix during the fabrication process; and the second system was made using the same matrix, but it was reinforced *in situ* with TiN and TiB_2 phases. Further improvement of the mechanical and wear properties of the Fe_3Al-based HVOF coatings was achieved via surface engineering where sputter-deposited CrN and DLC top coats were added. A summary of the mechanical and the tribological properties of the coatings fabricated in the context of this thesis are presented in Table 9.1. As mentioned in Chapter 3, all wear tests were performed using an Al_2O_3 ball (4.75 mm diameter) as a counterpart.

In the first powder system, we controlled the microstructure of the Fe_3Al matrix with different concentrations of the BN phases using ball-milling. Composite materials with different inclusion sizes (400 nm - 1.2 μm) were obtained after heat treatment and re-milling. Consequently, the mechanical performance of the SS304 substrate was significantly enhanced with the addition of the Fe_3Al-based HVOF coatings. The microhardness (4.3 GPa) of the pure Fe_3Al/SS304 coating was found to increase up to 7.8 GPa and 8.9 GPa when the BN, and a combination of AlN and Fe_2B phases were added, respectively; its wear rate ($\sim 10^{-6}$ mm^3/Nm) decreases by one order of magnitude when an optimum amount of ceramic inclusions was added.

Table 9.1: Summary of the mechanical and tribological properties of different coating systems fabricated in the context of this thesis.

	Coating systems	H (GPa)	E (GPa)	H/E	K (mm^3/Nm) at 5 N	K (mm^3/Nm) at 10 N	K (mm^3/Nm) at 15 N	μ	Wear mechanisms
First coating system HVOF/SS304	SS304	1.3 ± 0.04	175 ± 7	0.007	8.5×10^{-5}	$<3 \times 10^{-4}$	$> 3 \times 10^{-4}$	0.8	Fracture and adhesion
	Fe$_3$Al/SS304	4.3 ± 0.8	131 ± 9	0.033	9.7×10^{-6}	2.9×10^{-4}	-	0.7-0.8	Delamination and fracture
	Fe$_3$Al-BN/SS304	7.8 ± 2.1	141 ± 12	0.068	5×10^{-7}	-	-	0.8	Delamination
	Fe$_3$Al-AlN-Fe$_2$B/SS304	8.9 ± 1.7	195 ± 10	0.065	2.1×10^{-7}	-	-	0.6 - 0.7	Fracture and abrasion
Second coating system HVOF/SS304	Fe$_3$Al-TiN-TiB$_2$/SS304 (*in situ*)	14.2 ± 1.6	217 ± 10	0.064	-	9.3×10^{-7}	-	0.6	Delamination, abrasion
	Fe$_3$Al-TiN-TiB$_2$/SS304 (*in situ*)	9.3 ± 1.5	177 ± 13	0.053	1.2×10^{-6}	-	-	0.6 - 0.7	Abrasive and adhesion
	Fe$_3$Al-TiN-TiB$_2$/SS304 (*ex situ*)	6.5 ± 1.4	149 ± 12	0.044	5.6×10^{-6}	-	-	0.6 - 0.7	Abrasive and oxidation
PVD coated substrate*	CrN/SS304	19 ± 2.3	230 ± 11	0.083	3.5×10^{-7}	6.2×10^{-6}	1×10^{-5}	0.3	Fracture and Plastic deformation
	DLC/SS304	14 ± 1.8	150 ± 9	0.093	1.4×10^{-7}	2.6×10^{-7}	5.1×10^{-7}	< 0.1	Plastic deformation
PVD/HVOF/SS304 duplex systems*	CrN/Fe$_3$Al/SS304	-	-	-	2.6×10^{-7}	5.4×10^{-7}	7.8×10^{-5}	0.3 - 0.7	Fracture, abrasive and oxidation
	CrN/Fe$_3$Al-TiN-TiB$_2$/SS304	-	-	-	9×10^{-8}	3.8×10^{-7}	9.1×10^{-6}	0.3 - 0.7	Fracture, abrasive and oxidation
	DLC/Fe$_3$Al/SS304	-	-	-	1.0×10^{-7}	1.8×10^{-7}	3.6×10^{-7}	< 0.1	Plastic deformation
	DLC/Fe$_3$Al-TiN-TiB$_2$/SS304	-	-	-	7×10^{-8}	9×10^{-8}	2.3×10^{-7}	< 0.1	Plastic deformation and abrasion

* The mechanical properties of the top coat (CrN or DLC film) using nanoindentation. Sliding velocities are: 20 cm/s (dark gray), 14.7 cm/s (middle-gray), and 4.83 cm/s (light gray).

The tribo-mechanical properties of the Fe$_3$Al alloy was also enhanced using the second powder system: in this case, the homogeneous dispersion of fine *in situ* precipitates of the TiN and TiB$_2$ phases in the Fe$_3$Al matrix led to the increase of the hardness value by a factor of about

3.3 and 1.6 compared to the Fe_3Al and Fe_3Al-AlN-Fe_2B coatings, respectively. However, the wear rate of the HVOF coatings prepared with this powder system was of the same order of magnitude compared to the first powder system. The comparison of the HVOF coatings prepared from the composite powders fabricated via the *in situ* and *ex situ* routes showed that the presence of pre-formed ceramic particles in the Fe_3Al matrix exposes a large portion of the soft matrix which has a detrimental effect on the mechanical properties of coatings as opposed to *in situ* precipitated phases. The wear results have shown that the *in situ* HVOF coatings exhibit higher resistance to sliding wear compared to the *ex situ* coatings, irrespective of the sliding velocity.

In the continuation to further enhance the mechanical and the wear properties of the HVOF coatings fabricated in this thesis, we designed a thin-on-thick coating system in which sputter-deposited CrN and DLC top coats were added to the Fe_3Al-based HVOF coatings. It was shown that the wear resistance at low load (5 N) of the SS304 substrate and of the HVOF/SS304 system was increased with the addition of the sputtered top coats. We demonstrated that the wear resistance of the duplex coatings increases with the microhardness of the HVOF layer, which indicates an improved load-carrying capacity of the thick HVOF layer. The ability of the DLC film to maintain its integrity at high loads (10 N or 15 N), and to form a tribofilm on the counterpart that acts as a solid lubricant to reduce friction are the reasons for the better wear resistance of DLC-based coatings compared to the CrN-based ones.

Although the mechanical and the wear properties of the SS304 substrate and the pure Fe_3Al coating have been enhanced with the addition of hard secondary phases, no significant changes have been observed regarding the coefficient of friction. It remains relatively high (~0.6 - 0.7), irrespective of the composite powder system considered or test conditions employed. Nevertheless, surface engineering the HVOF coatings by the addition of a top coat led to a significant decrease of the friction coefficient from about 0.7 down to 0.3 and <0.1 for CrN and DLC films, respectively.

Following the study of the wear behavior of the Fe_3Al-based HVOF coatings including the thin-on-thick architecture, we focused our attention to their corrosion behavior. The influence of the sputter-deposited CrN and DLC top layers on the corrosion resistance of the Fe_3Al-based HVOF coatings in a chlorine-containing NaCl solution was particularly studied. It was found that the corrosion potential of the uncoated Fe_3Al coating, -0.71 V, was increased up to -0.34 V and

-0.09 V with the addition of the CrN and DLC top coats, respectively. Such improvement was attributed to the good corrosion resistance of the CrN and DLC films. In addition, the corrosion rate of the uncoated Fe_3Al coating (corrosion current density $\sim 10^{-7}$ A/cm^2) decreases by one or three orders of magnitude when the CrN or the DLC top layers were added, respectively. We have used the EIS method to demonstrate that the corrosion process in the Fe_3Al coating was governed by a diffusion process while in the case of the thin-on-thick structures, the corrosion was limited by a charge transfer process.

In tribology interactions, the material loss in a given system can occur under the influence of different wear mechanisms that can take place simultaneously. However, a predominant mode of deterioration can exist. We have shown that the wear mechanisms were strongly dependent on the microstructure of the HVOF coatings. In the case of the pure Fe_3Al coating which exhibited large unmelted particles, delamination was the predominant wear mechanism. The removal of the Fe_3Al particles from the surface was preceded by the propagation of cracks in the subsurface via defects in the HVOF coating. These cracks are initiated by the contact stresses induced by the hard counterpart. For coatings prepared from the first or the second composite powder systems, the abrasive wear was the main mechanism of material loss. The material removed from the surface of the coating contained boride and nitride particles. When entrapped between the coating and the counterpart, these hard particles act as abrasive components to accelerate material removal.

In summary, we believe that the first objective of this thesis, which was to develop wear-resistant Fe_3Al-based HVOF coatings, has been fulfilled. Specifically, we have shown that the mechanical and the wear properties of the pure Fe_3Al coating are significantly enhanced by precipitation strengthening and particle reinforcement with boride and nitride phases. For the first time, the tribo-mechanical properties of the Fe_3Al matrix have been enhanced with "hybrid" secondary phases *in situ* precipitated from the BN and Ti powders using the HEBM and the HVOF techniques.

In Chapters 4 and 6, we have shown that the wear rate is strongly related to the size and the distribution of the secondary phases in the matrix as well as the plastic coefficient (ratio of the *H*/*E*) of the coatings. This illustrate the accomplishment of the second objective which basically

referred to the characterization and the establishment of a relationship between the microstructure and the resulting tribo-mechanical properties of the coatings.

In Chapter 7, we have shown that the sputter-deposited top coats act as a barrier to a corrosive environment providing a good protection against corrosion of the pure Fe_3Al coatings under specific conditions. Therefore, the third objective which had been to evaluate the influence of the thin-on-thick structure on the corrosion behavior of the Fe_3Al coating has been justified as well.

Finally, for different types of coatings, the identified degradation mechanisms were described with respect to the test conditions used as presented in the last five chapters. We believe that the last objective which was in essence to identify and to understand the mechanisms of the materials loss has been fulfilled as well.

9.2 General discussion and conclusions

As mentioned in Chapter 1, the enhancement of the mechanical and wear properties of the iron aluminide has been mainly addressed via microstructural modifications by adding hard secondary phases. For effective protection of components in an industrial context, the physical properties, the applicability of the materials as well as the fabrication cost are considered. This is guided by a good understanding of the degradation mechanisms. From this point of view, the fabrication method for the MMC used in this thesis comprising a metal matrix component of Fe and Al, and a ceramic component, has been protected by a patent (number: US20150225301 A1) [190]. This invention was also related to the fabrication of protective coatings for tribological applications using the HVOF technique.

In practice, the composite materials developed in this thesis exhibit good mechanical and wear properties compared to stainless steel substrates, and their degradation mechanisms vary under the range of tribological conditions used. In the form of HVOF coatings, these materials can offer good wear protection which helps to extend the life time of various engineering surfaces under given application conditions. The results obtained in this work is compared to those published in the literature in Table 9.2.

Table 9.2: Tribo-mechanical characteristics of various Fe_3Al-based alloys found in the literature.

Coating	H (GPa)	E (GPa)	H/E	K (mm³/Nm)	μ	Wear mechanisms
Fe_3Al [191]	~4	121	0.03	10^{-3} - 10^{-4}	~0.7 - 0.8	Fracture, delamination and adhesion
Fe_3Al-TiC [191]	~6	-	-	10^{-5}	~0.7 - 0.8	Abrasion and oxidation
Fe_3Al-TiB_2 [91]	12	201	0.06	10^{-4} - 10^{-7}	~0.7 - 0.8	Oxidation and adhesion
Fe_3Al-WC [75]	3	-	-	10^{-5}	~0.7 - 0.8	Delamination, abrasion and oxidation
Fe_3Al-WC [192]	12			10^{-7}	~0.7 - 0.8	Abrasion and oxidation
Fe_3Al-Al_2O_3 [193]	~2	-	-	10^{-2} - 10^{-3}	0.5	Microploughing, adhesion and oxidation
Fe_3Al/SS304	4.3	131	0.03	9.7×10^{-6}	~0.7 - 0.8	Delamination and fracture
Fe_3Al-AlN-Fe_2B/SS304 (*in situ*)	8.9	195	0.07	2.1×10^{-7}	~0.7	Fracture and abrasion
Fe_3Al-TiN-TiB_2/SS304 (*in situ*)	14.2	217	0.06	9.3×10^{-7}	0.6	Delamination, abrasion

In this work, the effect of the mechanical ball-milling on the microstructure of the composite materials fabricated with BN and Ti powder additions was studied. The hard BN phases tend to refine the grain size of the matrix leading to materials with fine microstructure. This result is consistent with the findings of Rosas *et al.* [80]. These authors attempted to fabricate a composite material from the FeAl and the BN powders by mechanical ball-milling [80]; however, they limited their studies to the microstructural characterization of the ball-milled powders without evaluating the tribo-mechanical properties and the degradation mechanisms.

Our findings are further in agreement with various reports with respect to bulk materials [65, 71, 73, 78, 79, 138, 194-196]. In the form of HVOF coatings, the composite materials fabricated in this thesis exhibit better mechanical properties compared to those in the literature (see Table 9.2).

It is interesting to compare our results to those of Amiriyan *et al.* [91, 191, 197]. With the addition of 70 mol.% of *in situ* TiC phases, Amiriyan *et al.* showed that the microhardness of the

pure Fe_3Al-based HVOF alloys (~3 GPa) increased up to (~7 GPa) [191], and they also reported an increase up to ~12 GPa when 50 vol.% of TiB_2 phases were added [91]. These hardness values are lower compared to that obtained with the Fe_3Al-TiN-TiB_2 coating (~14 GPa) fabricated in our work (see Table 9.2).

The findings of this thesis reveal that there exists an optimum amount of secondary phases that can be added to the Fe_3Al matrix. Our result is thus consistent with Schneibel *et al.* who indicated that this is valid for different types of secondary phases [27]. The hardness of our coatings is higher compared to that of the pure Fe_3Al matrix reinforced with 10 wt.% of WC particles (12 GPa) obtained by Liu *et al.* [192]. The latter authors obtained high hardness of the WC-Fe_3Al material compared to WC-Co due to the presence of fine WC particles. In addition, Wang *et al.* [198] and Bai *et al.* [193] studied the Al_2O_3-reinforced Fe_3Al matrix. This system exhibits a hardness about 7 times lower compared to the coatings studied in this thesis.

We have found that the sliding wear rate of the pure Fe_3Al alloy (~10^{-5} $mm^3N^{-1}m^{-1}$) can be enhanced by one or two orders of magnitude by adding boride and nitride phases whereas its coefficient of friction remains relatively high (0.6 - 0.7). This finding is in agreement with the Amiriyan *et al.*'s study where the Fe_3Al matrix was reinforced with TiC or TiB_2 particles [91, 191], and Xu *et al.*'s [75] and Liu *et al.*'s [192] studies where WC particles were added to the Fe_3Al matrix. The latter authors reported that the wear performance of the WC-Fe_3Al coating is better than that of the WC-Co materials fabricated and tested under similar conditions. On the contrary to our work, some authors use the hardness of the material to predict the wear resistance of a given system [74, 75, 192] while we pointed out the importance of the *H/E* parameter.

In this research, the results from the wear degradation mechanisms depend on the type of materials tested. We have shown that the predominant degradation mechanisms for the unreinforced Fe_3Al alloy are fracture and delamination wear, while for the Fe_3Al matrix containing hard secondary phases abrasive wear prevails. At high sliding velocities, the oxidation wear seems to also contribute to the material's removal process in ambient atmosphere. These findings are supported by Amiriyan *et al.*'s [191] study that found that the large unmelted Fe_3Al particles fracture upon repeated loading and unloading during the wear test, and delamination follows. Moreover, when the sliding velocity increases, the contact temperature increases as well leading to localized oxidation of the surface [75]. For composite materials, the hard ceramic

particles dispersed in the matrix can debond, and act as abrasive components when they are entrapped between the counterpart and the surface of the coating [192].

CHAPTER 10   CONCLUSION AND RECOMMENDATIONS

This thesis has focused on two principal axes, namely the fabrication of HVOF coatings from composite powder materials, and the characterization of the tribo-mechanical properties. It is the first study in the area of tribology at the FCSEL in which all steps (the fabrication of powders, the deposition and characterization of coatings) have been investigated in collaboration with HQ. By comparing the wear results obtained in the literature, I can conclude that the materials fabricated in this thesis exhibit better mechanical and wear properties compared to stainless steel substrates and similar class of composites. Nevertheless, I believed that there exist possibilities for further improvement via the optimization of the microstructure. In fact, some aspects were more prioritized than others, meaning that there are still other ideas and interests that have not been explored yet. Below is a list of recommendations I believe should be explored at HQ and at FCSEL in the near future.

First of all, the preparation of composite powders by mechanical ball-milling and the fabrication of HVOF coatings involves complex thermodynamic reactions; understanding the thermodynamic properties (e.g. Gibb's energies, melting temperature of alloys, etc.) of such reactions can help to better control the fabrication process as well as the material's properties. The thermodynamic properties can be obtained using commercial software such as FactSage [199] or ThermoCalc [200]. These tools can reveal information such as the stable and meta-stable phase equilibria, the amounts of phases and their compositions, the driving force for phase transformations, the phase diagram of multi-components, etc. [200]. I trust that the knowledge of the theoretical prediction and of the thermodynamic calculations of a given system of powder mixture can have a positive influence on the mechanical properties of the materials.

The mechanical characteristics of coatings strongly depend on the microstructure [27]. Therefore, the control of the microstructure can be achieved by controlling the fabrication conditions. However, less attention was given to the deposition conditions such as the temperature of the substrate (or of the already deposited layers), the particle temperature and velocity at the exit of the HVOF gun, and the standoff distance (the distance between the substrate and the exit of the gun). The substrate temperature plays an important role in the buildup of the coating [201]. Moreau *et al*. have shown that with the substrate temperature above room temperature, the deposition efficiency can significantly increase as well as the density of

the coating [201]. They have also demonstrated that the particle temperature has a larger effect on the coating properties than the particle velocity [202]. Berghaus *et al.* [203] have shown that the particle velocity decreases with increasing standoff distance. The complications such as evaporation and oxidation of the powder materials can occur before impinging the substrate [203]. I believe that well-controlling these parameters can help to minimize the risk of oxidation between layers in the coating buildup, help to increase the coating-substrate adhesive as well as the inter-particle bonding, and reduce the porosity level.

In general, the degradation of the composite materials under sliding contact conditions occurs at the surface via fatigue, fracture, delamination and/or oxidation. These degradation mechanisms are enhanced by the presence of defects in the materials. Therefore, reducing the level of defects in the HVOF coatings can delay or inhibit some wear mechanisms. Finally, I believe that the remelting of the already deposited layers can increase the cohesion bond strength between particles and/or splats, and can help to further enhance the tribo-mechanical properties.

The analysis of the wear data can also be carried out in the form of a wear map in which the wear rate is related to more than one parameter (e.g., load, sliding velocity or sliding distance) as shown in Figure 9.1. Simultaneously, the wear mechanism can also be investigated under a wide range of experimental conditions [204]. In this way, it is possible to predict the wear behavior (wear rate, wear mechanisms and/or wear mechanism transitions) of coatings under defined conditions and avoid critical operating conditions where undesirable degradation mechanisms can occur. Wear maps can also be used to establish a relationship between the wear rate and the wear mechanisms [205], or as a tool to engineer surfaces in order to improve the resistance to wear [206].
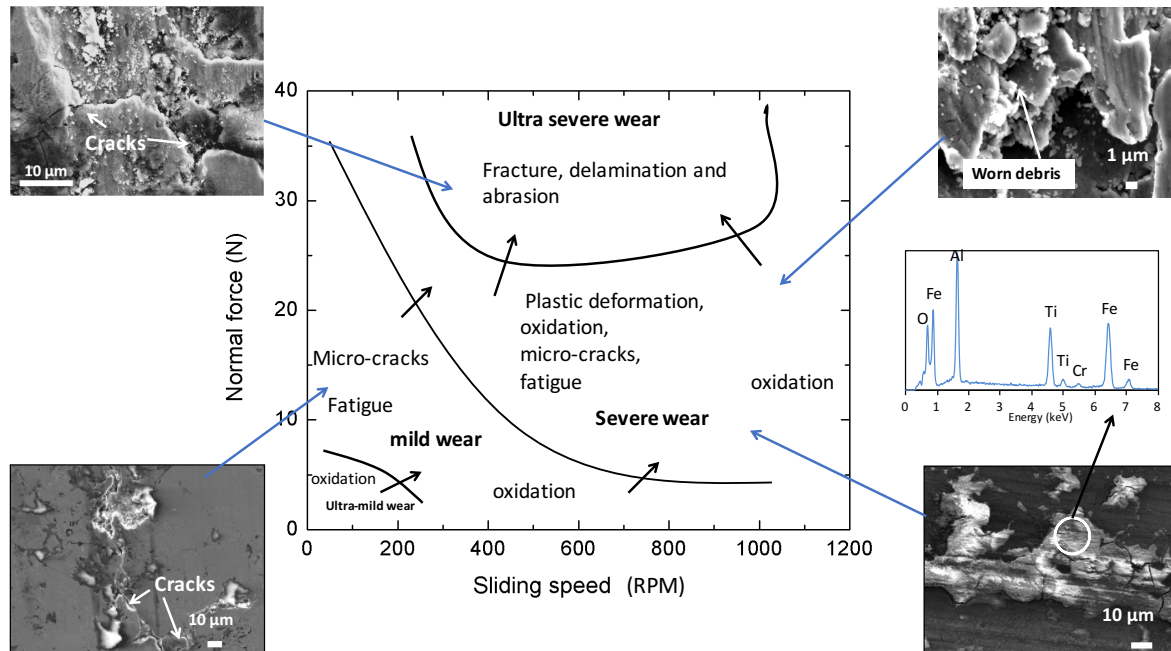
Figure 10.1: Wear mechanism map of the Fe$_3$Al-TiN-TiB$_2$/SS304 HVOF coating.

Finally, modelling can be helpful to predict the behavior of the coatings under well-defined contact conditions. I believe that it can be used to define more precisely the critical operation conditions for various test configurations. Modelling the tribological contact between the counterpart (the hard Al$_2$O$_3$ ball) and the coating surface in the micron scale using finite element can help to obtain tribological contact properties such as contact pressure, contact surface area, stress field and shear stress in order to better comprehend the mechanism of materials loss.

REFERENCES

[1] Hydro-Québec, "Rapport annuel 2016," Bibliothèque et Archives nationales du Québec, 2016.

[2] C. H. Association. (02/10/2017). *Five things you need to know about hydropower: Canada's number one electricity source*. Available: https://canadahydro.ca/facts/

[3] S. Wen and P. Huang, *Principles of tribology*. Hoboken, N.J: John Wiley and Sons, 2012.

[4] C. P. Dillon and Dale. R. MacIntrye, "Forms of Corrosion: Recognition and Prevention," *Chemical Engineering Progress,* vol. 94, p. 73, 1998.

[5] Hydro-Québec. (10-10-2017). *Comprendre l'électricité: les turbines*. Available: http://www.hydroquebec.com/comprendre/hydroelectricite/types-turbines.html

[6] M. A. Inc, "Best practice catalog: Francis turbine," ed. Chattanooge, TN, 2012.

[7] Oerlikon, "Solutions Flash: Robust coating solutions for hydropower turbines extend operating life and maintain efficiency," ed. www.oerlikon.com/metco, 2014.

[8] Voith, "Kaplan turbines," ed. http://www.voith.com/en/t3370e_Kaplan_turbine_screen.pdf, 2012.

[9] Directindustry, "Pelton turbines," ed. http://pdf.directindustry.com/pdf/voith-turbo/pelton-turbines/39449-368978.html, 2009.

[10] J. R. Davis, *Stainless steels*: ASM international, 1994.

[11] C. G. McKamey, "Iron Aluminides," in *Physical Metallurgy and Processing of Intermetallic Compounds*, ed: Springer 1996, pp. 351-391.

[12] R. R. Judkins and U. S. Rao, "Fossil energy applications of intermetallic alloys," *Intermetallics,* vol. 8, pp. 1347-1354, 2000.

[13] D. G. Morris and M. A. Muñoz-Morris, "Recent Developments Toward the Application of Iron Aluminides in Fossil Fuel Technologies," *Advanced Engineering Materials,* vol. 13, pp. 43-47, 2011.

[14] N. S. Stoloff and V. K. Sikka, *Physical metallurgy and processing of intermetallic compounds* New York: Chapman and Hall, 1996.

[15] D. G. Morris, M. A. Muñoz-Morris, and J. Chao, "Development of high strength, high ductility and high creep resistant iron aluminide," *Intermetallics,* vol. 12, pp. 821-826, 2004.

[16] Y.D Huang, W.Y Yang, G.L Chen, and Z. Q. Sun, "On the effect of the B2 thermomechanical treatment in improving the room temperature ductility of Fe_3Al-based alloys," *Intermetallics,* vol. 9, pp. 331 - 340, 2001.

[17] A. Bahadur, B. R. Kumar, and O. N. Mohanty, "Ductility improvement in iron aluminides," *Journal of Materials Science,* vol. 30, pp. 3690-3696, 1995.

[18] V. K. Sikka, "Ductility enhancement of iron-aluminide alloys," *Society of Aerospace Material and Process Engineers,* vol. 22, pp. 2-10, 1991.

[19] C. G. McKamey, J. H. DeVan, P. F. Tortorelli, and V. K. Sikka, "A review of recent developments in Fe₃Al-based alloys," *Journal of Materials Research,* vol. 6, pp. 1779-1805, 1991.

[20] S. Mischler, "Triboelectrochemical techniques and interpretation methods in tribocorrosion: A comparative evaluation," *Tribology International,* vol. 41, pp. 573-583, 2008.

[21] N. S. Stoloff. and C. T. Liu., "Environmental embrittlement of iron aluminides," *Intermetallics,* vol. 2, pp. 75-87, 1994.

[22] B. Cantor, F. P. Dunne, and I. C. Stone, *Metal and ceramic matrix composites*: CRC Press, 2003.

[23] N. S. Stoloff, "Iron aluminides: present status and future prospects," *Materials Science and Engineering: A,* vol. 258, pp. 1-14, 1998.

[24] A. K. Misra, "Identification of thermodynamically stable ceramic reinforcement materials for iron aluminide matrices," *Metallurgical Transactions A,* vol. 21, pp. 441-446, 1990.

[25] I. A. Ibrahim, F. A. Mohamed, and E. J. Lavernia, "Particulate reinforced metal matrix composites - A review," *Journal of Materials Science,* vol. 26, pp. 1137-1156, 1991.

[26] B. Basu and M. Kalin, "Overview: Mechanical Properties of Ceramics," in *Tribology of Ceramics and Composites*, ed: John Wiley and Sons, 2011, pp. 18-38.

[27] J. H. Schneibel, C. A. Carmichael, E. D. Specht, and R. Subramanian, "Liquid-phase sintered iron aluminide-ceramic composites," *Intermetallics,* vol. 5, pp. 61-67, 1996.

[28] S. Zhang, D. Sun, Y. Fu, and H. Du, "Recent advances of superhard nanocomposite coatings: a review," *Surface and Coatings Technology,* vol. 167, pp. 113-119, 2003.

[29] E. O. Hall, "The Deformation and Ageing of Mild Steel: III Discussion of Results," *Proceedings of the Physical Society. Section B,* vol. 64, pp. 747-753, 1951.

[30] N. J. Petch, "The Cleavage Strengh of Polycrystals," *Journal of the Iron and Steel Inst.,* vol. 174, pp. 25-28, 1953 1953.

[31] J. H. Schneibel and P. F. Becher, "Iron and nickel Aluminide composites," *Journal of the Chinese Institute of Engineers,* vol. 22, pp. 1-12, 1999.

[32] Z. GmbH. (04/10/2017). *Function Principle.* Available: http://gmbh.zoz.de/?page_id=1255

[33] A. Iasonna and M. Magini, "Power measurements during mechanical milling. An experimental way to investigate the energy transfer phenomena," *Acta Materialia,* vol. 44, pp. 1109-1117, 1996.

[34] A. Boschetto, M. Bellusci, A. La Barbera, F. Padella, and F. Veniali, "Kinematic observations and energy modeling of a Zoz Simoloyer high-energy ball milling device," *The International Journal of Advanced Manufacturing Technology,* vol. 69, pp. 2423-2435, 2013.

[35] A. Streletskii, D. Permenov, B. Bokhonov, I. Kolbanev, A. Leonov, I. Berestetskaya*, et al.*, "Destruction, amorphization and reactivity of nano-BN under ball milling," *Journal of Alloys and Compounds,* vol. 483, pp. 313-316, 2009.

[36] F. Pougoum, L. Martinu, P. Desjardins, J. Klemberg-Sapieha, S. Gaudet, S. Savoie, *et al.*, "Effect of high-energy ball-milling on the characteristics of Fe$_3$Al-based HVOF coatings containing boride and nitride phases," *Wear,* vol. 358, pp. 97-108, 2016.

[37] F. Pougoum, L. Martinu, J.-E. Klemberg-Sapieha, S. Savoie, and R. Schulz, "Wear properties of Fe$_3$Al-based HVOF coatings strengthened with in-situ precipitated nitride and boride particles," *Surface and Coatings Technology,* vol. 307, Part A, pp. 109-117, 2016.

[38] F. Cardellini, V. Contini, R. Gupta, G. Mazzone, A. Montone, A. Perin, *et al.*, "Microstructural evolution of Al–Fe powder mixtures during high-energy ball milling," *Journal of Materials Science,* vol. 33, pp. 2519-2527, 1998.

[39] S. Gialanella, "FeAl alloy disordered by ball-milling," *Intermetallics,* vol. 3, pp. 73-76, 1995.

[40] J. M. Guilemany, N. Cinca, L. Casas, and E. Molins, "Ordering and disordering processes in MA and MM intermetallic iron aluminide powders," *Journal of Materials Science,* vol. 44, pp. 2152-2161, 2009.

[41] R. McCune, A. Papyrin, J. Hall, W. Riggs, and P. Zajchowski, "An exploration of the cold gas-dynamic spray method for several materials systems," ASM International,, Materials Park, OH1995.

[42] J. R. Davis, "Handbook of thermal spray technology," ed. Materials Park, OH: ASM Thermal Spray Society, 2004.

[43] V. V. Sobolev, J. M. Guilemany, J. Nutting, M. Institute of Materials, and Mining, *High velocity oxy-fuel spraying: theory, structure-property relationships and applications*. London: Maney, 2004.

[44] P. D. Christofides, *Model-Based Control of Particulate Processes*. Los Angeles: Springer, 2002.

[45] D. Von Hofe, *Thermal Spray 2004 : Advances in Technology and Application, Proceedings of the International Thermal Spray Conference*. Materials Park: ASM International, 2004.

[46] L. Pawłowski, *The science and engineering of thermal spray coatings* vol. 2nd. Chichester, England: John Wiley and Sons, 2008.

[47] Sulzer Metco, "An Introduction to Thermal Spray ", www.sulzer.com2013.

[48] R. G. Maev, V. Leshchynsky, and A. Papyrin, *Cold Gas Dynamic Spray*. Boca Raton: CRC Press, 2016.

[49] P. M. Jedrzejowski, *Mechanical and optical properties of plasma deposited superhard nanocomposite coatings*, 2004.

[50] É. Bousser, "Solid particle erosion mechanisms of protective coatings for aerospace applications," Département de génie, physique, École polytechnique de Montréal, Montréal, 2013.

[51] G. W. Stachowiak, *Wear-materials, mechanisms and practice*. Chichester, England: John Wiley and Sons, 2005.

[52]   J. Halling, *Principles of tribology*. London: Macmillan, 1975.

[53]   B. Bhushan, *Principles and applications of tribology*. New York: John Wiley and Sons, 1999.

[54]   J. Archard and W. Hirst, "The wear of metals under unlubricated conditions," in *Proceedings of the Royal Society of London A: Mathematical, Physical and Engineering Sciences*, 1956, pp. 397-410.

[55]   J. Archard, "The temperature of rubbing surfaces," *Wear,* vol. 2, pp. 438-455, 1959.

[56]   W. Hu, T. Kato, and M. Fukumoto, "Synthesis and Characterization of Nanocrystalline Iron Aluminide Intermetallic Compounds," *Transactions of the Japan Institute of Metals,* vol. 44, pp. 2678-2687, 2005.

[57]   J. M. Guilemany, N. Cinca, J. Fernández, and S. Sampath, "Erosion, Abrasive, and Friction Wear Behavior of Iron Aluminide Coatings Sprayed by HVOF," *Journal of Thermal Spray Technology,* vol. 17, pp. 762-773, 2008.

[58]   T. Grosdidier, G. Ji, J.-P. Morniroli, S. Revol, and S. Launois, "Thermal Spraying: Effect of Feedstock Powder Size Fraction on the Nanostructure of Iron Aluminide Coatings Obtained by Thermal Spraying of Milled Powder," in *European Congress and Exhibition on Powder Metallurgy. European PM Conference Proceedings*, 2003, p. 1.

[59]   Su-Ming Zhu, Kazushi Sakamoto, Makoto Tamura, and K. Iwasaki, "Effects of titanium Addition on the microstructure and mechanical behavior of iron aluminide Fe_3Al," *Materials Transactions,* vol. 42, pp. 484-490, 2001.

[60]   Z. R. Zhang and W. X. Liu, "Mechanical properties of Fe3Al-based alloys with addition of carbon, niobium and titanium," *Materials Science and Engineering A-structural Materials Properties Microstructure and processing,* vol. 423, pp. 343-349, 2006.

[61]   M. Amiriyan, H. D. Alamdari, C. Blais, S. Savoie, R. Schulz, and M. Gariépy, "Dry sliding wear behavior of Fe_3Al and Fe_3Al/TiC coatings prepared by HVOF," *Wear,* vol. 342, pp. 154-162, 2015.

[62]   X. Chen, H. Zhai, W. Wang, S. Li, and Z. Huang, "A TiCx reinforced Fe(Al) matrix composite using in-situ reaction," *Progress in Natural Science: Materials International,* vol. 23, pp. 13-17, 2013.

[63]   X. zhang, J. Ma, J. Yang, Q. Bi, and W. Liu, "Dry-sliding tribological behavior of Fe–28Al–5Cr/TiC composites," *Wear,* vol. 271, pp. 881-888, 2011.

[64]   Y. Chen and H. M. Wang, "Microstructure and wear resistance of laser clad TiC reinforced FeAl intermetallic matrix composite coatings," *Surface and Coatings Technology,* vol. 168, pp. 30-36, 2003.

[65]   R. Subramanian and J. H. Schneibel, "FeAl–TiC and FeAl–WC composites—melt infiltration processing, microstructure and mechanical properties," *Materials Science and Engineering A,* vol. 244, pp. 103-112, 1998.

[66]   M. Krasnowski and T. Kulik, "Nanocomposites obtained by mechanical alloying in Fe–Al–Ti–C system," *Journal of Alloys and Compounds,* vol. 448, pp. 227-233, 2008.

[67] M. Z. Mehrizi, A. Saidi, and M. Shamanian, " Fe$_3$Al/TiC nanocomposite produced by mechanical alloying," *Powder Metallurgy,* vol. 54, pp. 408-411, 2011.

[68] S. H. Ko and S. Hanada, "In-situ production and microstructures of iron aluminide/TiC composites," *Intermetallics,* vol. 7, pp. 947-955, 1999.

[69] L.-H. Tian, C.-X. Li, C.-J. Li, and G.-J. Yang, "Effect of Dispersed TiC Content on the Microstructure and Thermal Expansion Behavior of Shrouded-Plasma-Sprayed FeAl/TiC Composite Coatings," *Journal of Thermal Spray Technology,* vol. 21, pp. 689-694, 2012.

[70] K. Matsuura and Y. Obara, "Combustion Synthesis of TiB$_2$ Particle Dispersed Metal Matrix Composites," in *Materials science forum*, 2007, pp. 809-813.

[71] R. Subramanian, C. G. McKamey, J. H. Schneibel, L. R. Buck, and P. A. Menchhofer, "Iron aluminide Al$_2$O$_3$ composites by in situ displacement reactions: processing and mechanical properties," *Materials Science and Engineering A-Structural Materials Properties Microstructure and Processing,* vol. 254, pp. 119-128, 1998.

[72] J. Li, F.-L. Kwong, R.-X. Shi, D. H. L. Ng, and Y.-S. Yin, "Microstructure and properties of in situ nanometric Al$_2$O$_3$ reinforced α-Fe(Al)– Fe$_3$Al-based composites," *Materials Science and Engineering: A,* vol. 526, pp. 50-55, 2009.

[73] J. Kim, B. Park, Y. Park, I. Park, and H. Lee, "Mechanical properties of in-situ FeAl-TiB$_2$ intermetallic matrix composites," *International Journal of Modern Physics B,* vol. 23, pp. 1479-1484, 2009.

[74] T. Itoi, S. Mineta, H. Kimura, K. Yoshimi, and M. Hirohashi, "Fabrication and wear properties of Fe$_3$Al-based composites," *Intermetallics,* vol. 18, pp. 2169 - 2177, 2010.

[75] B. Xu, Z. Zhu, S. Ma, W. Zhang, and W. Liu, "Sliding wear behavior of Fe–Al and Fe–Al/WC coatings prepared by high velocity arc spraying," *Wear,* vol. 257, pp. 1089-1095, 2004.

[76] S. Huang, O. Van der Biest, and J. Vleugels, "Pulsed electric current sintered Fe$_3$Al bonded WC composites," *International Journal of Refractory Metals and Hard Materials,* vol. 27, pp. 1019-1023, 2009.

[77] A. Y. Mosbah, D. Wexler, and A. Calka, "Abrasive wear of WC–FeAl composites," *Wear,* vol. 258, pp. 1337-1341, 2005.

[78] T. Grosdidier, G. Ji, and N. Bozzolo, "Hardness, thermal stability and yttrium distribution in nanostructured deposits obtained by thermal spraying from milled - Y$_2$O$_3$ reinforced - or atomized FeAl powders," *Intermetallics,* vol. 14, pp. 715-721, 2006.

[79] W. Yucheng, R. Rong, T. Wenming, W. Fengtao, and Z. Zhixiang, "Structural Evolution and Mechanical Properties of Nanocrystalline FeAl Intermetallic and its Composites Consolidated from Powders Prepared by Mechanical Alloying " *International Journal of Condensed Matter, Advanced Materials, and Superconductivity Research,* vol. 11, p. 1, 2012.

[80] G. Rosas, C. Patiño-Carachure, O. Tellez, and J. Reyes-Gasga, "Electron microscopy and X-ray diffraction characterization of FeAl-BN nanocomposites produced by mechanical alloying," *Acta Microscopica,* vol. 19, pp. 285-290, 2010.

[81]   A. Agarwal, M. J. Akhtar, and R. Balasubramaniam, "Effect of alloying on aqueous corrosion and mechanical behaviour of iron aluminide Fe$_3$Al," *Journal of Materials Science,* vol. 31, pp. 5207-5213, 1996.

[82]   J. G. Kim and R. A. Buchanan, "Pitting and crevice corrosion of iron aluminides in a mild acid-chloride solution," *Corrosion,* vol. 50, pp. 658-668, 1994.

[83]   V. S. Rao, R. G. Baligidad, and V. S. Raja, "Effect of carbon on corrosion behaviour of Fe$_3$Al intermetallics in 0.5 M sulphuric acid," *Corrosion Science,* vol. 44, pp. 521-533, 2002.

[84]   M. Azzi, P. Amirault, M. Paquette, J. E. Klemberg-Sapieha, and L. Martinu, "Corrosion performance and mechanical stability of 316L/DLC coating system: Role of interlayers," *Surface and Coatings Technology,* vol. 204, pp. 3986-3994, 2010.

[85]   R. Bayón, A. Igartua, X. Fernández, R. Martínez, R. J. Rodríguez, J. A. García*, et al.*, "Corrosion-wear behaviour of PVD Cr/CrN multilayer coatings for gear applications," *Tribology International,* vol. 42, pp. 591-599, 2009.

[86]   C. Liu, A. Leyland, Q. Bi, and A. Matthews, "Corrosion resistance of multi-layered plasma-assisted physical vapour deposition TiN and CrN coatings," *Surface and Coatings Technology,* vol. 141, pp. 164-173, 2001.

[87]   Horiba, "Laser scattering particle size distribution analyzer, LA-900," Kyoto, Japan1994.

[88]   W. C. Oliver and G. M. Pharr, "An improved technique for determining hardness and elastic modulus using load and displacement sensing indentation experiments," *Journal of Materials Research,* vol. 7, pp. 1564-1583, 1992.

[89]   ASTM-C1327-15, "Standard Test Method for Vickers Indentation Hardness of Advanced Ceramics," ed. West Conshohocken, PA: ASTM International, 2015.

[90]   A. C. Fischer-Cripps, *Nanoindentation* vol. 3rd. New York: Springer, 2011.

[91]   M. Amiriyan, C. Blais, S. Savoie, R. Schulz, M. Gariépy, and H. Alamdari, "Tribo-Mechanical Properties of HVOF Deposited Fe$_3$Al Coatings Reinforced with TiB$_2$ Particles for Wear-Resistant Applications," *Materials,* vol. 9, p. 117, 2016.

[92]   V. F. Lvovich, *Impedance spectroscopy: applications to electrochemical and dielectric phenomena*. Hoboken, N.J Wiley, 2012.

[93]   B. Jayaraj, S. Vishweswaraiah, V. H. Desai, and Y. H. Sohn, "Electrochemical impedance spectroscopy of thermal barrier coatings as a function of isothermal and cyclic thermal exposure," *Surface and Coatings Technology,* vol. 177, pp. 140-151, 2004.

[94]   M. E. Orazem and B. Tribollet, *Electrochemical impedance spectroscopy*. Hoboken, N.J: Wiley, 2008.

[95]   A. J. Bard and L. R. Faulkner, *Electrochemical methods: fundamentals and applications* vol. 2nd. New York: John Wiley and Sons, 2001.

[96]   N. Perez, *Electrochemistry and Corrosion Science*: Springer, 2004.

[97]   M. Azzi, "Role of synergy between wear and corrosion in degradation of materials," NR66642 Ph.D., McGill University (Canada), Ann Arbor, 2009.

[98]   B. D. Cullity, *Elements of x-ray diffraction* vol. 2d Reading, Mass: Addison-Wesley, 1978.

[99]   Z. Li. and W. Gao, "High temperature corrosion of intermetallics," in *Intermetallics Research Progress*, ed New York: Nava Science Publishers Inc, 2008, pp. 1-64.

[100]   V. Sikka, C. McKamey, C. Howell, and R. Baldwin, "Fabrication and mechanical properties of Fe$_3$Al-based iron aluminides," Oak Ridge National Laboratory, Oak Ridge, 1990.

[101]   L. M. Peng, H. Li, J. H. Wang, and M. Gong, "High strength and high fracture toughness ceramic−iron aluminide (Fe$_3$Al) composites," *Materials Letters,* vol. 60, pp. 883-887, 2006.

[102]   M. Krasnowski and T. Kulik, "Nanocrystalline FeAl–TiN composites obtained by hot-pressing consolidation of reactively milled powders," *Scripta Materialia,* vol. 57, pp. 553-556, 2007.

[103]   M. Krasnowski and T. Kulik, "Nanocrystalline FeAl matrix composites reinforced with TiC obtained by hot-pressing consolidation of mechanically alloyed powders," *Intermetallics,* vol. 15, pp. 1377-1383, 2007.

[104]   R. Subramanian and J. H. Schneibel, "Processing iron-Aluminide Composites Containing Carbides or Borides," *Journal of the Minerals, Metals and Materials Society,* pp. 50-68, 1997.

[105]   B. Xu., Z. Zhu., S. Ma., W. Zhang., and W. Liu., "Sliding wear behavior of Fe–Al and Fe–Al/WC coatings prepared by high velocity arc spraying," *Wear,* vol. 257, pp. 1089-1095, 2004.

[106]   K. Taylor and C. Lenie, "Some properties of aluminum nitride," *Journal of the Electrochemical Society,* vol. 107, pp. 308-314, 1960.

[107]   O. Ozdemir, M. Usta, C. Bindal, and A. H. Ucisik, "Hard iron boride (Fe$_2$B) on 99.97wt% pure iron," *Vacuum,* vol. 80, pp. 1391-1395, 2006.

[108]   B. Xiao, J. D. Xing, S. F. Ding, and W. Su, "Stability, electronic and mechanical properties of Fe$_2$B," *Physica B: Condensed Matter,* vol. 403, pp. 1723-1730, 2008.

[109]   L. Avril, B. Courant, and J. J. Hantzpergue, "Tribological performance of α-Fe(Cr)-Fe$_2$B-FeB and α-Fe(Cr)-h-BN coatings obtained by laser melting," *Wear,* vol. 260, pp. 351-360, 2006.

[110]   Q. Zheng, "In-situ processing of aluminum nitride particle reinforced aluminum alloy composites," Dissertation/Thesis Ph.D., Applied sciences, The university of Alabama, Ann Arbor, 2003.

[111]   C. Suryanarayana, "Mechanical alloying and milling," *Progress in Materials Science,* vol. 46, pp. 1-184, 2001.

[112]   P. Soni, *Mechanical alloying: fundamentals and applications*: Cambridge Int Science Publishing, 1998.

[113] E. H. Jazi, G. Borhani, and R. E. Farsani, "Preparation of Al-Fe/TiB$_2$ nanocomposite powder by ball milling and subsequent heat treatment," *Micro and Nano Letters,* vol. 7, pp. 448-452, 2012.

[114] R. Esparza, G. Rosas, J. A. Ascencio, and R. Pérez, "Effects of Minor Element Additions to the Nanocrystalline FeAl Intermetallic Alloy Obtained by Mechanical Alloying," *Materials and Manufacturing Processes,* vol. 20, pp. 823-832, 2005.

[115] H. Nakayama, S. Tada, K. Ozaki, and K. Kobayashi, "Fabrication of TiB$_2$–FeAl Cermet by Mechanical Milling and Subsequent Pulsed Current Sintering," *Materials Transactions,* vol. 52, pp. 1457-1461, 2011.

[116] K. Wolski, G. L. Caër, P. Delcroix, R. Fillit, F. Thévenot, and J. L. Coze, "Influence of milling conditions on the FeAl intermetallic formation by mechanical alloying," *Materials Science and Engineering,* vol. A207, pp. 97-104, 1996.

[117] A. I. Gusev and A. S. Kurlov, "Production of nanocrystalline powders by high-energy ball milling: model and experiment," *Nanotechnology,* vol. 19, p. 265302, 2008.

[118] A. Valeeva, H. Schroettner, and A. Rempel, "Preparation of nanocrystalline VOy by high-energy ball milling," *Inorganic Materials,* vol. 47, pp. 408-411, 2011.

[119] P. Bhattacharya, P. Bellon, R. S. Averback, and S. J. Hales, "Nanocrystalline TiAl powders synthesized by high-energy ball milling: effects of milling parameters on yield and contamination," *Journal of Alloys and Compounds,* vol. 368, pp. 187-196, 2004.

[120] F. J. Pérez, M. P. Hierro, J. A. Trilleros, M. C. Carpintero, L. Sánchez, J. M. Brossard*, et al.*, "Iron aluminide coatings on ferritic steels by CVD-FBR technology," *Intermetallics,* vol. 14, pp. 811-817, 2006.

[121] K. E. Schneider, V. Belashchenko, M. Dratwinski, S. Siegmann, and A. Zagorski, *Thermal spraying for power generation components*. Weinheim: John Wiley and Sons, 2006.

[122] V. V. Sobolev, J. M. Guilemany, and J. Nutting, *High velocity oxy-fuel spraying : theory, structure-property relationships and applications* London, Maney, 2004.

[123] W. C. Oliver. and G. M. Pharr., "Improved technique for determining hardness and elastic modulus using load and displacement sensing indentation experiments," *Journal of Materials Research,* vol. 7, pp. 1564-1583, 1992.

[124] R. J. D. Tilley, *Understanding Solids: The Science of Materials*: Wiley, 2004.

[125] A. L. Ortiz and L. Shaw, "X-ray diffraction analysis of a severely plastically deformed aluminum alloy," *Acta Materialia,* vol. 52, p. 2185, 2004.

[126] D. G. Morris, I. Gutierrez-Urrutia, and M. Munoz-Morris, "Hardening and softening in milled nanostructured FeAl on annealing," *Scripta materialia,* vol. 57, pp. 369-372, 2007.

[127] L. I. Berger, *Semiconductor Materials*: CRC Press, 1996.

[128] C. C. Degnan and P. H. Shipway, "The incorporation of self-propagating, high-temperature synthesis-formed Fe-TiB$_2$ into ferrous melts," *Metallurgical and Materials Transactions A,* vol. 33, pp. 2973-2983, 2002.

[129] Ghosh G. Al-B-Fe Phase diagram [Online]. Available: http://www1.asminternational.org/AsmEnterprise/APD

[130] B. Hallemans. B-Fe Phase diagram [Online]. Available: http://www1.asminternational.org/AsmEnterprise/APD

[131] F. A. Hummel, "Introduction to phase equilibria in ceramic systems," 1984.

[132] M. Balasubramanian, "Nanocomposites," in *Composite Materials and Processing*, ed: CRC Press, 2013, pp. 511-594.

[133] L. L. Shaw, D. Goberman, R. Ren, M. Gell, S. Jiang, Y. Wang, *et al.*, "The dependency of microstructure and properties of nanostructured coatings on plasma spray conditions," *Surface and coatings technology,* vol. 130, pp. 1-8, 2000.

[134] T. Grosdidier, H. Liao, and A. Tidu, "X-ray and TEM characterization of nanocristalline iron aluminide coatings prepared by HVOF thermal spraying," in *ITSC*, Canada-Montreal, 2000, pp. 1341-1344.

[135] B. Basu and M. Kalin, "Wear Mechanisms," in *Tribology of Ceramics and Composites*, ed: John Wiley and Sons, 2011, pp. 70-100.

[136] Z. Li and W. Gao, *High temperature corrosion of intermetallics*: Nova Science Publishers, 2009.

[137] N. S. Stoloff and V. K. Sikka, *Physical metallurgy and processing of intermetallic compounds*. London: Chapman & Hall, 1996.

[138] R. Krein, A. Schneider, G. Sauthoff, and G. Frommeyer, "Microstructure and mechanical properties of Fe$_3$Al-based alloys with strengthening boride precipitates," *Intermetallics,* vol. 15, pp. 1172 - 1182, 2007.

[139] S. Suryanarayana, "Mechanism of alloying," in *Mechanical Alloying and Milling*, ed New York CRC Press 2004, pp. 83-94.

[140] P. Schwarzkopf, R. Kieffer, and F. Benesousky, *Refractory hard metals: borides, carbides, nitrides and silicides*: Macmillan, 1953.

[141] Y. Li, K. Matsuura, M. Ohno, Y. Gao, and J. Yu, "Combustion synthesis of TiB2 based hard material cemented by Fe-Al intermetallics," *Powder Metallurgy,* vol. 55, pp. 162-167, 2012.

[142] D. E. Alman, J. A. Hawk, J. H. Tylczak, C. P. Dogan, and R. D. Wilson, "Wear of iron–aluminide intermetallic-based alloys and composites by hard particles," *Wear,* vol. 251, pp. 875-884, 2001.

[143] J.-H. Shim, J.-S. Byun, and Y. W. Cho, "Mechanochemical synthesis of nanocrystalline TiN/TiB$_2$ composite powder," *Scripta materialia,* vol. 47, pp. 493-497, 2002.

[144] J. Li, K. Hu, and Y. Zhou, "Formation of TiB$_2$/TiN nanocomposite powder by high energy ball milling and subsequent heat treatment," *Materials Science and Engineering: A,* vol. 326, pp. 270-275, 2002.

[145] L. X. Qiu, B. Yao, Z. H. Ding, W. T. Zheng, Y. J. Zheng, and X. P. Jia, "Characterization of structure and properties of TiN–TiB$_2$ nano-composite prepared by ball milling and high pressure heat treatment," *Journal of Alloys and Compounds,* vol. 456, pp. 436-440, 2008.

[146] S. Deevi, "Self-propagating high-temperature synthesis of molybdenum disilicide," *Journal of materials science,* vol. 26, pp. 3343-3353, 1991.

[147] G. L. Humphrey, "The heats of combustion and formation of titanium nitride (TiN) and titanium carbide (TiC)," *Journal of the American Chemical Society,* vol. 73, pp. 2261-2263, 1951.

[148] C. Degnan and P. Shipway, "The incorporation of self-propagating, high-temperature synthesis-formed Fe-TiB$_2$ into ferrous melts," *Metallurgical and Materials Transactions A,* vol. 33, pp. 2973-2983, 2002.

[149] W. D. Kingery, H. K. Bowen, and D. R. Uhlmann, *Introduction to ceramics*. New York: John Wiley and Sons, 1976.

[150] B. Bharat, "Wear," in *Principles and applications of tribology*, ed New York: John Wiley and Sons, 1999, pp. 479-585.

[151] N. Chawla and K. K. Chawla, *Metal matrix composites* vol. 2nd New York: Springer, 2013.

[152] M. Balasubramanian, *Composite Materials and Processing*. Baton Rouge: CRC Press, 2013.

[153] P. Matteazzi, G. L. Caër, and A. Mocellin, "Synthesis of nanostructured materials by mechanical alloying," *Ceramics International,* vol. 23, pp. 39-44, 1997.

[154] P. Chagnon and P. Fauchais, "Thermal spraying of ceramics," *Ceramics International,* vol. 10, pp. 119-131, 1984.

[155] V. V. Sobolev, J. M. Guilemany, and J. Nutting, *High velocity oxy-fuel spraying : theory, structure-property relationships and applications*: London, Maney, 2004.

[156] N. Cinca and J. M. Guilemany, "Thermal spraying of transition metal aluminides: An overview," *Intermetallics,* vol. 24, pp. 60-72, 2012.

[157] X. Guan, K. Iwasaki, K. Kishi, M. Yamamoto, and R. Tanaka, "Dry sliding wear behavior of Fe–28Al and Fe–28Al–10Ti alloys," *Materials Science and Engineering: A,* vol. 366, pp. 127 - 134, 2004.

[158] G. Taillon, F. Pougoum, S. Lavigne, L. Ton-That, R. Schulz, E. Bousser*, et al.*, "Cavitation erosion mechanisms in stainless steels and in composite metal-ceramic HVOF coatings," *Wear,* vol. 364, pp. 201-210, 2016.

[159] F. Pougoum, T. Schmitt, L. Martinu, J.-E. Klemberg-Sapieha, S. Savoie, and R. Schulz, "Wear behavior of Fe$_3$Al-TiN-TiB$_2$ HVOF coatings: A comparative study between in situ and ex situ powder processing routes," *Ceramics International,* vol. 43, pp. 8040-8050, 2017.

[160] J. Archard, "Contact and rubbing of flat surfaces," *Journal of applied physics,* vol. 24, pp. 981-988, 1953.

[161] S.-C. Lee, W.-Y. Ho, and W.-L. Pao, "Process and properties of CrN coating deposited on plasma nitrided high-speed steel," *Surface and Coatings Technology,* vol. 73, pp. 34-38, 1995.

[162] E. I. Meletis, A. Erdemir, and G. R. Fenske, "Tribological characteristics of DLC films and duplex plasma nitriding/DLC coating treatments," *Surface and Coatings Technology,* vol. 73, pp. 39-45, 1995.

[163] E. Bemporad, M. Sebastiani, D. De Felicis, F. Carassiti, R. Valle, and F. Casadei, "Production and characterization of duplex coatings (HVOF and PVD) on Ti–6Al–4V substrate," *Thin Solid Films,* vol. 515, pp. 186-194, 2006.

[164] E. Bemporad, M. Sebastiani, M. H. Staia, and E. Puchi Cabrera, "Tribological studies on PVD/HVOF duplex coatings on Ti6Al4V substrate," *Surface and Coatings Technology,* vol. 203, pp. 566-571, 2008.

[165] T. Fu, Z. F. Zhou, Y. M. Zhou, X. D. Zhu, Q. F. Zeng, C. P. Wang*, et al.*, "Mechanical properties of DLC coating sputter deposited on surface nanocrystallized 304 stainless steel," *Surface and Coatings Technology,* vol. 207, pp. 555-564, 2012.

[166] P. C. Wo, P. R. Munroe, Z. T. Jiang, Z. F. Zhou, K. Y. Li, and Z. H. Xie, "Enhancing toughness of CrN coatings by Ni addition for safety-critical applications," *Materials Science and Engineering A-structural materials Properties Microstructure and Processing,* vol. 596, pp. 264-274, 2014.

[167] R. K. Singh, Z. Zhou, L. K. Y. Li, P. Munroe, M. Hoffman, and Z. Xie, "Design of functionally graded carbon coatings against contact damage," *Thin Solid Films,* vol. 518, pp. 5769-5776, 2010.

[168] H. S. Kim and M. B. Bush, "The effects of grain size and porosity on the elastic modulus of nanocrystalline materials," *Nanostructured Materials,* vol. 11, pp. 361-367, 1999.

[169] B. Warcholiński, A. Gilewicz, Z. Kukliński, and P. Myśliński, "Arc-evaporated CrN, CrN and CrCN coatings," *Vacuum,* vol. 83, pp. 715-718, 2008.

[170] C. Donnet and A. Erdemir, *Tribology of diamond-like carbon films: fundamentals and applications*. New York Springer, 2008.

[171] Y. Liu, A. Erdemir, and E. I. Meletis, "A study of the wear mechanism of diamond-like carbon films," *Surface and Coatings Technology,* vol. 82, pp. 48-56, 1996.

[172] A. Matthews, S. Franklin, and K. Holmberg, "Tribological coatings: contact mechanisms and selection," *Journal of Physics D: Applied Physics,* vol. 40, pp. 5463-5475, 2007.

[173] Q. Wang, F. Zhou, X. Ding, Z. Zhou, C. Wang, W. Zhang*, et al.*, "Microstructure and water-lubricated friction and wear properties of CrN(C) coatings with different carbon contents," *Applied Surface Science,* vol. 268, pp. 579-587, 2013.

[174] A. C. Ferrari and J. Robertson, "Interpretation of Raman spectra of disordered and amorphous carbon," *Physical Review B,* vol. 61, pp. 14095-14107, 2000.

[175] V. S. Rao, "A review of the electrochemical corrosion behaviour of iron aluminides," *Electrochimica Acta,* vol. 49, pp. 4533-4542, 2004.

[176] J. Nachman and E. Duffy, "Effect of alloying additions on sea water corrosion resistance of iron-aluminum base alloys," *Corrosion,* vol. 30, pp. 357-365, 1974.

[177] G. Sharma, P. Singh, R. Sharma, K. Gaonkar, and R. Ramanujan, "Aqueous corrosion behavior of iron aluminide intermetallics," *Journal of Materials Engineering and Performance,* vol. 16, pp. 779-783, 2007.

[178] S. Lavigne, F. Pougoum, S. Savoie, L. Martinu, J. E. Klemberg-Sapieha, and R. Schulz, "Cavitation erosion behavior of HVOF CaviTec coatings," *Wear,* vol. 386-387, pp. 90-98, 2017.

[179] G. Ji, O. Elkedim, and T. Grosdidier, "Deposition and corrosion resistance of HVOF sprayed nanocrystalline iron aluminide coatings," *Surface and Coatings Technology,* vol. 190, pp. 406-416, 2005.

[180] W.-M. Zhao, Y. Wang, L.-X. Dong, K.-Y. Wu, and J. Xue, "Corrosion mechanism of NiCrBSi coatings deposited by HVOF," *Surface and Coatings Technology,* vol. 190, pp. 293-298, 2005.

[181] C. Godoy, M. M. Lima, M. M. R. Castro, and J. C. Avelar-Batista, "Structural changes in high-velocity oxy-fuel thermally sprayed WC–Co coatings for improved corrosion resistance," *Surface and Coatings Technology,* vol. 188–189, pp. 1-6, 2004.

[182] F. Mindivan and H. Mindivan, "The Study of Electroless Ni-P/Ni-B Duplex Coating on HVOF-Sprayed Martensitic Stainless Steel Coating," *Acta Physica Polonica A,* vol. 131, pp. 64-67, 2017.

[183] G. Bolelli, L. Lusvarghi, M. Montecchi, F. P. Mantini, F. Pitacco, H. Volz*, et al.*, "HVOF-sprayed WC-Co as hard interlayer for DLC films," *Surface and Coatings Technology,* vol. 203, pp. 699-703, 2008.

[184] R. S. Lillard, D. P. Butt, T. N. Taylor, K. C. Walter, and M. Nastasi, "The breakdown mechanism of diamond-like carbon coated nickel in chloride solution," *Corrosion Science,* vol. 39, pp. 1605-1624, 1997.

[185] P. Papakonstantinou, J. F. Zhao, P. Lemoine, E. T. McAdams, and J. A. McLaughlin, "The effects of Si incorporation on the electrochemical and nanomechanical properties of DLC thin films," *Diamond and Related Materials,* vol. 11, pp. 1074-1080, 2002.

[186] C. Liu, Q. Bi, and A. Matthews, "EIS comparison on corrosion performance of PVD TiN and CrN coated mild steel in 0.5 M NaCl aqueous solution," *Corrosion Science,* vol. 43, pp. 1953-1961, 2001.

[187] A. Lasia, " Electrochemical impedance spectroscopy and its applications," in *Modern aspects of electrochemistry: No. 32*, ed New York: Kluwer Academic, 2002.

[188] D. Li, S. Guruvenket, S. Hassani, E. Bousser, M. Azzi, J. A. Szpunar*, et al.*, "Effect of Cr interlayer on the adhesion and corrosion enhancement of nanocomposite TiN-based coatings deposited on stainless steel 410," *Thin Solid Films,* vol. 519, pp. 3128-3134, 2011.

[189] M. Azzi and J.-E. Klemberg-Sapieha, "Tribocorrosion test protocols for sliding contacts," in *Tribocorrosion of passive metals and coatings*, ed Cambridge: Woodhead Publishing Limited, 2011, pp. 222 - 237.

[190] R. Schulz, S. Gaudet, and S. Savoie, "Metal-Ceramic Nanocomposites With Iron Aluminide Metal Matrix And Use Thereof As Protective Coatings For Tribological Applications," 2015.

[191] M. Amiriyan, H. D. Alamdari, C. Blais, S. Savoie, R. Schulz, and M. Gariepy, "Dry sliding wear behavior of Fe$_3$Al and Fe$_3$Al/TiC coatings prepared by HVOF," *Wear,* vol. 342, pp. 154-162, 2015.

[192] Y. L. Liu, J. Cheng, B. Yin, S. Y. Zhu, Z. H. Qiao, and J. Yang, "Study of the tribological behaviors and wear mechanisms of WC-Co and WC-Fe$_3$Al hard materials under dry sliding condition," *Tribology International,* vol. 109, pp. 19-25, 2017.

[193] Y. Bai, J. Xing, Z. Liu, S. Ma, E. Liu, and Y. Gao, "The microstructure and tribological property of in-situ Al$_2$O$_3$/Fe–25Al composites in argon atmosphere," *Intermetallics,* vol. 38, pp. 107-115, 2013.

[194] I. Baker, "An Overview of the Mechanical Properties of FeAl," *Materials Research Society Symposia Proceedings. Materials Research Society,* vol. 1128, 2011.

[195] J. M. Guilemany, N. Cinca, S. Dosta, and I. G. Cano, "FeAl and NbAl3 Intermetallic-HVOF Coatings: Structure and Properties," *Journal of Thermal Spray Technology,* vol. 18, pp. 536-545, 2009.

[196] A. Radhakrishna, R. G. Baligidad, and D. S. Sarma, "Effect of carbon on structure and properties of FeAl based intermetallic alloy," *Scripta Materialia,* vol. 45, pp. 1077 - 1082, 2001.

[197] M. Amiriyan, C. Blais, S. Savoie, R. Schulz, M. Gariepy, and H. D. Alamdari, "Mechanical Behavior and Sliding Wear Studies on Iron Aluminide Coatings Reinforced with Titanium Carbide," *Metals,* vol. 7, p. 177, 2017.

[198] C. Wang, Y. B. Lin, X. Z. Guo, and J. Tao, "Al$_2$O$_3$ reinforced Fe-Al composite coatings prepared by double glow discharge technique," *Surface Engineering,* vol. 29, pp. 572-579, 2013.

[199] Factsage. (2017, 01-11-2017). *Factsage*. Available: http://www.factsage.com

[200] ThermoCalc-Software. (2017, 01-11-2017). *Thermo-Calc*. Available: http://www.thermocalc.com/products-services/software/thermo-calc/

[201] J. G. Legoux, E. Irissou, and C. Moreau, "Effect of Substrate Temperature on the Formation Mechanism of Cold-Sprayed Aluminum, Zinc and Tin Coatings," *Journal of Thermal Spray Technology,* vol. 16, pp. 619-626, 2007.

[202] M. Prystay, P. Gougeon, and C. Moreau, "Structure of plasma-sprayed zirconia coatings tailored by controlling the temperature and velocity of the sprayed particles," *Journal of Thermal Spray Technology,* vol. 10, pp. 67-75, 2001.

[203] O. J. Berghaus, J. G. Legoux, C. Moreau, R. Hui, C. Decès-Petit, W. Qu*, et al.*, "Suspension HVOF Spraying of Reduced Temperature Solid Oxide Fuel Cell Electrolytes," *Journal of Thermal Spray Technology,* vol. 17, pp. 700-707, 2008.

[204] S. Wilson and A. T. Alpas, "Wear mechanism maps for metal matrix composites," *Wear,* vol. 212, pp. 41-49, 1997.

[205] S. Lim, "Recent developments in wear-mechanism maps," *Tribology International,* vol. 31, pp. 87-97, 1998.

[206] M. Roy, "Use of wear mechanism map to engineer surfaces for enhanced wear resistance," *Transactions of the Indian Institute of Metals,* vol. 62, pp. 197-208, 2009.